Power System Disturbance Analysis and Detection Based on Wide-Area Measurements

Jingyuan Dong

Dissertation submitted to the faculty of the Virginia Polytechnic Institute and State University in partial fulfillment of the requirements for the degree of

Doctor of Philosophy
In
Electrical Engineering

Committee Members:
Dr. James S. Thorp (Chair)
Dr. Yilu Liu
Dr. Virgilio A. Centeno
Dr. Pushkin Kachroo
Dr. Irene E. Leech

December 10, 2008
Blacksburg, Virginia

Keywords: Wide-Area Measurements, Frequency Monitoring Network, Power System Dynamics, Power System Monitoring, Disturbance Detection.

Power System Disturbance Analysis and Detection Based on Wide-Area Measurements

by

Jingyuan Dong

Abstract

Wide-area measurement systems (WAMS) enable the monitoring of overall bulk power systems and provide critical information for understanding and responding to power system disturbances and cascading failures. The North American Frequency Monitoring Network (FNET) takes GPS-synchronized wide-area measurements in a low-cost, easily deployable manner at the 120 V distribution level, which presents more opportunities to study power system dynamics. This work explores the topics of power system disturbance analysis and detection by utilizing the wide-area measurements obtained in the distribution networks.

In this work, statistical analysis is conducted based on the major disturbances in the North American Interconnections detected by the FNET situation awareness system between 2006 and 2008. Typical frequency patterns of the generation and load loss events are analyzed for the three North American power Interconnections: the Eastern Interconnection (EI), the Western Electricity Coordinating Council (WECC), and the Electric Reliability Council of Texas (ERCOT). The linear relationship between frequency deviation and frequency change rate during generation/loss mismatch events is verified by the measurements in the three Interconnections. The relationship between the generation/load mismatch and system frequency is also examined based on confirmed generation loss events in the EI system. And a power mismatch estimator is developed to improve the current disturbance detection program. Various types of power system disturbances are examined based on frequency, voltage and phase angle to obtain the event signatures in the measurements.

To better understand the propagation of disturbances in the power system, an automated visualization tool is developed that can generate frequency and angle replays of disturbances, as well as image snapshots. This visualization tool correlates the wide-area measurements with geographical information by displaying the measurements over a geographical map. This work makes an attempt to investigate the visualization of the angle profile in the wide-area power system to improve situation awareness.

This work explores the viability of relying primarily on distribution-level measurements to detect and identify line outages, a topic not yet addressed in previous works. Line outage sensitivity at different voltage levels in the Tennessee Valley Authority (TVA) system is examined to analyze the visibility of disturbances from the point of view of wide-area measurements. The sensor placement strategy is proposed for better observability of the line trip disturbances. The characteristics of line outages are studied extensively with simulations and real measurements. Line trip detection algorithms are proposed that employs the information in frequency and phase angle measurements. In spite of the limited FDR coverage and confirmed training cases, an identification algorithm is developed which uses the information in the real measurements as well as the simulation cases to determine the tripped line.

Acknowledgments

I would like to offer my first and foremost appreciation to Dr. James Thorp and Dr. Yilu Liu for their patient guidance, support and encouragement, without which this dissertation would not have been possible. I thank Dr. Liu for her support and encouragement both in my academic and personal life. I can not be more grateful for her invaluable counsel that has consistently inspired me to make research progress and pursue personal improvement.

Thanks are extended to members in my advisory committee: Dr. Virgilio Centeno, for providing encouragement and guidance in my academic progress and teaching assistant assignments; Dr. Pushkin Kachroo and Dr. Irene Leech, for their participation on my committee and valuable advices and comments.

Special thanks go to Dr. Richard Conners, for offering valuable suggestions to my work. I would also like to thank Dr. Hengxu Zhang and Dr. Wei Li who had happily shared with me their experiences and ideas concerning this work. I am thankful for the foundational work and contributions especially from Dr. Jian Zuo, Dr. Kyung Soo Kook, Dr. R. Matthew Gardner, Dr. Mark Baldwin, Kevin Khan, Lei Wang, Tao Xia, Jason Bank, Yingchen Zhang, Dr. Jin Tao, Joshua K. Wang, and Jon Burgett.

Much appreciation goes to my colleagues in the power group: Dr. Dawei Fan, Dr. Ming Zhou, Andrew Arana, Emanuel Bernabeu, Yishan Liang, for their support and friendship.

Thanks to Lisa Beard and Gary Kobet of TVA for providing line outage data and information, Tony Weekes of Manitoba Hydro for providing PMU measurements and valuable insights, and Dave Bertagnolli of ISO New England for his industry insights.

Finally, I would like to express my deepest gratitude to my family: my father Zhenxing Dong, my mother Qiutao Song and my brother Xiaolei Dong, for their endless love and support. I thank my parents for being by my side while I am preparing this dissertation. To me, their support is the most important thing in the world that encourages me to fulfill my pursuit of a doctorate.

Table of Contents

List of Figures

List of Tables

Chapter 1 Introduction

With the increase of loading of power grids and massive inter-area power transfers enabled by the deregulation in the 80's and 90's, power systems are operated close to the stability limit. The bulk power systems are continuously subject to disturbances which necessitates the improvement of situation awareness including reliable and timely information of the systems' dynamic performance. The time-synchronized phasor measurement is acknowledged as the revolutionary technology that enables the wide-area monitoring of the bulk power systems in order to better understand and respond to the disturbances [1][2]. Since the invention of the first Phasor Measurement Unit (PMU) in 1988 [3], extensive research has been conducted to utilize the information obtained from PMUs for better situation awareness including state estimation [4]-[6] and visualization [7].

1.1 Frequency Monitoring Network (FNET)

The North American Frequency Monitoring Network (FNET) implements Wide-Area Measurement System (WAMS) in a low-cost, easily deployable manner such that the entire North America power grid can be monitored at the distribution voltage level. The Frequency Disturbance Recorders (FDRs) collect frequency, single-phase voltage and angle with high precision. GPS-synchronized measurements are taken at 120 V typical office outlets, sent via Internet and managed on a central server located at Virginia Tech [8]. Over 50 FDR units have been deployed covering the four Interconnections of the North America power grid: the Eastern Interconnection (EI), the Western Electricity Coordinating Council system (WECC), the Electric Reliability Council of Texas system (ERCOT), and the Quebec Interconnection. Figure 1.1 depicts the current and future locations of FDRs.

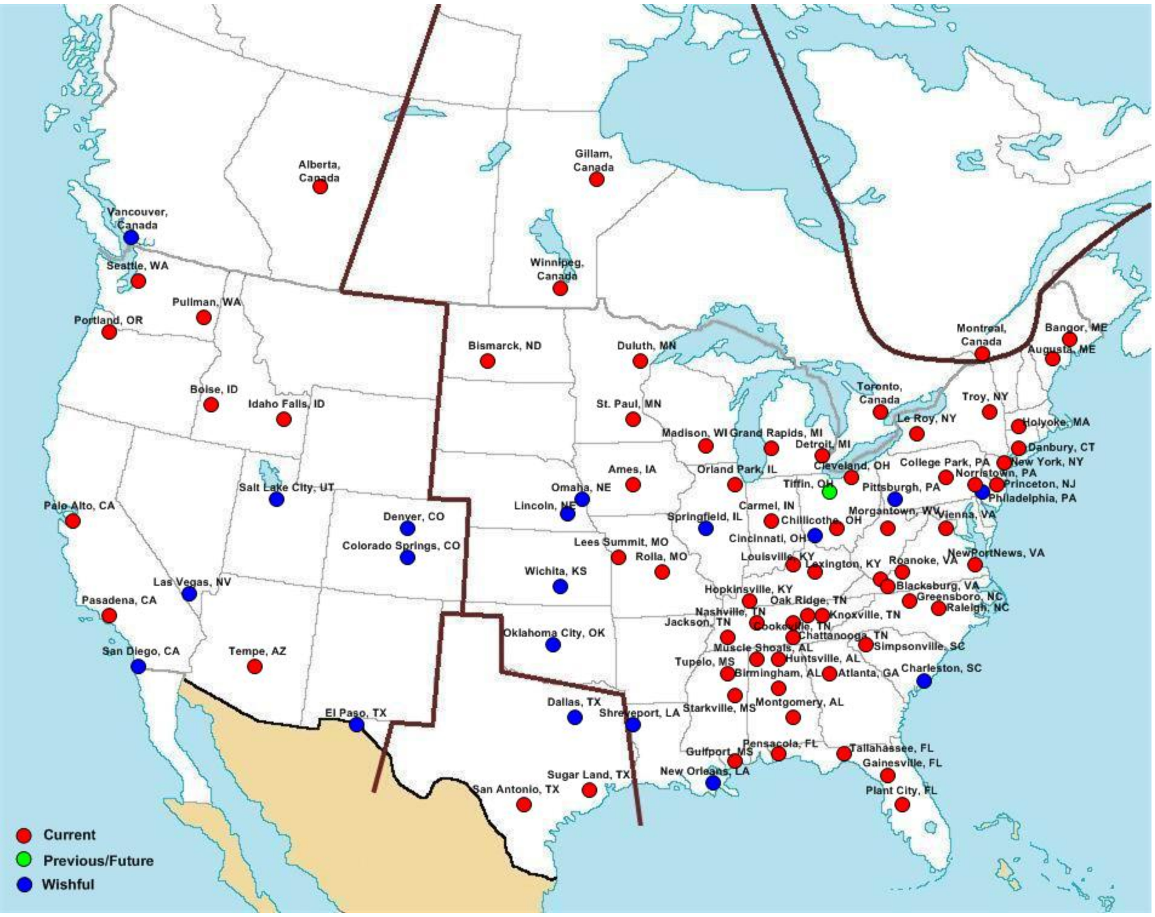

Figure 1.1 Current FDR locations as of November 2008 (map source: USGS)

A situation awareness system has been implemented on the FNET server to detect and analyze power system disturbances in near-real time based on frequency measurements [9]. Once the FNET server detects a significant disturbance, it will automatically classify the event as generation-trip like or load-rejection like, estimate the generation-load mismatch amount, and triangulate event location. Since its implementation in 2006, the situation awareness system has been continuously detecting and recording the information of the disturbances in the EI, the WECC and the ERCOT power systems. In addition, over 4 years worth of dynamic data have been recorded including frequency, voltage and phase angle in the North American power Interconnections, which presents opportunities for studies in various areas of the system dynamics and performances.

1.2 Organization of Study

With the wealth of information provided by FNET, this work explores the analysis and detection of the disturbances in bulk power systems by utilizing the wide-area measurements obtained at the distribution voltage level.

Chapter 2 illustrates the statistical analysis based on the disturbances detected by FNET situation awareness system in 2006 to 2008. Comparisons are made for the EI system and the WECC system on the occurrences of major disturbances during a day and different seasons. Typical frequency excursion patterns in the Interconnections and their possible causes are analyzed. The relationship between generation/load mismatch and frequency is investigated based on confirmed generator trips from 2007 to 2008, and then a power mismatch estimator is developed. The recovery patterns following disturbances are also studied to evaluate control performances of the Interconnections.

Chapter 3 continues the discussion of power system disturbances by analyzing several major events in the EI in 2007 and 2008. Frequency, voltage and phase angle measurements are examined in order to understand the ‘signatures’ of the disturbances such as three-phase fault, islanding, system outage and HVDC faults, etc. The measurements from PMU and FDR are compared to validate the data quality at lower voltage level. The dynamic performance of AC/DC systems is analyzed based on the measurements obtained from two sides of several HVDC links.

Chapter 4 develops an automated visualization tool that is aimed to generate frequency and angle replays of disturbances. This chapter starts with the description of the software tool design and development. Then several application examples are demonstrated including angle visualization and additional visualization options with Google Earth. An attempt is made to display the angle profile in the EI with both simulation results and real measurements.

Chapter 5 and Chapter 6 focus on the detection and identification of single line trips in the Tennessee Valley Authority (TVA) system. Chapter 5 studies line trip sensitivity and sensor placement strategy based on the simulations in Power System Simulator for Engineering (PSS/E) and real line trip measurements. A detection algorithm is proposed that detects the oscillations in frequency caused by line trips.

Different signals obtained from angle are compared and two detection algorithms based on phase angle are developed.

Chapter 6 examines closely the characteristics of the line trip disturbances to find the information in frequency and angle measurements that uniquely describes a certain line trip. A single-line outage case library for all the 500 kV transmission lines in the TVA system is then formed with simulations on the large Eastern Interconnection model. An identification algorithm is developed which identifies a tripped line by matching the measurements with the cases in the library. The visibility of the line trips at 161 kV is studied and the number of sensors required for detection is estimated. This chapter also discusses the factors that may affect the algorithm development and proposes future directions for line trip detection study.

Chapter 7 concludes the dissertation and proposes potential future work.

Chapter 2 Statistical Analysis of Disturbances in the North American Interconnections

Power systems are continuously exposed to disturbances whose impacts on the whole system may vary. The dynamic performance of power systems is reflected by important parameters such as frequency, voltage and phase angle. If θ is the angle position of a generator rotor,

$$\theta(t) = \omega_{syn} t + \delta \tag{2.1}$$

where ω_{syn} is the synchronous angular velocity of the system, and δ is the angular displacement with respect to the synchronous rotating reference. Then the angular velocity ω is

$$\omega = \frac{d\theta}{dt} = \omega_{syn} + \frac{d\delta}{dt} \tag{2.2}$$

Similarly, frequency can be written as

$$f = f_{syn} + \frac{1}{2\pi}\frac{d\delta}{dt} \tag{2.3}$$

When there is any generation-load imbalance, the motion of a generator motor is given by the swing equation:

$$P_m - P_e = \frac{2H}{\omega_{syn}}\frac{d\omega}{dt} \tag{2.4}$$

where H is the rotor inertia constant.

From (2.2), (2.3) and (2.4) we can see that in a disturbance (generation trip, load loss or line trip) where generation and load are not balanced, generators in the system accelerate or decelerate to reduce the power imbalance. Local phase angle and frequency will change simultaneously in response to the disturbance [10]. Therefore, by monitoring those parameters, valuable information about system dynamics can be obtained.

The FNET event trigger has been implemented since January 2006 and has detected over 1200 events in the three North American Interconnections by January 2008. This chapter investigates the dynamic behavior of the bulk transmission systems by examining the frequency measurements from FNET.

The topics about analysis and comparison of disturbances included in this chapter are: 1. Statistical analysis and comparison of noticeable disturbances. 2. Comparison of typical frequency excursions of disturbances. 3. Analysis of the relationship between frequency change rate and frequency variation amount in generation-loss like events. 4. Analysis of the relationship between frequency and generation/load mismatch amount. 5. Analysis and comparison of post-disturbance frequency recovery performances.

2.1 Statistical Analysis and Comparison of Major Disturbances in the Three Interconnections

Any disturbance that leads to a large or sudden mismatch of active power causes a frequency variation [11]. When a generator is tripped, the local frequency will drop suddenly. When there is a significant loss of load, the system frequency will rise sharply. Either case may happen when transmission line trip occurs. The FNET situation awareness system implements an online disturbance detection program that triggers based on the rate of frequency change, and classifies the disturbance type as generation-loss like (generation loss for abbreviation), and load-drop like (load drop for abbreviation) according to its frequency signature.

The online event detection program has identified 960 significant frequency disturbances in the three North America Interconnections from January 23, 2006 to January 31, 2008. Among them, 263 events occurred in the EI system, 468 events in the WECC system, and 229 events in the ERCOT system. The statistical analysis in this section is based on disturbance records in the EI and the WECC, because the trigger of the ERCOT was active after August 2006.

Figure 2.1 through Figure 2.4 show the numbers of events in the EI and WECC systems, respectively. Some common facts shared by disturbances in the two Interconnections are:

1. Generation loss events are more common than load-drop events. Among the 263 identified events in the EI system, 23 of them are load drops and 240 of them are generation loss events. For the WECC system, 135 out of 468 events are load drops, and the others fall into the generation loss category.
2. Generation loss events are more likely to occur in heavy load season. The peak for such disturbances in the EI was in January, and for the WECC, it

appeared in July. Reasons may include weather, lower reserve margins during heavy load periods, and also a greater number of committed generators.

3. Load drop events are more likely to occur in the early morning of local time (0300 to 0700 EST for the EI and PST for the WECC); Generation loss events are more likely to occur in the afternoon of local time (1400 to 1500 EST for the EI and 1300 to 1400 PST for the WECC). The switching-off of the pumped storage which appears as a fast rise in frequency may play a major role on this.

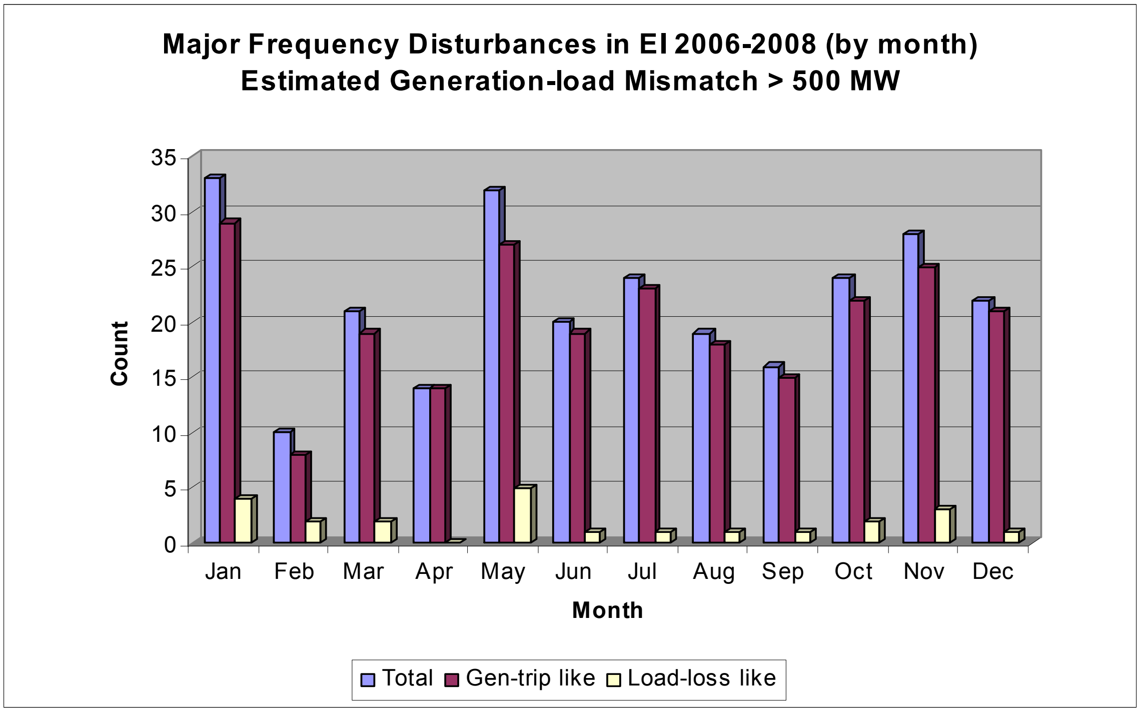

Figure 2.1 Major frequency disturbances (estimated generation-load mismatch > 500MW) in the EI for each month

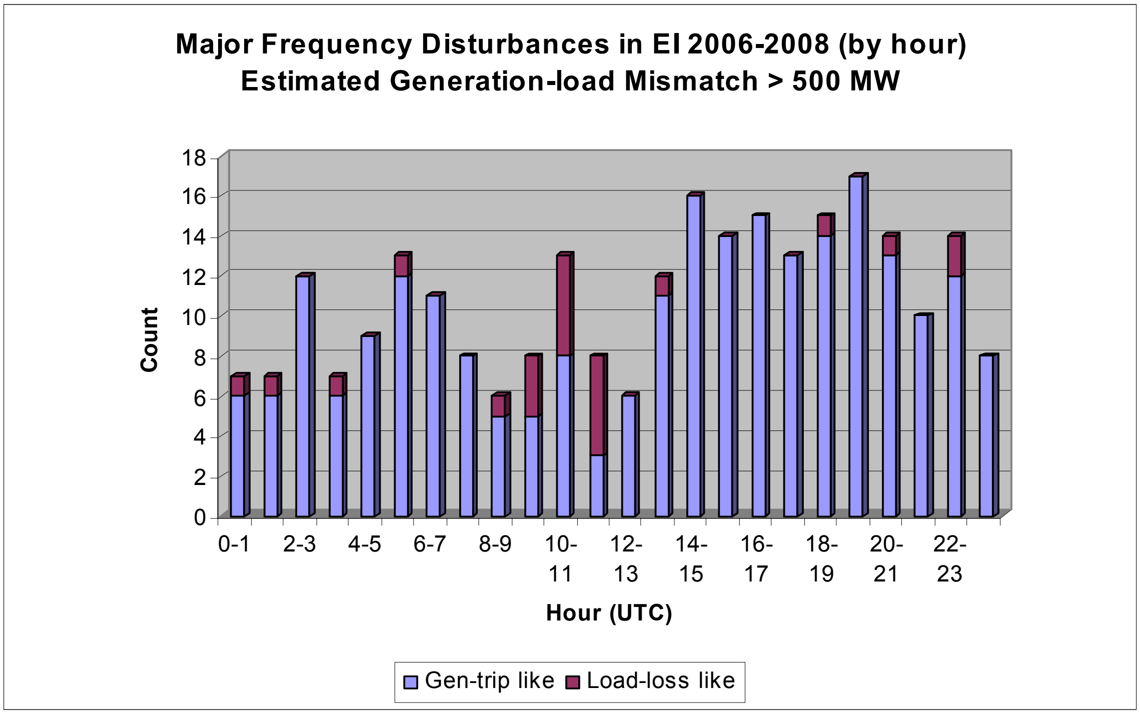

Figure 2.2 Major frequency disturbances (estimated generation-load mismatch > 500MW) in the EI for each hour

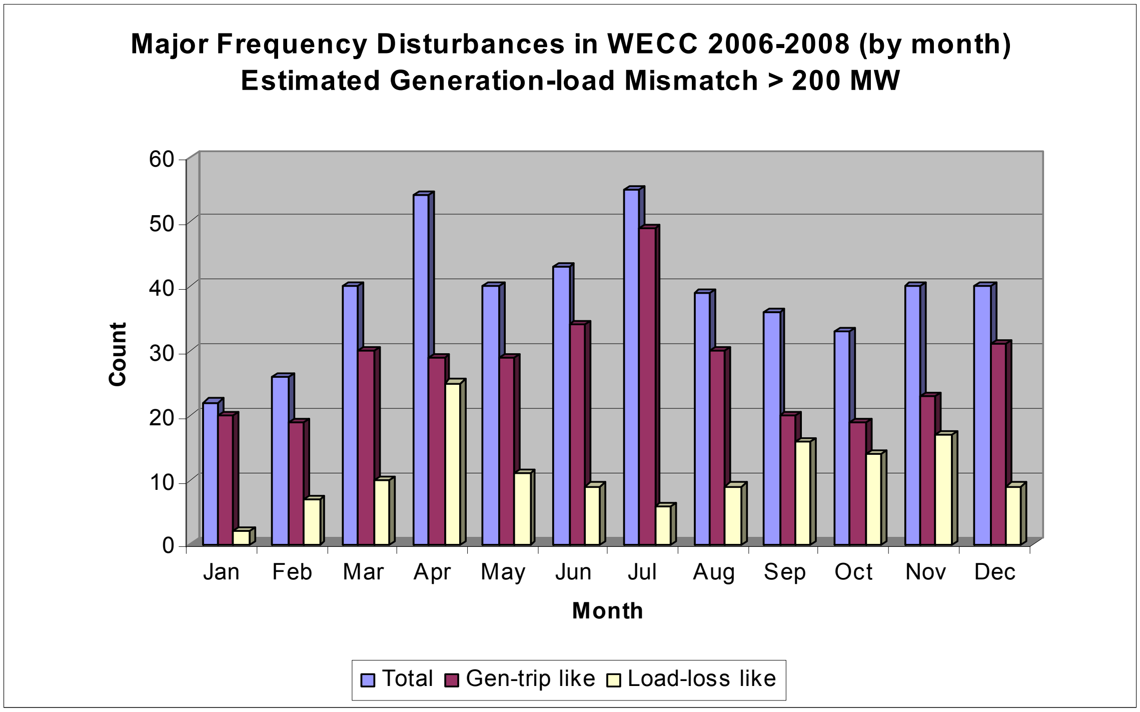

Figure 2.3 Major frequency disturbances (estimated generation-load mismatch > 200MW) in the WECC for each month

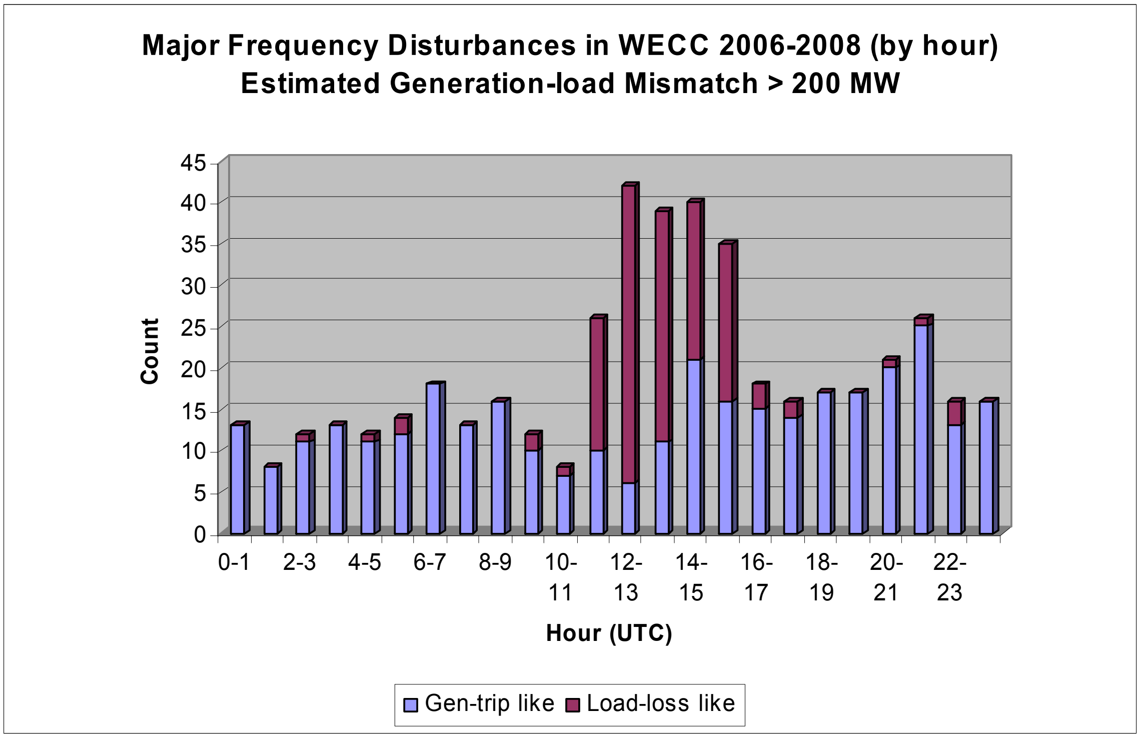

Figure 2.4 Major frequency disturbances (estimated generation-load mismatch > 200MW) in the WECC for each hour

Some distinct characteristics for events in the two Interconnections can be found from the diagrams:

1. The peak of all events in the EI occurred in January, while the peak in the WECC occurred in July.
2. Load drop events in the WECC are more likely to occur in April.
3. Disturbances are more likely to occur between 1400 to 1500 EST in the EI and the generation loss events are more likely to occur between 0900 to 1500 EST. For the WECC system, the peak of disturbances is between 0400 to 0500 PST. Moreover, the generation loss events are more evenly distributed over 24 hours in the WECC system.

On average, about every 3 days (739/263), where 739 is the total number of days and 263 is the total number of identified events in the EI during these days, a major event (defined as generation-load mismatch > 500 MW) is seen in the EI system. The WECC system experiences an event (defined as generation-load mismatch > 200 MW) every 1.5

days (739/468). It may be either generator-trip like or load-rejection like.

Figure 2.5 and Figure 2.6 show the hourly distribution of the generation loss events in the EI and the WECC systems during different seasons over the two years from 2006 to 2008. All the time displayed is standard local time: EST for the EI and PST for the WECC. The disturbances in the winter season (December to the following February) are relative fewer than those during the summer season (June to September) and other months due to fewer winter months. Among the 240 generation loss events in the EI system, the numbers of events during winter, summer and other months are 58, 75 and 107, respectively. And in the WECC system those numbers are 70, 133 and 130 for winter, summer and other seasons respectively among 333 generation loss disturbances.

As is shown in Figure 2.5, in the EI system the generation loss events are more likely to occur around midnight during summer, while the hour between 1300 and 1400 EST during spring and fall sees more disturbances of this kind. Generation loss disturbances are more evenly distributed over hours in winter and most of the generation loss disturbances (37/58) occur during 0900 to 1800 EST.

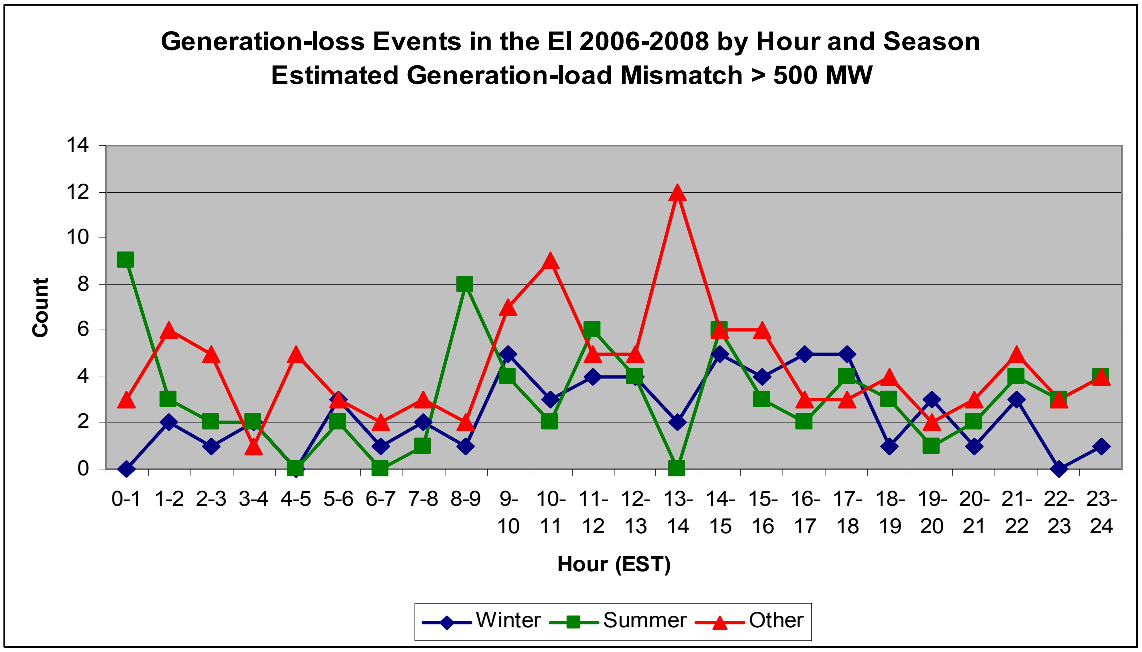

Figure 2.5 Generation-loss like events in the EI for each hour during different seasons

In the WECC system, the generation loss events are more likely to occur between 1100 to 1300 PST in winter and between 1200 to 1400 PST in summer. The disturbances in the WECC are more evenly distributed during other seasons.

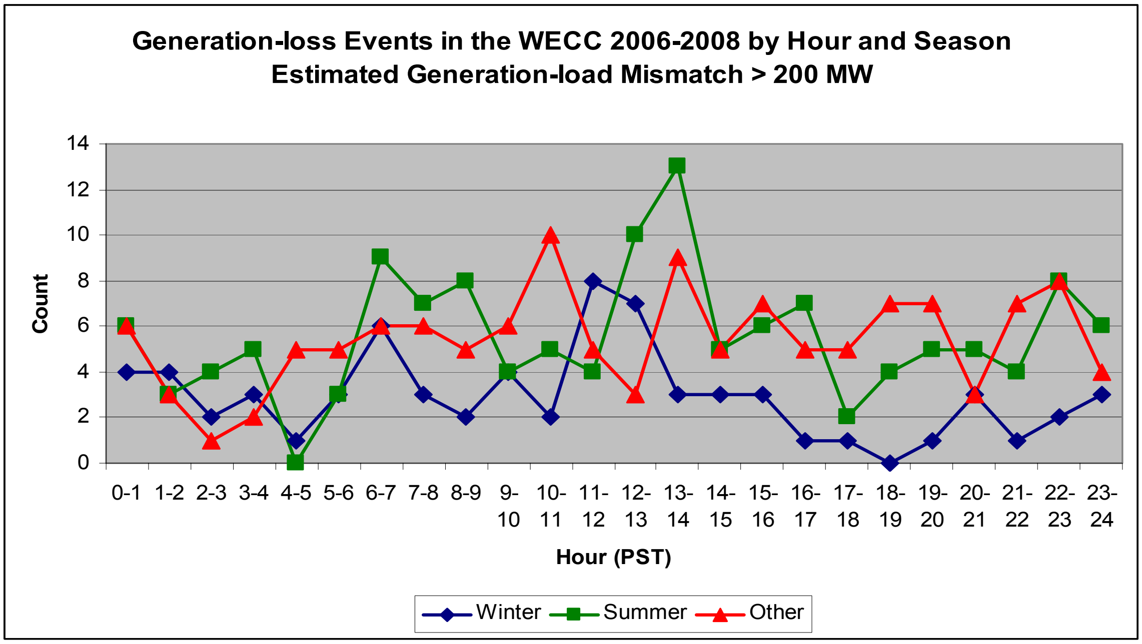

Figure 2.6 Generation-loss like events in the WECC for each hour during different seasons

In order to compare the hourly variations of the generation loss events during different seasons for the EI and the WECC, the percentage of the events in each hour to the total number of events during the season is shown in Figure 2.7 to Figure 2.9. The comparisons in Figure 2.7 and 2.8 show distinct characteristics of the disturbance occurrences during winter and summer in the EI and the WECC, which may indicate the different generation and load profile, reserve distribution and development. For instance, in summer generation loss events are more likely to occur in the hour 0000 to 0100 EST in the EI system whereas the peak of such events occurs during 1300 to 1400 PST in the WECC as shown in Figure 2.8. And no generation loss greater than 500 MW is recorded during this hour in EST in the EI system. Moreover, higher percentage of the generation loss disturbances occurs in the summer in the WECC (39.9%) than in the EI (31.2%).

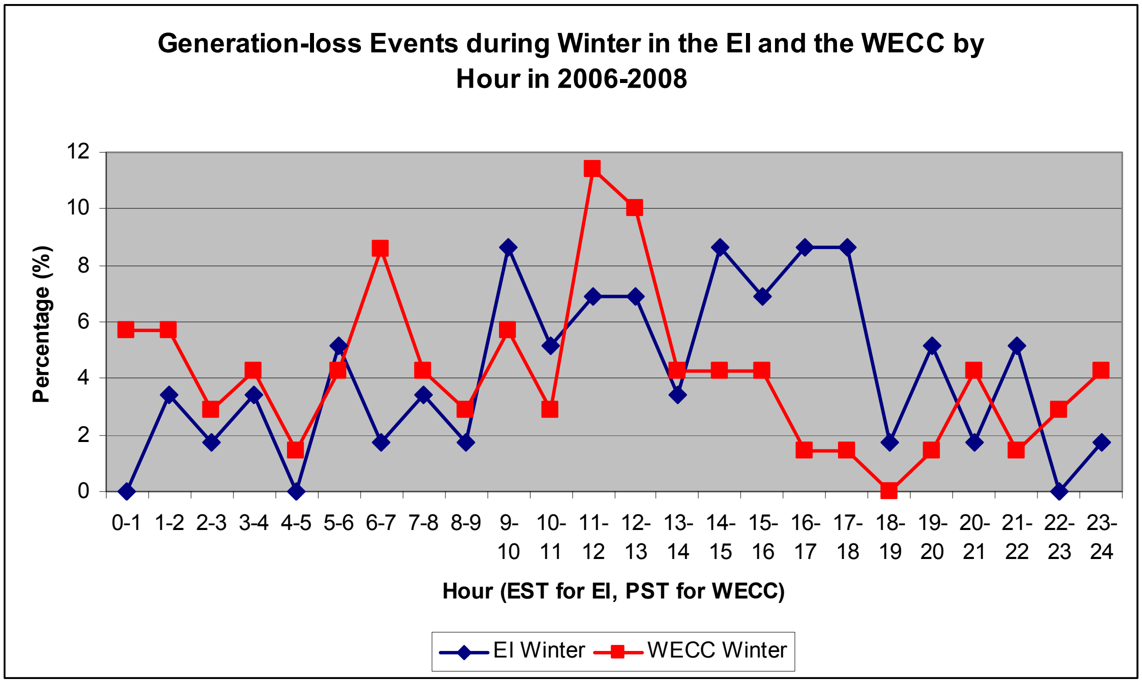

Figure 2.7 Generation-loss like events during winter in the EI and the WECC for each hour

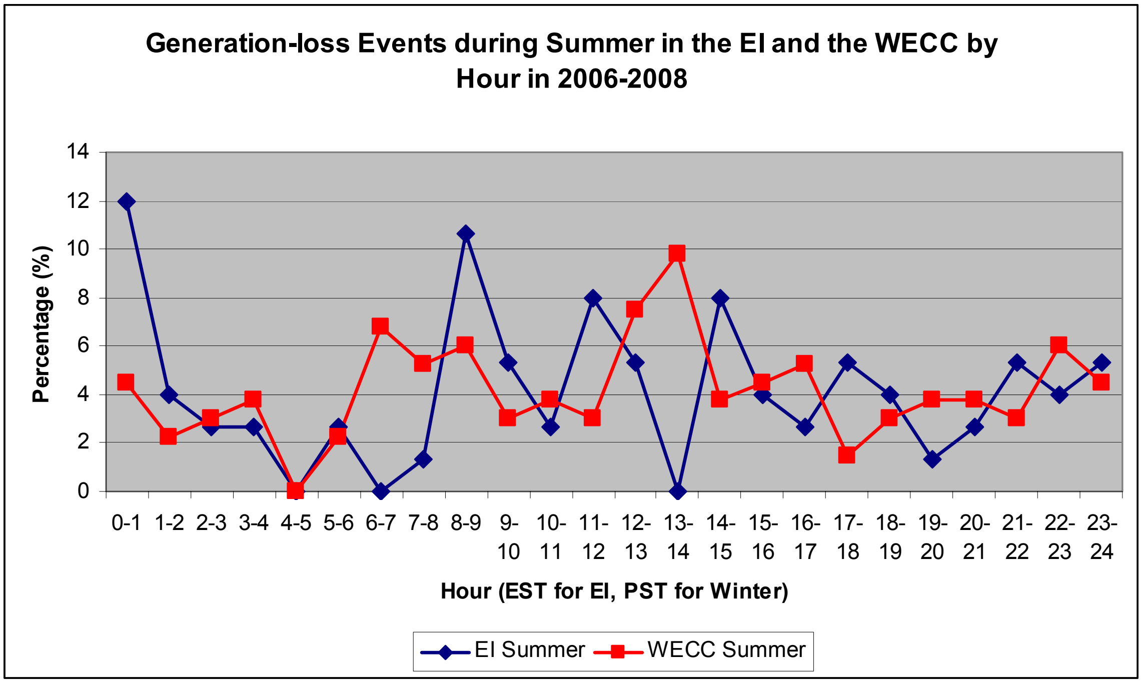

Figure 2.8 Generation-loss like events during summer in the EI and the WECC for each hour

The event distribution by hour in the EI and the WECC demonstrates some similarities. It can be seen from Figure 2.9 that in spring and fall both the WECC and the

EI see more generation loss events during the hours 1000 to 1100 and 1300 to 1400 at local time but the events in the WECC are more evenly distributed over the hours compared with those in the EI.

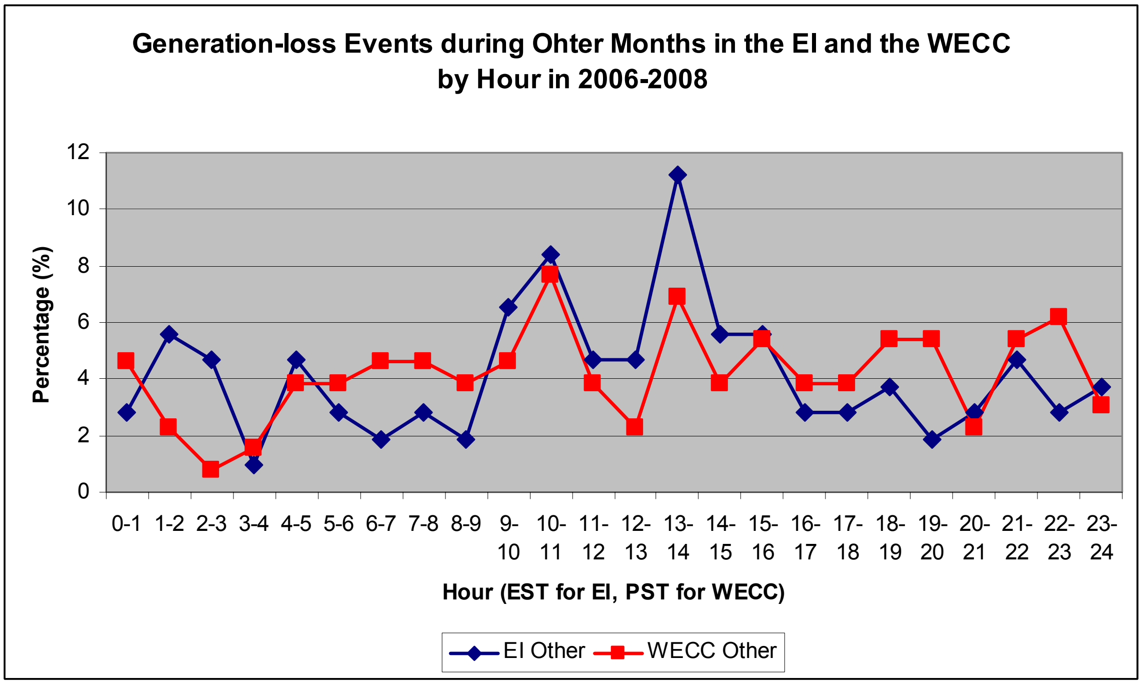

Figure 2.9 Generation-loss like events during other months in the EI and the WECC for each hour

2.2 Typical Frequency Excursions of the Disturbances

Steady-state frequency in an Interconnection is almost on top of each other at different locations, as can be seen in Figure 2.10. Transient frequency during disturbances shows distinct delays between units, but the trends and total amount of frequency deviations are close as in Figure 2.11. Therefore, we can investigate the dynamic situation of an Interconnection by studying its frequency at one observing point. The following analysis is based on data from one FDR unit in each Interconnection.

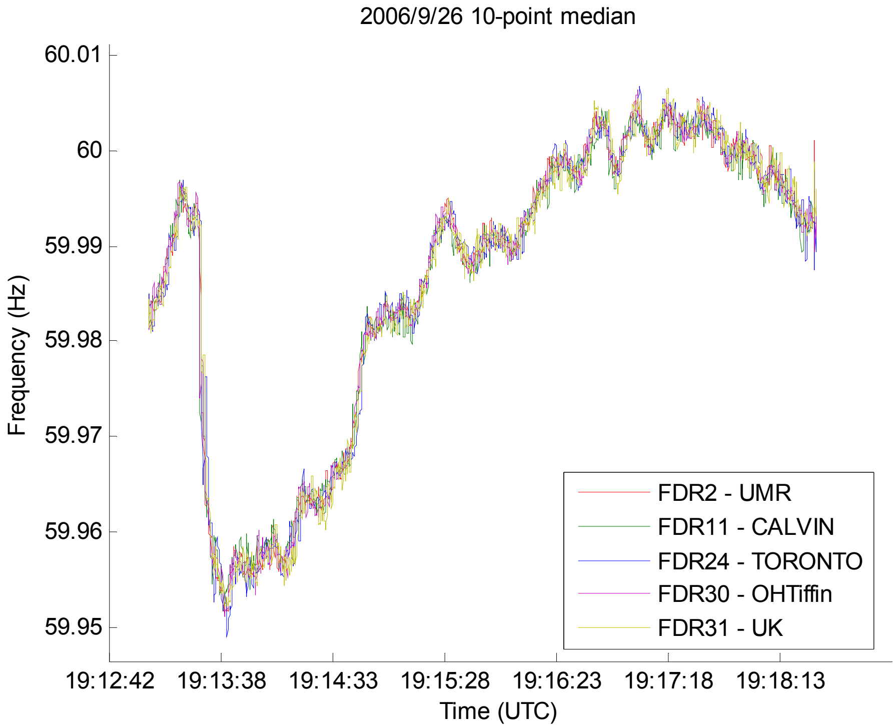

Figure 2.10 Frequency excursion of a generator trip in the EI

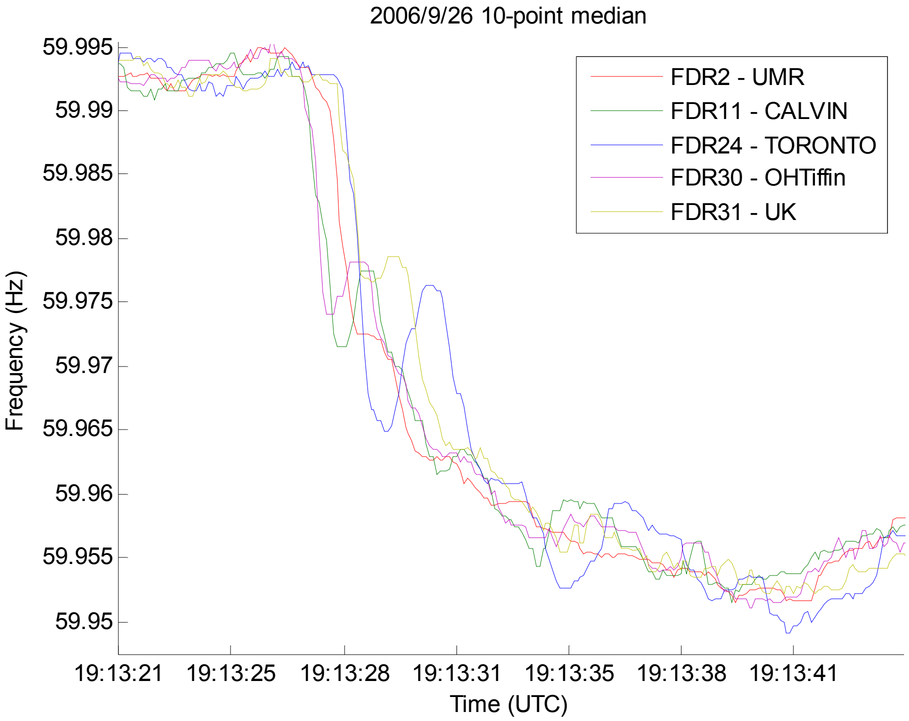

Figure 2.11 Detail of the initial frequency drop of the generator trip event in Figure 2.10

Typical frequency excursions of generation-loss like and load-drop like events in three North America Interconnections: the EI, the WECC and the ERCOT, are shown in Figure 2.12 through Figure 2.17. As can be seen, although all the generation-loss like events initiate sharp frequency drop and load-drop like events, sudden frequency rise, frequency excursions in the three Interconnections show quite distinct characteristics. The difference indicates different generation and load characteristics, and control schemes in the three Interconnections.

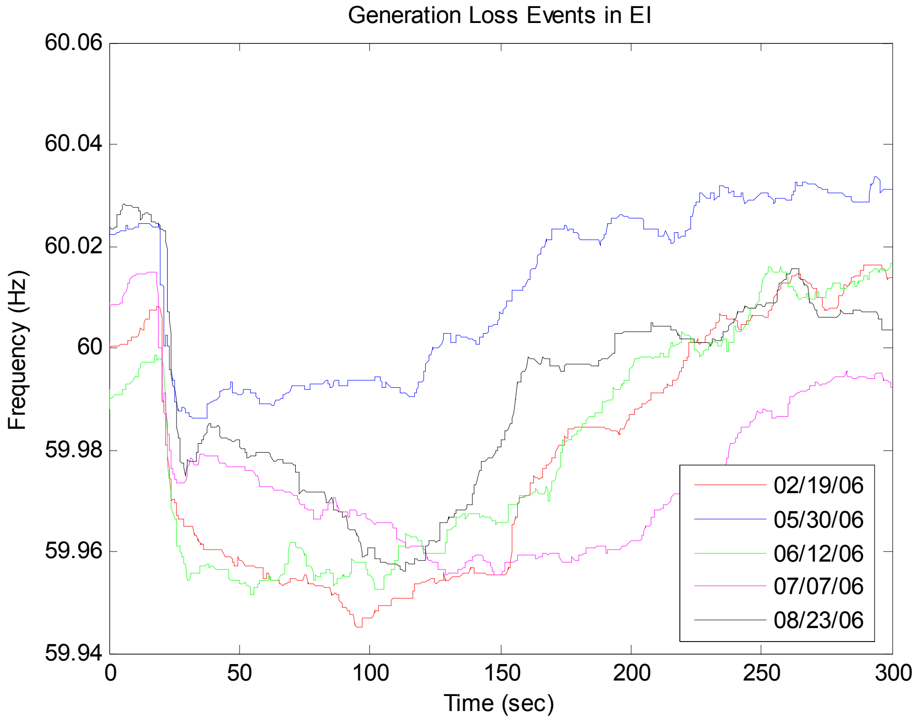

Figure 2.12 Typical generation-loss like events in the EI system

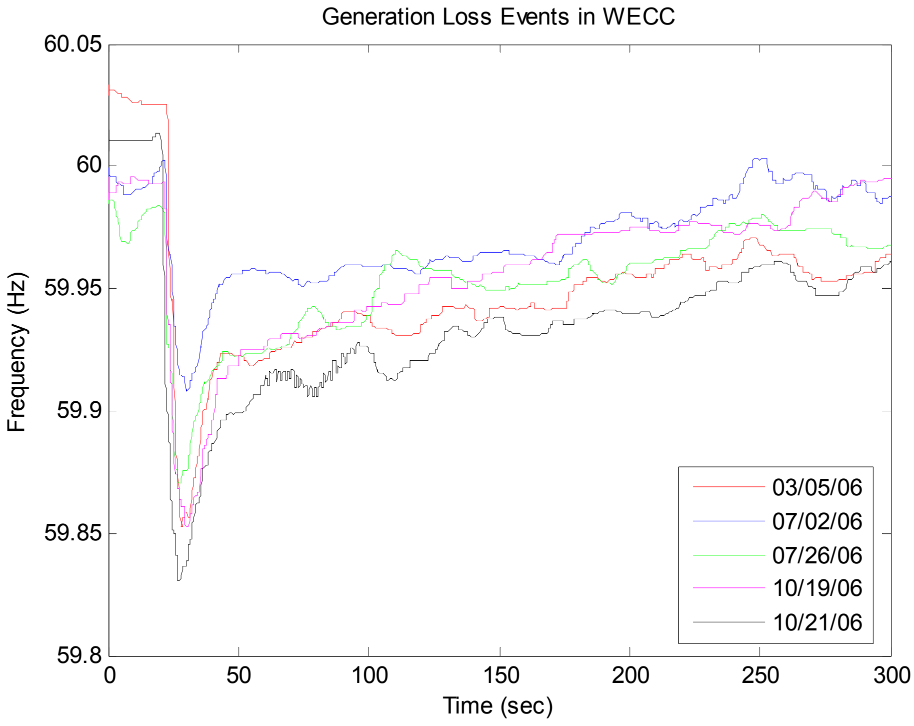

Figure 2.13 Typical generation-loss like events in the WECC system

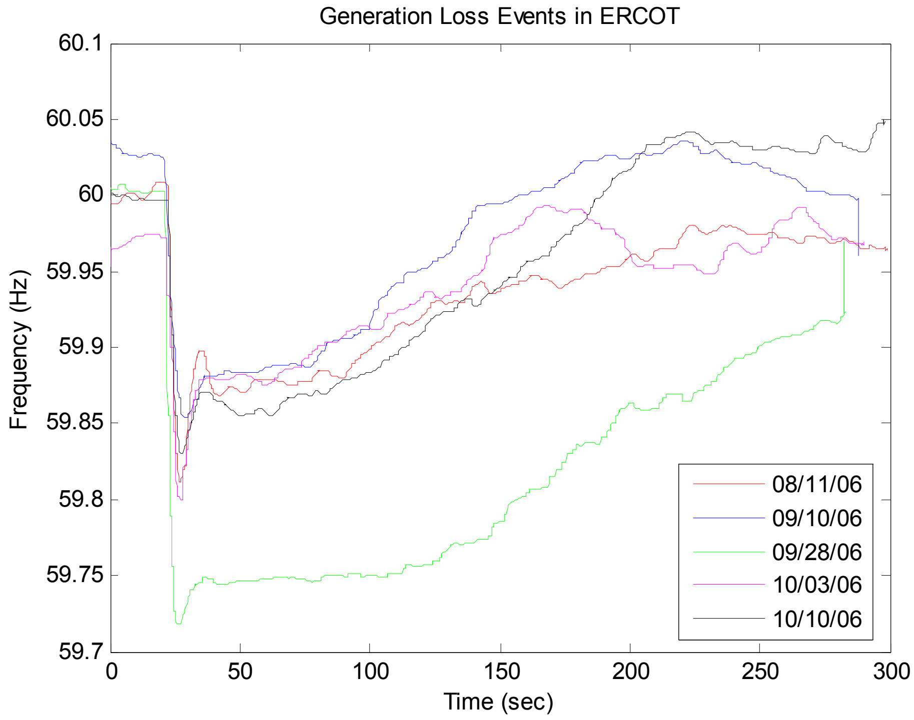

Figure 2.14 Typical generation-loss like events in the ERCOT system

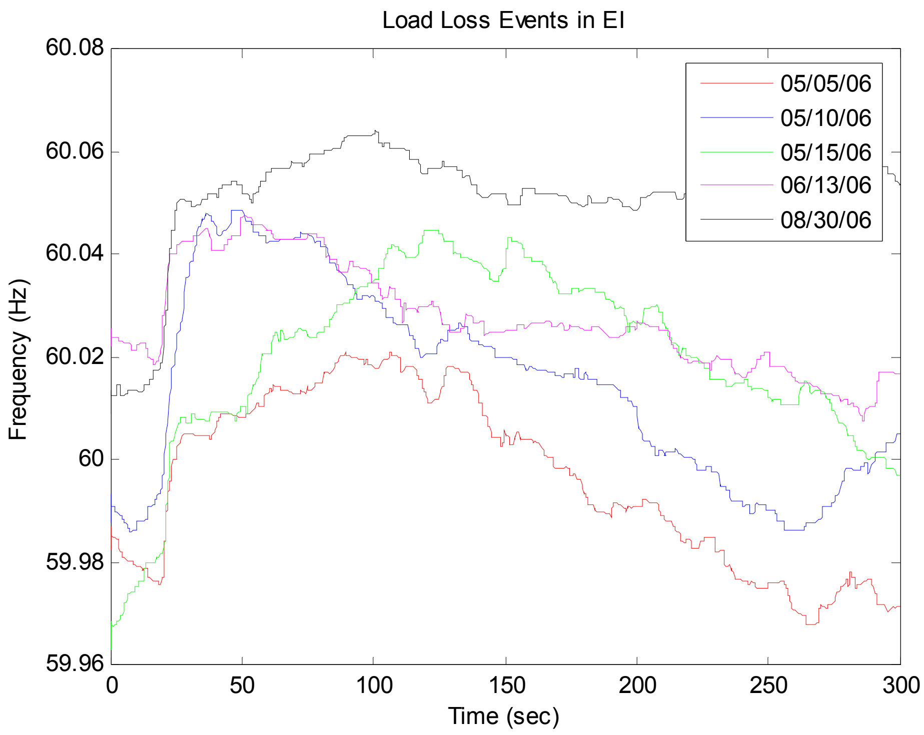

Figure 2.15 Typical load-drop like events in the EI system

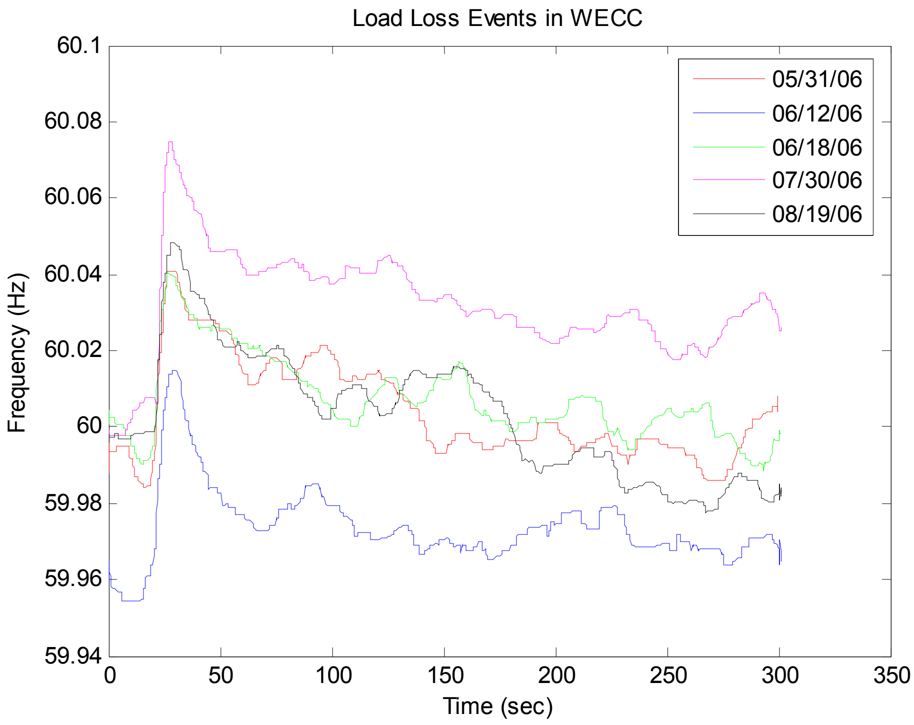

Figure 2.16 Typical load-drop like events in the WECC system

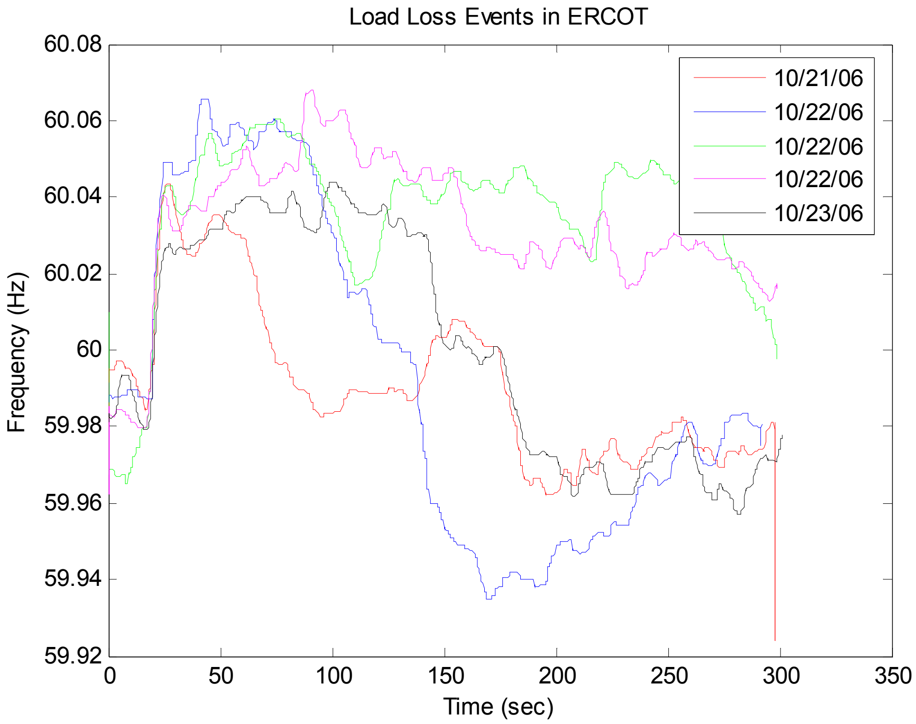

Figure 2.17 Typical load-drop like events in the ERCOT system

The comparison of frequency excursions of generation-loss like and load-drop like events in the three Interconnections can be seen in Figure 2.18 and Figure 2.20. The generation/load loss amount can be estimated from the equation:

$$\Delta P = \beta \Delta f \qquad (2.5)$$

where β is the frequency response characteristic [12] or load-frequency sensitivity coefficient [13]; Δf is the total frequency change amount following the disturbance by $\Delta f = f_{ss2} - f_{ss1}$, where f_{ss1} is the pre-disturbance steady state frequency, f_{ss2} is the post-disturbance steady state frequency. The amount of frequency change from certain amount of generation/load loss varies in different Interconnections, because the EI, the WECC and the ERCOT systems have different β values, which can be found in [12].

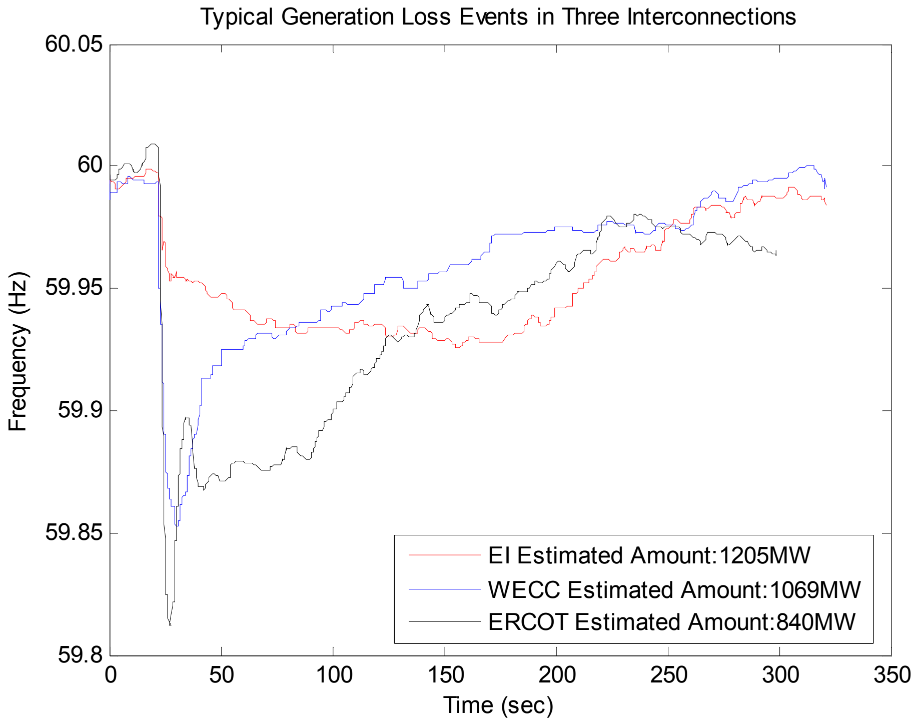

Figure 2.18 Generation-loss like events in the three Interconnections

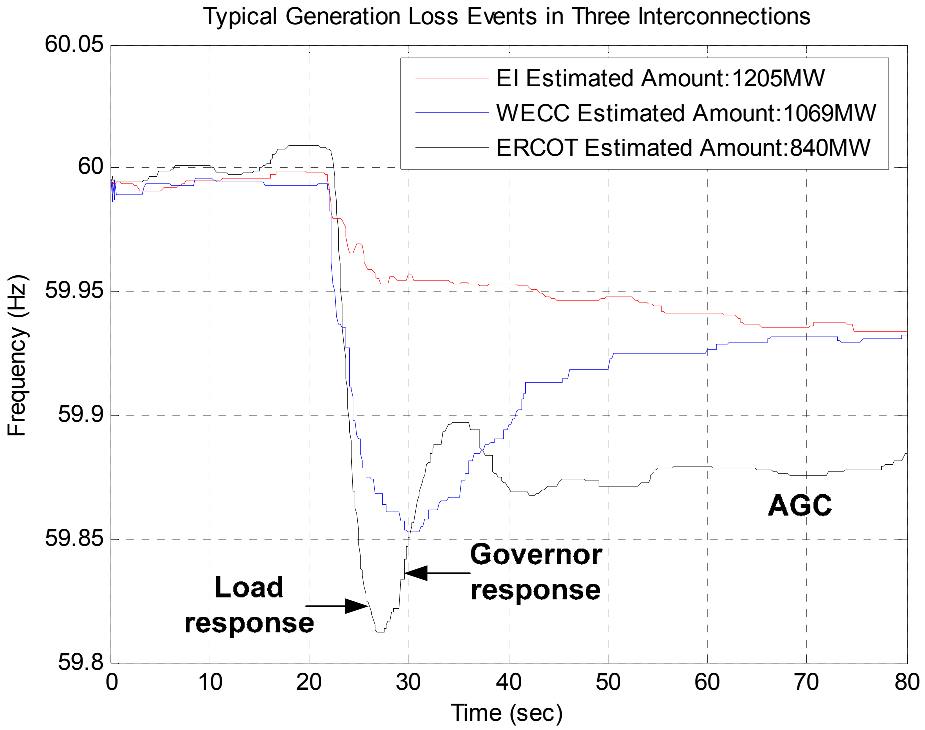

Figure 2.19 Detail of the initial frequency drop for generation-loss like events in the three Interconnections

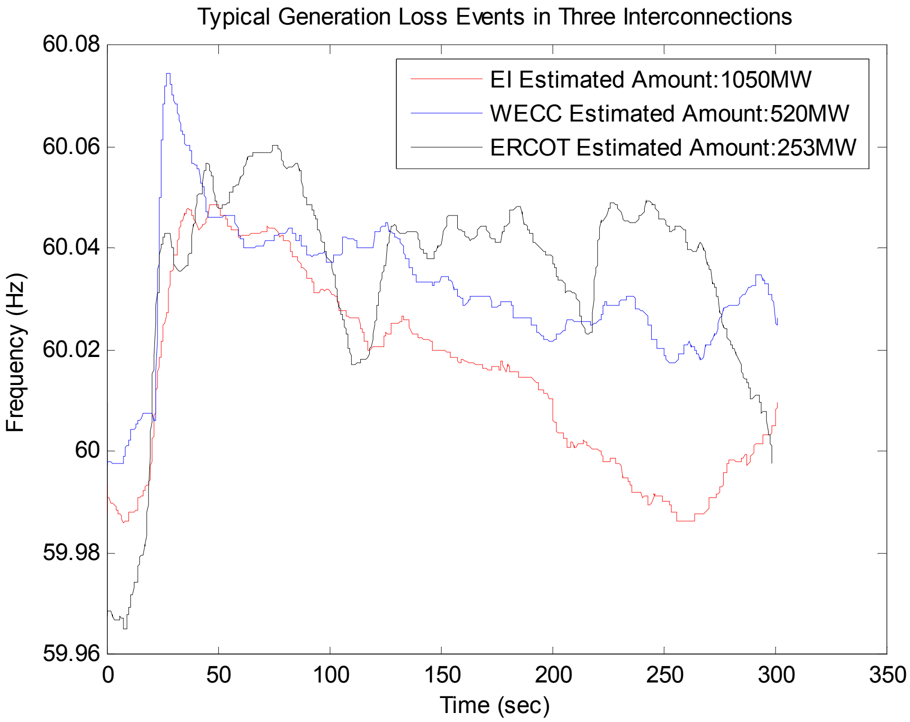

Figure 2.20 Load-drop like events in the three Interconnections

Frequency excursions also indicate characteristics of load profiles and control practices in the three Interconnections. As in Figure 2.19, the rate of frequency change is not constant following the initial drop. Rather, the rate becomes smaller after 4 to 5 seconds following the trip instant because of load sensitivity to frequency [14]. When frequency drops, motor-type loads will slow down, which results in less load-generation mismatch and therefore the rate of frequency change decreases. Then the governor control of generators starts to arrest the frequency decline within 10 seconds and tends to halt it as in Figure 2.19, a procedure known as primary control. Frequency in the EI system does not have an as obvious increase as those in the WECC and the ERCOT systems within 20 seconds following the disturbance. One of the possible reasons is that the smaller frequency responses in the WECC and the ERCOT allow larger frequency variations for a change of load.

Furthermore, different contingency reserve distribution in the Interconnections may also cause the difference in restored frequency amount during primary control. Contingency reserve includes spinning reserve and controllable load. If spinning reserve is the first option, the type of generating units will decide the response time. Comparison shows that gas-fired and hydro units have faster response time than coal-fired units. Gas and hydro turbines also have higher ramp rates than coal-fired units [15]. In the WECC system, the largest part of capacity is hydro-type. And in the ERCOT system, gas-fired capacity constitutes most of its total capacity [16], [17]. If contingency reserve in the WECC and the ERCOT consists of large portion of hydro or gas-fired units, those units will response fast to pick up the frequency drop, which will also contribute to the obvious frequency rise following its initial dip.

Governor control can bring frequency back to some extent but it does not necessarily recover frequency to the pre-disturbance level. The Automatic Generation Control (AGC) actions and reserve development, known as secondary control, continue to recover the frequency by replacing the amount of lost generation, which generally takes 5 to 15 minutes. The detailed discussion about secondary control performances of the three interconnections is in section 2.5.

2.3 Relationship between Frequency Change Rate and Total Frequency Variation Amount

As discussed above, generation loss introduces steep frequency decline. The answers to questions such as how much and how fast the frequency drops, and how they relate to the generation loss amount help us better understand power system dynamics and therefore improve control measures. In this section, generation loss events are considered to investigate the relationship between the rate of frequency change and total frequency deviation amount.

Consider an M generator system shown in Figure 2.21. When there is any generation-load imbalance, the motion of each generator rotor is governed by the swing equation as in (2.4):

$$P_m - P_e = \frac{2H}{\omega_s}\frac{d\omega}{dt}$$

where H is the rotor inertia constant, and ω_s is the system synchronous angular velocity. For a single generator, the imbalance between its mechanical and electrical power output is proportional to the rate of frequency change.

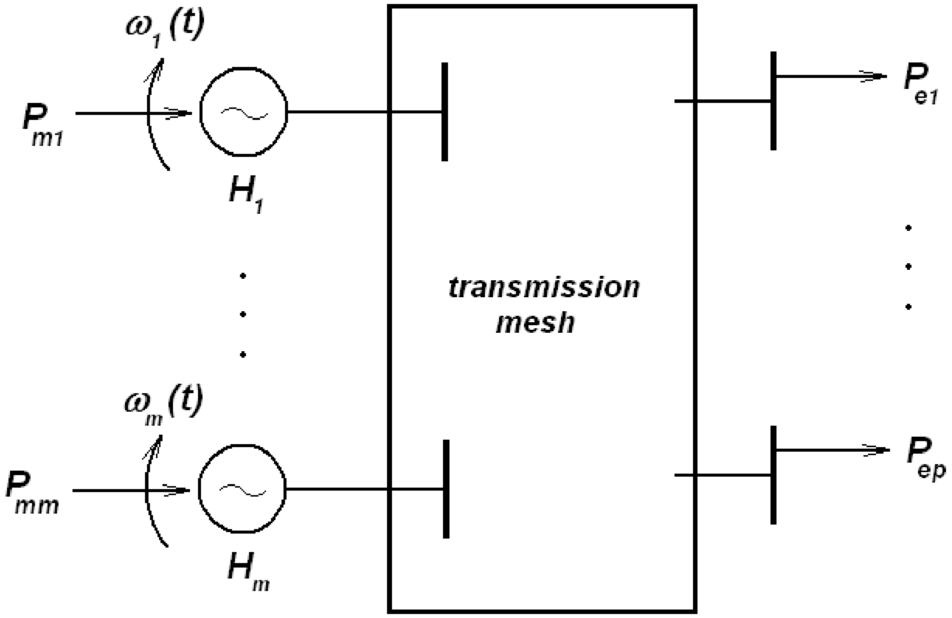

Figure 2.21 An example synchronous power system with m machines and p loads

If the M generator system is modeled as an equivalent single-generator system as shown in Figure 2.22, the swing equation in (2.4) would be:

$$\Delta P = P_{mech} - P_{elec} = \frac{2H_{equiv}}{\omega_s}\frac{d\omega}{dt} \tag{2.6}$$

where H_{equiv} is the system inertia, ω is the system frequency. If a generation trip event occurs, the total amount of generation loss in a multi-generator system is proportional to the rate of system frequency change at the instant of the trip. Note that the rate of frequency change in (2.6) is the steepest part of the frequency drop. Afterwards, the rate will decrease because the load may decrease due to deceleration of motor-type loads, and generation will increase because of governor control.

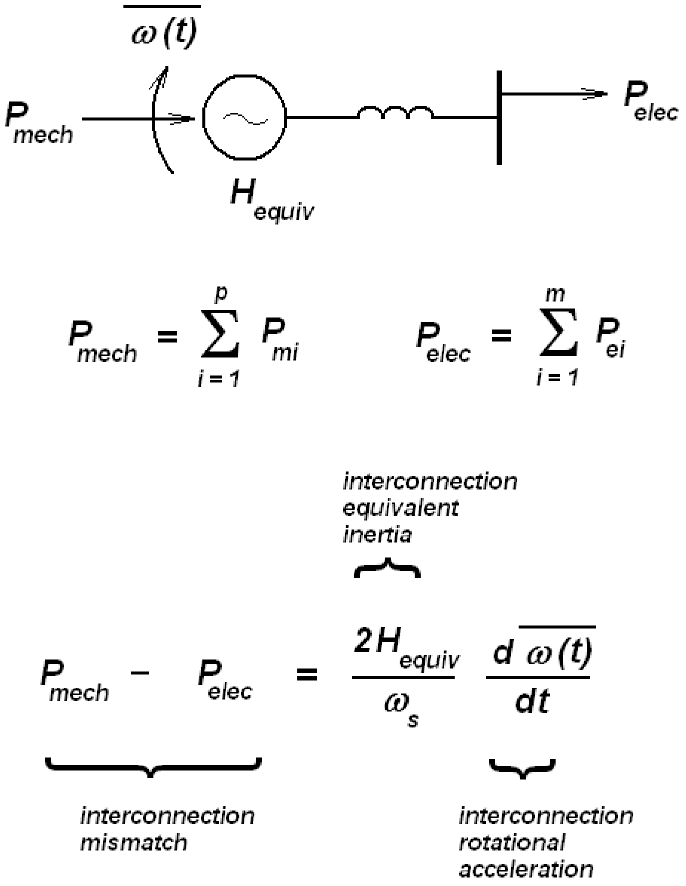

Figure 2.22 Equivalent one-machine system of the example multiple machine system

Moreover, the amount of real power loss ΔP is proportional to the total amount of frequency deviation as indicated in (2.5). We can expect that the largest frequency change rate would be similarly related to the total amount of frequency change. The relationship is verified as follows. The average frequency change rate in a 2-second time frame is used to approximate df/dt. The reason to choose the 2-second window is that frequency drops the fastest within the first 2 seconds following the trip based on our observations. Twelve cases have been studied for each of the three North America Interconnections. The results are shown in Figure 2.23, in which the data points are plotted as maximum df/dt versus total amount of frequency change. Straight lines can be obtained by first-order curve fitting as:

$$\max df/dt = a\Delta f + b \tag{2.7}$$

where a in the EI, the WECC and the ERCOT are: 0.34352, 0.3254, and 0.31382, respectively; b in three Interconnections are -1.3871, -6.6917, and -1.7305, respectively. We can see that the linear relationship between maximum df/dt and Δf as described above exists in all the three Interconnections, and the coefficient a, which is the slope of the fitted line, slightly differs in the three North American Interconnections.

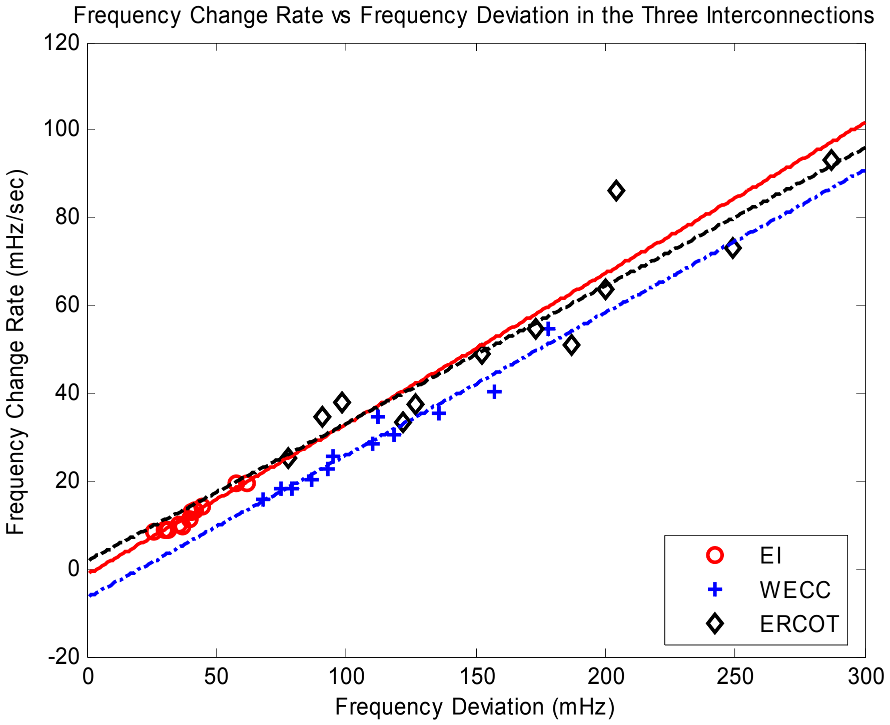

Figure 2.23 Relationship between maximum frequency change rate and total amount of frequency deviation

2.4 Power System Inertia and Frequency Response Characteristic

The swing equation in (2.4) can be simplified as follows considering small damping effects during early onset of generation loss events.

$$-\Delta P = M\frac{df}{dt} \tag{2.8}$$

where ΔP is the generation/load mismatch (pu in system load base), $\frac{df}{dt}$ is the rate of frequency change in Hz/second, and M $(=2H)$ is the inertia constant in seconds [18]. The system inertia is largely determined by the quantity and types of on-line generators at the time of disturbances. The inertia constant can be calculated by developing model for each generator in the system and simulating the response of its generation to frequency change. However, this approach becomes very difficult for such a large power system as the Eastern Interconnection. The system inertia can be estimated if the exact generation-load loss amount and accurate frequency transient measurements, as can be provided by FNET, are available. References [19] and [20] estimate the system inertia constants in the Japan 60 Hz system and the WECC system respectively by using frequency transients. The estimated inertia constants in the two systems are quite different due to large differences between the two systems.

The relationship between the generation/load mismatch and the frequency change rate described by the swing equation is further demonstrated by Figure 2.24, which shows the actual generation loss amount versus the maximum frequency change rate for 129 generator trip events in the EI system form January 2007 to October 2008. The information of these confirmed events can be found in Appendix I.

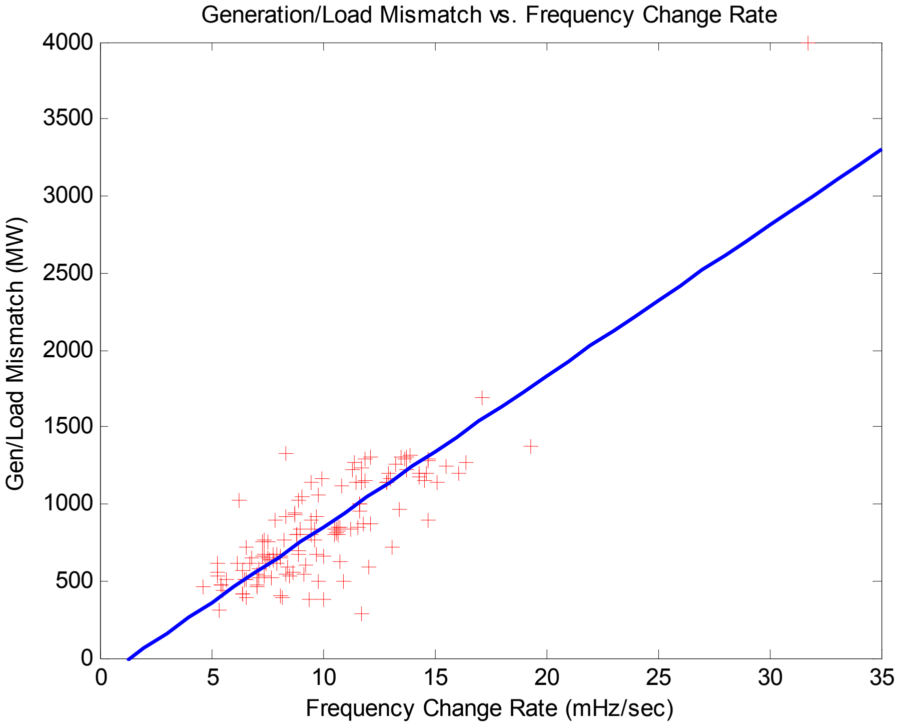

Figure 2.24 Generation/load mismatch vs. frequency change rate for generator trip events in the EI from 2007 to 2008

Although the per unit inertia constant *M* is not obtained directly in this work because the information of system load during each event is not available, the system inertia can be estimated by first-order curve fitting over these data points. The maximum frequency change rate at the onset of a generation outage event is approximated in the same way as in section 2.3 and the first-order curve fitting coefficients are (98.031, -131.99). Then the polynomial can be written as

$$\text{Generation/Load Mismatch (MW)} = 98.031(GW \cdot \sec^2) \times \max df / dt(mHz/\sec) - 131.99$$

The slope of the regression model (98.031) is an estimate of the system inertia in GW·sec². The obtained coefficients are possibly affected by the seasonal variations in load and generation scheduling. The estimation accuracy can be affected by several factors including the error in the maximum frequency change rate estimation and inaccurate actual generation loss amount. How the various factors contribute to the estimation error can be further analyzed once more information about the system load variation and the accuracy of the generation/demand mismatch is available.

Among the confirmed generation trip events, 43 occurred in the summer season between June and September, 36 in winter from December to the following February and 50 in spring and fall. The disturbances are also divided into two groups by the generation loss amount: above 1000 MW and below 1000 MW. The system inertia in the EI is estimated and the first-order polynomial coefficients for different seasons and disturbance sizes are listed in Table 2.1. The generation/load mismatch versus frequency change rate for different seasons is shown from Figure 2.25 to Figure 2.27 and such relationship for different disturbance sizes is shown in Figure 2.28 and Figure 2.29.

Table 2.1 Estimation of the inertia in the EI

Season/Size	# of Events	a (GW·sec²)	b (MW)
Summer	43	114.7	-261.78
Winter	36	82.547	-2.7294
Other	50	74.841	52.205
> 1000 MW	41	96.717	-3.8803
< 1000 MW	88	43.848	280.19
Total	129	98.031	-131.99

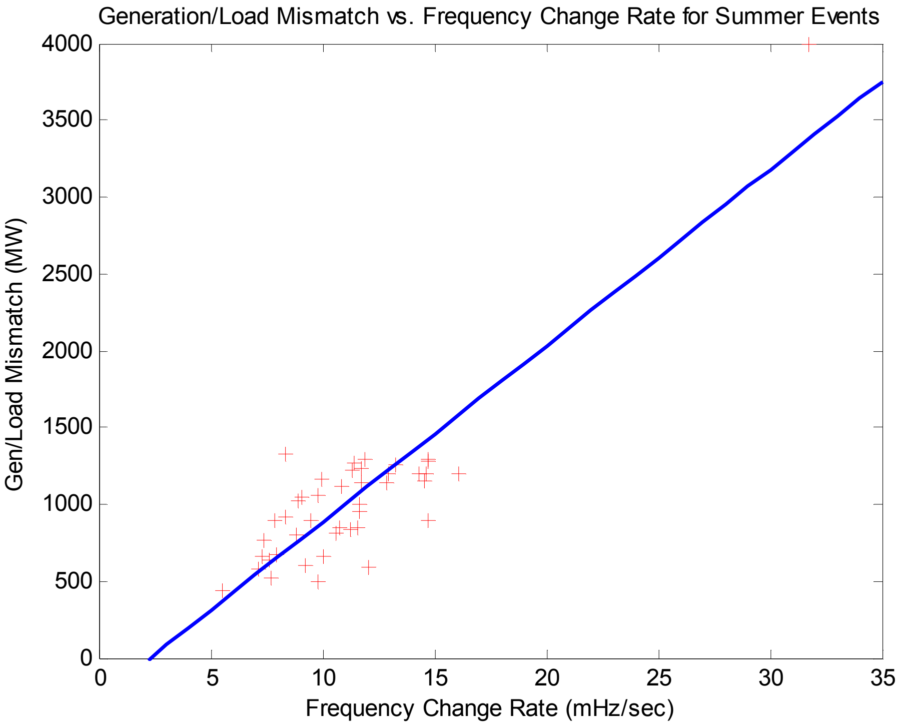

Figure 2.25 Generation/Load mismatch vs. frequency change rate for summer generator trips

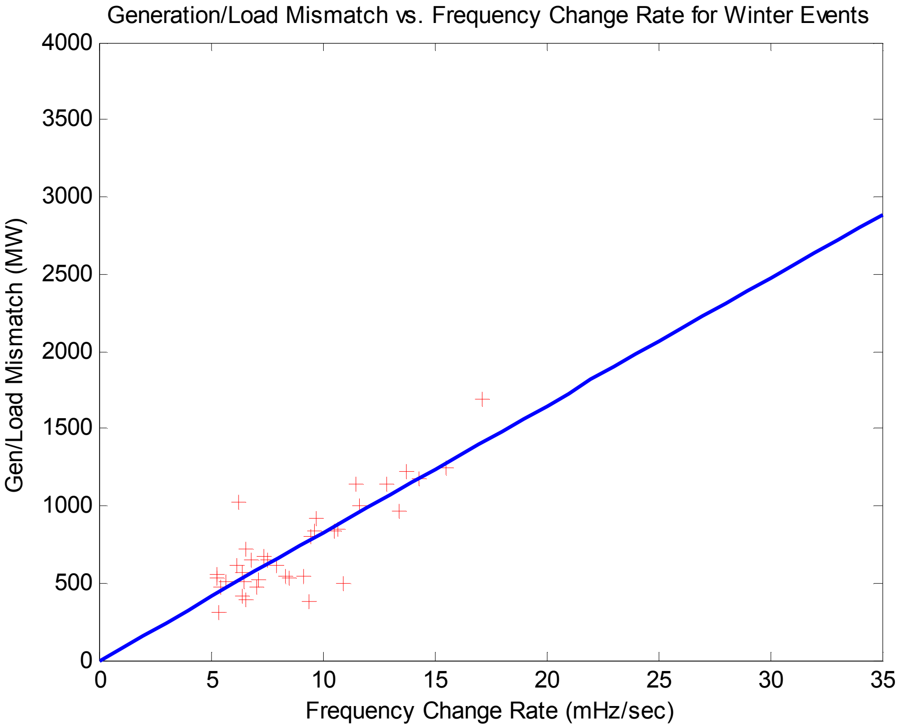

Figure 2.26 Generation/Load mismatch vs. frequency change rate for winter generator trips

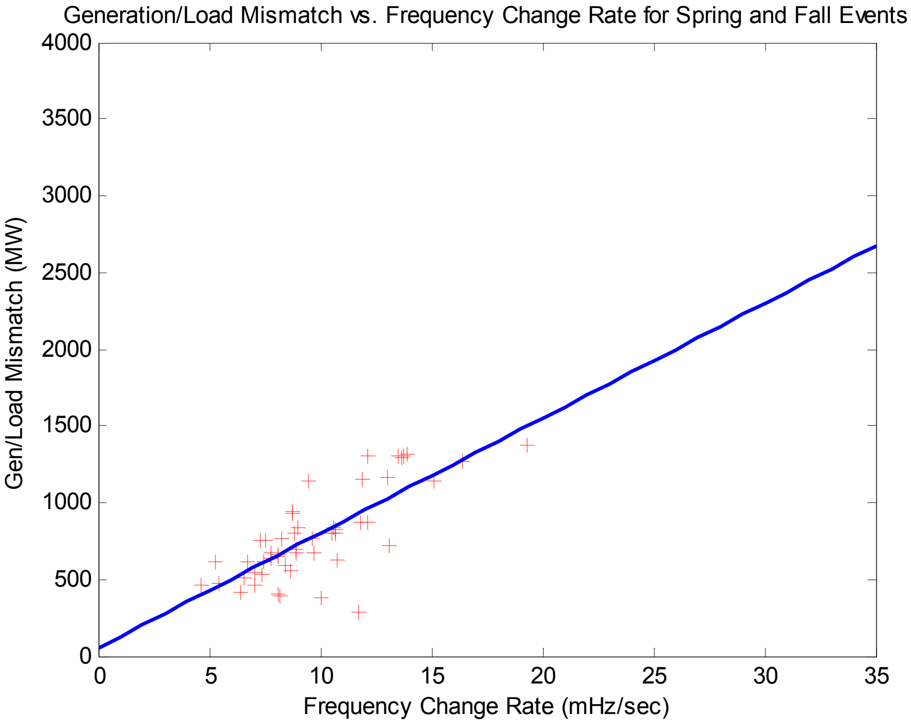

Figure 2.27 Generation/Load mismatch vs. frequency change rate for spring and fall generator trips

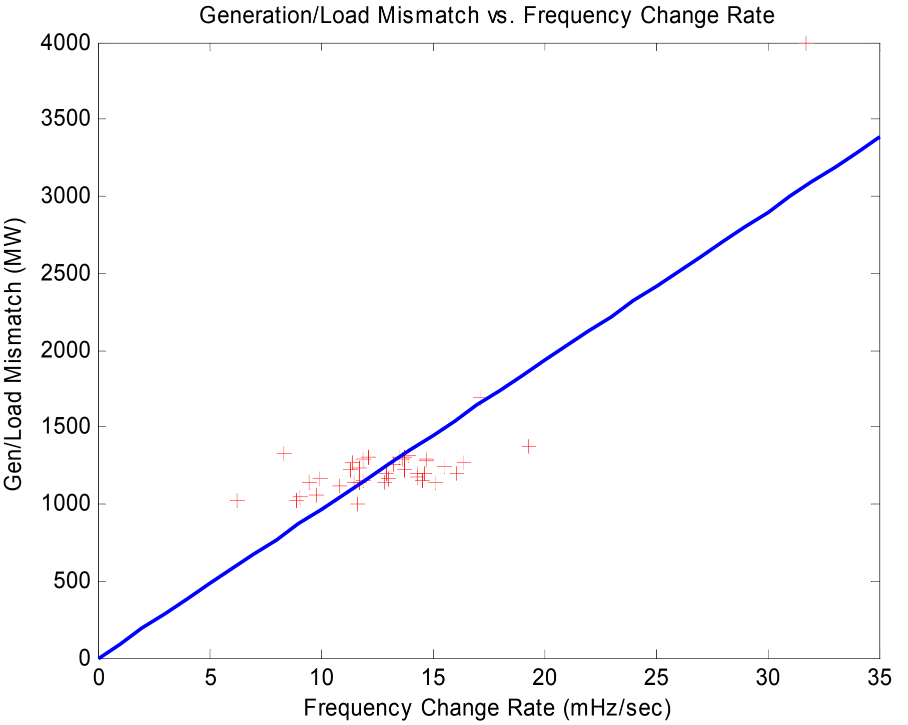

Figure 2.28 Generation/Load mismatch vs. frequency change rate for generator trips larger than 1000 MW

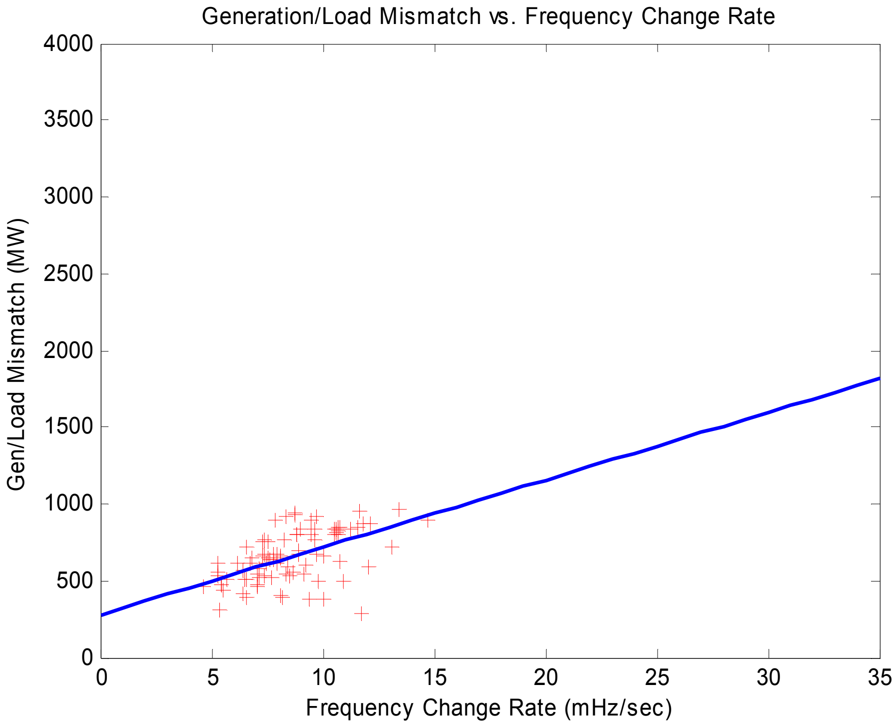

Figure 2.29 Generation/Load mismatch vs. frequency change rate for generator trips smaller than 1000 MW

The frequency response characteristic or load frequency sensitivity (β) of the EI system is also estimated based on the 129 confirmed generation trip events by the relationship described in (2.5). The frequency deviation due to the generation loss for each event is obtained from measurements collected by FNET. The first-order polynomial that fits the data set is estimated as

$$\text{Generation/Load Mismatch (MW)} = 28.169(\text{MW/mHz}) \times \Delta f\,(mHz) - 77.75$$

Therefore the β estimate based on the generation trip events is the coefficient 28.169 MW/mHz as shown in Figure 2.30. The polynomial coefficients for summer, winter and other seasons and different generation loss amount are listed in Table 2.2. The load frequency sensitivity estimate for different seasons is shown in Figure 2.31 to Figure 2.33. The relationship between generation/load unbalance and system frequency deviation during disturbances of different sizes are shown in Figure 2.34 and Figure 2.35.

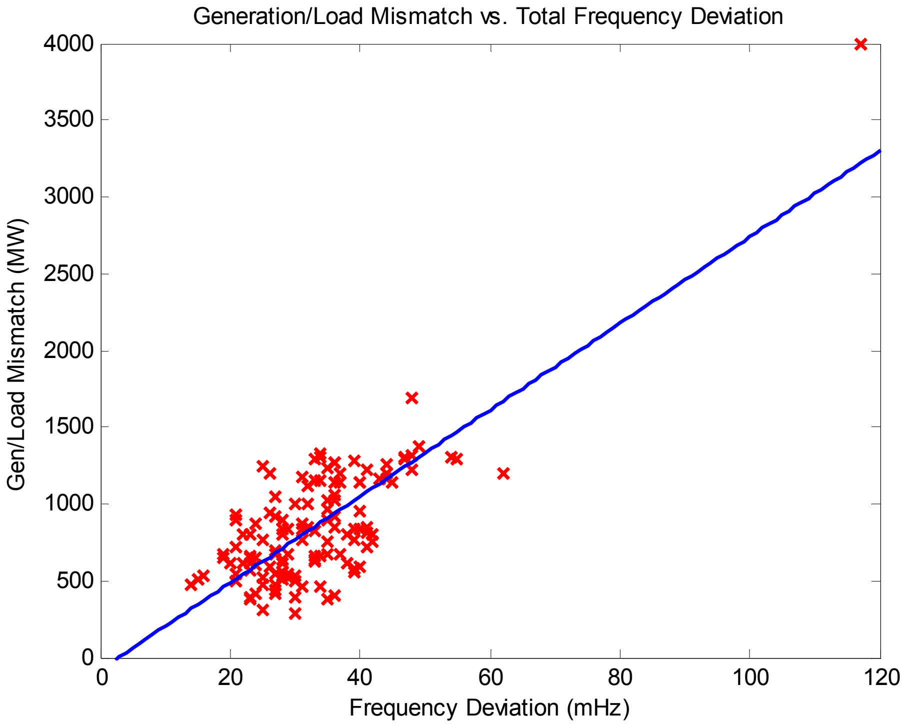

Figure 2.30 Generation/load mismatch vs. frequency deviation for generator trip events in the EI from 2007 to 2008

Table 2.2 Estimation of the frequency response characteristic in the EI

Season/Size	# of Events	c (MW/mHz)	d (MW)
Summer	43	30.132	-51.365
Winter	36	30.487	-146.62
Other	50	19.951	115.83
> 1000 MW	41	26.956	166.11
< 1000 MW	88	7.0358	449.78
All	129	28.169	-77.75

From the above analysis, both the system inertia and the frequency response characteristic are significantly smaller when the generation loss amount is less than 1000 MW, which indicates that smaller generating units demonstrate smaller frequency responses. The analysis implies that a consistent threshold for disturbance size may be required for the estimation otherwise the results will be skewed.

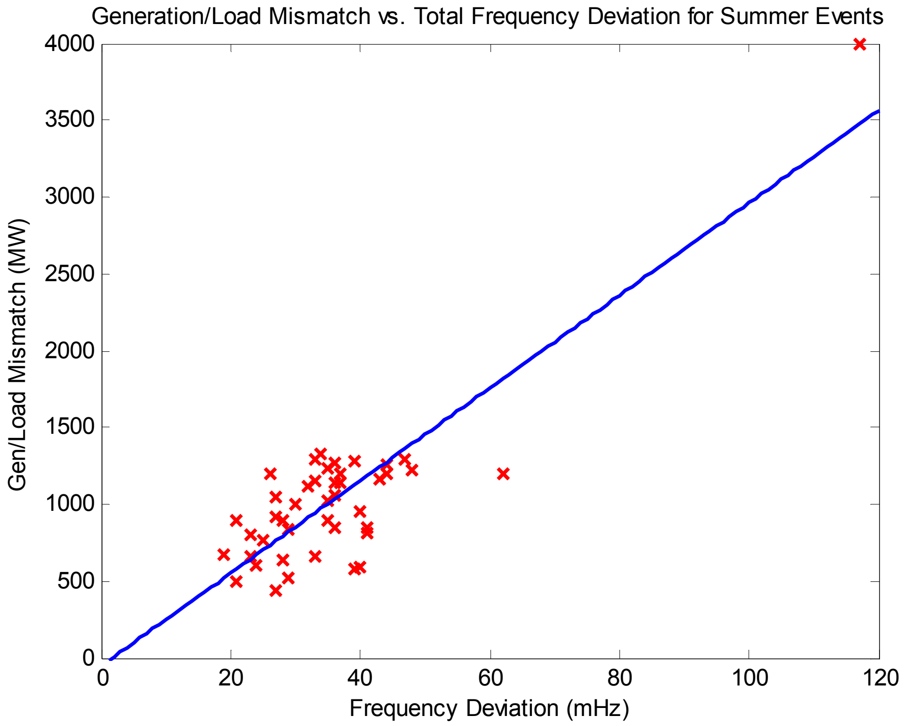

Figure 2.31 Generation/load mismatch vs. frequency deviation for summer generator trips

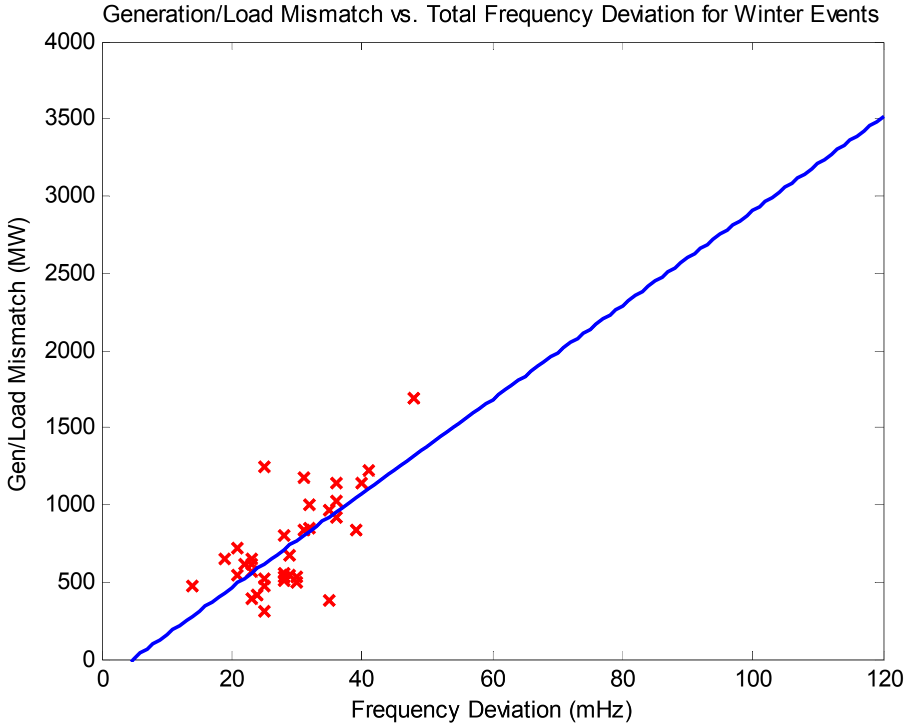

Figure 2.32 Generation/load mismatch vs. frequency deviation for winter generator trips

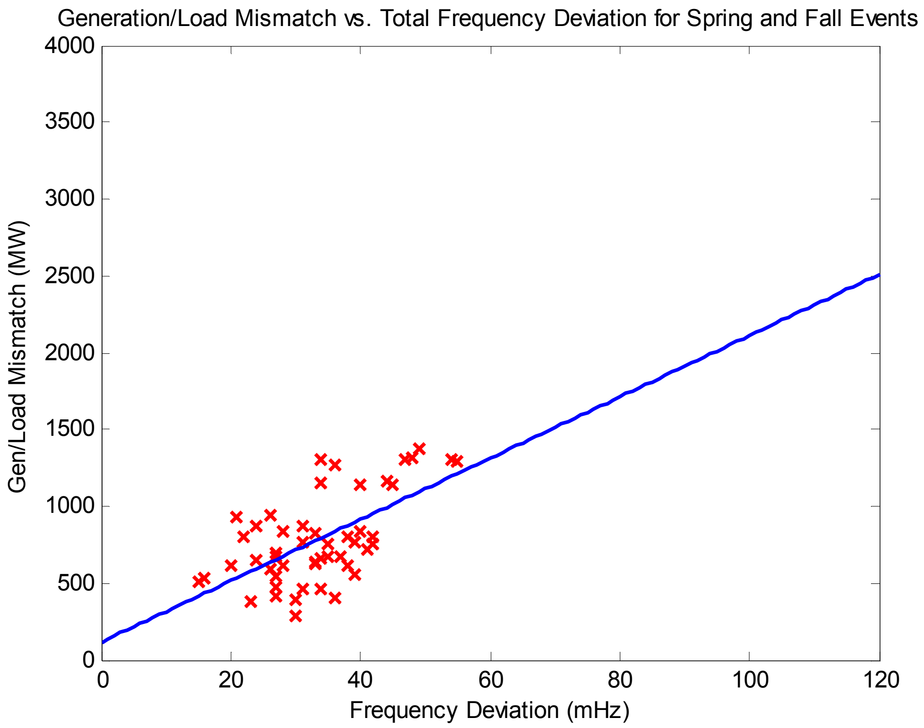

Figure 2.33 Generation/load mismatch vs. frequency deviation for spring and fall generator trips

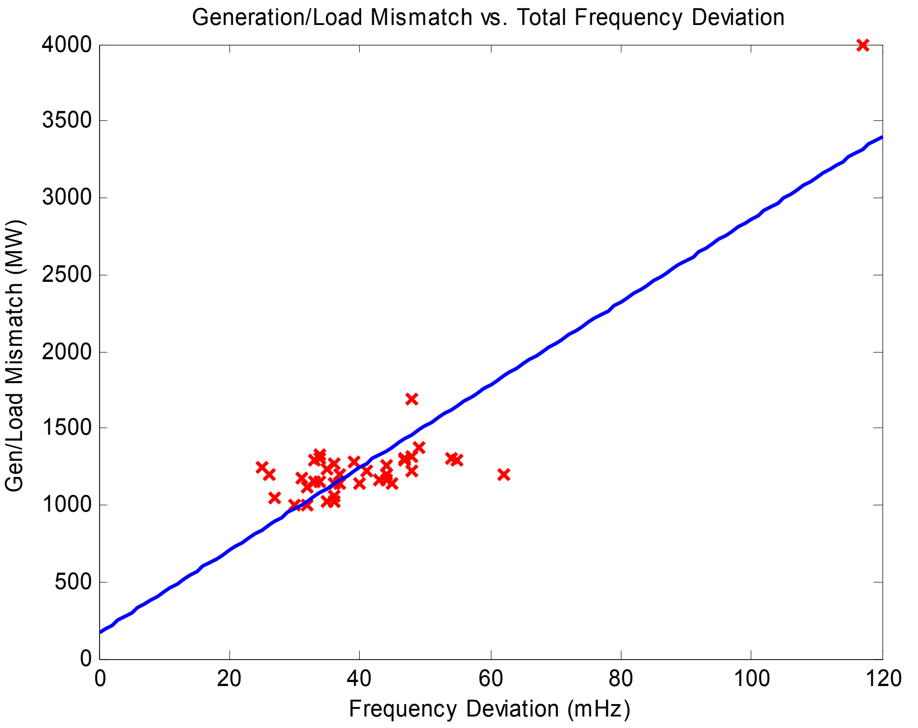

Figure 2.34 Generation/Load mismatch vs. frequency deviation for generator trips larger than 1000 MW

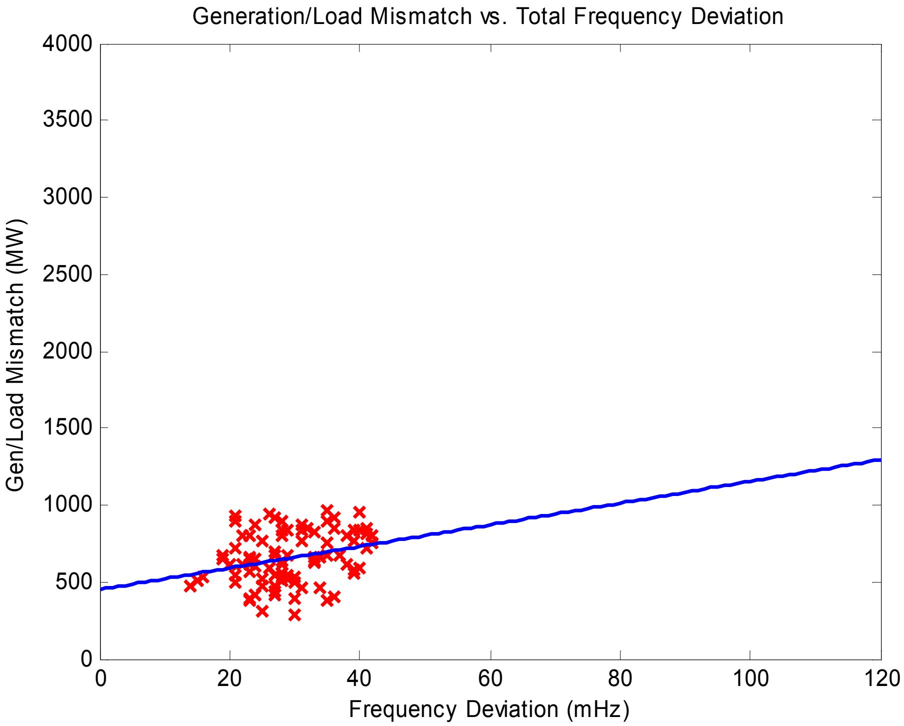

Figure 2.35 Generation/Load mismatch vs. frequency deviation for generator trips smaller than 1000 MW

A positive correlation between the inertia constant and system load is observed in [20]. The estimated system inertia confirms this in that it is larger in summer than in other seasons (Table 2.1) as load in the EI system is generally heavier in summer. The frequency response characteristic varies over seasons and is typically larger in summer because there is a larger proportion of motor loads thus generally more generators in service to meet the higher demand [12].

One application of the relationships described above is generation/load mismatch estimation for generation or load loss events. Provided the seasonal inertia or load frequency sensitivity estimate, the generation or load loss amount can be estimated easily by feeding the frequency change rate or frequency deviation data into the estimator, as demonstrated in Figure 2.36. The coefficients a, b, c and d in the estimator can be obtained from the above analysis as listed in Table 2.1 and Table 2.2.

With the wide-area frequency measurements made available by FNET, the system inertia and frequency response characteristic can be continuously monitored to assist establishing system response models to study the behavior of frequency sensitive loads and how they affect the total system inertia.

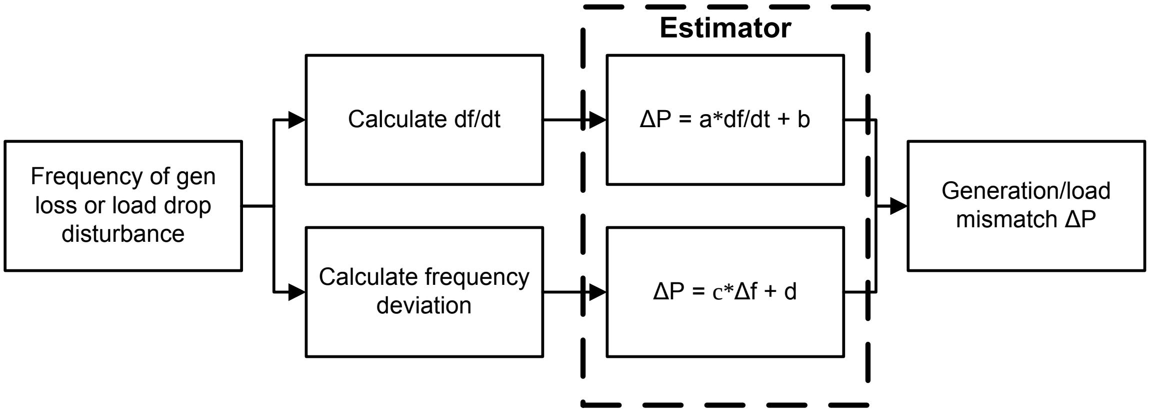

Figure 2.36 Generation/load mismatch estimator

2.5 Frequency Restoration Characteristics

As is shown in Figure 2.18, frequencies in the three North American Interconnections experience different recovery procedures following the initial steep frequency drop from loss of generation. To restore the frequency to nominal frequency value (60Hz) during the period of secondary control, AGC actions will change generation or interchange schedules. North American Electric Reliability Corporation (NERC) standards measure disturbance control performances of a control area by assessing its Area Control Error (ACE), stating that at the end of the recovery time (15 minutes by default), ACE should be brought back to the pre-disturbance level if the pre-disturbance ACE is negative, or ACE should return to zero if its pre-disturbance value is equal to or greater than zero [14], [21]. Since all the control actions are directly reflected on the system frequency, we can examine the disturbance control performance by looking at frequency data. In this section, frequency restoration characteristic (FRC) is introduced as an indicator of the Interconnection's performance to raise the system frequency back to normal (60Hz) over a 5-minute period following a generation loss disturbance. Its calculation is as follows:

If $f_1 < 60Hz$,

$$FRC = \frac{\Delta f - \max\left(0, \left(f_1 - f_2\right)\right)}{\Delta f} \times 100\% \qquad (2.9)$$

If $f_1 \geq 60Hz$

$$FRC = \frac{\Delta f - \max\left(0, \left(60 - f_2\right)\right)}{\Delta f} \times 100\% \qquad (2.10)$$

where f_1 is the pre-disturbance frequency, f_2 is the frequency at the end of 5 minutes after the disturbance, Δf is the total amount of frequency decline. Generally, the higher the FRC value, the closer the frequency is restored to 60Hz, the better the disturbance control performance.

Frequency restoration characteristic values are calculated for 35 generation-loss like events in the EI, 31 cases for the WECC and 12 cases for the ERCOT between January and October, 2006. The results and comparisons are listed in Table 2.3. The standard deviation values of FRC indicate variation of frequency restoration performance in an Interconnection. The average frequency restoration performances of the three Interconnections are close, as indicated by their similar average FRC values. This observation is based on the 5-minute data window. The result may change if a smaller data window is chosen. The EI system has the highest median FRC value and largest standard deviation values, which indicates that the frequency restoration characteristic of the EI system varies greatly in different cases. Figure 2.12 also supports this. If different seasons are considered, the EI has better frequency restoration performances in summer than in other months. For generation-loss like events in the ERCOT, however, the frequency restoration actions may be more effective in other seasons than in summer. The average FRC values of events in the WECC do not vary much with seasons, which indicates that disturbance control performance in the WECC maintains at a comparatively stable level.

Among the examined 31 events in the EI, 25 of them are confirmed generation trip events, which are distributed in five control areas in the EI. The statistics of FRC values of these trips in each control area are listed in Table 2.4.

The scheduled normal frequency may not be exactly 60Hz in all the Interconnections, but may have ± 0.02 Hz offset for time error correction [12]. Despite that, the analysis in this section still provides some ideas of the control performances of

Interconnections as well as control areas. The frequency restoration characteristic can still serve as an indicator of the reliability of an Interconnection.

Table 2.3 Statistics of frequency restoration characteristic of generation-loss like events in the three Interconnections from Jan. to Oct. 2006

Interconnection	Number of cases	FRC average (%)	FRC median (%)	FRC standard deviation
Total				
EI	35	84.21	100	27.77
WECC	31	84.22	89.08	16.91
ERCOT	12	89.47	95.1	12.42
Summer (Jun. to Sep.)				
EI	15	90.83	100	19.73
WECC	12	82.7	93	22.29
ERCOT	5	83.63	80.8	10.15
Other months (Mar. to May, Oct.)				
EI	18	76.93	99.25	33.128
WECC	14	83.39	85.21	13.73
ERCOT	7	93.65	100	12.86

Table 2.4 Statistics of frequency restoration characteristic of some generation trips in the EI control areas

Control Area	Number of cases	FRC average (%)	FRC median (%)
ECAR	7	86.41	100
MAAC	2	81.22	81.22
NPCC	1	98.51	98.51
SERC	12	75.41	84.49
SPP	3	100	100

Chapter 3 Analysis of Major Disturbances in the Eastern Interconnection

Power systems are continuously exposed to disturbances whose impacts on the whole system may vary. Statistical analysis in section 2.1.1 shows that every 3 days FNET sees a disturbance in EI in which the estimated generation-load mismatch exceeds 500 MW. During a disturbance (generation trip, load loss or line trip) where generation and load are not balanced, generators in the system accelerate or decelerate to reduce the power imbalance. Local phase angle and frequency will change simultaneously in response to the disturbance [10]. Therefore, by monitoring those parameters, valuable information about system dynamics can be obtained. A situation awareness system has been implemented on the FNET server to detect and analyze power system disturbances in near-real time [9].

This section discusses several major disturbances in the EI observed by FNET in year 2007 and 2008 including a three-phase fault at transmission level, a multiple-disturbance incident that involves line trips and generator trips, an islanding event, the Florida outage, HVDC line faults, and events showing the dynamic performance of AC/DC systems. Frequency, voltage and phase angle recordings are examined to study the system dynamics during disturbances and understand the signatures of different types of events. Comparisons of data from PMU and FDR are also included to evaluate data quality measured at distribution voltage level.

3.1 Three-phase Fault

In summer 2007 a three-phase fault at transmission network triggered the situation awareness system of FNET. The fault occurred at 00:28:42 UTC, and was cleared after 23 cycles. An estimation of 800 MW load loss occurred at 00:28:52 UTC.

The measurements from 7 FDR units at different locations are shown in Figure 3.1 through Figure 3.4. For the ease of comparison, voltage at each measuring point is normalized by dividing by a base voltage which is the average pre-event value over a 20-second time period at that measuring point. The phase angles at all locations are scaled to start at zero to eliminate arbitrary angle offsets caused by phase shift from transmission to distribution networks.

This fault caused obvious frequency oscillations (Figure 3.2) and large voltage dip (Figure 3.3). FDR17 is close to the fault location, and the voltage measured there clearly reflected the voltage depression at the transmission level. It took about 9 seconds before the voltage was recovered to pre-fault level from its lowest value.

Voltage depression due to the fault caused significant decrease in power consumption by voltage-dependent loads. Thus at the instant of the fault, generators in the system all accelerated to adapt to the power imbalance [18]. Frequency as a direct indicator of generator rotor speed experienced a sharp rise at the time of fault. Loads close to the fault experienced more severe voltage depression, which contributed to larger generation-load mismatch, since they consumed less power. As a result, FDRs closer to the accelerating generators near the fault location measured larger frequency swings.

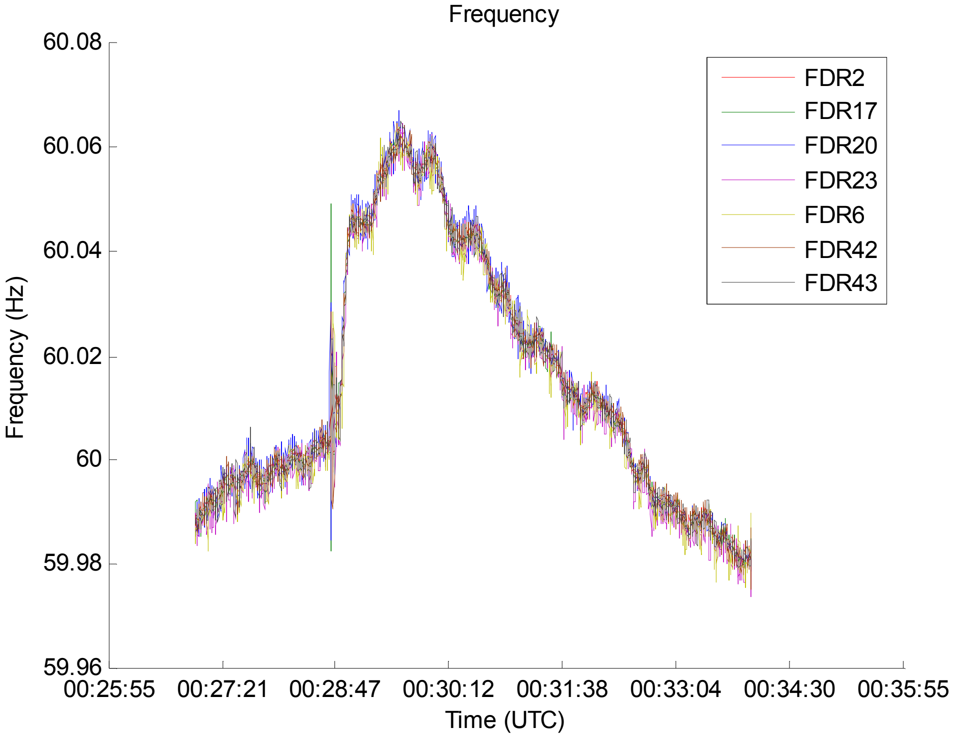

Figure 3.1 Frequency excursion during the three-phase disturbance

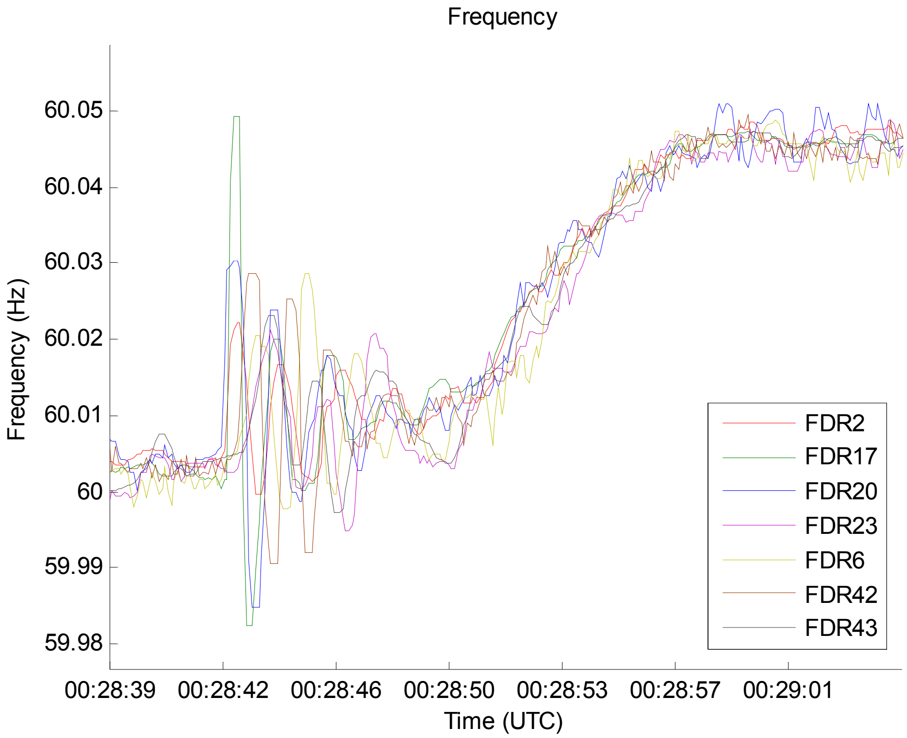

Figure 3.2 Frequency detail of the three-phase disturbance

Loss of load is indicated clearly in frequency and phase angle as well. As is shown in Figure 3.2, frequency started to rise quickly at 00:28:52 UTC, because generators in the system started to accelerate due to loss of load. The rate of frequency change became smaller after 9 seconds possibly because frequency control mechanisms such as governor control came to play. However, frequency continued to increase indicating that generation was still in excess until it reached 60.06 Hz, and returned to 60 Hz at 00:33 UTC (Figure 3.1). Phase angle in Figure 3.3 also tells the same fact that generator acceleration started at the time of load loss and ended when generation and load came to a balanced state.

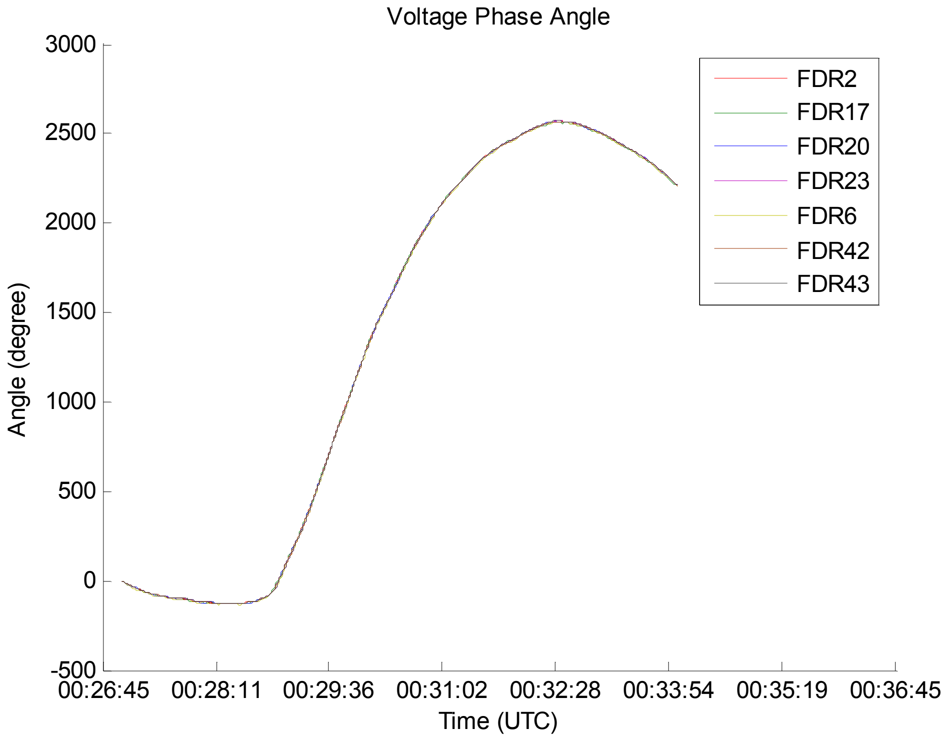

Figure 3.3 Phase angle during the three-phase disturbance

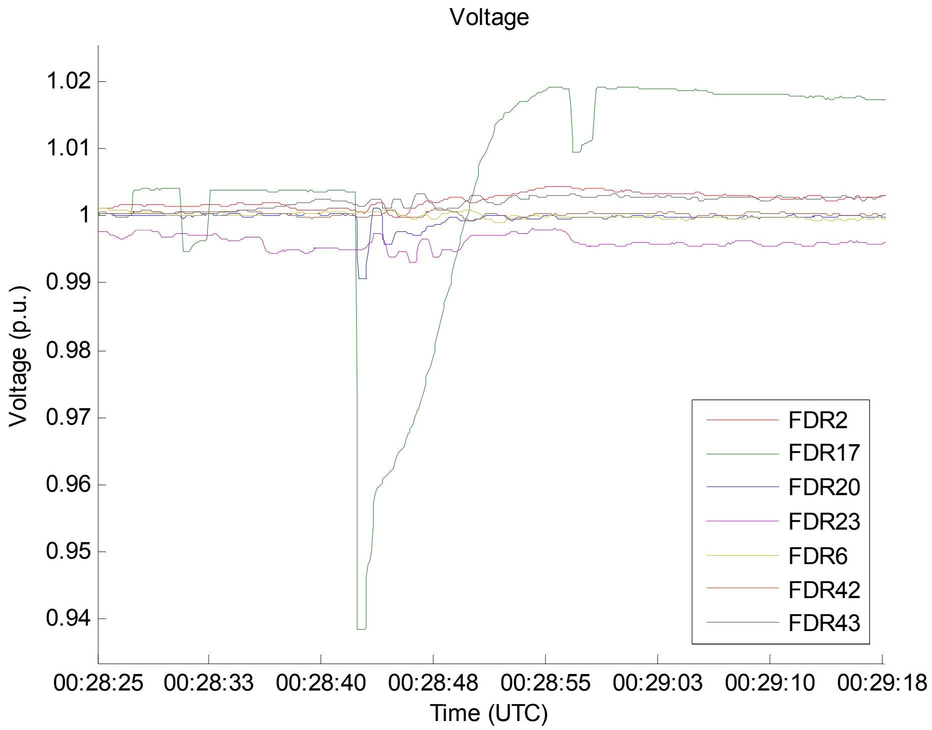

Figure 3.4 Voltage dip caused by the three-phase disturbance

3.2 Multi-disturbance Event

Also in summer 2007, FNET event trigger captured a large generation trip event in EI with about 4000 MW generation loss. It was later confirmed that several generating units were tripped at that time, and more than one 765 kV transmission lines were disconnected around the generation trip incident. Although the detailed sequence of events is still under investigation, much information about what might have happened during the disturbance can be obtained from real measurements, as is shown in Figure 3.5 to Figure 3.9.

Before the large generation trip, some possible line events occurred between 21:43 UTC and 21:44 UTC (Figure 3.6). Associated with frequency oscillations at 21:43:34 UTC which could be a sign of line trip, a fast frequency decline of about 20 mHz can be noticed, but the frequency returned back fairly quickly. Fast-valving action at one or more units following the line trip might have contributed to the frequency decline, which could also explain the frequency's fast return. It has been found that fast-valving of units at fault area help minimize the accelerating power and hence reduces transient power swings by varying the turbine mechanical power [22][23]. Another group of oscillations can be observed about 15 seconds later, which is possibly due to line re-closing action that causes similar oscillations in frequency as line opening. The 15-second delay may be related to the re-closing relay settings.

Immediately before the large frequency decline in Figure 3.7, frequency oscillations indicate that there might be one or more line trip events. Oscillations in voltage may also be caused by the line trip events (Figure 3.9). At the onset of a line trip, generators at sending end of the line will accelerate due to the excessive generation with respect to load; whereas generators at receiving end of the line will decelerate.

During this disturbance, frequency dropped as low as 59.86 Hz and took 7 minutes to be recovered to 60 Hz (Figure 3.5). Since frequency and phase angle change simultaneously, phase angle declined after loss of generation, which indicates load was in excess of generation (Figure 3.8). In addition, the decline did not stop until all lost generation was replaced by Automatic Generation Control (AGC) and frequency was restored to its initial equilibrium value.

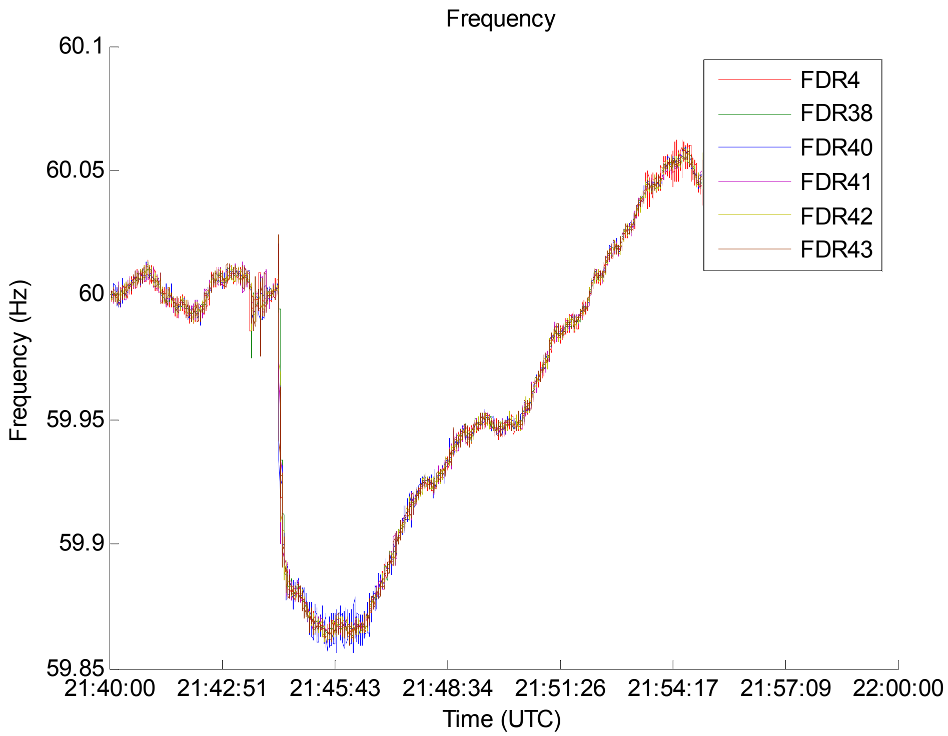

Figure 3.5 Frequency excursion during the multi-disturbance event

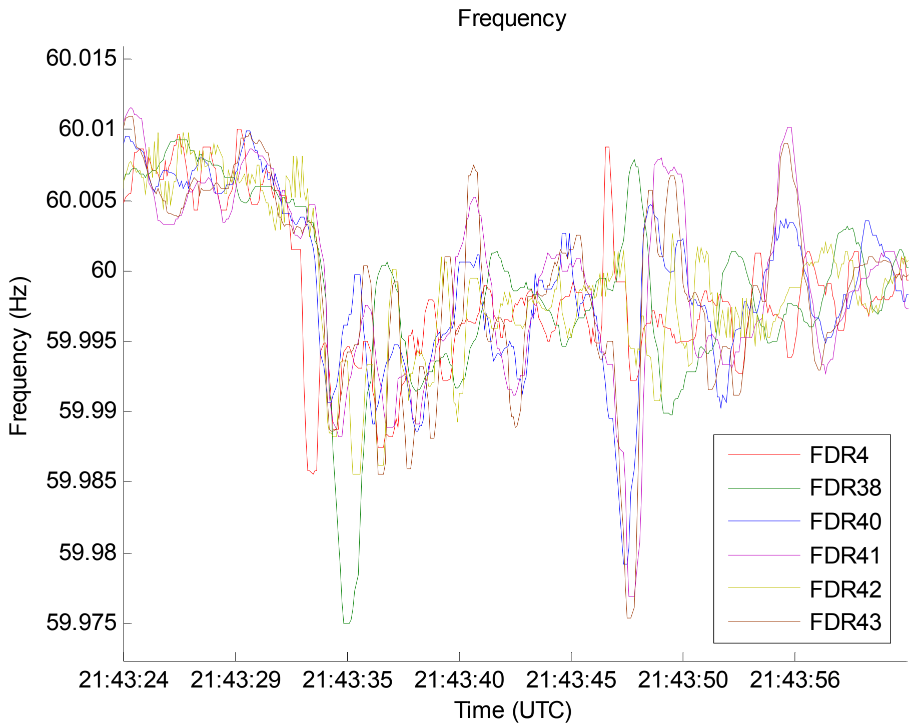

Figure 3.6 Frequency detail of line events before the generation trip

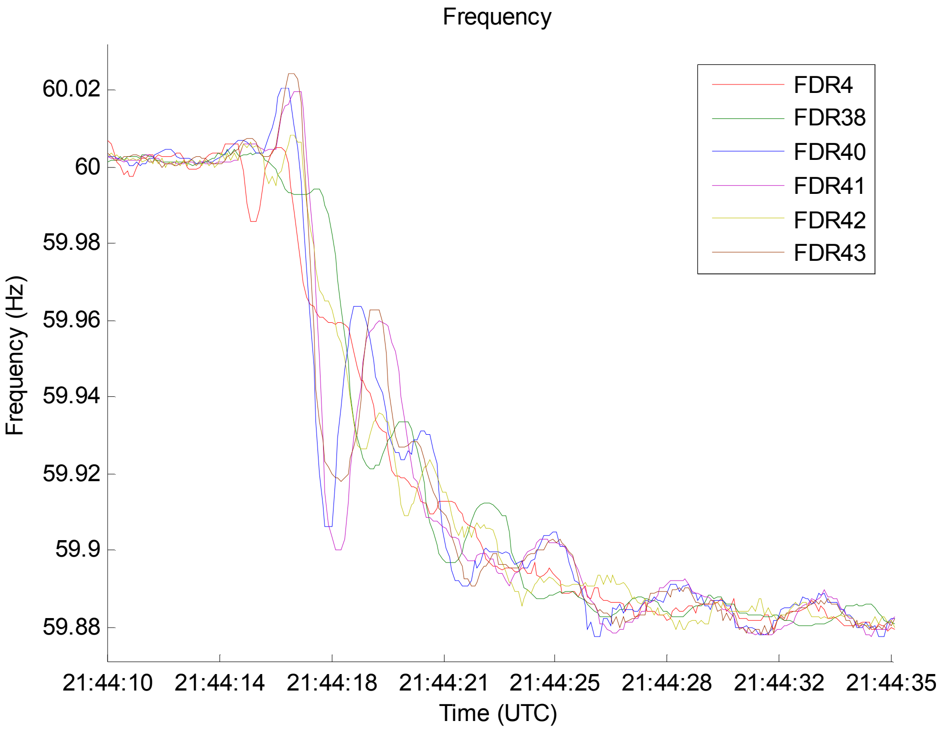

Figure 3.7 Frequency detail of the generation trip during the multi-disturbance event

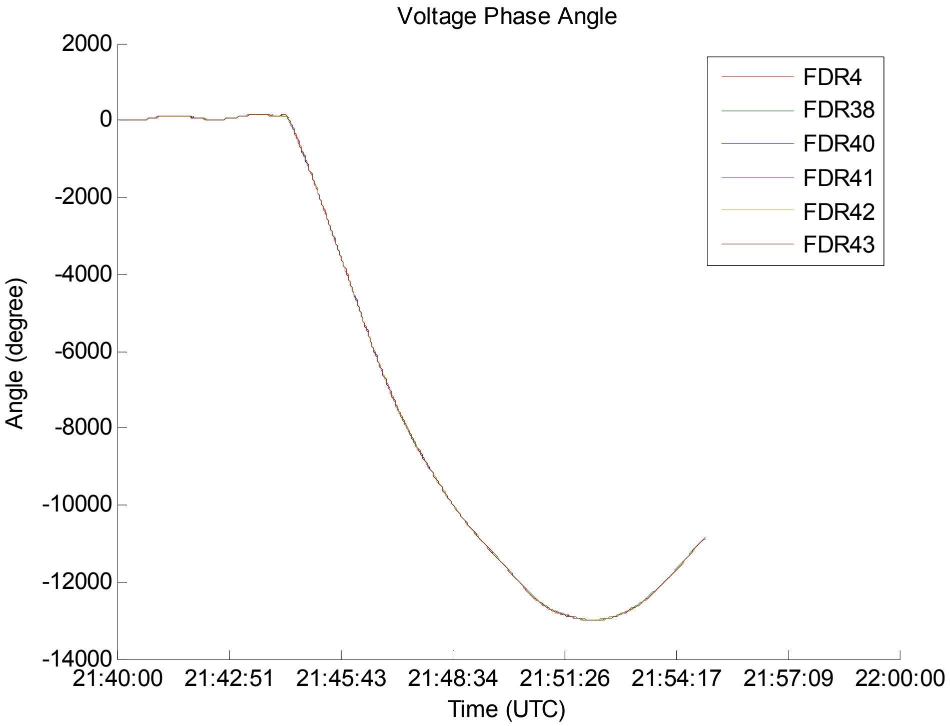

s

Figure 3.8 Phase angle during the multi-disturbance event

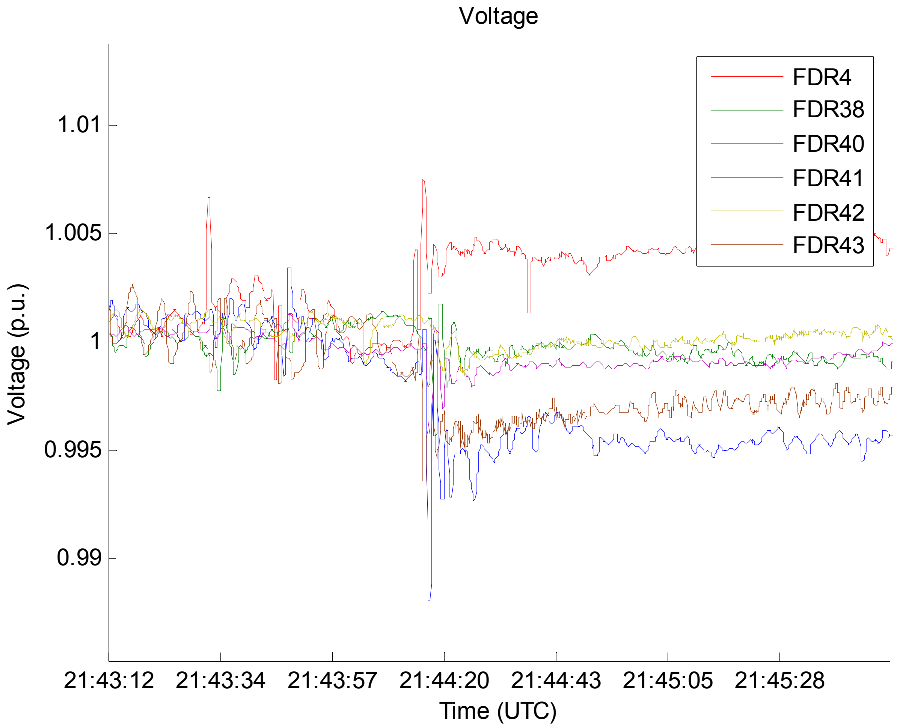

Figure 3.9 Voltage magnitude during the multi-disturbance event

3.3 *Islanding*

Another significant event observed by FNET in 2007 was an islanding case. A part of the EI was isolated, and the separation lasted about 9 minutes before the island and the other parts of the EI were reconnected. Possible initial cause was that storms in the isolated area led to outages of several lines. Islanding occurs when a part of a power interconnection containing generation and load is isolated from the remainder of the system [24]. If multiple disturbances occur, synchronism of interconnected power systems could be destroyed, in which case out-of-step protection systems can help to detect angular instability and isolate the asynchronous part to preserve stability [25]. A brief timeline of the islanding event observed from the FNET measurements is as follows and all time is UTC.

10:15 – 10:16: Initial line trip events occurred;

10:21:19: The separation of the EI started. The frequency of the islanded part went up sharply while the rest of the EI experienced quick frequency decline;

10:21:24: Oscillation in the frequency of the island due to possible 230 kV line opening;

10:21:24 – 10:21:34: Frequency in the island declined because of HVDC reduction;

10:21:34: Fast increase in the frequency of the island possibly due to another 230 kV line trip by out-of-step protection;

10:30: The EI system was reconnected.

3.3.1 Recordings from FDRs

There are 3 FDR units in the island area, so events in both parts could be observed. Frequency, phase angle, and voltage recordings during this disturbance are shown in Figure 3.10 through Figure 3.16, respectively. As is shown in Figure 3.11, the line opening events before islanding caused frequency oscillations between 10:15 and 10:16 UTC. About 5 minutes later, at 10:21:19 UTC, the EI was divided into 2 parts, hence an island was created. System frequency split into two groups, as can also be seen in phase angle (Figure 3.14). One group of angles increased, while the other decreased. The frequency in the isolated network went up as high as 60.98 Hz, but this part of system remained synchronized within itself, at least for the part FDR measurements were taken.

Immediately after the separation, at around 10:21:24 UTC, there occurred a steep frequency drop of about 60 mHz in the remainder of the EI, which was possibly due to generation deficit caused by separation of the island. Meanwhile, the frequency in the islanded part rose to 60.86 Hz within 6 seconds (Figure 3.13). Some DFR records confirmed that a 230 KV line in the island area was tripped at 10:21:24 UTC as the relays detected low voltage (Figure 3.15), which possibly caused frequency oscillations associated with the rise (Figure 3.13). The sharp rise in frequency shows that the island had an excess of generation.

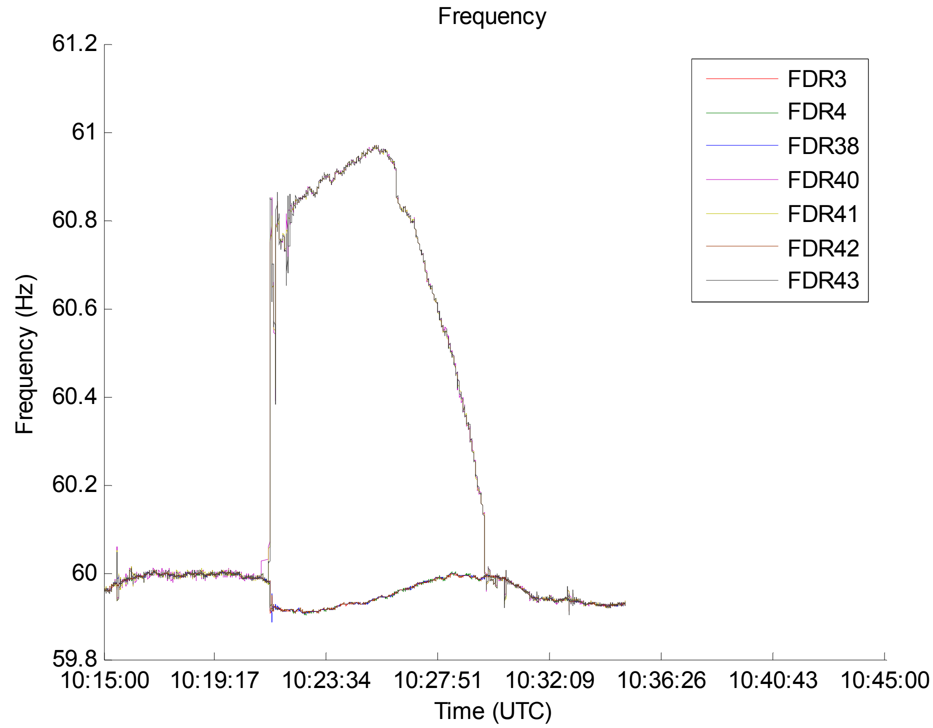

Figure 3.10 Frequency excursion during the islanding event. Note 3 FDRs in this plot show frequency excursions close to 61 Hz in the islanded system.

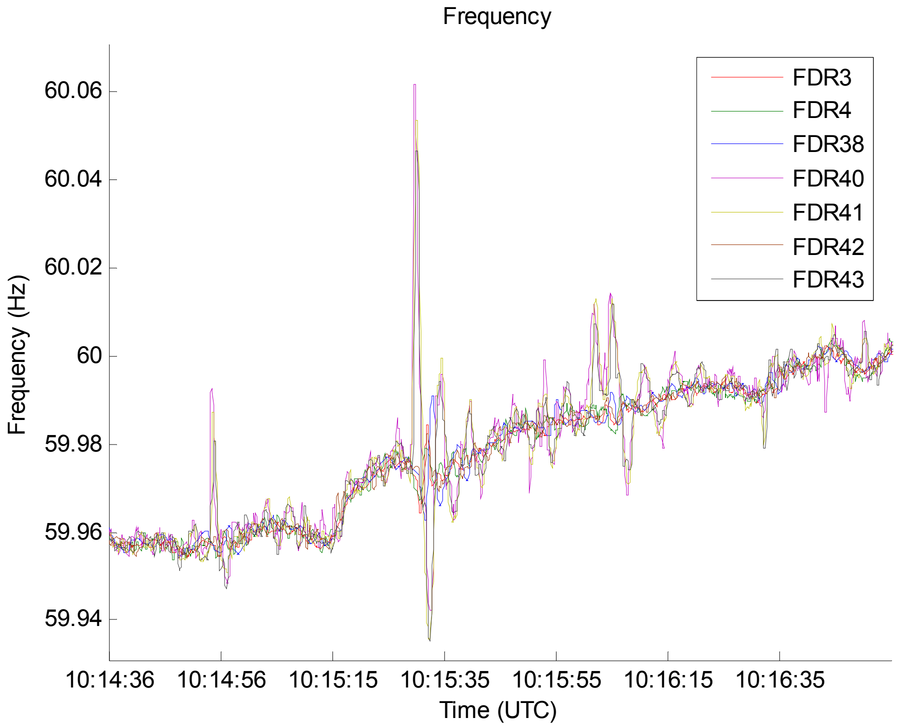

Figure 3.11 Frequency detail of line trip events before the islanding started

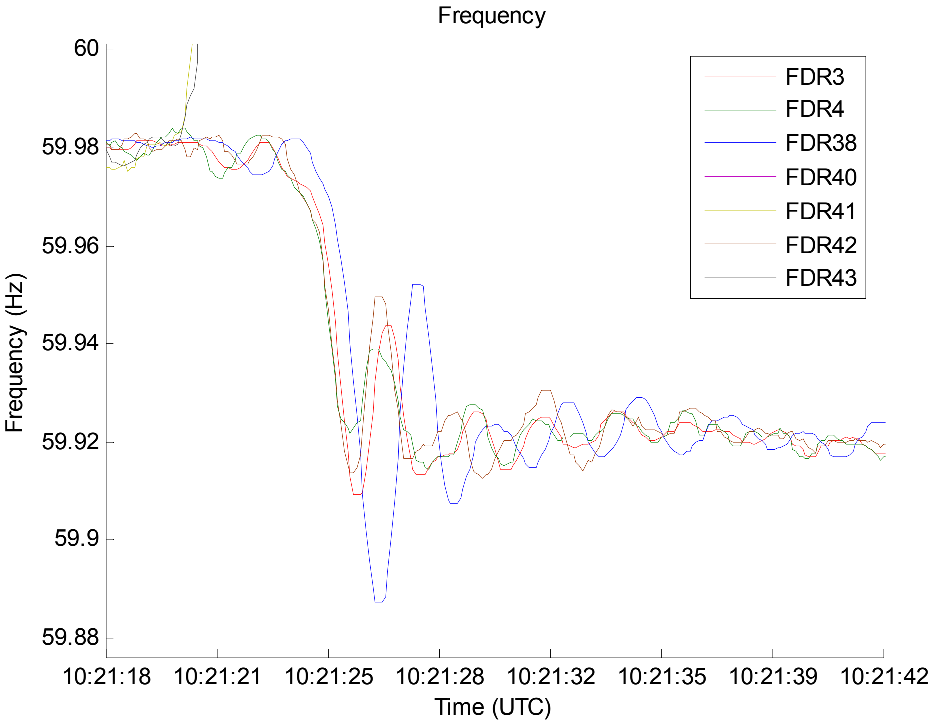

Figure 3.12 Frequency detail showing the start of the islanding - the remainder of the interconnection

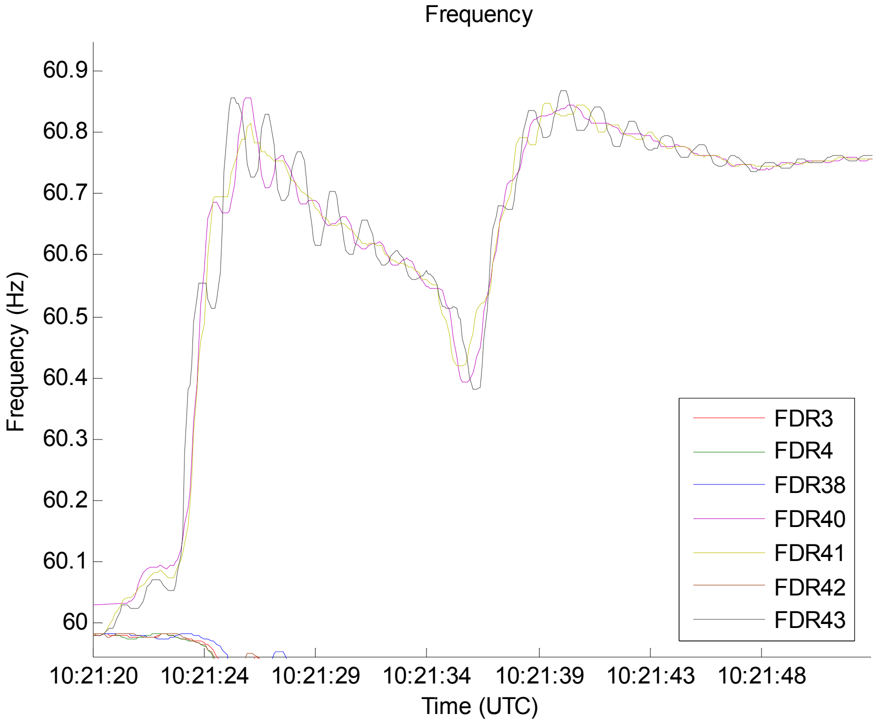

Figure 3.13 Frequency detail showing the start of the islanding - island

The frequency started to go down after 10:21:26 UTC. One of the possible reasons was the HVDC transmission system which looks like a generator to the rest of the system. During a transient disturbance, the DC power transmitted on the HVDC line can be ramped down rapidly to reduce the generation-load imbalance on both sides of the line. The rapid control of the DC power has the same beneficial effect as generator or load tripping from the view point of the AC system performance [26]. The HVDC transmission system involved in this disturbance is equipped with sending end and receiving end frequency control schemes by measuring the frequency deviation from 60 Hz and modifying the power transmitted on the HVDC lines [27]. As the island frequency started a rapid increase the HVDC frequency damping controls reduced HVDC transmission. Later, there was an HVDC reduction for the trip of a tie line. Later still, two HVDC valve groups (VGs) blocked on the overfrequency of 60.8 Hz, as well as there were automatic HVDC reductions initiated from another tie line trip and also initiated from an SVC overload. These reductions in HVDC transmission within the island arrested the frequency rise and attempted to reduce the generation-load imbalance.

At around 10:21:34 UTC, there was reportedly another trip of a 230 kV line by the out-of-step protection scheme, which might be responsible for the fast frequency rise after that time. Then frequency continued to increase at a much lower speed until 10:25 UTC, and started to decrease gradually until the island was successfully reconnected with the remainder of the EI at about 10:30 UTC (Figure 3.10). Both parts of the interconnections were able to remain stable during this islanding disturbance, which shows that protection and control actions were effective.

It can be noted that within the island the frequency from FDR43 beats against FDR40 (Figure 3.13). This is an interesting area of future work with regards to trying to identify mode shapes and controllability from the FNET data.

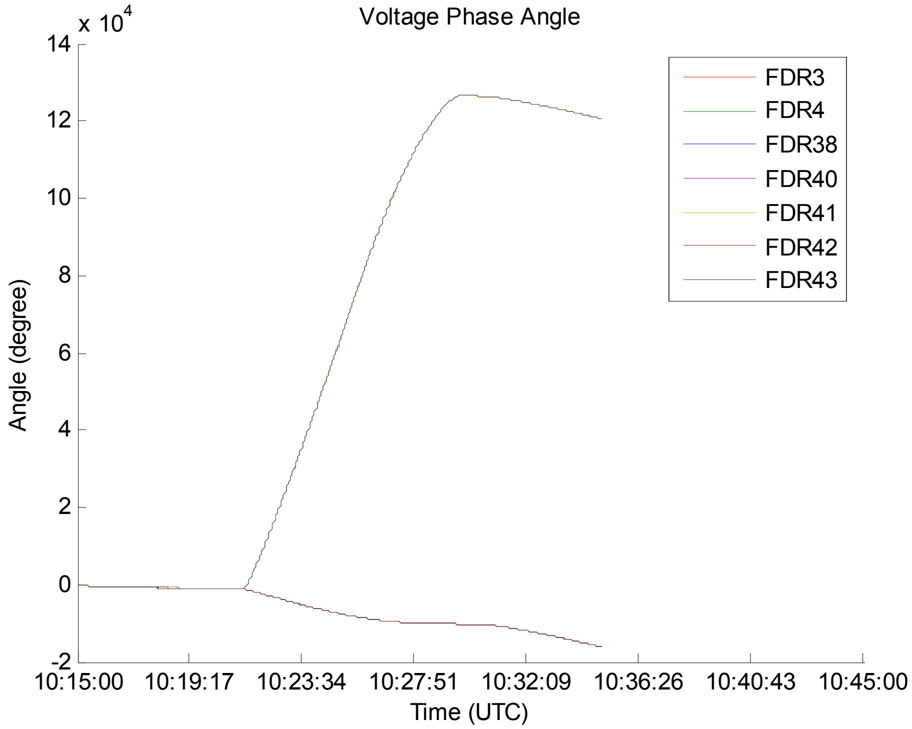

Figure 3.14 Phase angle of the islanding event. 3 FDRs (40, 41 and 43) provided the angle data in the runaway system as indicated by the angle acceleration top part while the rest are in the main system.

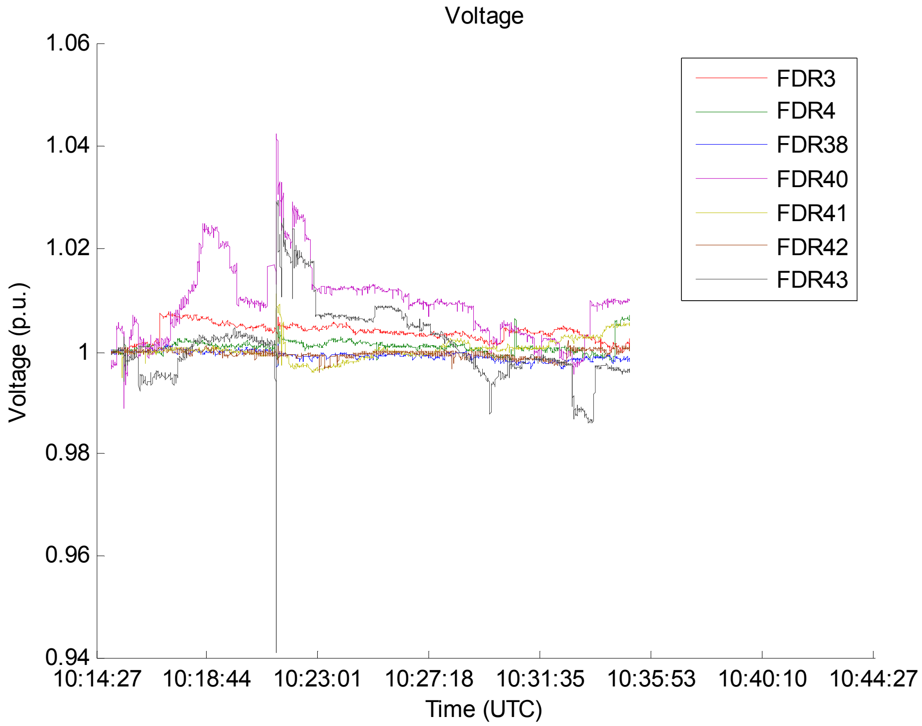

Figure 3.15 Voltage magnitude of the islanding event

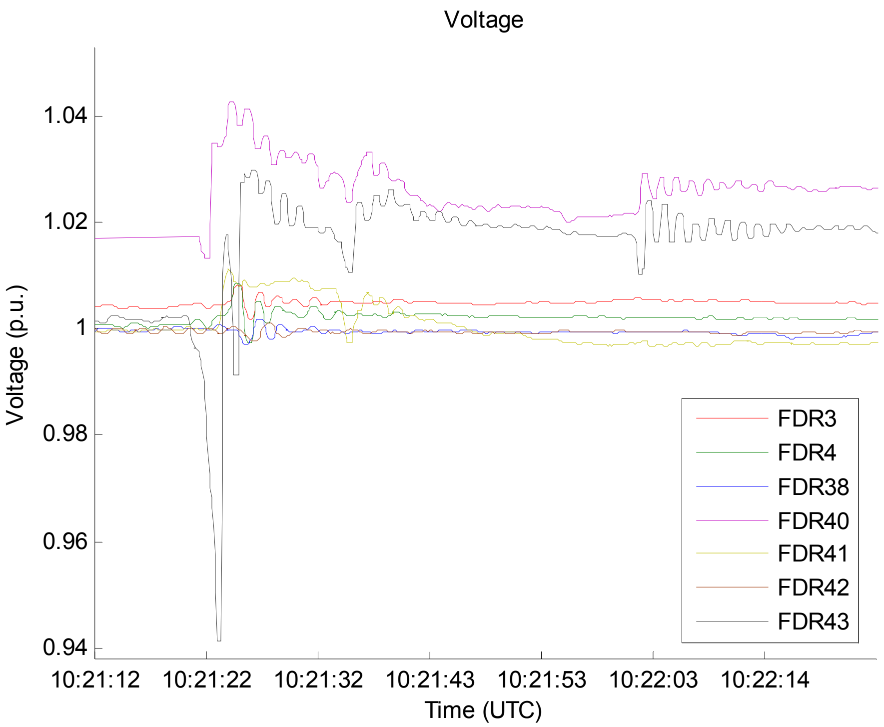

Figure 3.16 Voltage detail showing the start of the islanding event

3.3.2 Comparisons of Measurements from FDR and PMU

One of the FDR units is located at a 120 V outlet at a substation in the island area. A PMU (phasor measurement unit) is installed at a 230 kV bus in the same substation. In this section the measurements over a 10-minute time frame from FDR and PMU are plotted together for comparison, as in Figure 3.17 to Figure 3.20.

Both FDR and PMU provide GPS synchronized measurements. It can be seen from the figures that measurements from FDR match very well with those from PMU. Frequency measurements are almost the same in Figure 3.17.

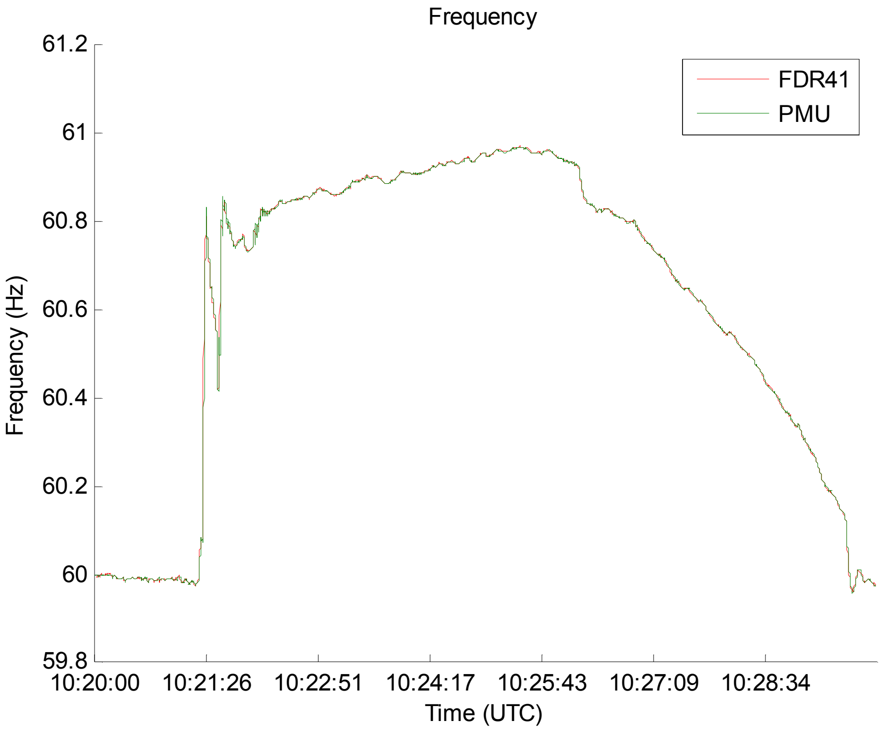

Figure 3.17 Frequency comparison of PMU and FDR both in the islanded area

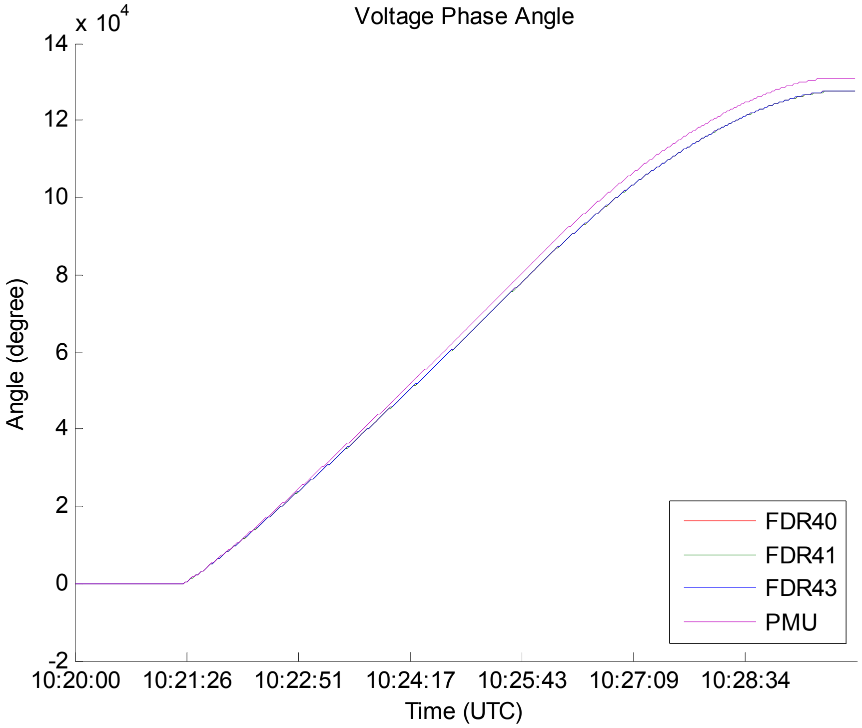

Figure 3.18 Phase angle comparison of PMU and FDR showing the islanding event. Note that the 3 FDR plots are on top of each other shown as one lower curve.

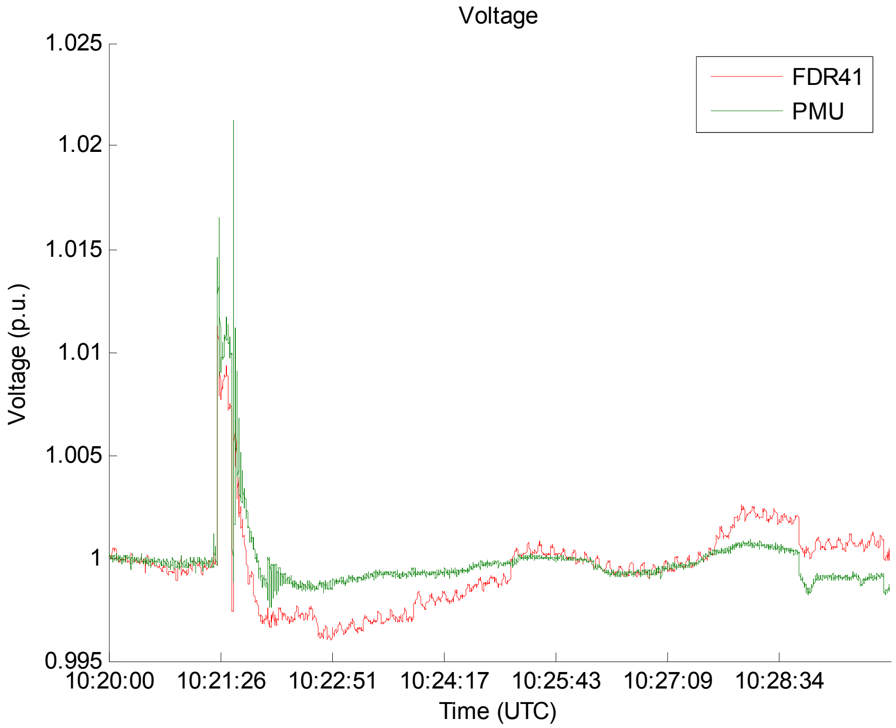

Figure 3.19 Voltage magnitude comparison of PMU and FDR both in the islanded area

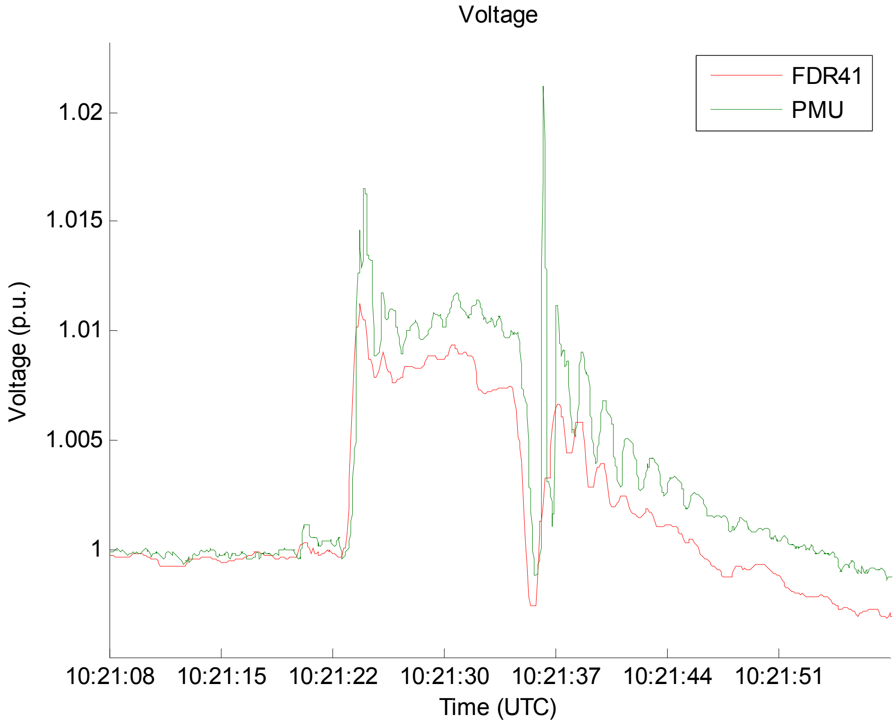

Figure 3.20 Voltage magnitude comparison detail of PMU and FDR both in the islanded area

One may notice that in Figure 3.19 there exist some differences between FDR and PMU in voltage magnitude measurements. Note that the FDR is placed at the distribution voltage level, so it is quite possible that other electrical devices such as transformers and loads will affect the transient voltage measured by FDR. Though not in this particular case, if the step-down transformer has OLTC (on-load tap changers), the turns ratio could change such that the voltage during transients measured at a lower voltage level will not be the exact reflection of the voltage measured on transmission lines. Furthermore, switching of reactive compensation in distribution systems can also affect voltage [28]. Despite that, abundant information of this islanding disturbance was captured by FDR units. Voltage details shown in Figure 3.20 demonstrate that voltage dynamics observed by the PMU also show up clearly in FDR measurements.

3.4 Florida Outage

At about 13:09 EST on February 26, 2008 the Florida power system was impacted by an outage initiated by a circuit-breaker failure at a substation west of Miami [29]. The Florida outage was ranked as a category four disturbance on NERC's system event classification scale for the loss of roughly 4500 MW of customer load, 4300 MW of generation, and 26 transmission lines, although most of the affected load was reported to be recovered within one hour of the initiating events [30]. NERC's event classification scale has five levels and is designed to designate the severity of bulk power system disturbances; category five is the most severe on this scale [31]. This event was captured by the FDRs throughout the Eastern Interconnection. As of June 2008, the causes and all other aspects of the outage are still under investigation of the Florida Reliability Coordinating Council (FRCC) and the North American Electric Reliability Corporation's (NERC) [30]. Yet the recordings from the FDRs in the distribution network help to shed some light on the sequence of the events.

The frequency excursions observed by three FDRs close to the outage area over one hour are shown in Figure 3.21 and the "spike" at 18:09 UTC is actually large oscillations resulted from the delayed clearing of the initial fault as magnified in Figure 3.22 and Figure 3.23. As noted in FRCC's interim report in [29] the initiating event was a three-phase fault on a failed 138 kV switch at a transmission substation in south Florida. The disabling of all local protective relay equipment while troubleshooting a transmission switch led to delayed clearing of the fault which remained on the system for approximately 1.7 seconds.

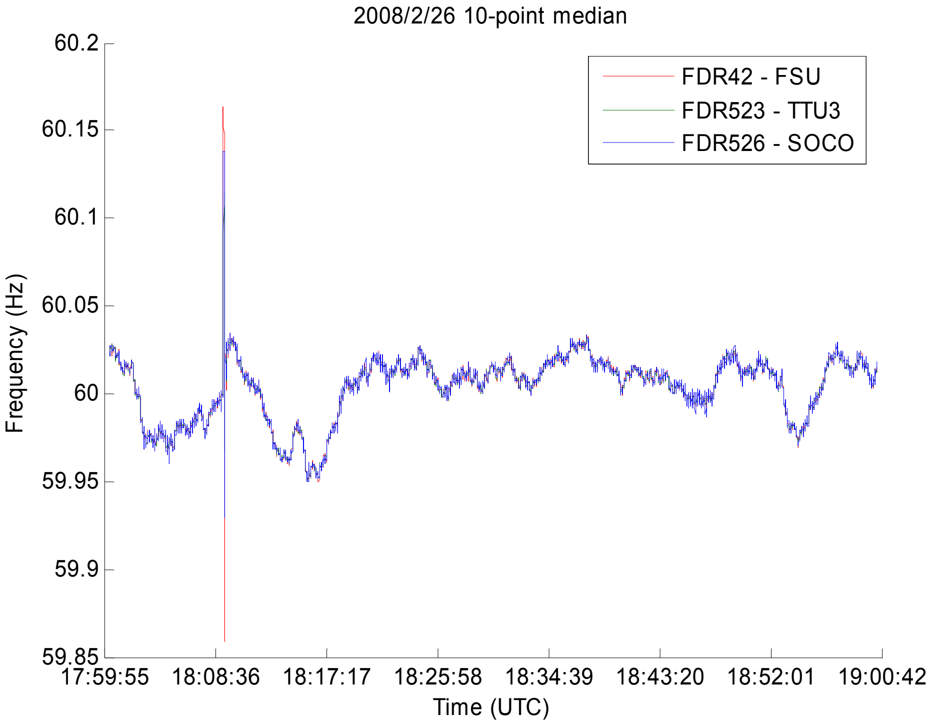

Figure 3.21 Frequency excursion between 18:00 to 19:00 UTC for the Florida outage

The depressed voltage (Figure 3.24) due to the fault led to protective trip of the two Turkey Point generating units as well as some fossil generation in the region. The FDR42 unit is in Florida therefore it clearly saw the voltage depression. The frequency and angle swings radiated in the system as shown in Figure 3.23 and Figure 3.25 but the frequency and angle perturbation was damped out within 10 seconds due to the isolation of the fault and tripping of generators.

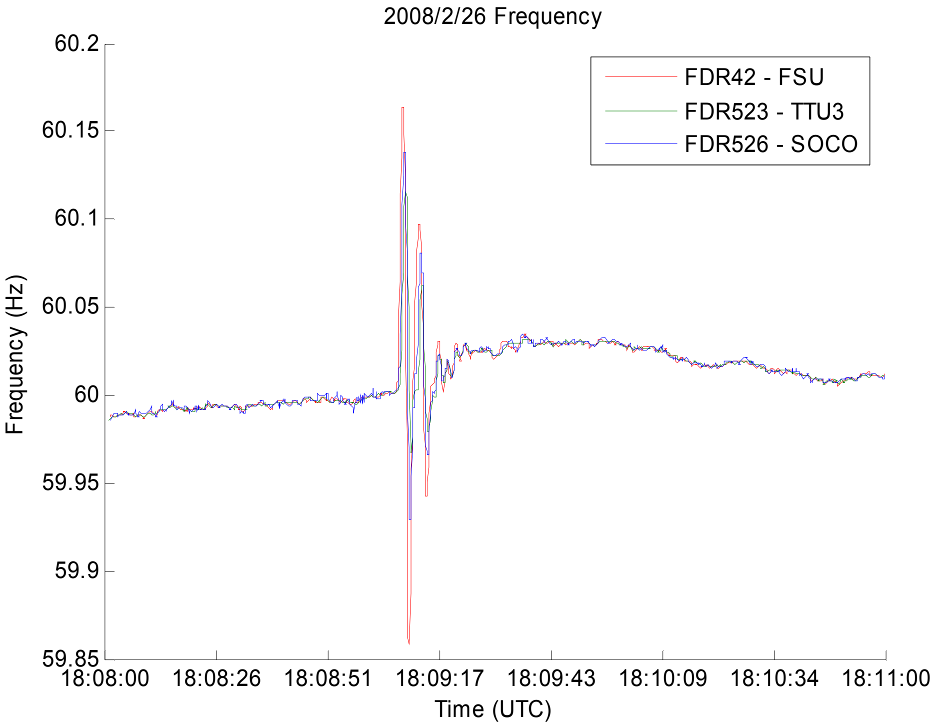

Figure 3.22 Frequency excursion over a three-minute time window for the Florida outage

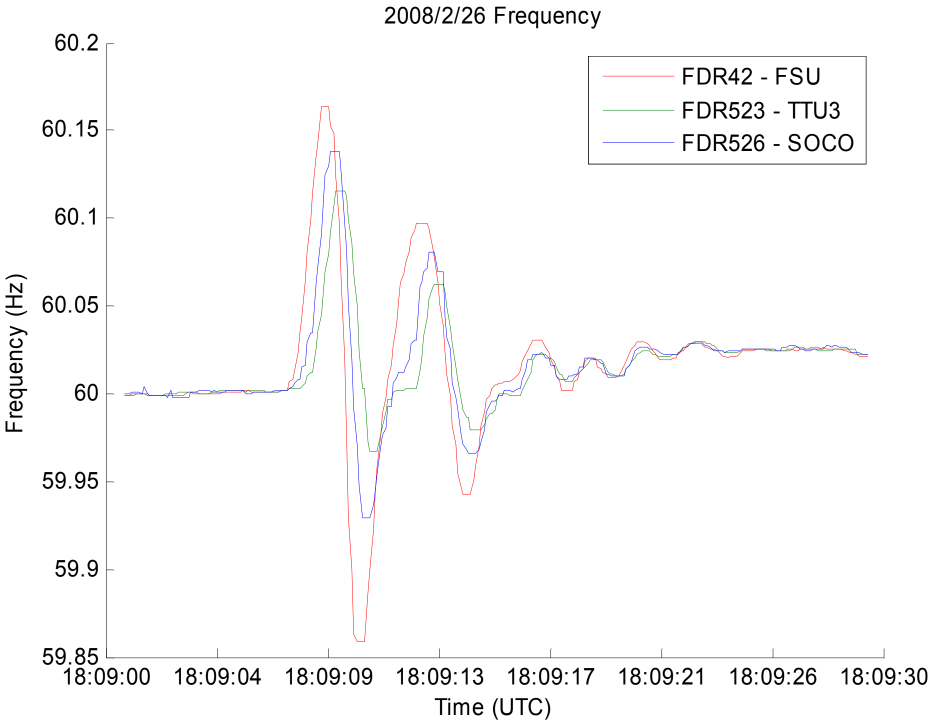

Figure 3.23 Detail of frequency oscillations during the Florida outage

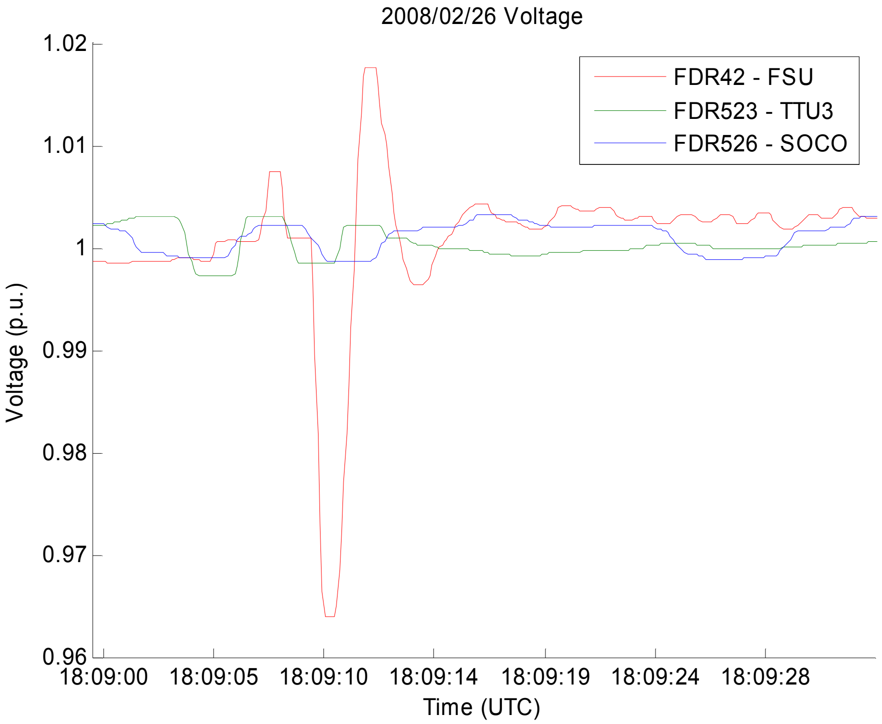

Figure 3.24 Normalized voltage showing the voltage depression during the Florida outage

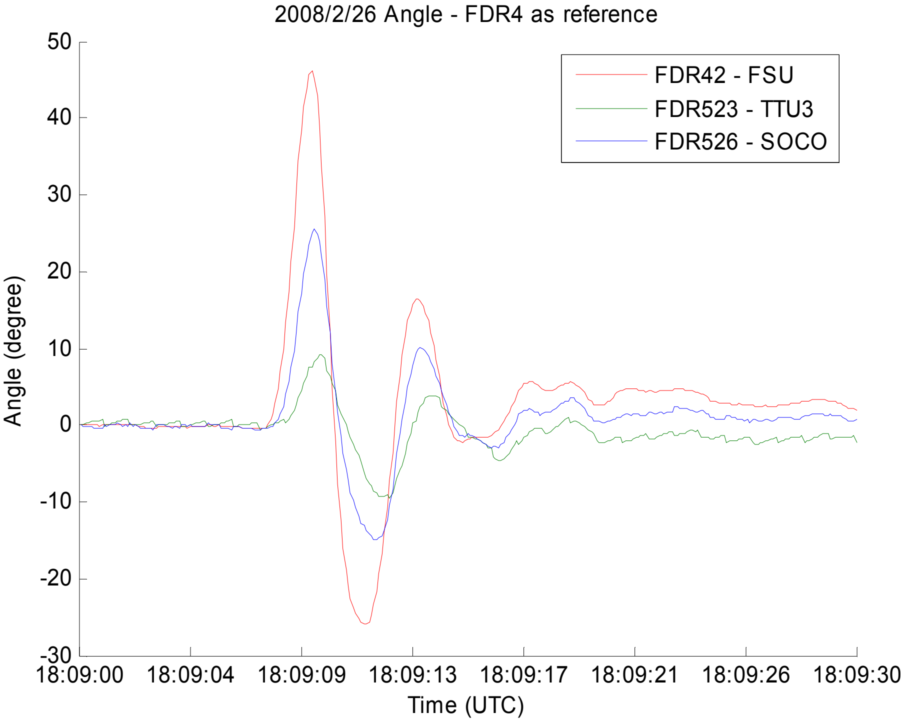

Figure 3.25 Detail of angle oscillations during the Florida outage (referred to FDR4)

The frequency increased immediately after the oscillations, which indicates possible load loss but it started to decrease shortly. It is reported that the massive generation loss drove the region to an under-frequency condition at about 59.95 Hz between 18:10 to 18:16 UTC that led to under-frequency load shedding (Figure 3.21). The Florida system was able to keep synchronized with the bulk EI system during the frequency and voltage perturbations.

3.5 Faults in HVDC Systems

Three High-Voltage Direct-Current (HVDC) transmission related events observed in the EI by FNET in 2008 are examined in this section. Two of them are the loss of the Quebec – New England HVDC interconnection at different time, and the other is an event at the Nelson River HVDC system. Both HVDC systems are bipolar transmission and the configuration of a two-terminal bipolar link is depicted in Figure 3.26.

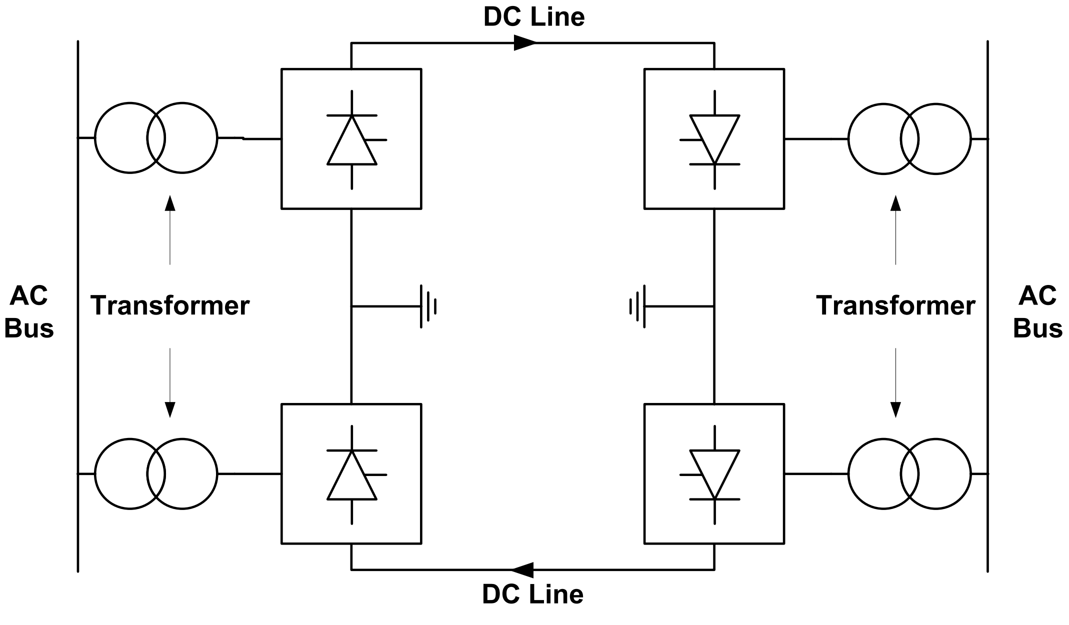

Figure 3.26 Configuration of bipolar HVDC link

A pair of conductors is used in opposite polarity. The system can operate with only one pole in service (mono-polar mode) transferring half of the total rated capacity when the other pole is out due to fault or maintenance. Each terminal has two converters of equal rated voltage connected in series on the DC side. The junctions between the converters are grounded. The valves in the converters are controlled electronic switches that conduct in only in one direction.

3.5.1 Events in the Quebec – New England HVDC Interconnection on June 20 and October 25, 2008

As shown in Figure 3.27, the 920 mile long Quebec – New England HVDC line connects the asynchronous Hydro Quebec system and the EI system with its north terminal at Radisson, Canada and south terminal at Sandy Pond in Ayer, Massachusetts [32]. The ± 450 kV multi-terminal HVDC lines can transmit about 2000 MW in either direction [33].

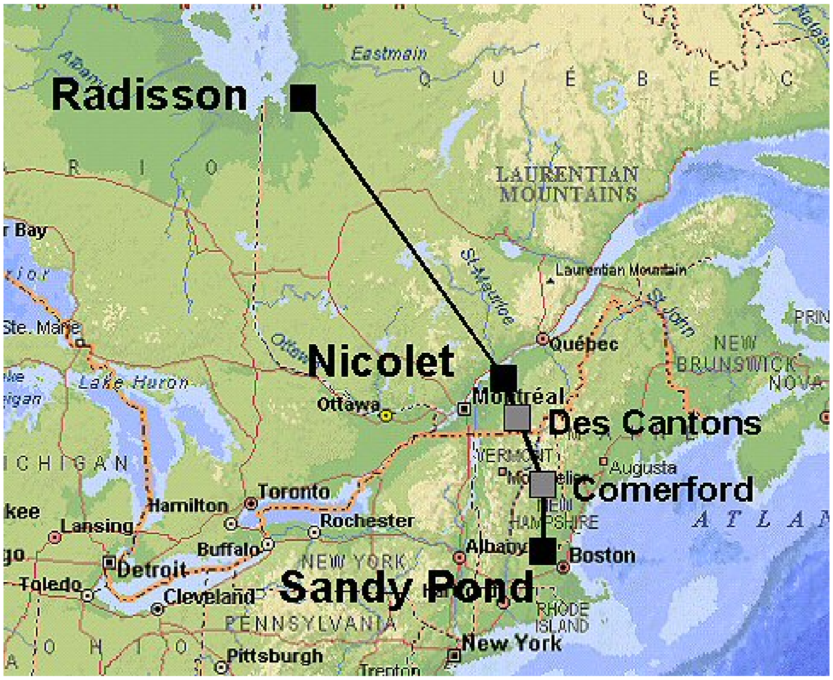

Figure 3.27 Location of the Quebec – New England Phase II HVDC transmission line (map source: USGS)

At 19:29:41 UTC on June 20, 2008 the frequency in the northeast EI experienced large swings because of the disconnection of the Quebec – New England HVDC line due to a failure of the protection and control system at Radisson. The loss of one pole also resulted in a power loss of 500 MW which initiated a frequency decline of about 17 mHz (Figure 3.28). It can be seen from the figure that the New England area was the power receiving end that saw a loss of generation. The relative angle in the EI in Figure 3.29 reveals that the loss of the HVDC line accounted for an angle change and angle swings at each of the three FDR locations. The initial decline in the angle also confirms that the power was transmitted from Quebec to the EI system where the measurements were taken. The angle signature is similar to that of the loss of an AC transmission line, which will be discussed in detail in Chapter 5 and 6.

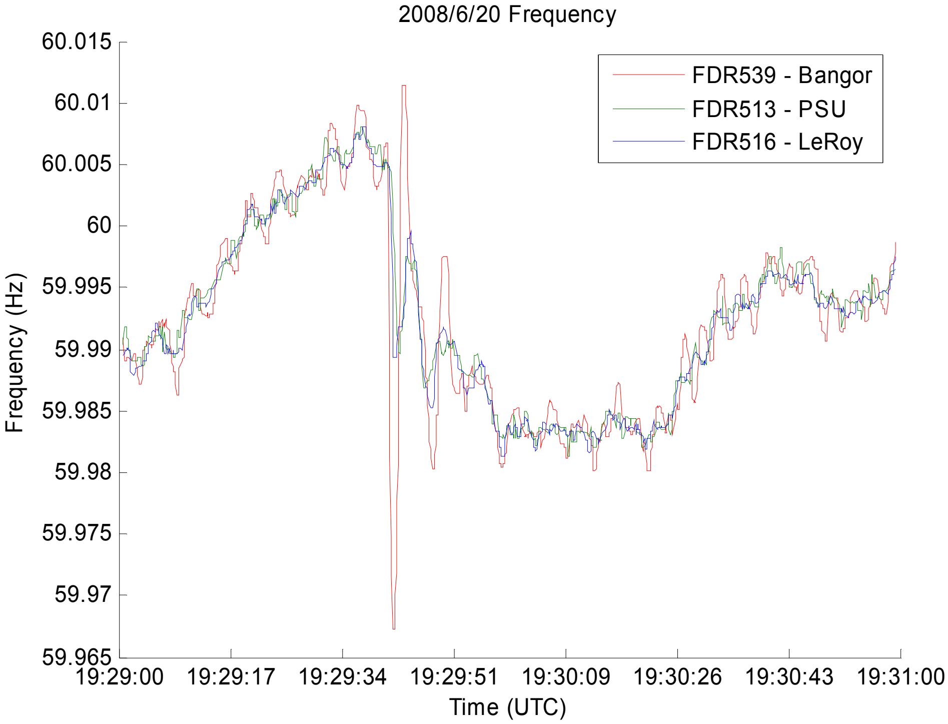

Figure 3.28 Frequency of the Quebec – New England HVDC event on June 20, 2008

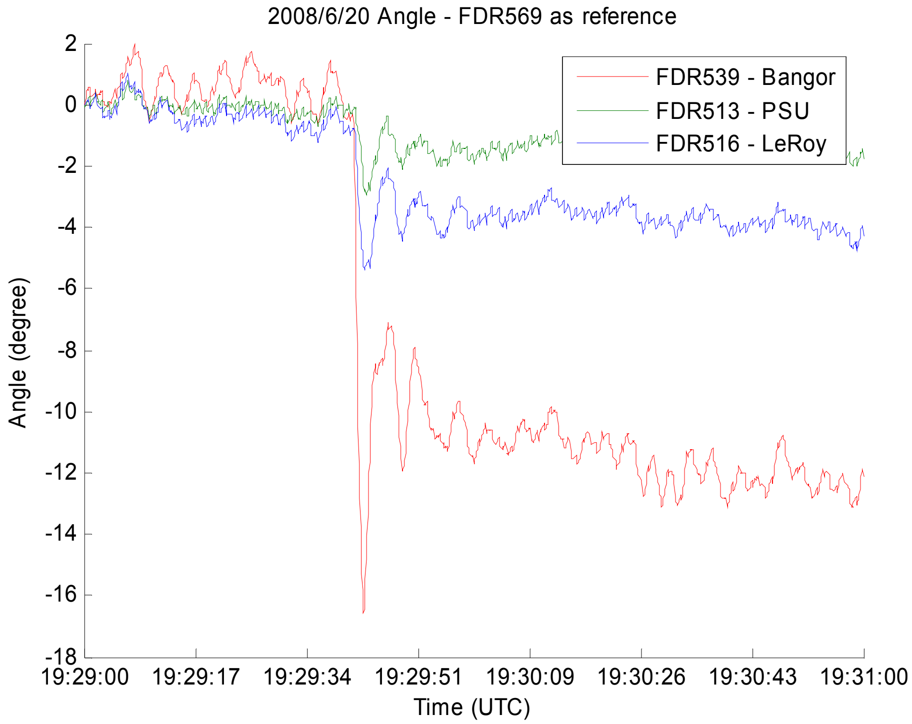

Figure 3.29 Relative Angle of the Quebec – New England HVDC event on June 20, 2008 (FDR 569 as reference)

The FNET situation awareness system detected a load-shedding like event at 6:05:46 UTC on October 25, 2008 in the New England area, which was later confirmed as the loss of the Quebec – New England HVDC line due to loss of the cooling. At the time of this event the New England system was selling about 500 MW power to Hydro Quebec. Therefore, as shown in Figure 3.30, the New England area saw a quick rise in frequency indicating the sending end of the line, whereas the frequency at Montreal experienced a clear sudden decline. It is noticeable that the frequency at Montreal is quite different from the frequency in the EI since the Quebec system operates asynchronously relative to the EI system. The angle at the three FDR locations in Figure 3.31 saw oscillations similar to those in the event on June 20 but the initial angle change is positive unlike the previous event due to the different power transfer direction in these two cases. Among the three FDRs in the EI, FDR38 which is close to the Sandy Pond terminal of the HVDC line, saw the largest swing both in frequency and in angle indicating that the machines in the New England area responded more to the HVDC line trip than other further away machines.

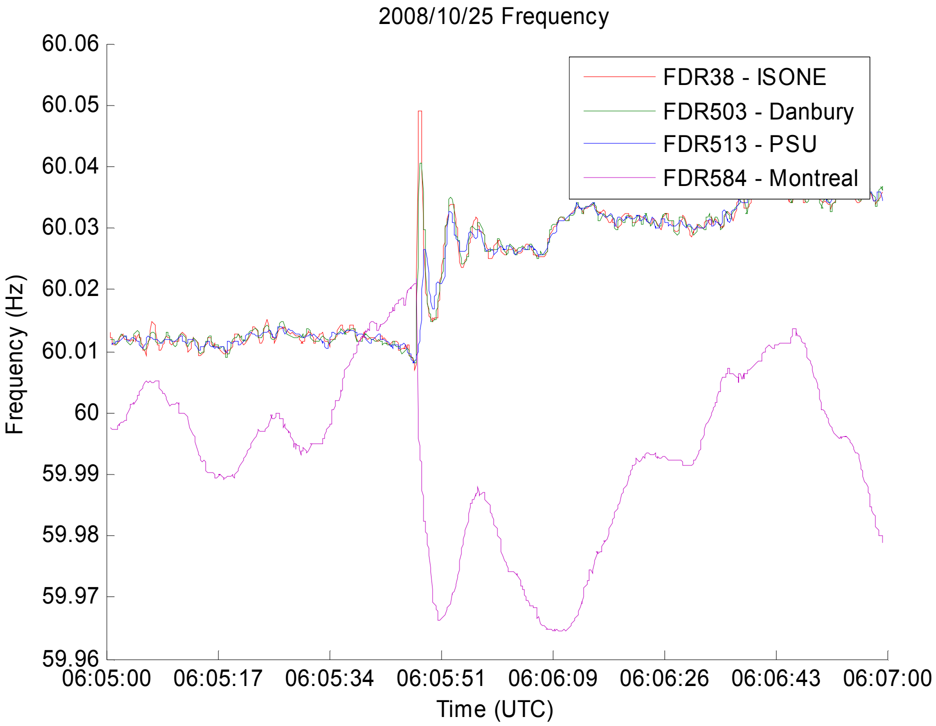

Figure 3.30 Frequency of the Quebec – New England HVDC event on October 25, 2008

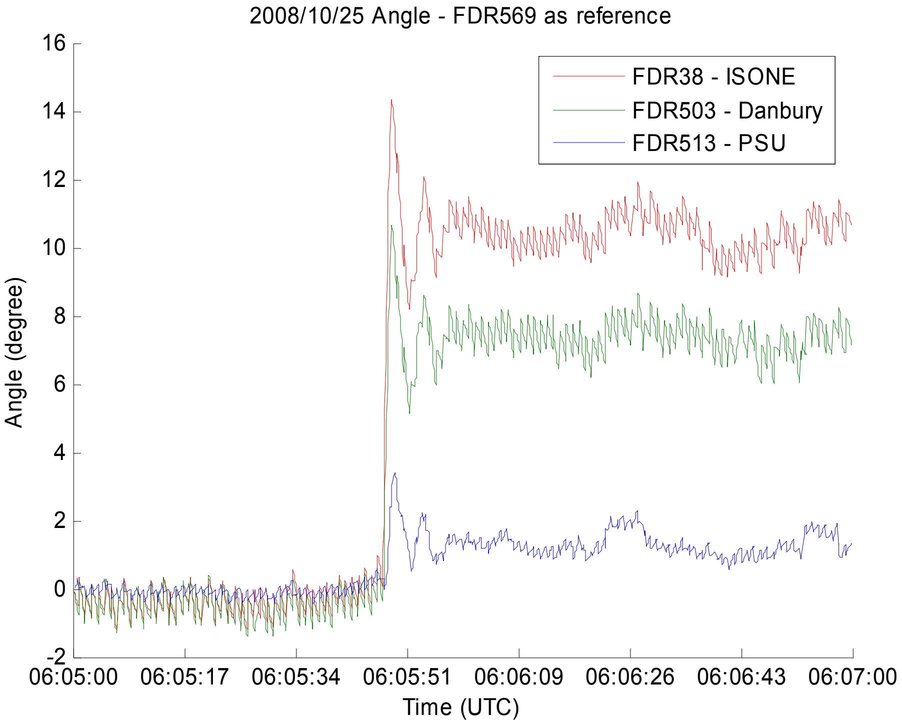

Figure 3.31 Angle of the Quebec – New England HVDC event on October 25, 2008 (FDR 569 as reference)

It can be seen from the above two cases that disconnection of the Quebec – New England HVDC line will appear as generation loss in one Interconnection and as load loss in the other depending on the power flow direction on the line at the time it is tripped.

3.5.2 Event in the Nelson River HVDC System on June 2, 2008

Another HVDC related event in 2008 occurred on June 2 in the Nelson River HVDC transmission system which consists of two HVDC lines (Bipole 1 and Bipole 2) from Radisson and Henday Converter Stations (from AC to DC) southward to Dorsey Converter Station, located near Winnipeg as depicted in Figure 3.32. Bipole 1 (Radisson – Dorsey) is 556 miles long and rated at ± 450 kV, 1800 MW; while Bipole 2 (Henday – Dorsey) is 581 miles long and rated at ± 500 kV, 2000 MW. The HVDC system bridges the hydro power plants in north Manitoba to the load centers in the south of the province [34].

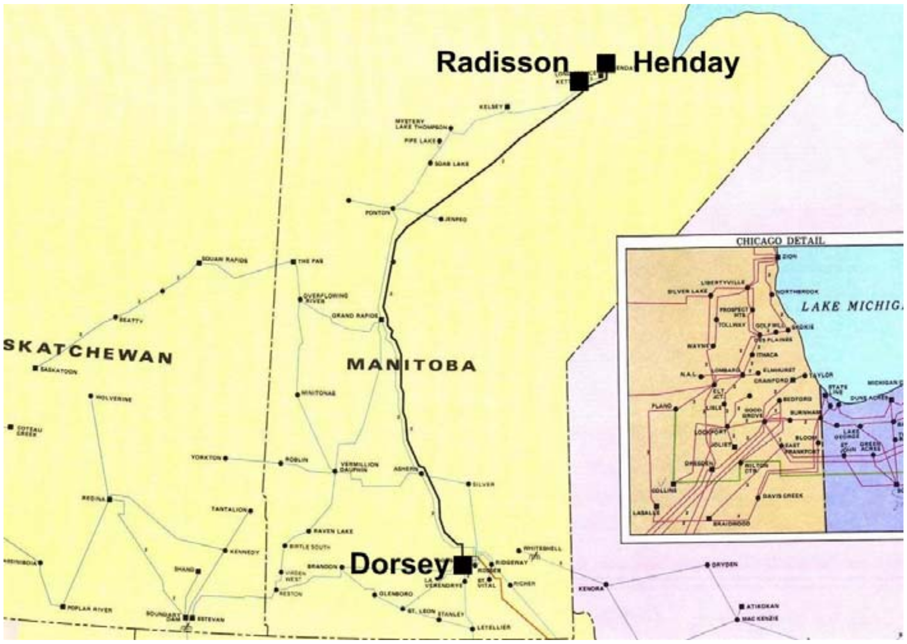

Figure 3.32 Location of the Nelson River HVDC transmission system (map source: NERC)

The event on June 2 was initiated by simultaneous high resistance faults due to forest fires in the area. It has been observed that forest fires resulted in high resistance faults on more than one pole in some instances and in others caused a short circuit between two poles in the Nelson River HVDC system [35]. High-impedance faults are short-circuit faults caused mainly by tree branches touching a phase conductor and failing or dirty insulators that result in flashovers between a phase conductor and the ground [36].

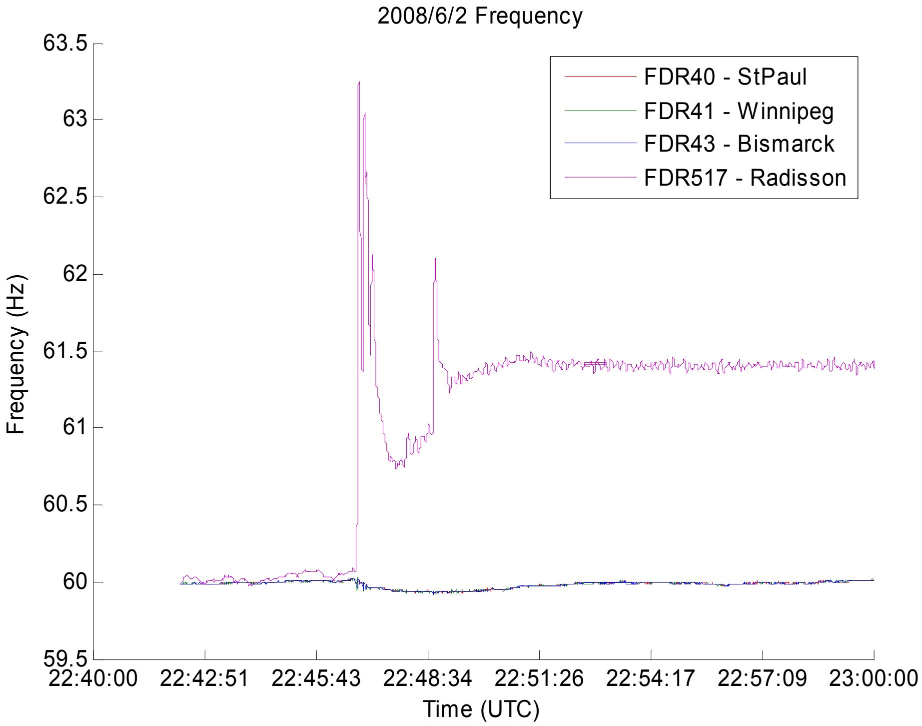

Figure 3.33 20-minute frequency excursion of the Nelson River HVDC system event at both sides of the HVDC lines

During this disturbance, 3 poles of the two HVDC lines were disconnected resulting in a 1900 MW loss to the EI system. The frequency excursions captured by 4 FDR units around the Manitoba area are shown in Figure 3.33 and Figure 3.34. It has been confirmed by Manitoba Hydro that the frequency at Radisson varies greatly as can be seen in Figure 3.33. The Kettle Generating Station is an isolated hydro plant supplying power directly to the Radisson Converter Station and the generated power enters the Manitoba AC transmission system at Dorsey, which may account for the large frequency deviations at Radisson [37][38].

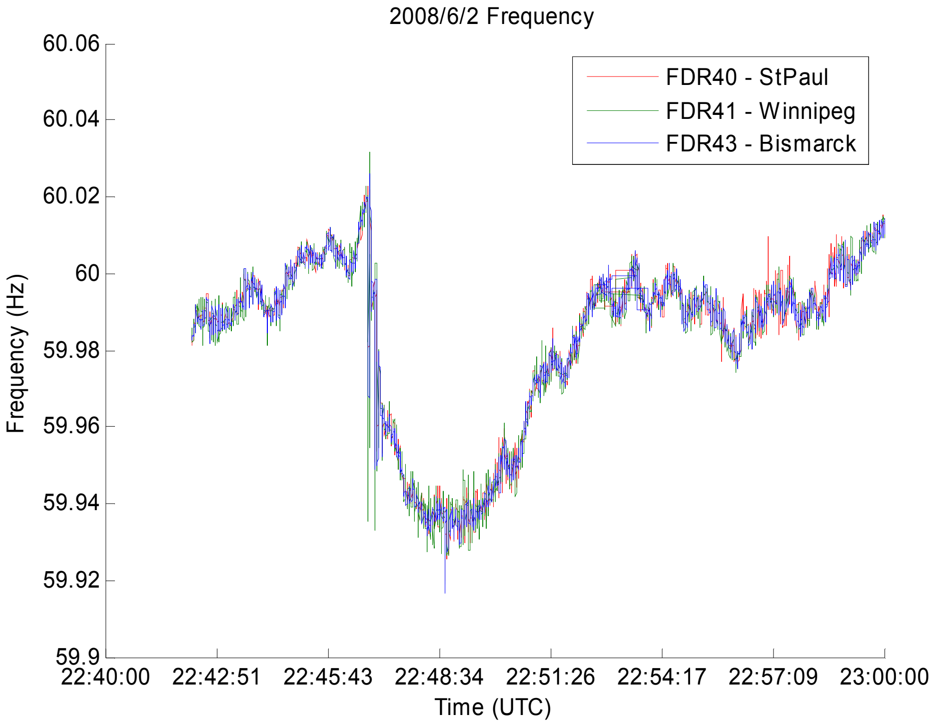

Figure 3.34 20-minute frequency excursion of the Nelson River HVDC system event at the Dorsey side

Two FDR units, FDR41 and FDR 517 are installed at the Dorsey and Radisson stations, the two ends of Bipole 1. Therefore this disturbance was clearly observed in the measurements. The effects of the HVDC system control actions are reflected in the measurements. When a fault occurs in the HVDC system, valve blocking is achieved by interrupting the positive pulses to the gates of all the valves in a bridge, thus extinguishing the current. At the same time, the bridge is bypassed by closing the bypass switch to prevent overvoltage on the bridge due to current extinction [35].

A timeline of events can be obtained from the FDR measurements as well as fault records from Manitoba Hydro, as can be seen from Figure 3.35 to Figure 3.38 that show the frequency excursions at the two ends of the HVDC link. During this event pole 1 and pole 2 of Bipole 1, and pole 4 of Bipole 2 were disconnected. The time listed below is UTC.

22:46:43: Low voltage was detected at pole 1 of Bipole 1 and three valve groups were blocked and the bypass switches were closed.

22:46:53: The differential protection at pole 4 of Bipole 2 detected the fault and operated. Two valve groups were blocked and bypassed.

22:46:57: Low voltage was detected at pole 2 of Bipole 1. The valve group VG21 were blocked and bypassed.

22:47:04: One valve group (VG22) of pole 2 of Bipole 1 was blocked and bypassed.

22:48:40: The valve group VG23 of pole 2 was blocked and the bypass switches were closed.

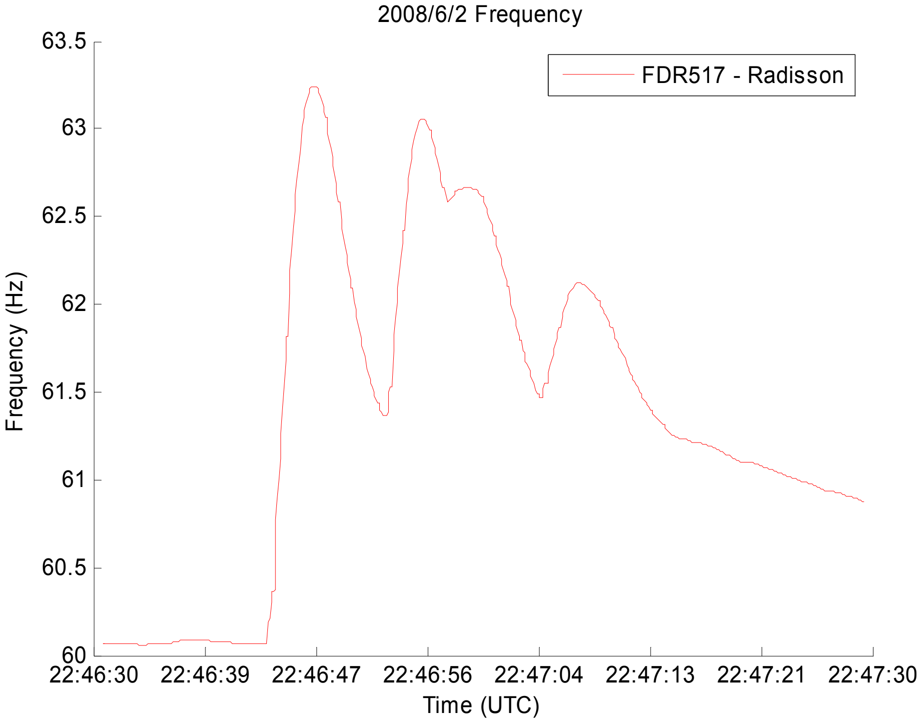

Figure 3.35 Frequency detail of the Nelson River HVDC system event at Radisson (1)

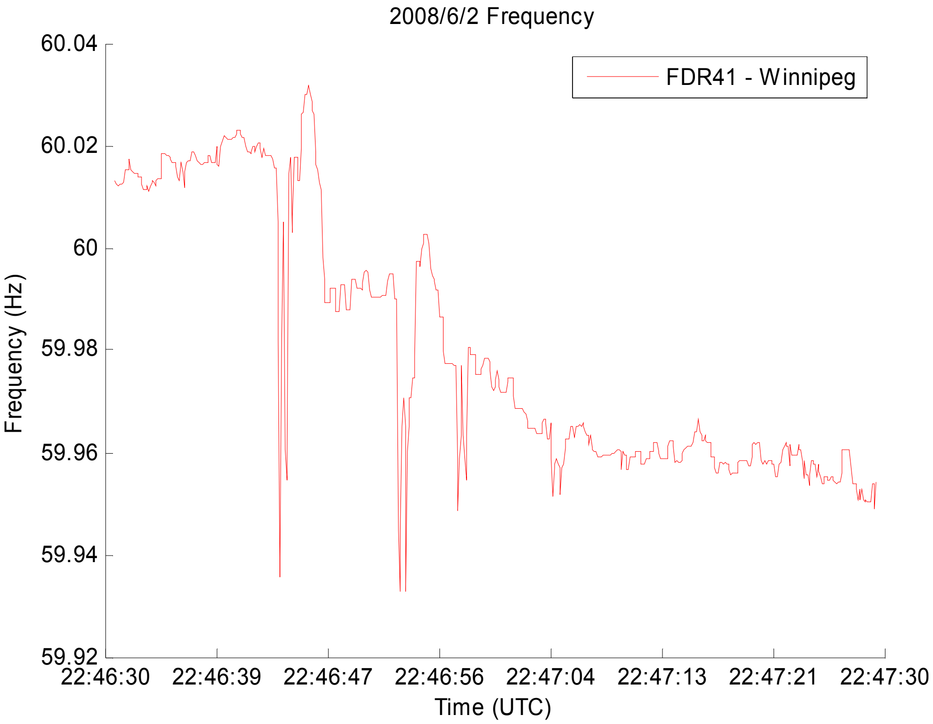

Figure 3.36 Frequency detail of the Nelson River HVDC system event at Winnipeg (1)

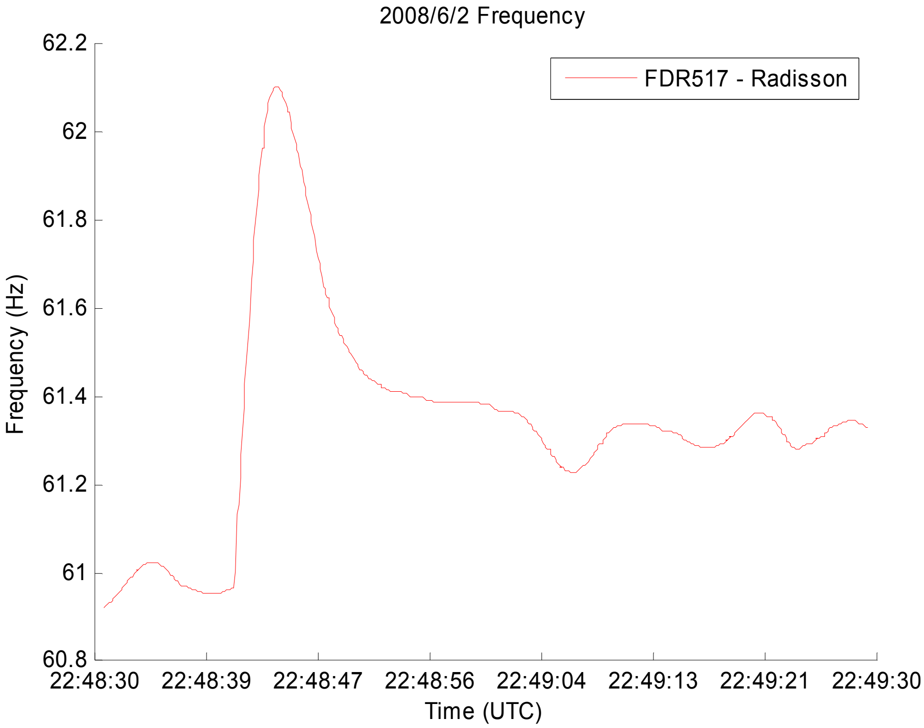

Figure 3.37 Frequency detail of the Nelson River HVDC system event at Radisson (2)

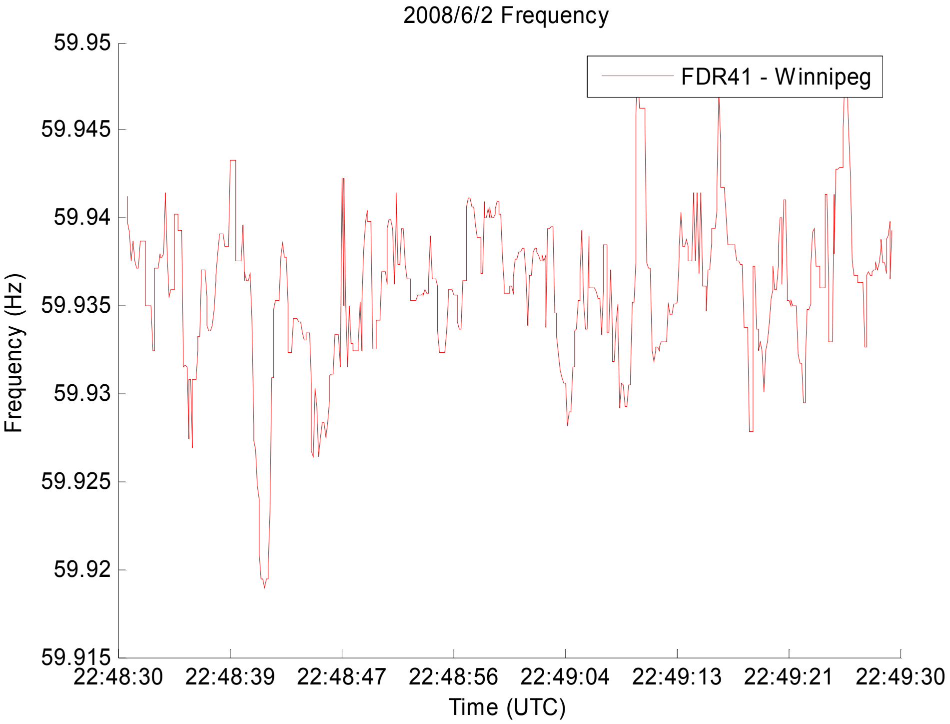

Figure 3.38 Frequency detail of the Nelson River HVDC system event at Winnipeg (2)

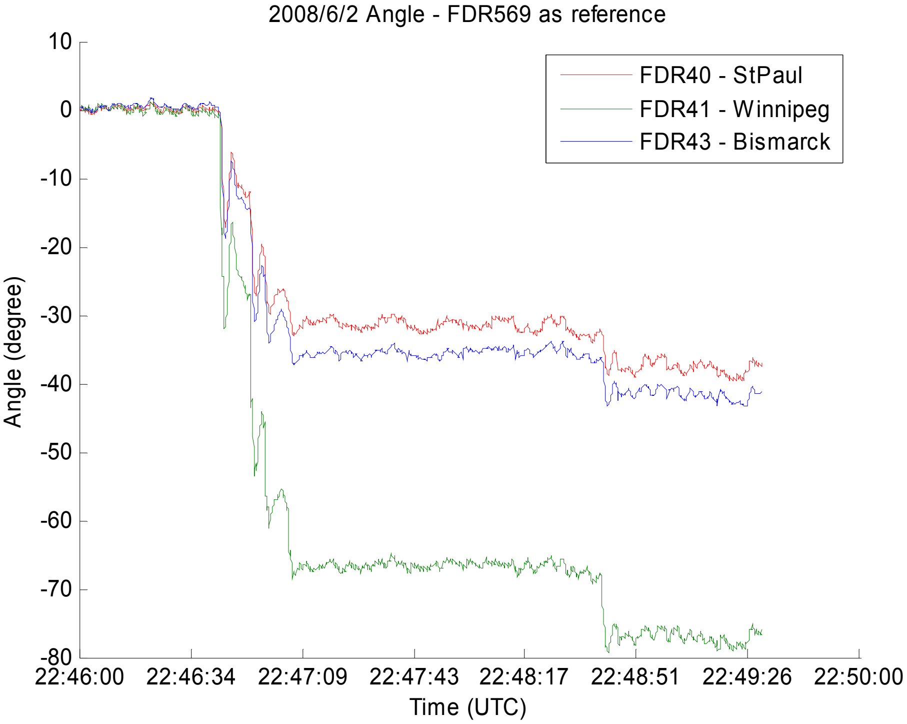

Figure 3.39 Relative Angle of the Nelson River HVDC system event at the Dorsey side (FDR569 as reference)

From the timeline and the figures one can tell that each time when a pole loss occurs frequency oscillations can be observed but the frequency change was opposite at the two ends of the HVDC connection. The angle observed at the Dorsey side of the HVDC line demonstrates a step change of angle decline at each pole loss and valve group blocking, together with angle swings, while FDR41 at the Dorsey station saw the largest angle change (Figure 3.39).

3.6 Dynamic Performance of AD/DC Systems

As mentioned in section 3.5, the hydro power plants at the north terminal of the Nelson River HVDC system are isolated with no AC loads, thus the generators have no benefit of the load damping. Moreover, the neighboring AC systems Manitoba Hydro is interconnected with are relatively weak in the area. The HVDC links, when controlled in the constant power mode, appear to be frequency insensitive loads to the AC systems and may provide negative damping to system swings. DC links do not inherently allow the flow of synchronizing power in response to a disturbance. Due to this system characteristic, special auxiliary power controls have been studied and implemented to improve the dynamic performance of the interconnected AC/DC systems as described in references [27] and [38].

With the installation of the FDRs at the two terminals (Radisson and Dorsey) of the Nelson River HVDC Bipole 1, they dynamic performance of the AC/DC systems and the effects of the damping controls are able to be observed in the time-synchronized measurements. Each bipole in the Nelson River HVDC system has frequency control at both the sending end and the receiving end. The sending-end frequency control provides power order modulation according to the frequency deviation at the Radisson and Henday stations, thus making the DC link load frequency sensitive. Without such control the generators feeding the DC load are subject to a torque which varies inversely with the frequency since

$$P = T\omega \tag{3.1}$$

where T is the torque in $N \cdot m$ and ω is the angle velocity in rad/s.

The receiving-end frequency control is provided to minimize the frequency deviation in the system. In addition, the damping controls also include receiving-end phase angle control that helps to maintain the stability of the south Manitoba system during disturbances.

In this section three disturbances near south Manitoba detected by the FNET are investigated to illustrate the effects of the damping controls in the HVDC system. The frequency is observed on both ends of the HVDC links. Figure 3.40 and Figure 3.41 show the frequency of a generation loss event detected on June 24, 2008 and a load loss event on November 2, 2008, respectively.

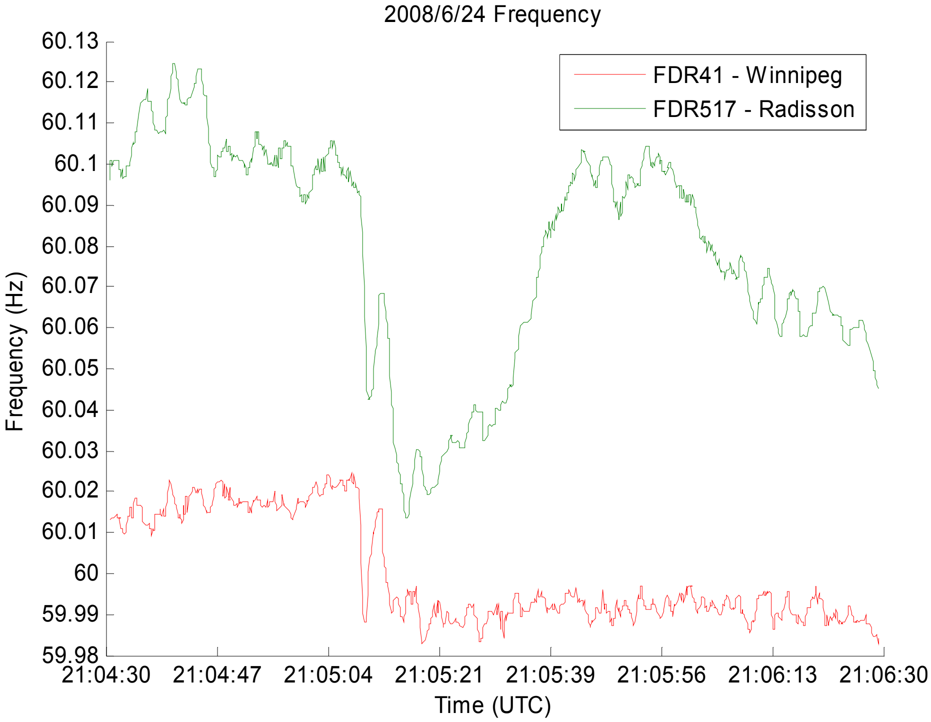

Figure 3.40 Frequency observed at both sides of the HVDC line during a generation loss event in the EI on June 24, 2008

As can be seen from Figure 3.40, the fast frequency decline and swings at Winnipeg due to the disturbance are clearly observed at Radisson. The frequency deviation during the disturbance is different at the two ends of the HVDC line because of different frequency response characteristics due to different amount of inertia.

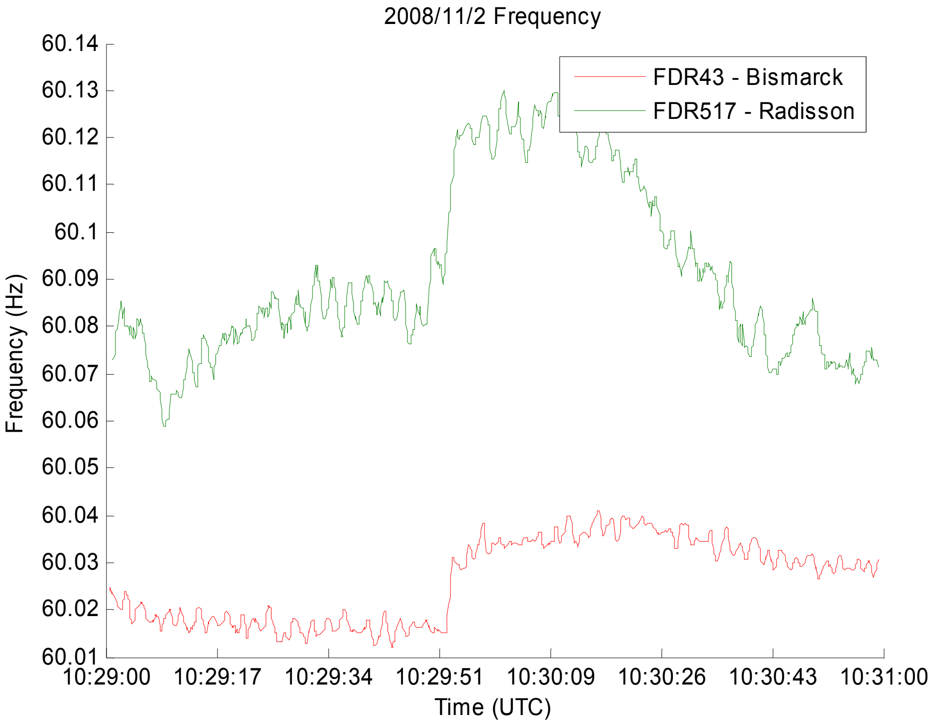

Figure 3.41 Frequency observed at both sides of the HVDC line during a load loss event in the EI on November 2, 2008

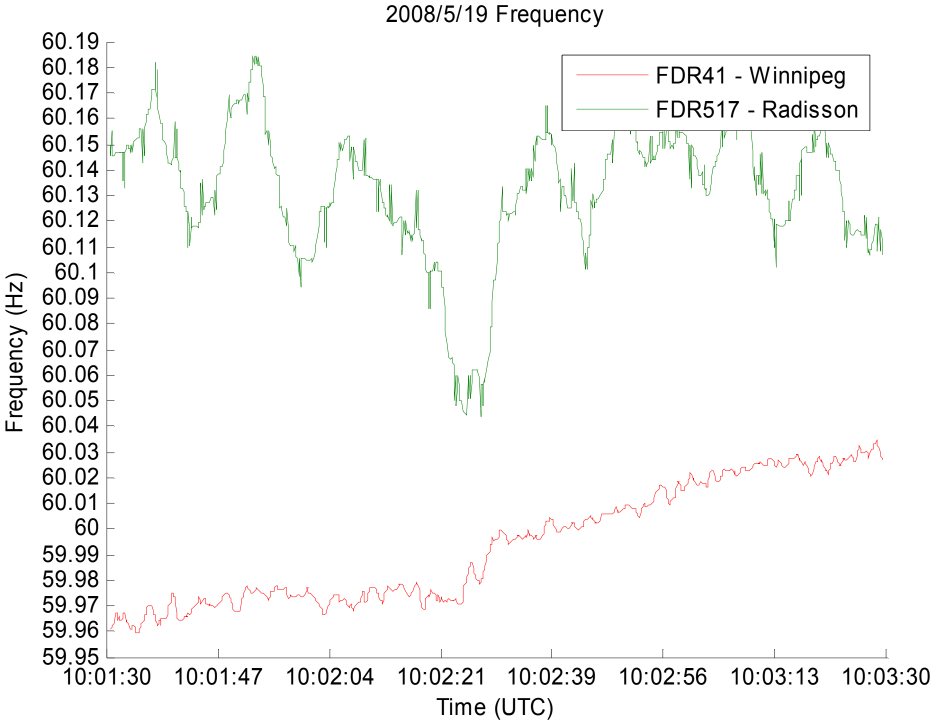

Figure 3.42 Frequency observed at both sides of the HVDC line during a load loss event in the EI on May 19, 2008

Such correlation is not obvious during steady state since the damping controls described above are designed to respond to fast transients caused by disturbances and not steady-state variations [38]. The instance in Figure 3.41 agrees with this concept in that the sharp frequency rise at the Dorsey end of the system is also ‘translated’ to the other end of the DC link.

Figure 3.42 shows a load loss event in the EI system south to the HVDC system but not observed by the FDR at Radisson. The frequency at Winnipeg and Radisson does not show much similarity perhaps because the frequency transient resulted from the load loss is not large enough or too gradual to be reflected across the DC link.

In summary, for large fast changes in frequency we can expect to see the continuation of the frequency excursion temporarily across the DC link given the DC link has damping controls. For gradual frequency changes we can expect no frequency information on the other side of the DC interconnections. By monitoring the DC links with damping controls, the impact of the HVDC transmission system on the overall dynamic performance of the AC/DC systems can be studied, which may benefit the study of disturbance location and system inertia calculation. Furthermore, the wide-area measurements from PMU and FNET can provide system-wide information to assist designing the HVDC damping controllers to enhance the dynamic performance of the interconnected power systems [39].

While the damping controls in the Nelson River HVDC system adjust the power flow on the DC links as the frequency in the AC systems changes, controls in other HVDC systems may not be frequency sensitive in order to prevent the disturbances in one area from propagating to the other. The North America bulk power systems consist of four main asynchronous Interconnections: the EI, the WECC, the ERCOT and the Quebec. They are interconnected by HVDC ties that can buffer one AC system from disturbances in the other. Three events detected in the EI shown in Figure 3.43 to Figure 3.45 confirm that the disturbances in one Interconnection will not be detected in others that do not operate synchronously.

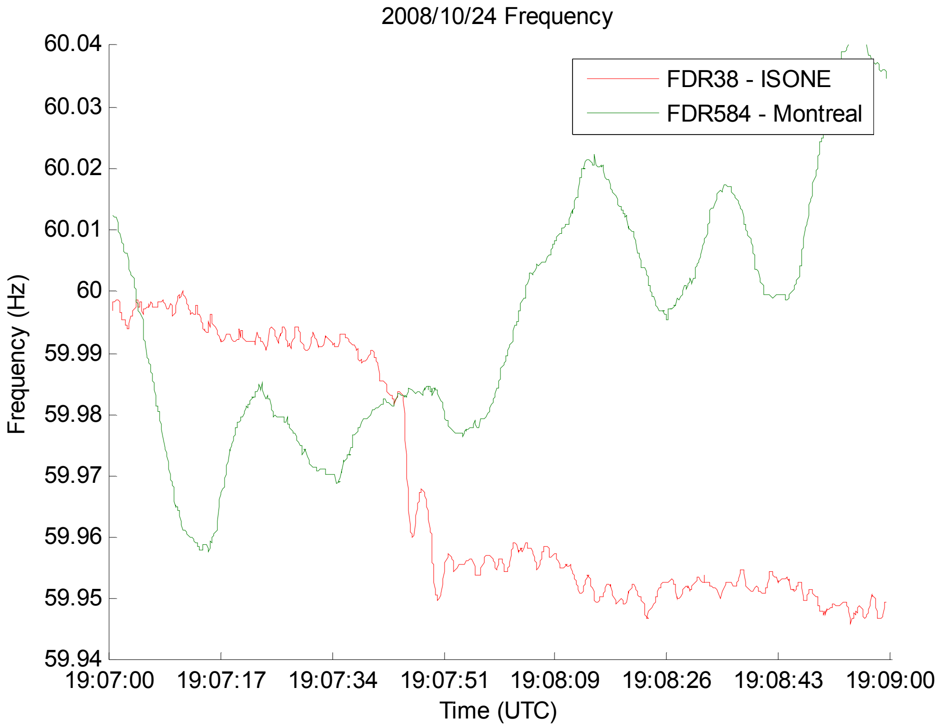

Figure 3.43 Frequency in the EI and Quebec during a generator trip event in the EI

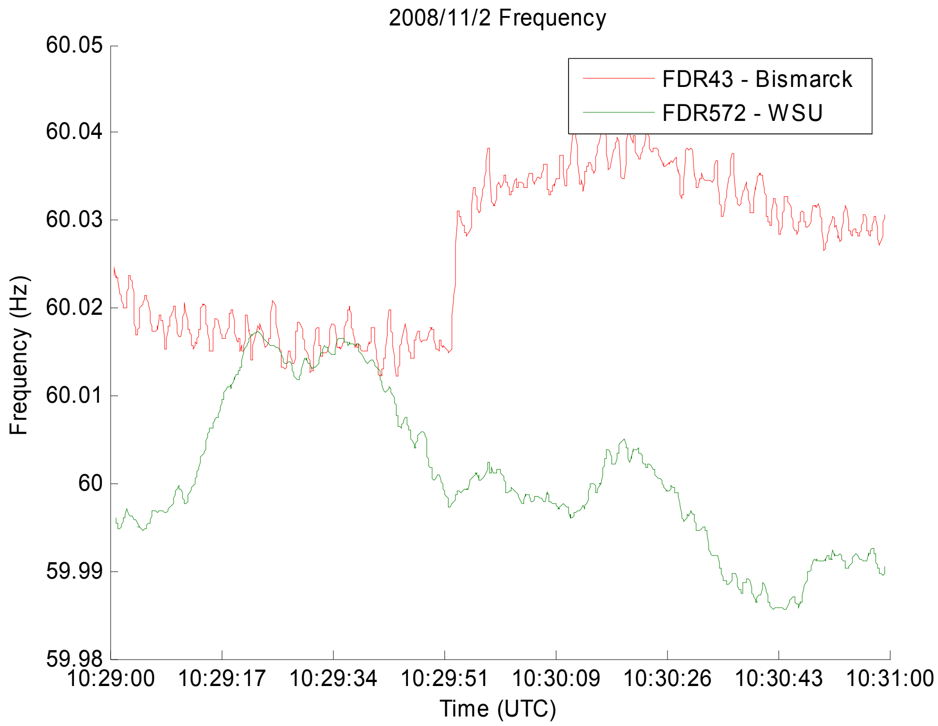

Figure 3.44 Frequency in the EI and the WECC during a load loss event in the EI

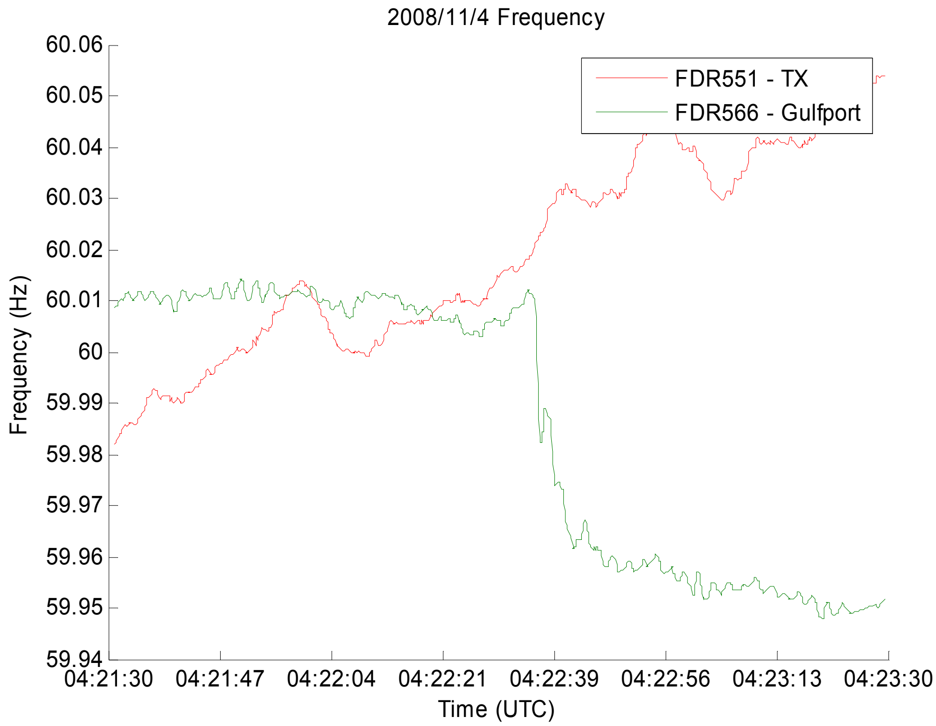

Figure 3.45 Frequency in the EI and the ERCOT during a generator trip event in the EI

Further, the HVDC controls may vary for different control needs and various AC system conditions [21][27]. In the case of the Quebec – New England HVDC system, the power network at the south end of the HVDC link is very strong thus no need for frequency dependent HVDC power modulation. The power generating station La Grande 2A at the north Radisson end is usually isolated from the Quebec system and feeds the HVDC link directly. Therefore, HVDC power is modulated to maintain the frequency in the collector system within the range between 59.5 Hz and 61.5 Hz. The effect of the DC power flow modulation is expected to be observed if a sensor is installed at the Radisson station in Quebec.

Chapter 4 Visualization of Wide-Area Measurements

4.1 Motivation Example

Take the Florida outage in section 3.4 as an example to explain the motivation behind the visualization tool development. The frequency oscillations from all available FDRs in the EI system are shown in Figure 4.1. It can be seen from the frequency delays at different locations that the perturbation propagates in the system as electromechanical waves [40]. The phase difference in the oscillations is also noticeable for different FDR locations. However, it is hard for a person to tell how the disturbance travels geographically in the EI system by only viewing the frequency plot in Figure 4.1.

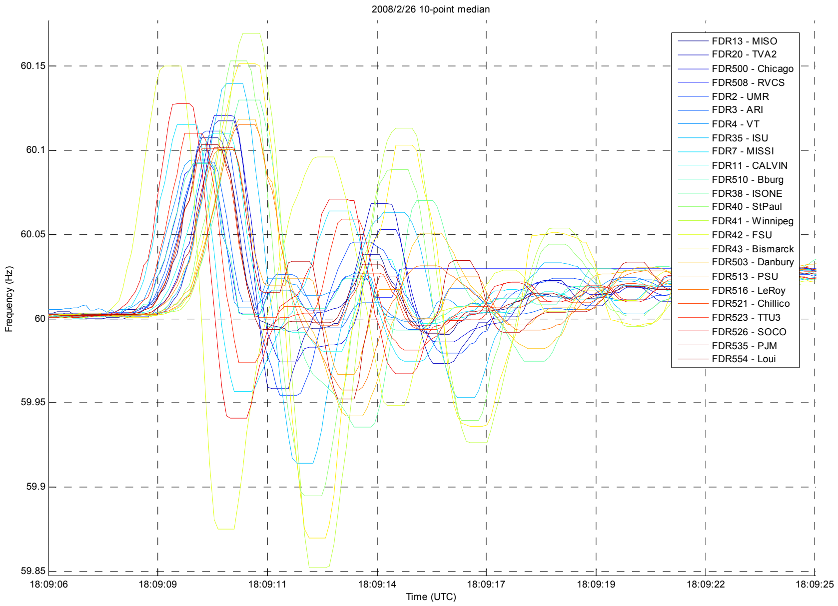

Figure 4.1 Frequency oscillations measured by all available FDRs in the EI during the Florida outage on February 26, 2008

Figure 4.2 to Figure 4.5 are four snapshots of the frequency replay generated by the visualization tool developed in this chapter, by which the frequency measurements are displayed as color contours over the EI area map. With the help of the visualization software tool, the information in the frequency data is packed into the computer generated images. Thus the whole picture of the disturbance is more vivid to people. One can tell easily that the northwest part of the EI was oscillating against the southeast part of EI.

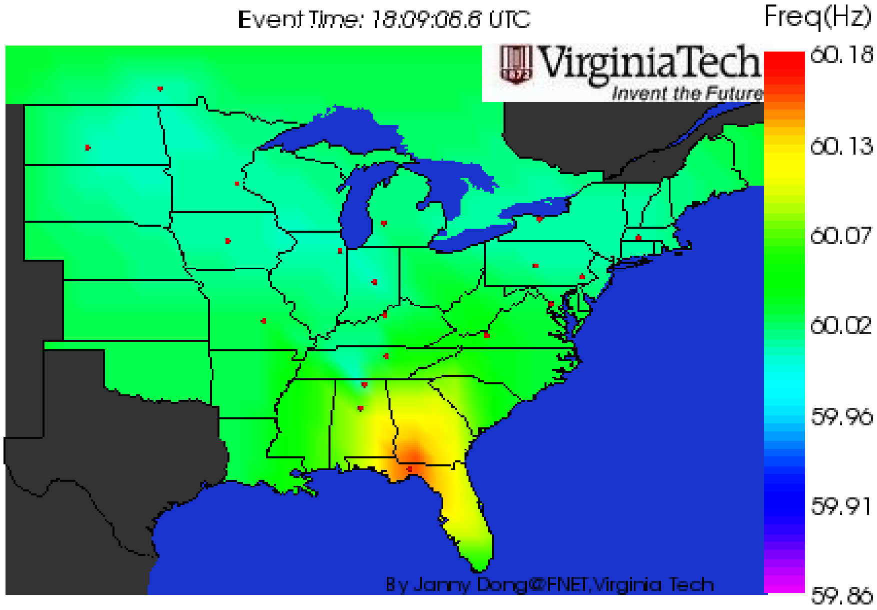

Figure 4.2 Snapshot of the frequency replay of the Florida outage (1)

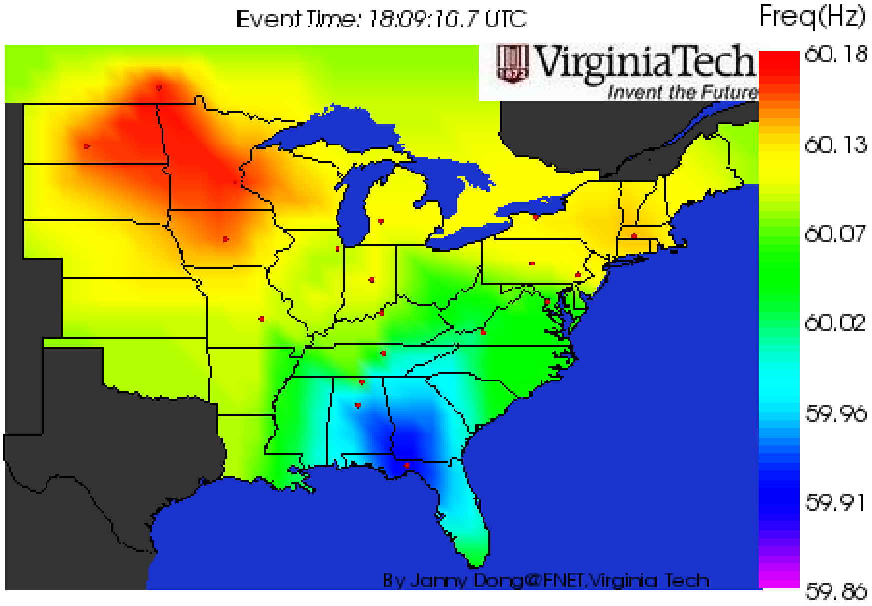

Figure 4.3 Snapshot of the frequency replay of the Florida outage (2)

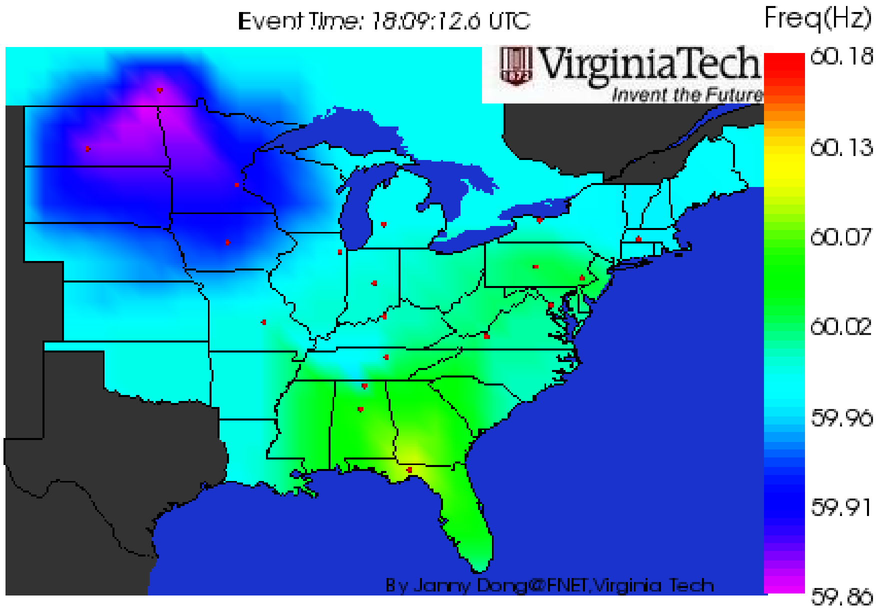

Figure 4.4 Snapshot of the frequency replay of the Florida outage (3)

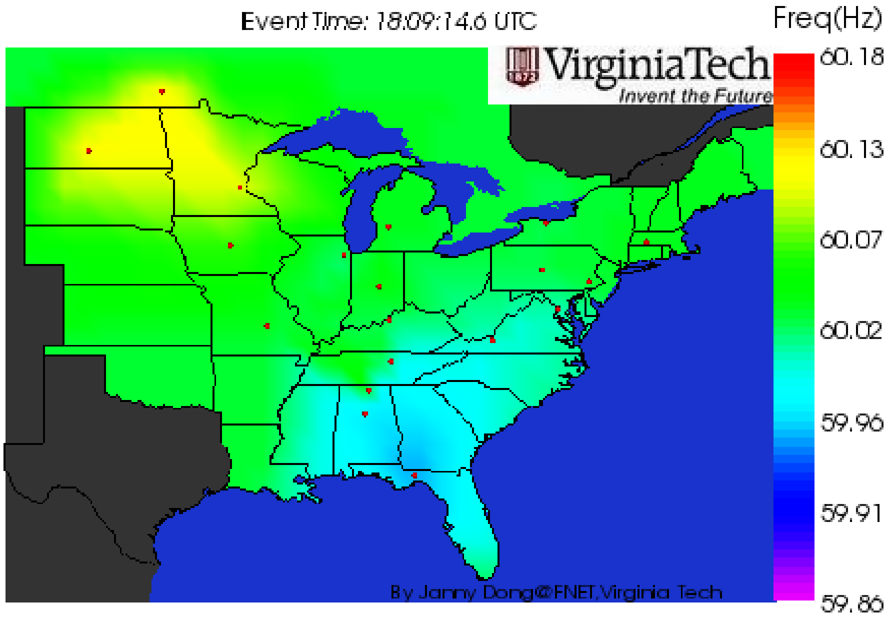

Figure 4.5 Snapshot of the frequency replay of the Florida outage (4)

Effective visualization helps viewers to understand and interpret power system dynamic situation more easily and rapidly [41]. Visualization tools are playing an increasingly important role in interpreting the massive data available to the power system engineers and improve situation awareness [42]. Various applications have been studied and developed for visualizing power system states such as voltage [43] and load flow [44]; as well as for educational purpose [45][46]. There also exist a variety of visualization types: diagrams, pie charts, color contours and animations, etc. [47].

In order to better observe and understand the system dynamics during disturbances, a visualization tool is developed in this chapter that correlates the wide-area measurements with their geographical information by displaying the measurements as 2-D colored surfaces over the EI map.

4.2 Visualization Tool Overview

The visualization tool developed in this chapter collects frequency and angle measurements to form color contours over a geographical area, thus the generated disturbance replay provides insights to electromechanical wave propagation in major events. The saved frequency data of the Interconnection, combined with geographic and system topology information, will be mapped to colors and displayed as color contours which are obtained by a linear fit through all the active measuring points in each major disturbance. The visualization is realized by using objects provided by the Visualization Toolkit (VTK), which is an open-source, object-oriented software system for computer graphics, visualization, and image processing [48]. C++ is chosen as the programming language because the tool is expected to be implemented online as one function module of the present FNET situation awareness system which is developed with C++.

4.2.1 The Visualization Toolkit

The Visualization ToolKit (VTK) is an open source, freely available software system for 3D computer graphics, image processing, and visualization. VTK includes a textbook published by Kitware [49], a C++ class library, and several interpreted interface layers including Tcl/Tk, Java, and Python. The design and implementation of the library has been strongly influenced by object-oriented principles.

The graphics model in VTK is at a higher level of abstraction than rendering libraries like OpenGL or PEX. This means it is much easier to create useful graphics and visualization applications. In VTK applications can be written directly in C++, Tcl, Java, or Python. In this work, objects provided by VTK are used to map frequency measurements to colors to generate frequency contours, and write image frames to form AVI movies.

4.2.2 MATCOM Math Library

MATCOM is a Matlab to C++ complier developed by MathTools Ltd. which enables easy integration of m-files code and algorithms into existing C++ projects. MATCOM creates MEX files, DLL files for Excel and Visual Basic and standalone C++ applications, with royalty free distribution. MATCOM includes the supporting Matrix<LIB> C++ matrix library that allows employing functions built in MATLAB in C++ projects, which saves development time. The library is supplied as a group of DLLs for Windows, resulting in very small executables.

Matrix<LIB> is a scientific C++ library which provides a double-precision matrix type, Mm, that may be complex, real, sparse or n-dimensional. Over 600 functions and overloaded operators are available. Included are basic operators, such as + - / * and flexible indexing operations. Functions are provided for linear algebra, polynomial arithmetic, signal processing, file I/O and more. The functions supplied were carefully optimized for best matrix performance [50]. The Matrix<LIB> library is employed to interpolate the measurements to be visualized to form a two dimension data mesh for the color surface.

4.3 Design of the Visualization Tool

The procedures to generate measurement playbacks are shown in Figure 4.6. The program can be divided to four main parts: obtain information about FDR locations and measurement data, form interpolation matrix, map measurement values to colors and conceal irrelevant areas, and write image frames into an AVI file.

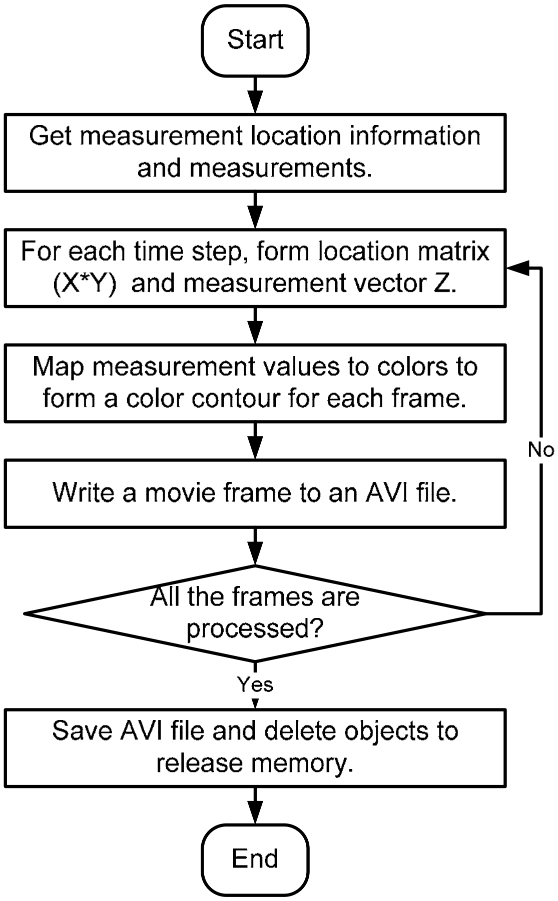

Figure 4.6 Flowchart of the automated replay tool

When an event occurs in power systems, the event detection program in the FNET situation awareness system will detect it and measurement data within a pre-determined time frame (both before and after event) will be saved. The saved frequency data of the Interconnection, combined with geographic and system topology information, will be mapped to colors and displayed as color contours by using objects provided by the Visualization Toolkit (VTK). A map of the Eastern Interconnection is divided into mesh grids, each with a frequency value, which is obtained by a linear fit through all the active measuring points in each major disturbance. Finally, the color contour map of each time step will be lined up along the time axis to create the animation. It could provide operators a prompt analysis of system operation situation and eventually help them to take appropriate steps to prevent future system deterioration.

4.3.1 Read Measurements

The design objective of the visualization tool is to develop a stand-alone program as well as an application module that can be easily integrated into the FNET situation awareness system. The current disturbance detection program captures a generation loss or a load shedding event then saves 40 seconds worth of data around the event time. Taking into account of the FNET server structure, the visualization tool takes the event data saved by the disturbance detection program as input. The procedure of reading data is illustrated in Figure 4.7.

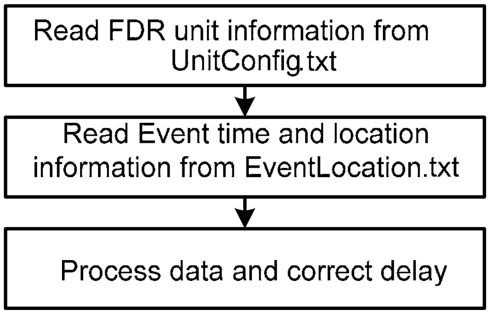

Figure 4.7 Procedures to read data

1) Read Unit Information

The FDR information is obtained from the "UnitConfig.txt" file as shown in Figure 4.8. This unit configuration file contains the name and location information in latitudes and longitudes that is necessary for the map display.

The FDR information is stored and managed in the vectors of the C++ Standard Template Library (STL). The vector data structure allows quick and easy memory allocation for specific data storage without explicit memory management. This makes them particularly useful for storing data in lists whose length may not be known prior to setting up the variable [51]. The management of the FDR information in vectors is illustrated in Figure 4.9, where N is the total number of units in the EI, for example.

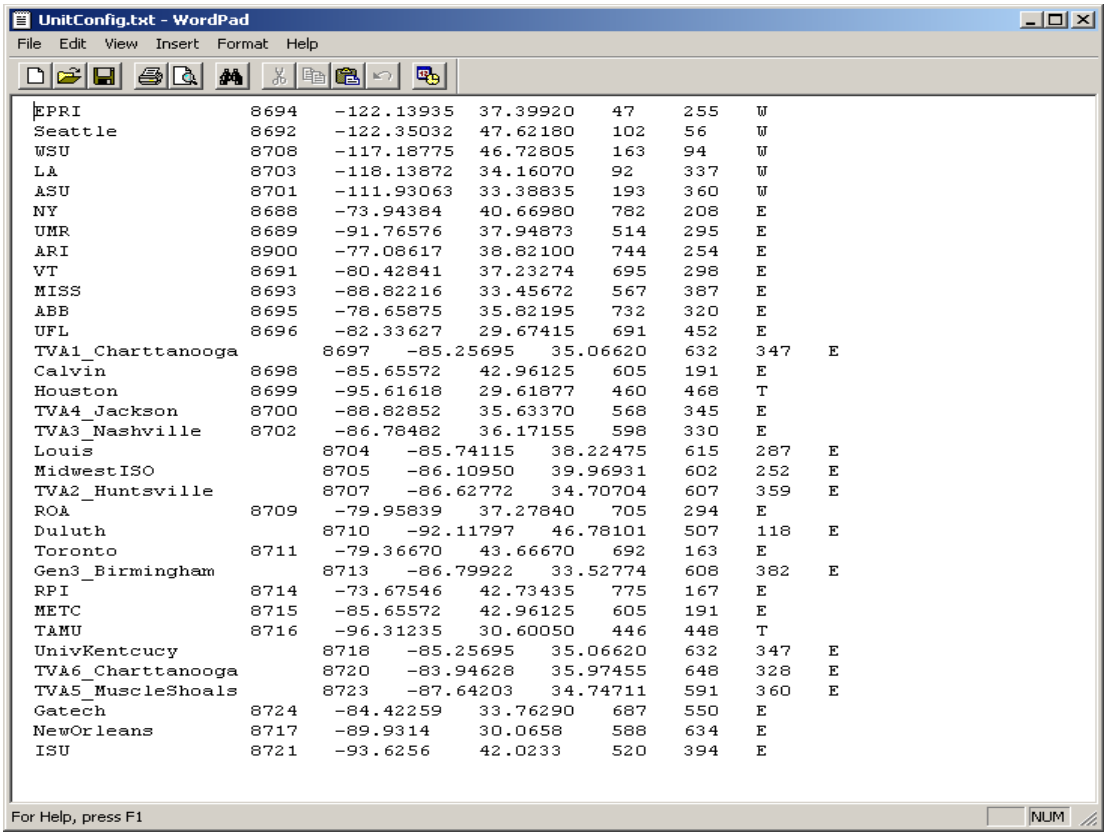

```
EPRI              8694   -122.13935  37.39920    47    255   W
Seattle           8692   -122.35032  47.62180    102   56    W
WSU               8708   -117.18775  46.72805    163   94    W
LA                8703   -118.13872  34.16070    92    337   W
ASU               8701   -111.93063  33.38835    193   360   W
NY                8688   -73.94384   40.66980    782   208   E
UMR               8689   -91.76576   37.94873    514   295   E
ARI               8900   -77.08617   38.82100    744   254   E
VT                8691   -80.42841   37.23274    695   298   E
MISS              8693   -88.82216   33.45672    567   387   E
ABB               8695   -78.65875   35.82195    732   320   E
UFL               8696   -82.33627   29.67415    691   452   E
TVA1_Charttanooga       8697   -85.25695   35.06620    632   347   E
Calvin            8698   -85.65572   42.96125    605   191   E
Houston           8699   -95.61618   29.61877    460   468   T
TVA4_Jackson      8700   -88.82852   35.63370    568   345   E
TVA3_Nashville    8702   -86.78482   36.17155    598   330   E
Louis                   8704   -85.74115   38.22475    615   287   E
MidwestISO              8705   -86.10950   39.96931    602   252   E
TVA2_Huntsville         8707   -86.62772   34.70704    607   359   E
ROA               8709   -79.95839   37.27840    705   294   E
Duluth                  8710   -92.11797   46.78101    507   118   E
Toronto           8711   -79.36670   43.66670    692   163   E
Gen3_Birmingham         8713   -86.79922   33.52774    608   382   E
RPI               8714   -73.67546   42.73435    775   167   E
METC              8715   -85.65572   42.96125    605   191   E
TAMU              8716   -96.31235   30.60050    446   448   T
UnivKentcucy            8718   -85.25695   35.06620    632   347   E
TVA6_Charttanooga       8720   -83.94628   35.97455    648   328   E
TVA5_MuscleShoals       8723   -87.64203   34.74711    591   360   E
Gatech            8724   -84.42259   33.76290    687   550   E
NewOrleans        8717   -89.9314    30.0658     588   634   E
ISU               8721   -93.6256    42.0233     520   394   E
```

Figure 4.8 An example of UnitConfig.txt

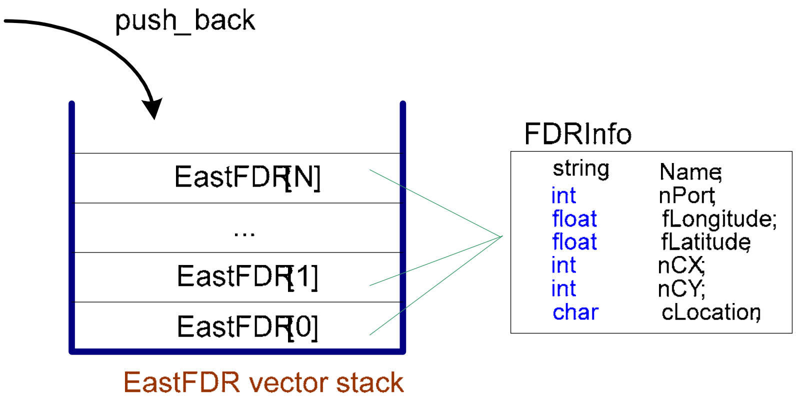

Figure 4.9 Illustration of managing the FDR information with the vector structure

2) *Read Event Information*

The event information such as the event time and the estimated location is saved in the file "EventLocation.txt" as shown in Figure 4.10, which is automatically created by the location estimation module of the server program once a disturbance is detected.

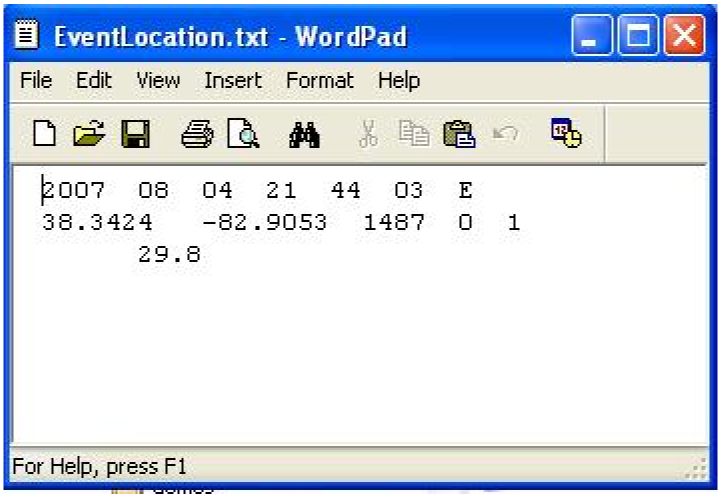

```
2007  08  04  21  44  03  E
38.3424  -82.9053  1487  0  1
      29.8
```

Figure 4.10 An example of EventLocation.txt

3) Data Conditioning

The FNET server is designed to receive data from each FDR and save it. Each FDR sends a packet of measurements 10 times each second. The packet consists of such data as the GPS date, GPS time, frequency, phase angle, and voltage magnitude. Comparisons and studies have confirmed that the time stamp of a FDR output is 11 seconds ahead of the PMU measurements for the same time period. The timing buffer design of the FDR hardware accounts for this delay as elaborated with details in [52]. However, the delay may be occasionally 10 seconds for some devices when the buffers are not filled due to loss of GPS messages. It is critical to correct such delays between FDR units to achieve valid analysis results.

Figure 4.11 shows the format of the event data file automatically created for a captured disturbance. The third column in the data file indicated the time delay of a certain unit and normally it is around 11 seconds. The one-second delay problem between FDR units is fixed by searching the units with incorrect time delay and subtracting one second from their time stamps. After the measurements are correctly aligned, they are fed into a 9-point moving median filter to remove the high-frequency noises.

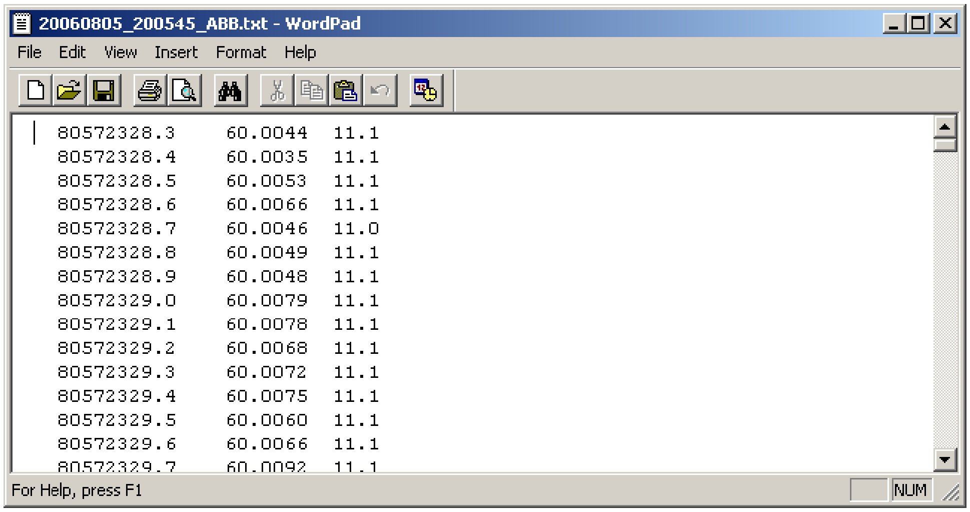

```
80572328.3     60.0044   11.1
80572328.4     60.0035   11.1
80572328.5     60.0053   11.1
80572328.6     60.0066   11.1
80572328.7     60.0046   11.0
80572328.8     60.0049   11.1
80572328.9     60.0048   11.1
80572329.0     60.0079   11.1
80572329.1     60.0078   11.1
80572329.2     60.0068   11.1
80572329.3     60.0072   11.1
80572329.4     60.0075   11.1
80572329.5     60.0060   11.1
80572329.6     60.0066   11.1
80572329.7     60.0092   11.1
```

Figure 4.11 An example of the event data file

4.3.2 Generate Measurement Matrices for Display

Several matrices are required for the benefit of visualization: the matrices (X, Y) that define the 2-D location plane and the measurement value matrix to be displayed as a colored surface over the EI map defined as the area between -105 and -66 degrees longitude and 24 and 52 degrees latitude. The defined area is divided into $N \times M$ small mesh grids where N and M are the number of sections along the longitude and latitude, respectively. The size of each small grid can be adjusted by alternating the section size. For simplicity the visualization program assumes Simple Cylindrical map projection method [53] to display FDRs on a map of the EI, hence longitudes and latitudes are projected directly to the display image. The coordinates of the small grids are defined by the matrices (X, Y) above which the measurement-determined surface will exist. The frequency or angle measurements from limited number of FDR units distributed in the EI are then interpolated over the whole EI area by the linear method. The procedure described above is shown as the flow chart in Figure 4.12.

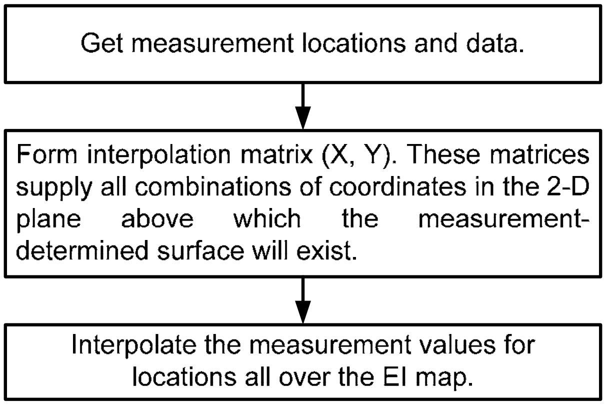

Figure 4.12 Procedures to generate measurement matrices for display

4.3.3 Form Animation Frames

Each animation frame is a colored surface over the EI map for each time stamp. The VTK library is utilized to generate each movie frame and save all the frames to an Audio Video Interleave (AVI) file, a commonly used video format.

In VTK a visualization project is executed through a ‘pipeline’, which is a sequence of process objects that operate on data objects to generate geometry that can be rendered by the graphics engine. The pipeline execution model is shown in Figure 4.13. The source data are represented with datasets, then processed by filters, and mapped to graphics by mappers. A dataset is a data object with structure that consists of cells (e.g., polygons, lines, voxels), points (x-y-z coordinates), cells defined by connectivity list referring to points, etc. [48]. Figure 4.14 shows some examples of datasets.

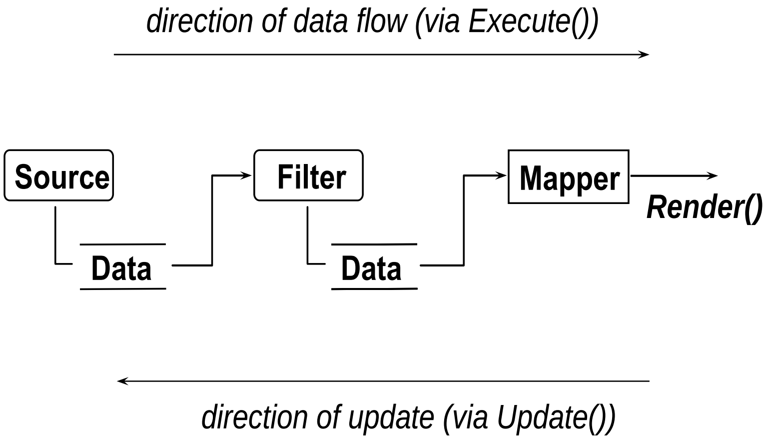

Figure 4.13 The pipeline execution model in VTK

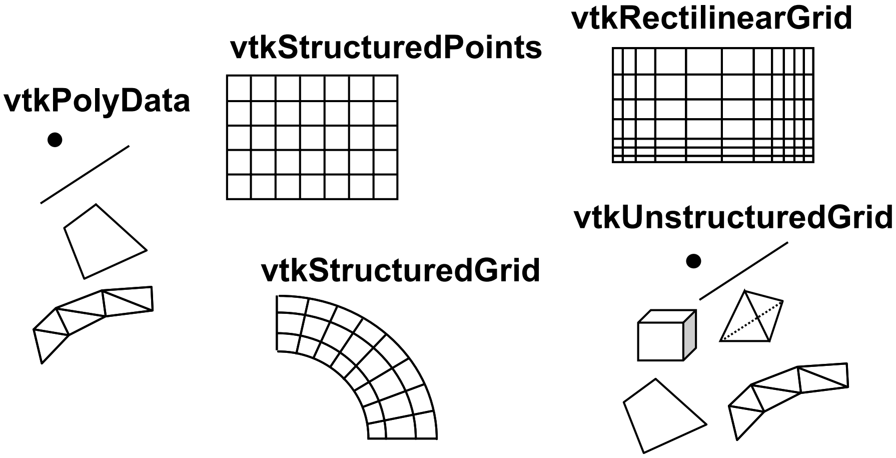

Figure 4.14 Dataset types in VTK

For example, the visualization program developed in this chapter uses an instance of vtkPolyData to represent measurements. The coordinates of each measurement are represented by points, and the corresponding frequency or angle values are represented by scalars. Then vtkLookupTable maps the frequency scalars to colors. Finally vtkActor represents all the geometries (lines, points, etc.) in a render window and a movie frame is thus created. The detailed procedure can be found in Figure 4.15. More information about the development of the visualization tool and the C++ code are listed in Appendix II.

Some graphic models and their functionalities are

- RenderWindow - contains final image
- Renderer - draws into render window
- Actor - combines properties / geometry
- Mappers - represent geometry
- Transformations - position actors

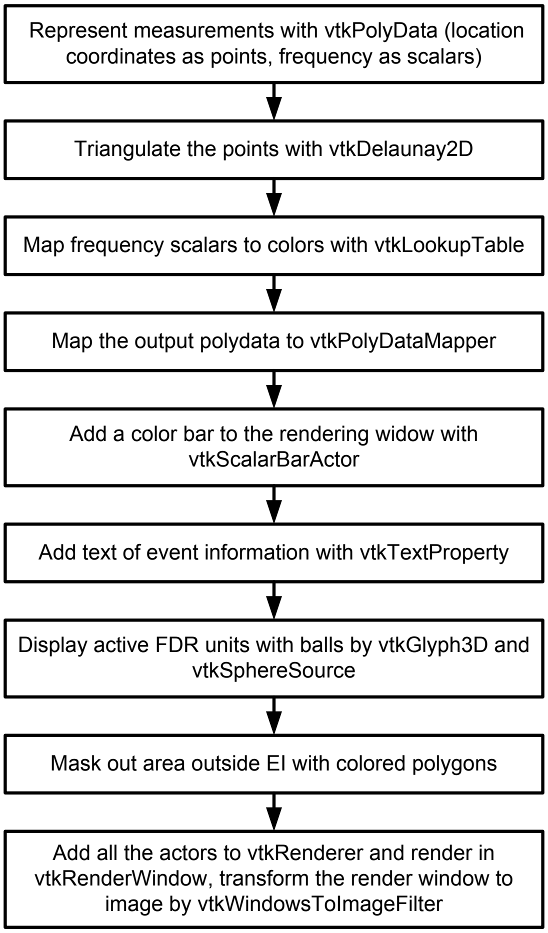

Figure 4.15 Procedures to form animation frames

4.4 Application Examples

The frequency replay of the Florida outage on February 26, 2008 has been described at the beginning of this chapter. The automated visualization tool is designed to have the capability to display various power system parameters such as frequency and phase angle. In addition, the tool also provides the flexibility of generating animations and static images.

4.4.1 Angle Replay for the Florida Outage

The Florida outage is taken as an example of angle visualization and more information of this disturbance can be found in section 3.4. The angles measured by FDRs are unwrapped and referred to a reference FDR (FDR4 in this example). In order to view the angle transients during the disturbances, the angle difference is shown in Figure 4.16, which is obtained by scaling all the relative angles to start from zero. Large oscillations resulted from the disturbance are noticeable and similar to the oscillations in frequency in that the Florida area is out of phase to the northwest of the EI system. From the snapshots of the angle replay in Figure 4.17 to Figure 4.20, it is clear that the disturbance starts in the Florida and radiates to the rest of the system appearing as angle swings.

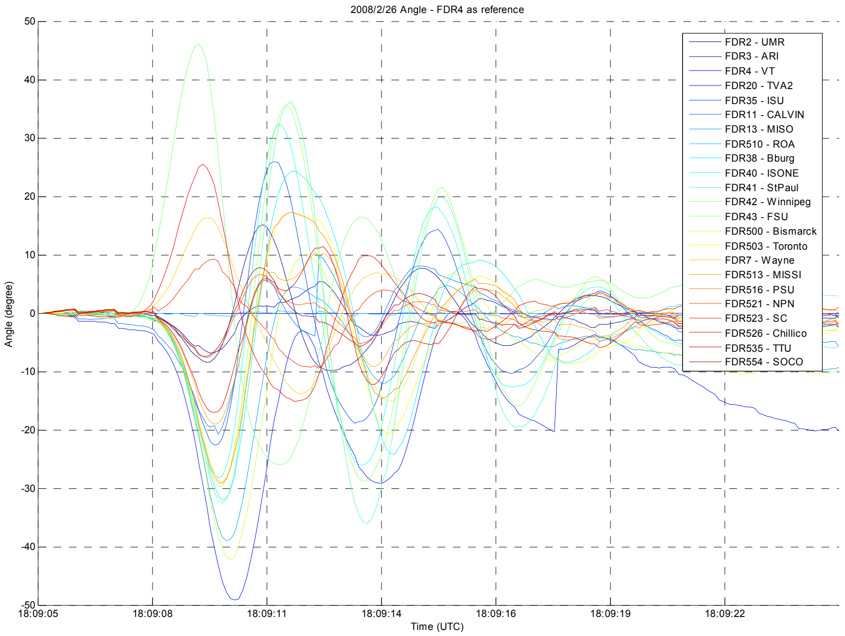

Figure 4.16 Pre-processed angle of the Florida outage (FDR4 as reference)

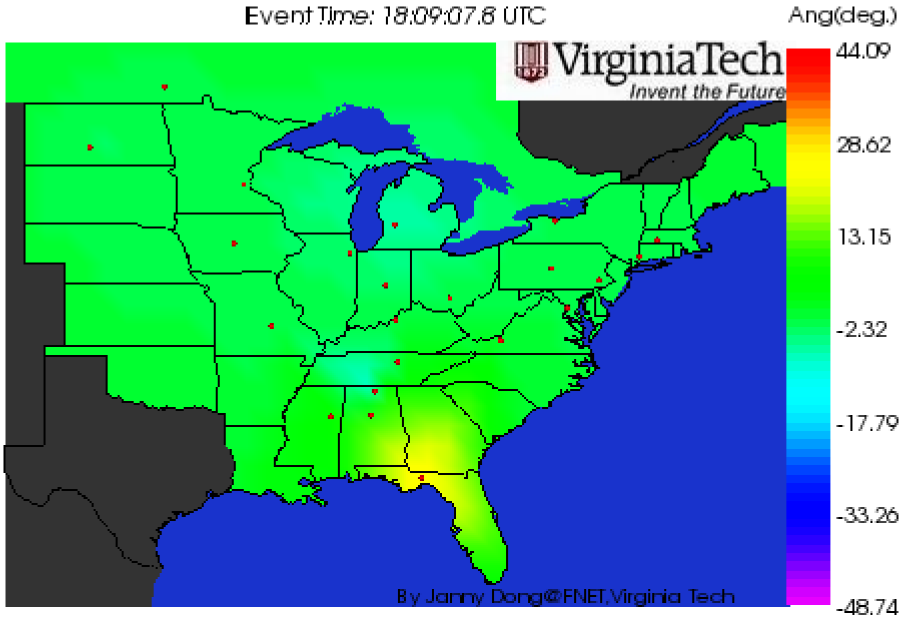

Figure 4.17 Snapshot of the angle replay of the Florida outage (1)

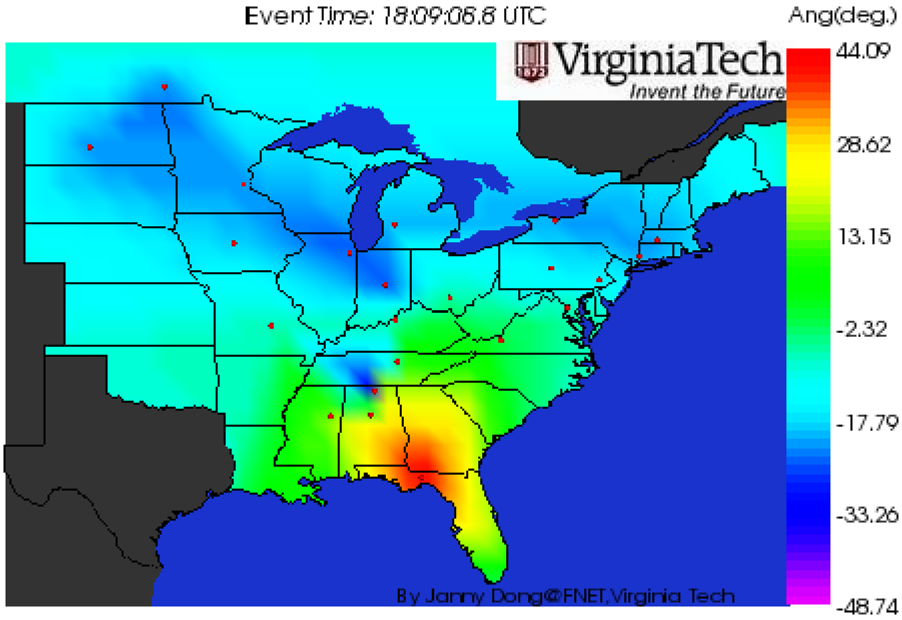

Figure 4.18 Snapshot of the angle replay of the Florida outage (2)

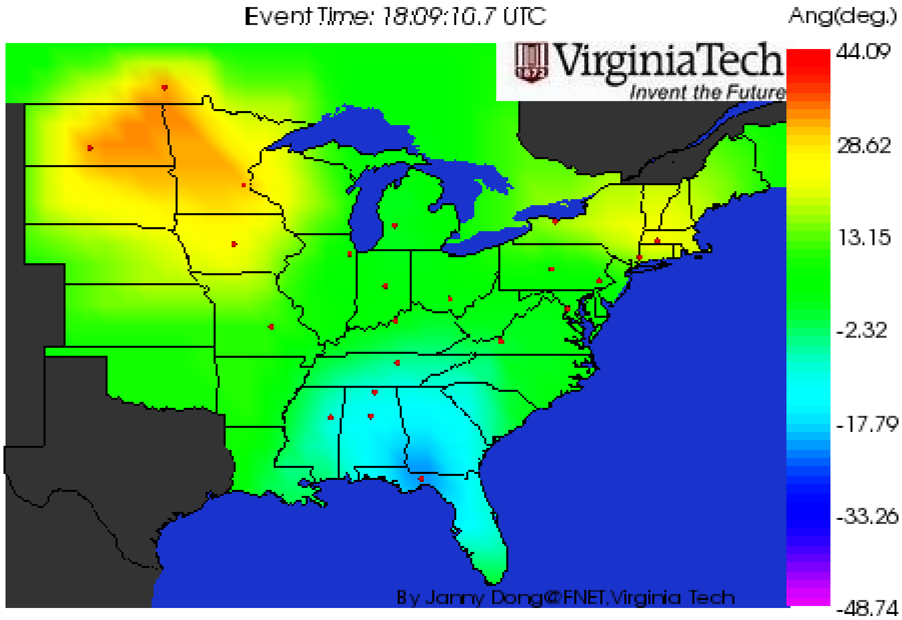

Figure 4.19 Snapshot of the angle replay of the Florida outage (3)

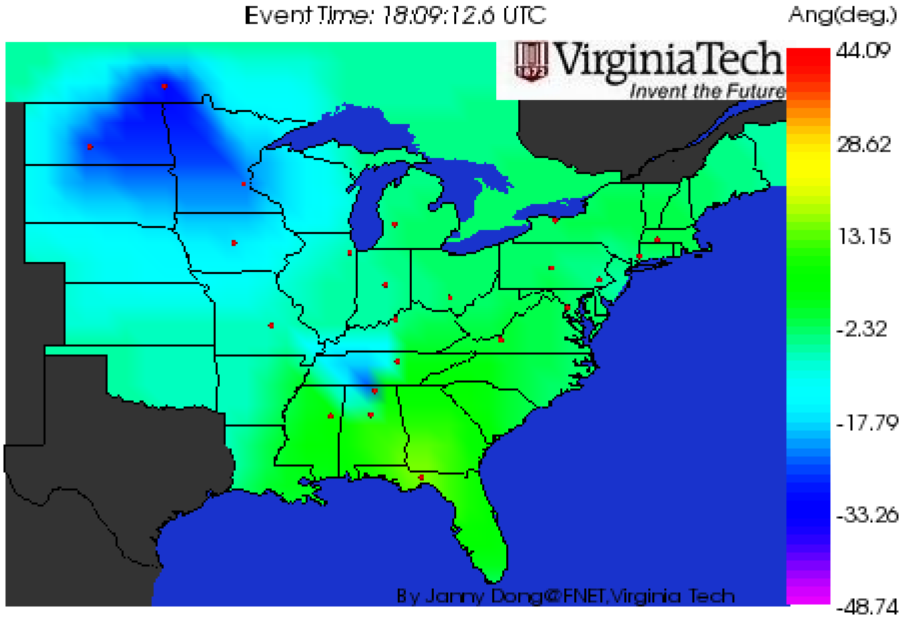

Figure 4.20 Snapshot of the angle replay of the Florida outage (4)

4.4.2 Angle Distribution from PSS/E

The visualization tool developed in this chapter is suitable for the measurements taken form FNET but not limited to them. Rather, it can be utilized to visualize any measurements with certain data format including the data output from the PSS/E simulation. In the example shown in Figure 4.21, 57 current FDR locations in the EI system are monitored in the PSS/E dynamic simulation and their steady state angle are output to display the angle distribution in the Eastern Interconnection. It can be seen that the phase angle in the EI does not follow any obvious geographical trend. The angle is the lowest in New Jersey while the highest around south Louisiana and Mississippi. The largest angle difference is about 85.4 degrees, as can be seen in Figure 4.22. The angle distribution map reflects the angle profile of the whole EI system under the operating condition modeled in PSS/E and the result is obtained based on the condition that the swing bus is a 345 kV bus in Ohio. A finer angle distribution map is shown in Figure 4.23 where angles are monitored at 154 buses in the EI system. The two maps agree on the highest and lowest angle areas.

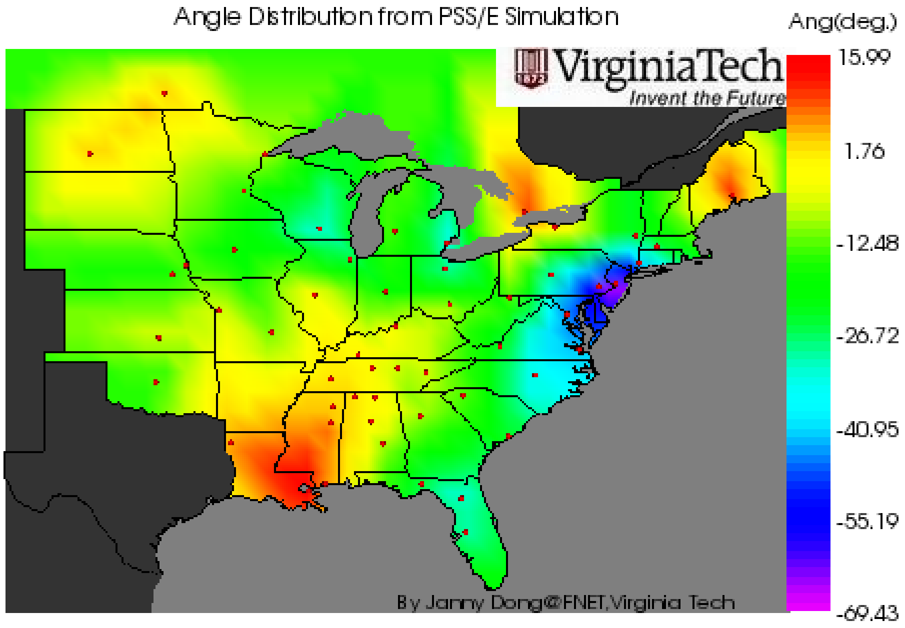

Figure 4.21 Angle distribution in the EI from PSS/E simulation with 57 buses monitored

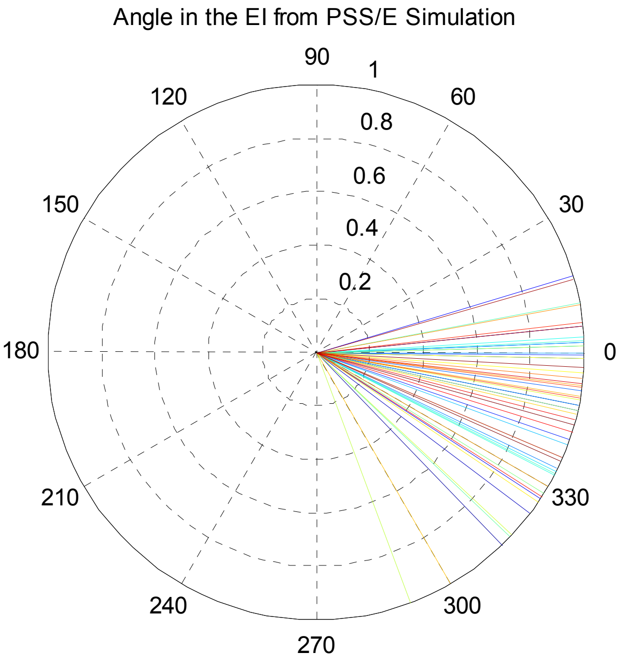

Figure 4.22 Steady-state angles in the EI from PSS/E simulation on polar plane

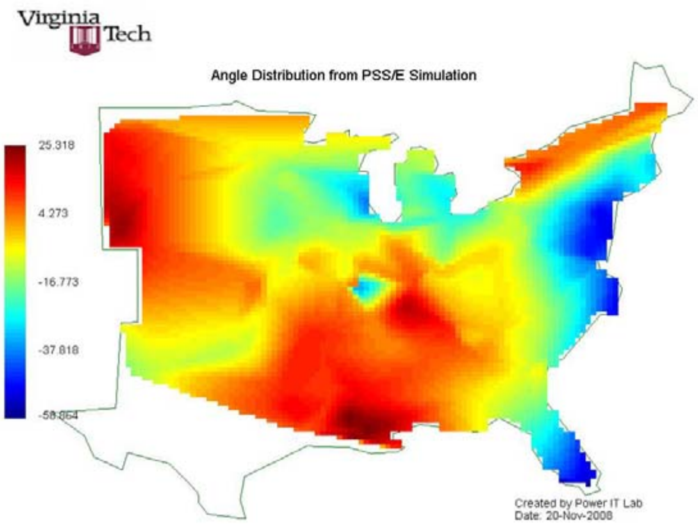

Figure 4.23 Angle distribution in the EI from PSS/E simulation with 154 buses monitored

4.4.3 Angle Distribution from Real Measurements

Frequency from FNET has been mainly used for power system analysis and visualization [54]. In [55] event analysis is based on angle which is obtained indirectly by integrating frequency. However, no attempt has been made to observe the angle distribution during normal condition. One of the main reasons is that the FDRs are measuring at one phase of the three-phase power system at the distribution level but the phase information is not readily available. Moreover, there exists possible phase shift caused by the transformer connection and under load tap changer (ULTC).

As a first attempt to observe the angle distribution in the EI, the real angle measurements are first unwrapped and one FDR unit in Ohio is selected as the reference to compare with the simulation results. Figure 4.24 displays the angle distribution map of a snapshot at 06:00 UTC on August 16, 2008. The angle measurements are also plotted on polar plane as in Figure 4.25.

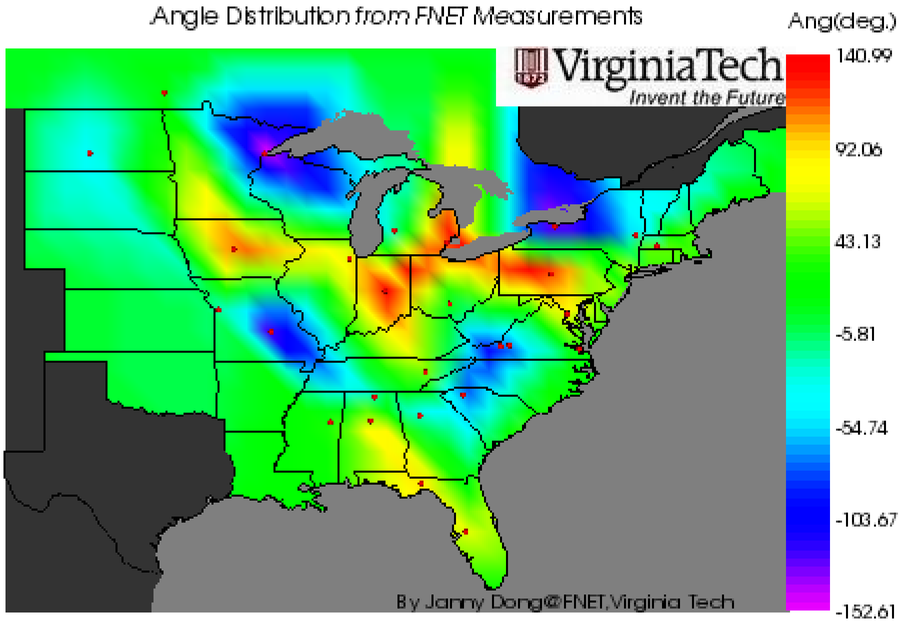

Figure 4.24 Angle distribution in the EI from real measurements at 06:00 UTC on August 16, 2008

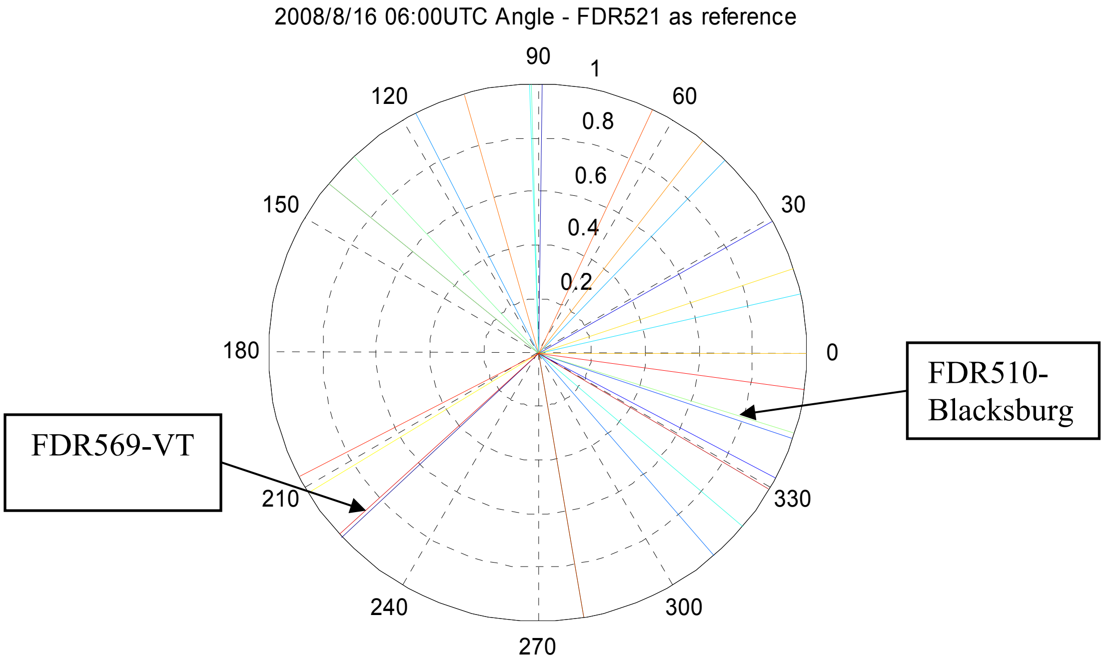

Figure 4.25 Angles in the EI on polar plane at 06:00 UTC on August 16, 2008

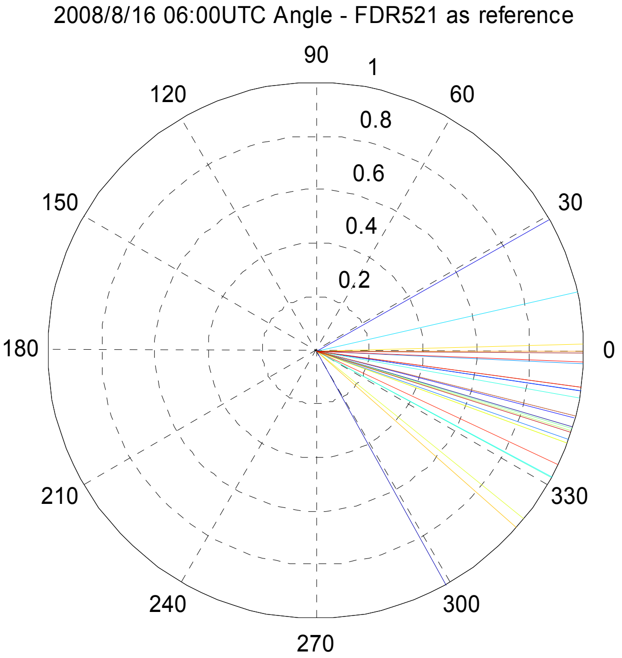

Figure 4.26 Angles in the EI on polar plane after adjusting phase shifts

The angle distribution from real measurements is not similar to the simulation results in Figure 4.21 and Figure 4.22, but such results are expected. The measured angles are distributed all over the polar plane whereas the angles from simulation are within in a range smaller than 90 degrees. As shown in Figure 4.25, the two units FDR569 and FDR 510 are about 120 degrees apart in angle but both are in Blacksburg, which confirms that the two units are at different phases.

This work makes an attempt to adjust the phase angle measurements according to the simulation results. The angles are adjusted by adding or subtracting the possible angle shifts caused by phase difference and transformer connections, which include 30, 60, 90, 120, 150 and 180 degrees. After the adjustment, an angle distribution map closer to the simulation results is obtained and shown in Figure 4.27. Of note is that the operating condition of the real system may be different from the simulation model. In addition, there are 28 available FDRs at the time when the measurements are taken. Less monitoring points may also attribute to the difference in the visualization results.

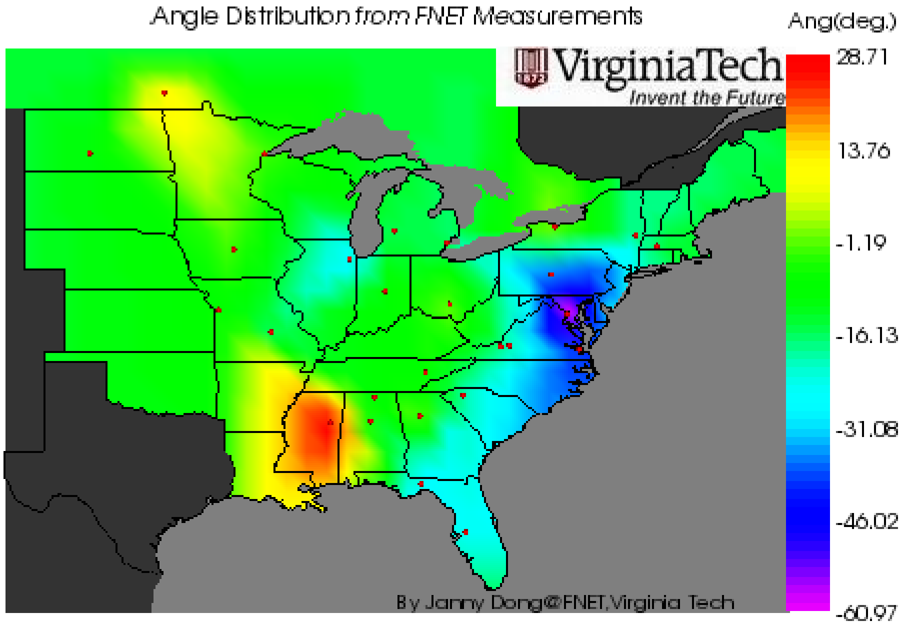

Figure 4.27 Angle distribution in the EI from real measurements after adjusting phase shifts

The objective of visualizing the steady state angle is more than to get the same distribution map with simulation. Rather, this work explores the visualization capabilities with wide-area measurements to improve situation awareness. By monitoring the angle distribution change over a day and during different seasons, more meaningful information about the system operating conditions and performances can be obtained.

4.4.4 Visualization with Google Earth

Google Earth is a popular free virtual globe program developed originally by Keyhole, Inc, a company acquired by Google in 2004. It maps the earth by superposition of satellite images and aerial photography [56] and has the capability to show a variety of objects such as 3D buildings by using SketchUp, a 3D modeling program; pin objects to indicate points of interest; and line objects to display a track. Google Earth provides a good platform to display user-defined data through Keyhole Markup Language (KML), an Extensible Markup Language (XML)-based language for expressing geographic annotation and visualization on Google Earth browser [57]. Although a relatively new tool, some applications have been developed based on Google Earth to visualize energy sources dynamically on earth [58] and wind farm [59]; to model 3D city [60]; and to track and manage objects [61].

In light of the visualization capability of Google Earth, it is feasible to integrate the visualization tool with the Google Earth platform to display power system measurements. The images generated by the visualization tool can be overlaid on Google Earth thus the animation can be displayed in Google Earth. One example is shown in Figure 4.28, in which a snapshot of the frequency replay of the Florida outage is overlaid on the surface of the earth by using KML. The overlaid image fits the Google map well and can be zoomed together with the map, which automatically utilizes the geographic information provided by Google Earth. Furthermore, Google Earth enables more possibilities to enrich the visualization such as displaying power grid information as different layers. The KML code for overlaying an image on Google Earth can be found in Appendix III.

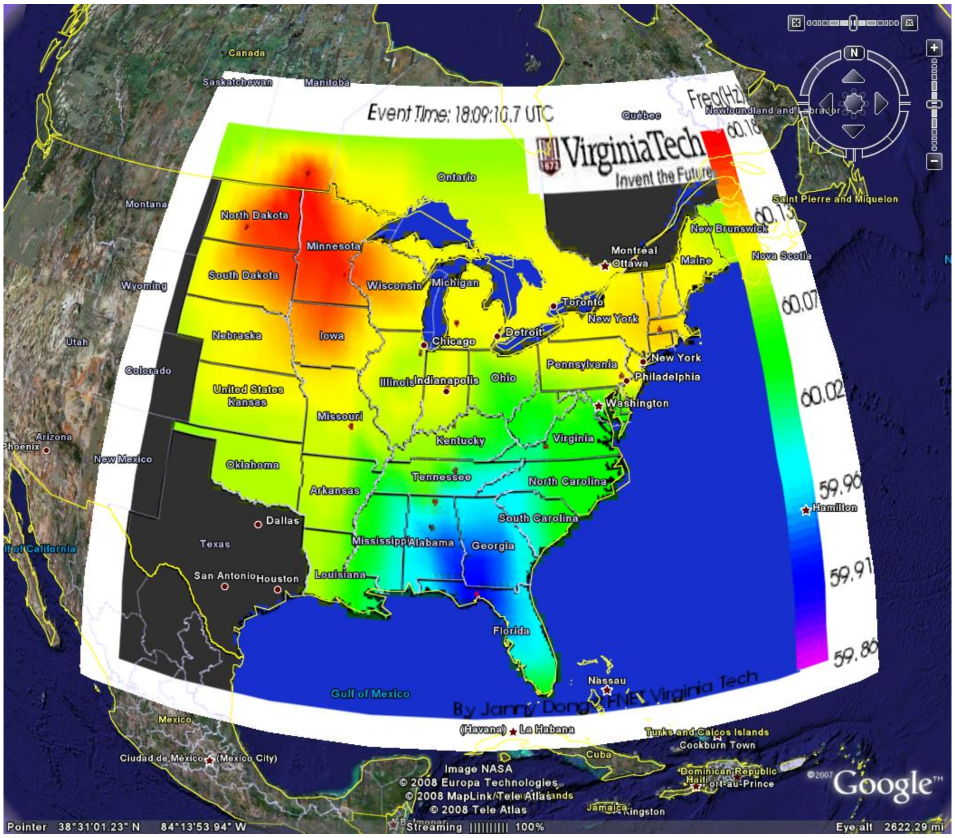

Figure 4.28 Frequency replay image overlaid on Google Earth (http://earth.google.com/)

Chapter 5 Line Trip Detection

With the increase of loading of power grids and massive inter-area power transfers enabled by the deregulation, it is very important to improve operators' situation awareness, which includes the knowledge of system topology. A collaborative project between FNET and TVA is to increase the FDR density in the area, which will enable closely monitoring of bulk transmission systems with more widely available measurements. This chapter discusses line outage detection using measurements provided by FNET. The line trip sensitivity and the FDR placement strategy are studied to answer such questions as how far a line trip can be observed by the sensors and where to place the FDRs to better observe the line trips. The characteristics of line trip disturbances are investigated and detection algorithms based on frequency and voltage angle are developed.

5.1 Line Trip Sensitivity Study

An ongoing project of FNET group is to deploy more sensors in the TVA system for line trip detection study. Therefore, it is significant to know how far away a line trip event can be observed by the sensors. It should be noted that the simulation work for the line trip detection and identification study in Chapter 5 and 6 all focuses on the scenario of single line trip without any fault involved since such disturbances are generally less severe than those with faults thus less visible in measurements. Further discussion on line trip signatures is described in detail in Chapter 6. In this chapter, the line trip sensitivity study based on PSS/E (Power System Simulator for Engineering), a software package for power system simulation, is carried out as follows:

(1) Select several transmission lines at different voltage levels in the TVA system. The selected lines are listed in Table 5.1 and their locations are depicted in Figure 5.1.

Table 5.1 Selected transmission lines for the sensitivity study

Voltage (kV)	Bus from	Bus to	Loading (MW)
500	Watts Bar	Roane	708.9
169	Volunteer	Knoxville	328.6
69	Melton Hill	Farragut	73.0
230	Widows Creek	Crawfish	337.0
230	West Ringgold	Alpha	162

From the TVA transmission system map in Figure 5.1, one can see that the transmission system of TVA area consists of two main voltage levels: 500 kV (in orange) and 161 kV (in black). There are some 230 kV lines on the borders of the system. The Watts Bar – Roane, Volunteer – Knoxville and Melton Hill – Farragut lines are within the Knoxville sub-area. The two 230 kV lines are selected in order to observe the impact of the line loading conditions on the line trip sensitivity region.

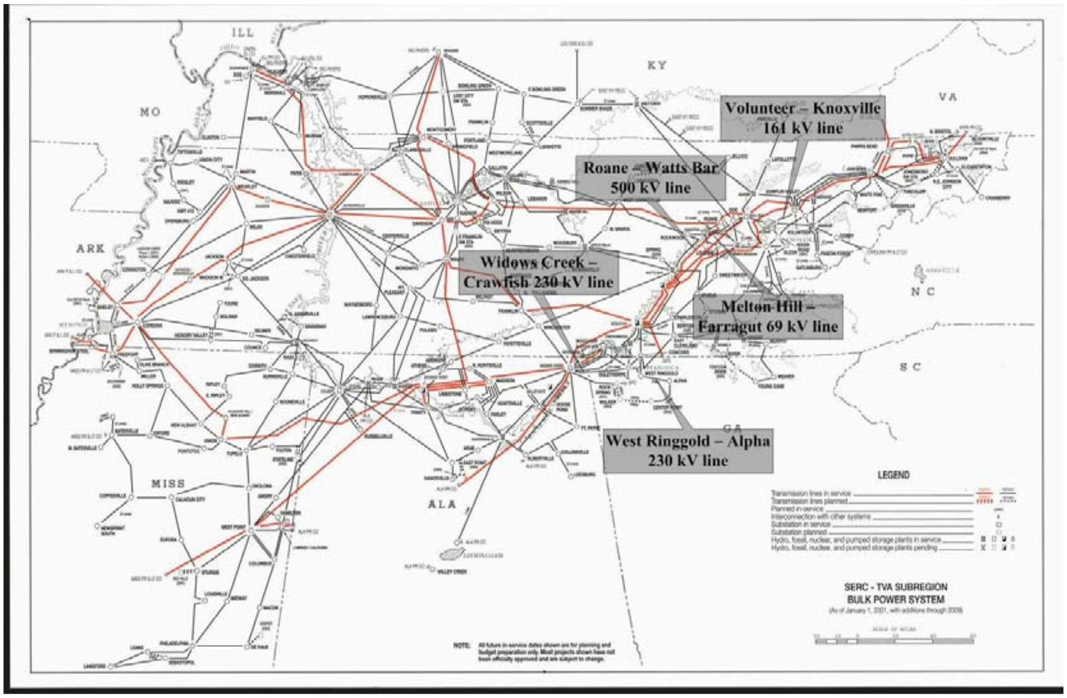

Figure 5.1 Locations of selected transmission lines in the TVA system for line trip sensitivity study (map source: TVA)

(2) Trip the selected transmission lines one by one and monitor frequency and

voltage phase angle. 45 generator buses covering the whole TVA system are selected as monitoring points in order to examine the impact of a line outage on the entire system. The reason to select the frequency and voltage phase angle as parameters is two-fold. The two parameters are very informative as frequency variations directly reflect the machine rotational speed thus related to the generation and load; and voltage phase angle is related to the power flow distribution in the power network. Another practical consideration is that the FDRs are taking frequency and angle. Therefore the two parameters are closely monitored in the simulation in order to assist analyzing the real measurements.

The simulation scenario is tripping a transmission line at 0.1 second, and then running the simulation for 5 seconds, which is adequate to observe first swings initiated by the line outage. Figure 5.2 and Figure 5.3 show the simulation results of tripping the 500 kV Roane – Watts Bar line. The angles are scaled to start from zero for the ease of comparison.

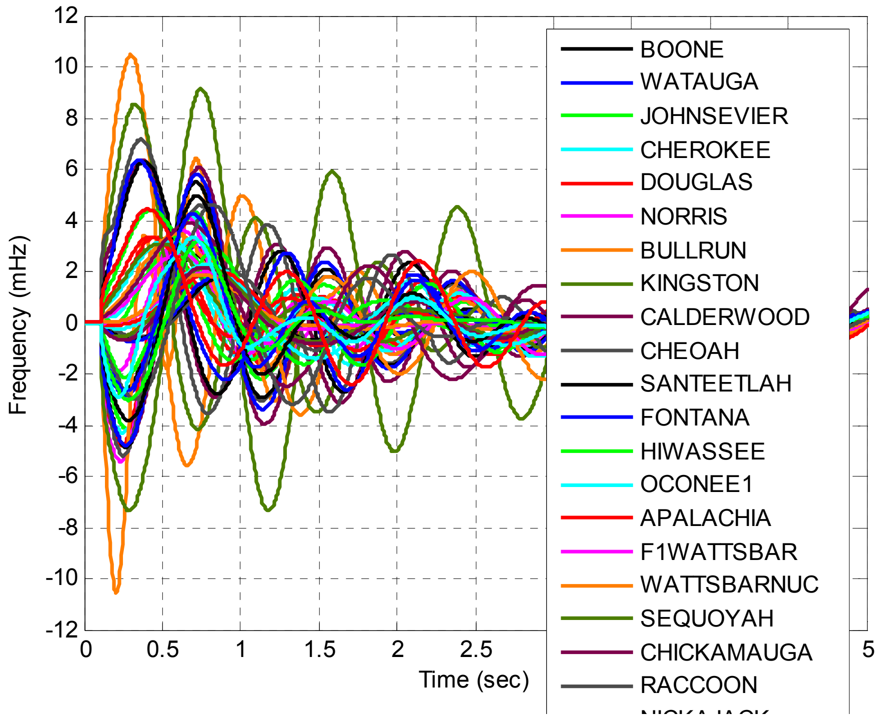

Figure 5.2 Frequency of the 500 kV Roane – Watts Bar line trip from PSS/E simulation

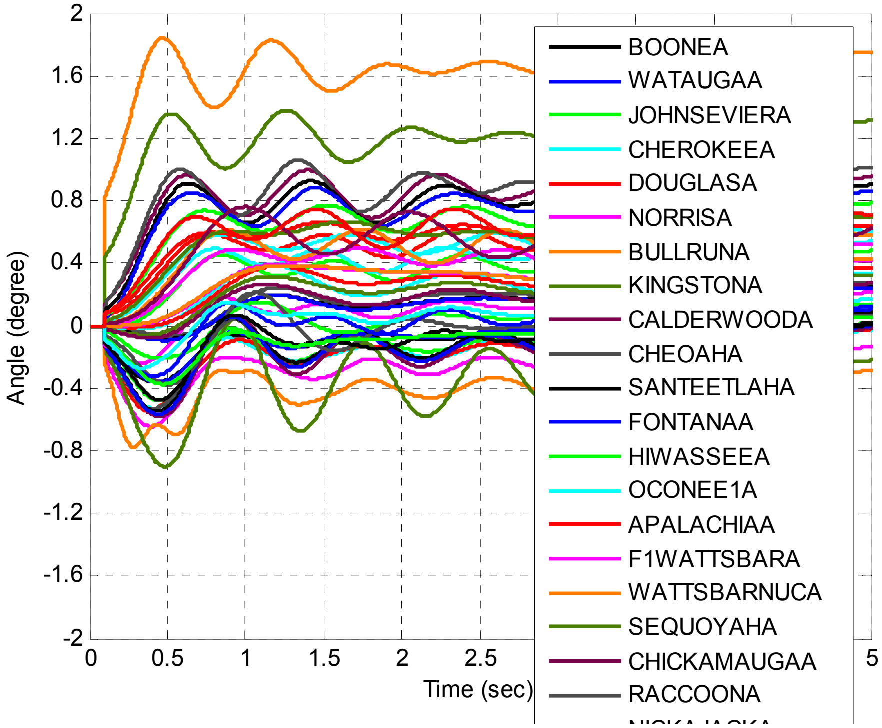

Figure 5.3 Angle of the 500 kV Roane – Watts Bar line trip from PSS/E simulation

(3) Find the magnitudes of frequency and angle values during the first swing following each line trip. Based on experience and measurement sensitivity of FDR units, 3 mHz and 0.4 degree are selected as sensitivity thresholds. Generally the peak values above these two thresholds can be observed by FDRs in the area; whereas the measurements below the thresholds may be disguised by noises, thus hard to distinguish. It is also found that the simulation results tend to demonstrate smaller frequency variations to a certain disturbance than real measurements possibly due to a smaller inertia in the simulation than in the real system.

(4) Use columns of different diameters to depict the peak values found in (3) on the TVA system map. The line trip sensitivity maps for tripping the 500 kV Roane – Watts Bar line are shown in Figure 5.4 and Figure 5.5. The red color indicates an initial rise in the measurements at the locations; whereas the blue color indicates an initial decline. It can be seen that the frequency and phase angle have similar sensitivity regions. That is, FDRs in the shaded area are more likely to observe the line trip of interest than those outside of the region.

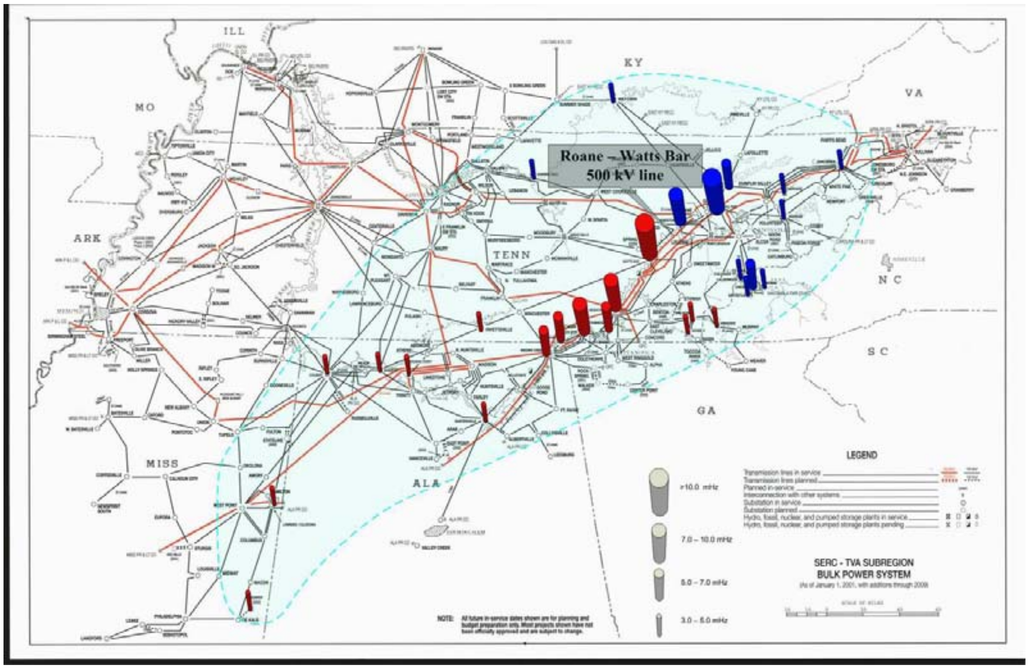

Figure 5.4 Frequency sensitivity map for the 500 kV Roane – Watts Bar line trip (map source: TVA)

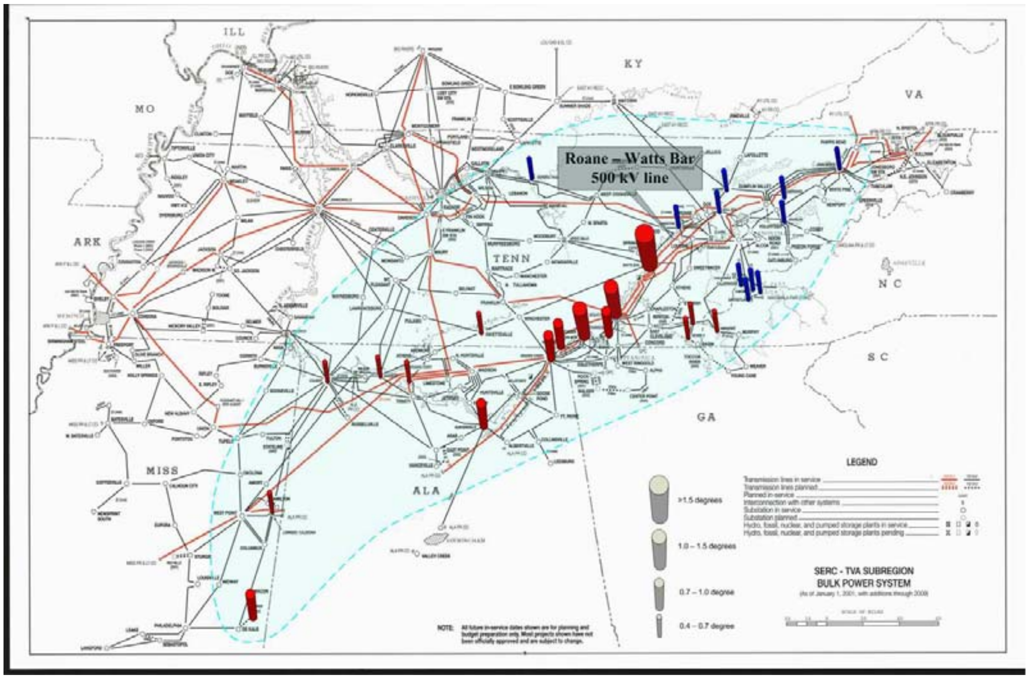

Figure 5.5 Angle sensitivity map for the 500 kV Roane – Watts Bar line trip (map source: TVA)

Figure 5.6 to Figure 5.9 show the frequency and angle results from the simulation and the obtained sensitivity maps for tripping the 161 kV Volunteer – Knoxville line. As can be seen in Figure 5.6 and Figure 5.7, the frequency and angle changes due to the outage of the 161 kV line are much smaller than those to the outage of the 500 kV line. As a result, the sensitivity regions are much smaller than in the 500 kV line trip case.

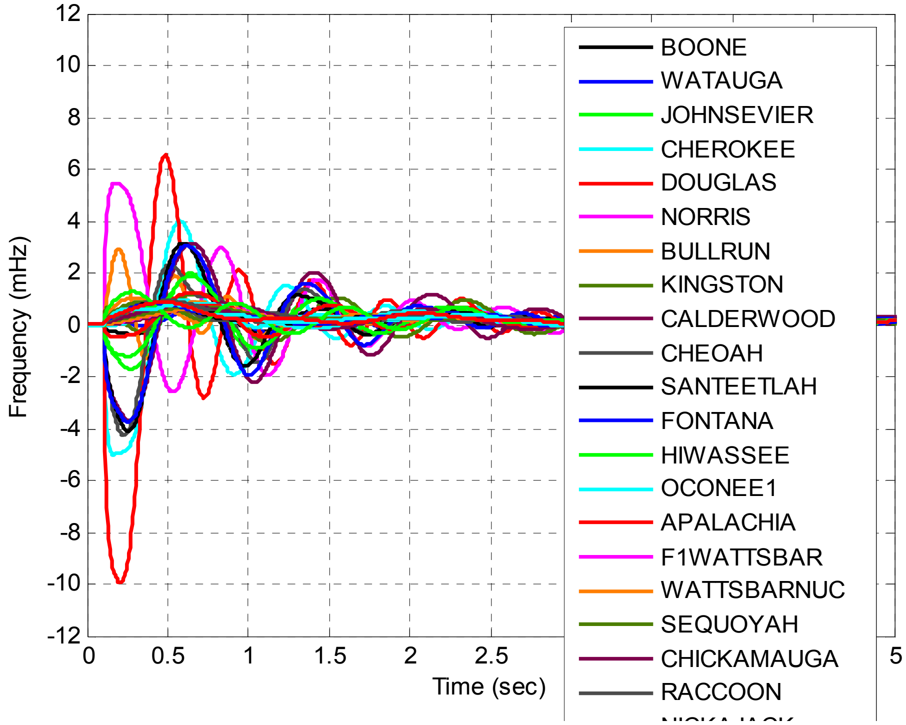

Figure 5.6 Frequency of the 161 kV Volunteer – Knoxville line trip from PSS/E simulation

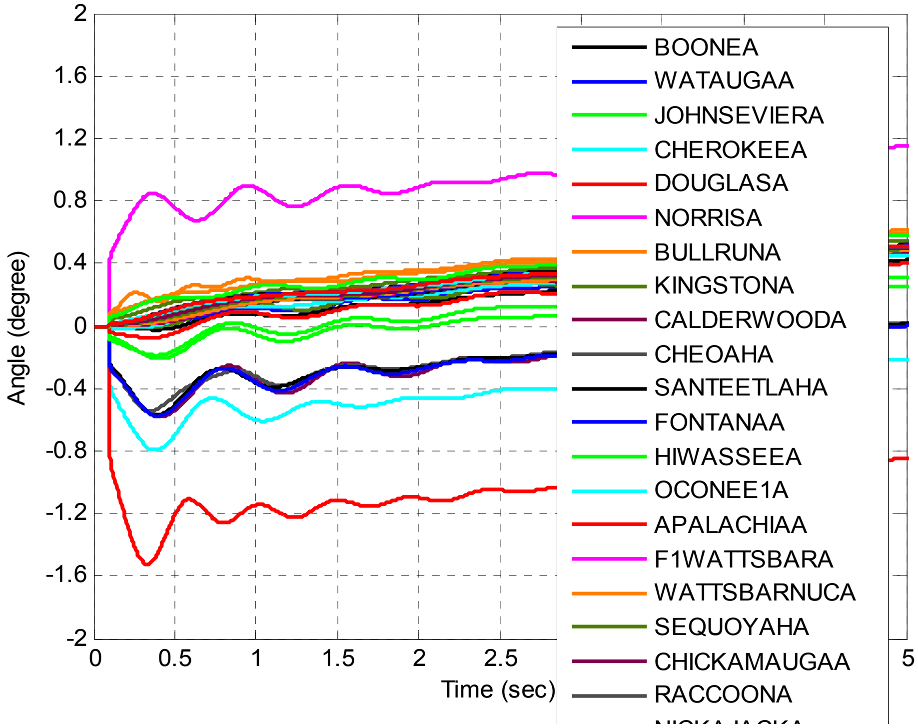

Figure 5.7 Angle of the 161 kV Volunteer – Knoxville line trip from PSS/E simulation

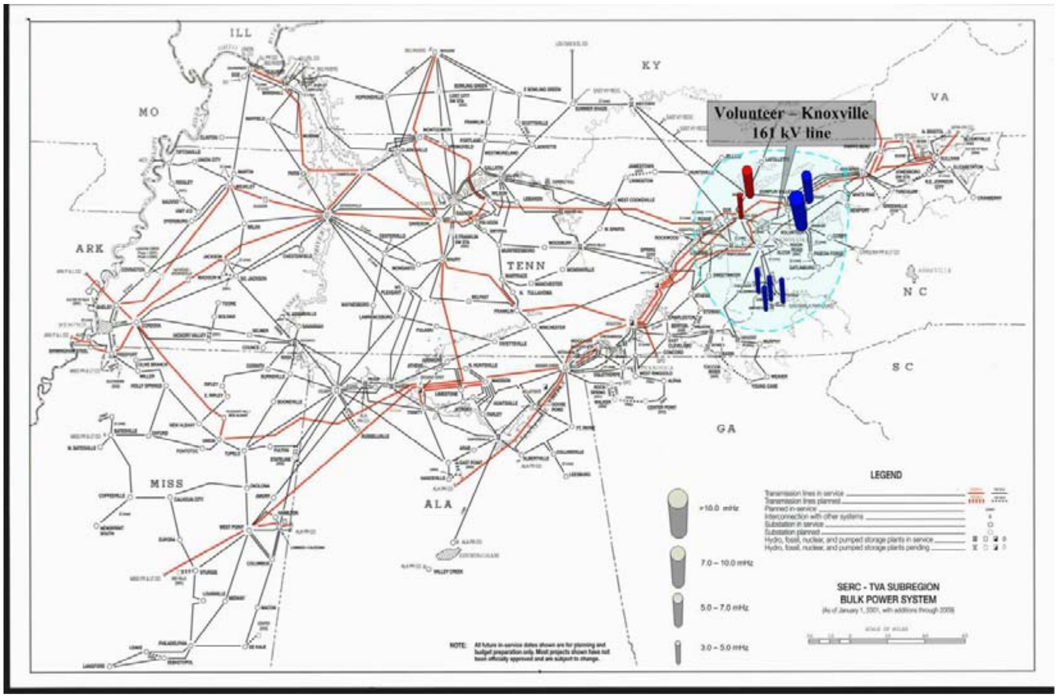

Figure 5.8 Frequency sensitivity map for the 161 kV Volunteer – Knoxville line trip (map source: TVA)

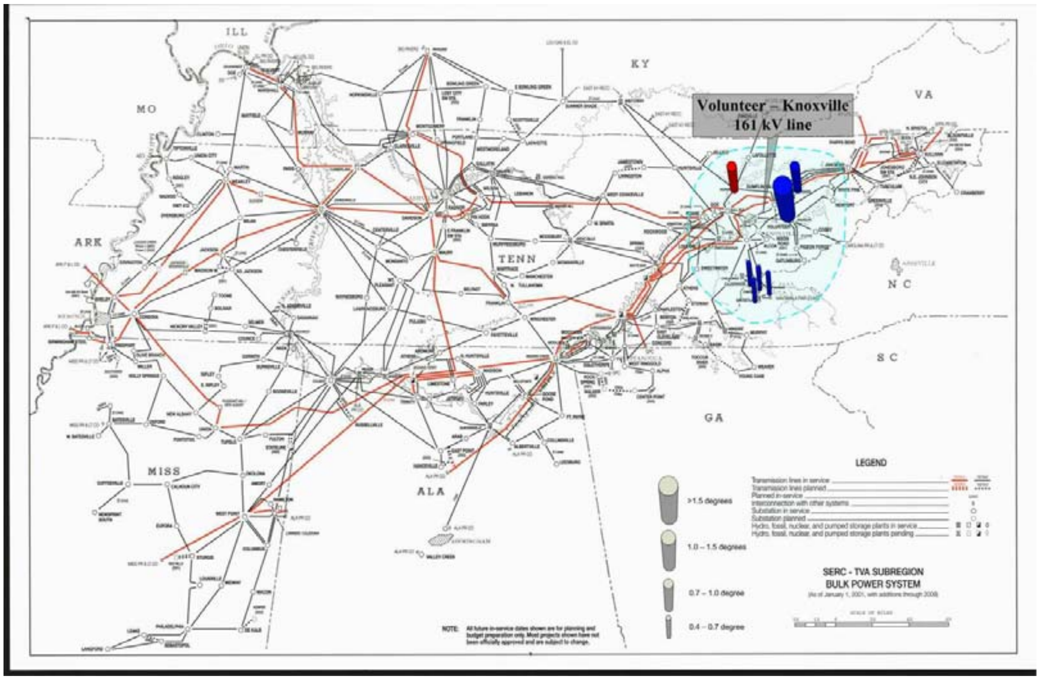

Figure 5.9 Angle sensitivity map for the 161 kV Volunteer – Knoxville line trip (map source: TVA)

The simulation results and sensitivity maps for tripping the 69 kV Melton Hill – Farragut line are shown in Figure 5.10 to Figure 5.13.

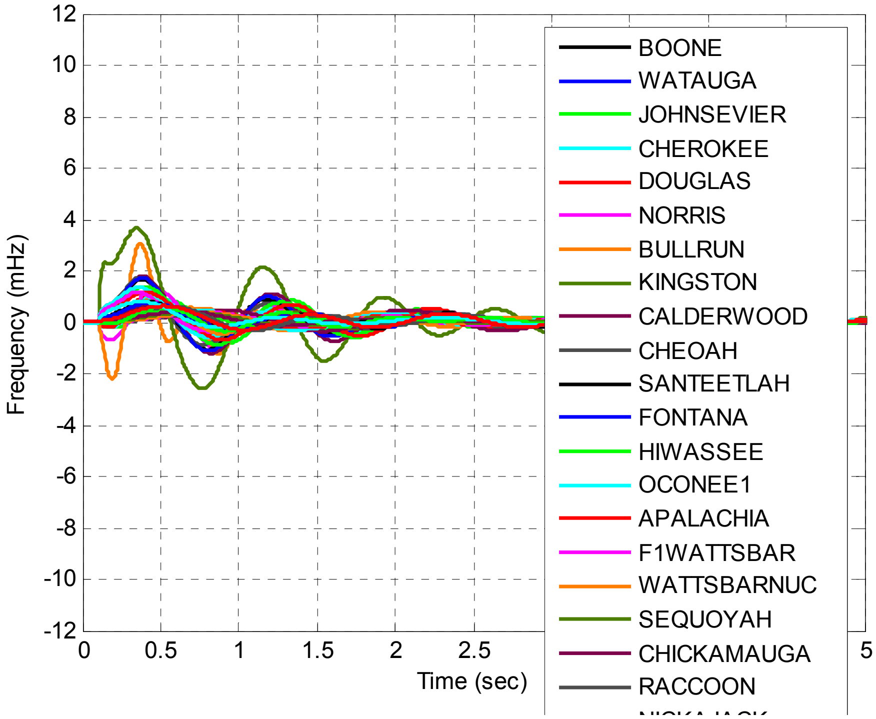

Figure 5.10 Frequency of the 69 kV Melton Hill – Farragut line trip from PSS/E simulation

It can be seen from the figures that the impact of a line outage disturbance is reduced as the voltage level is lowered in the Knoxville region.

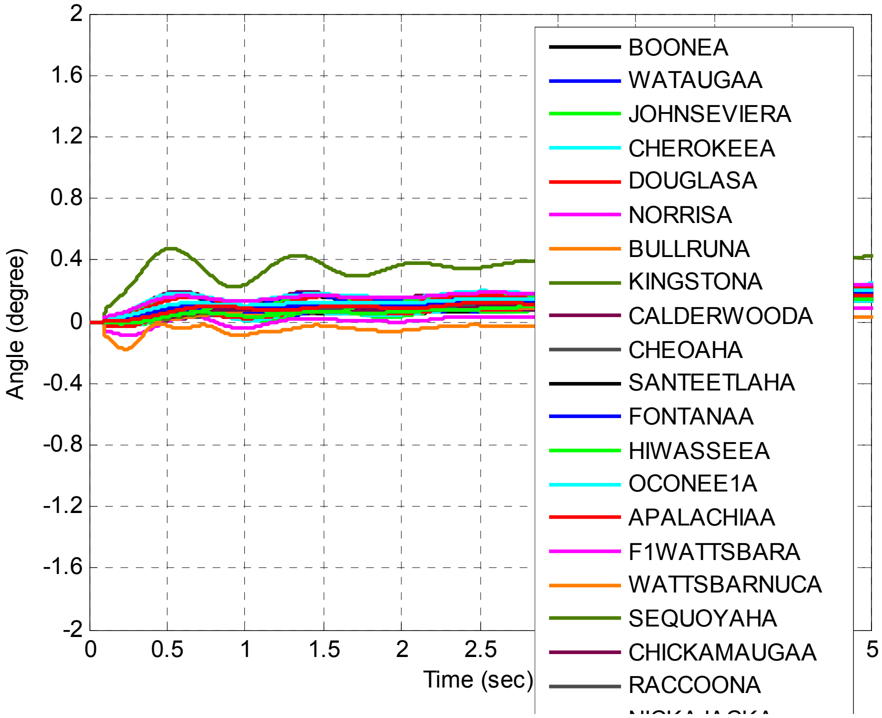

Figure 5.11 Angle of the 69 kV Melton Hill – Farragut line trip from PSS/E simulation

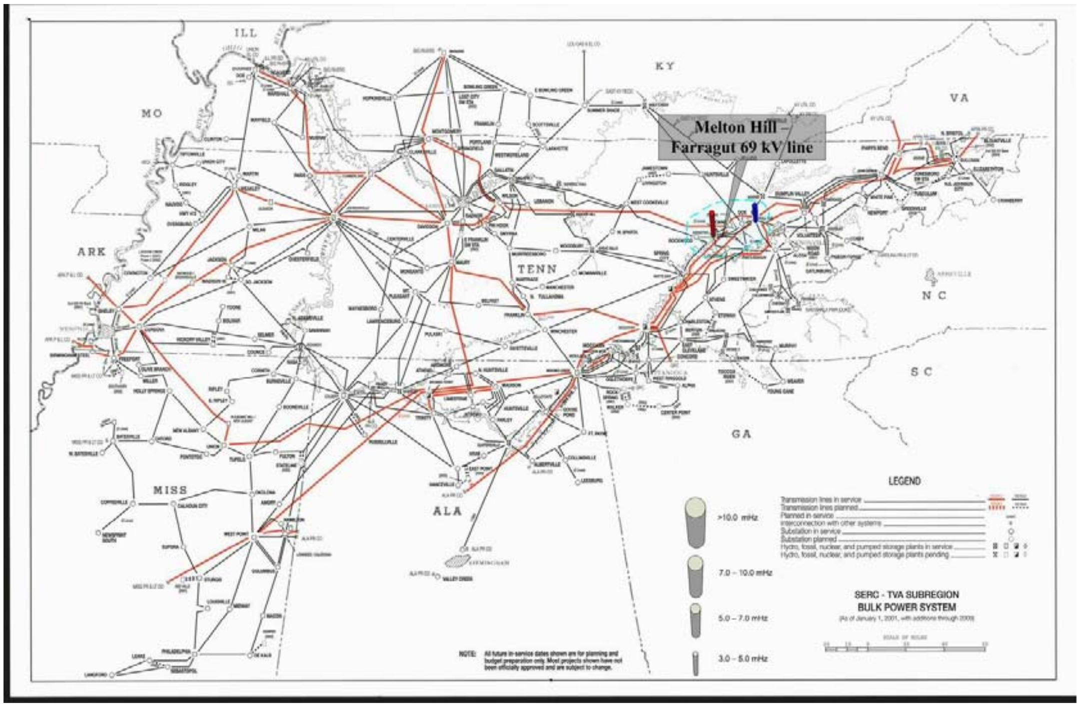

Figure 5.12 Frequency sensitivity map for the 69 kV Melton Hill – Farragut line trip (map source: TVA)

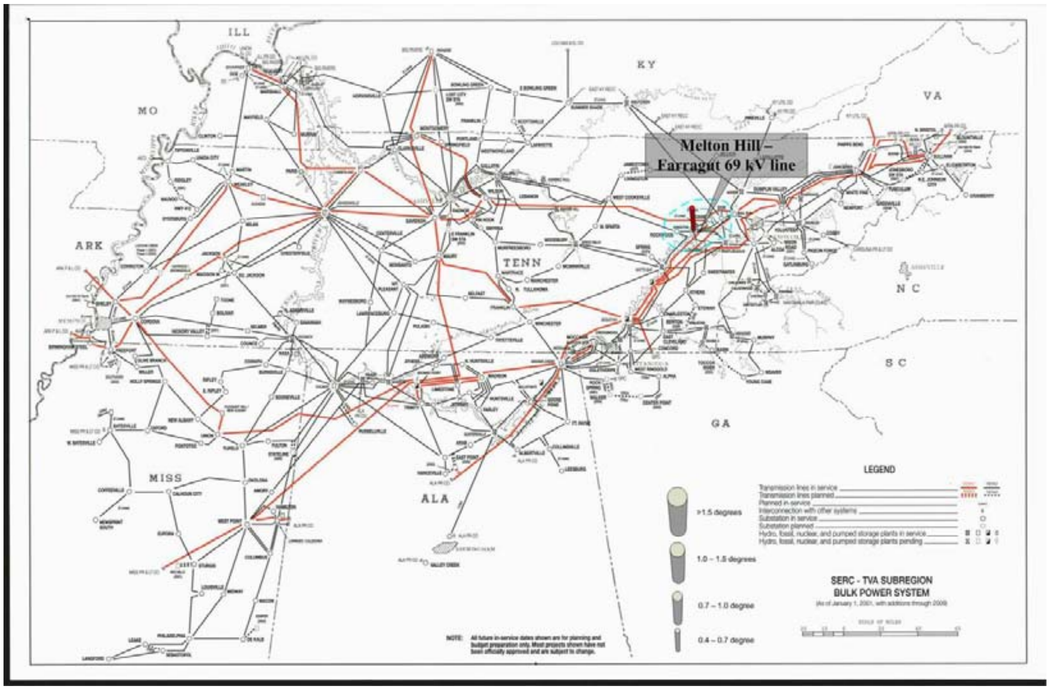

Figure 5.13 Angle sensitivity map for the 69 kV Melton Hill – Farragut line trip (map source: TVA)

The frequency and angle changes due to tripping of the 230 kV Widows Creek – Crawfish line are shown in Figure 5.14 and Figure 5.15. The corresponding frequency and angle sensitivity maps are depicted in Figure 5.16 and Figure 5.17. It can be noticed that frequency and angle at all the monitoring locations experience a fast initial rise at the time of the line trip. This line is at the boundary of the TVA system so that all the monitoring points in the TVA system are located at one side (the sending end in this case) of the tripped line. As a result, the sensitivity area at the receiving end of the line is not observed in this case, thus all the columns in the sensitivity maps are all in the red color.

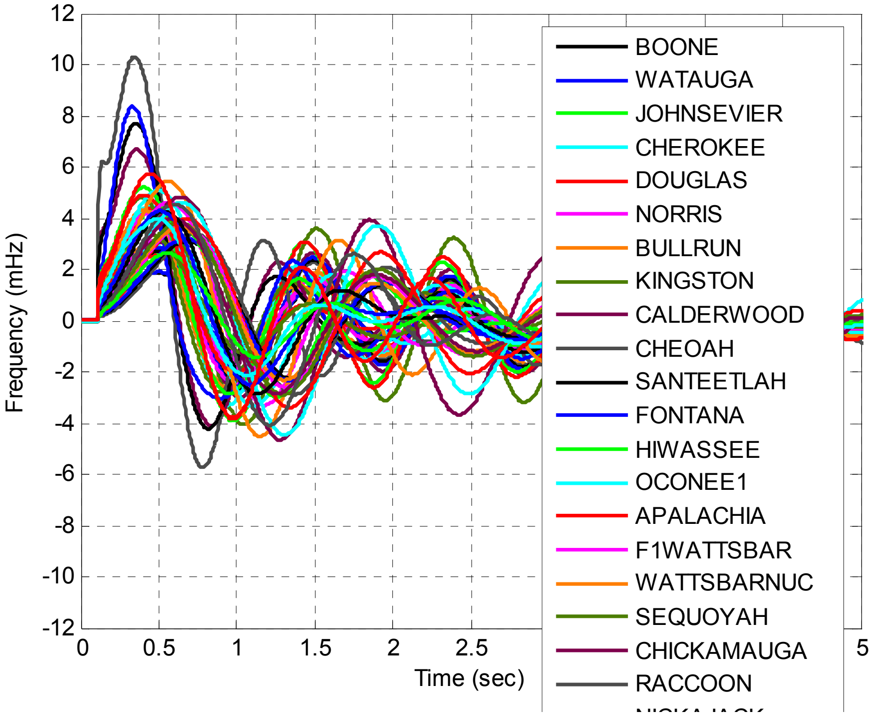

Figure 5.14 Frequency of the 230 kV Widows Creek – Crawfish line trip from PSS/E simulation

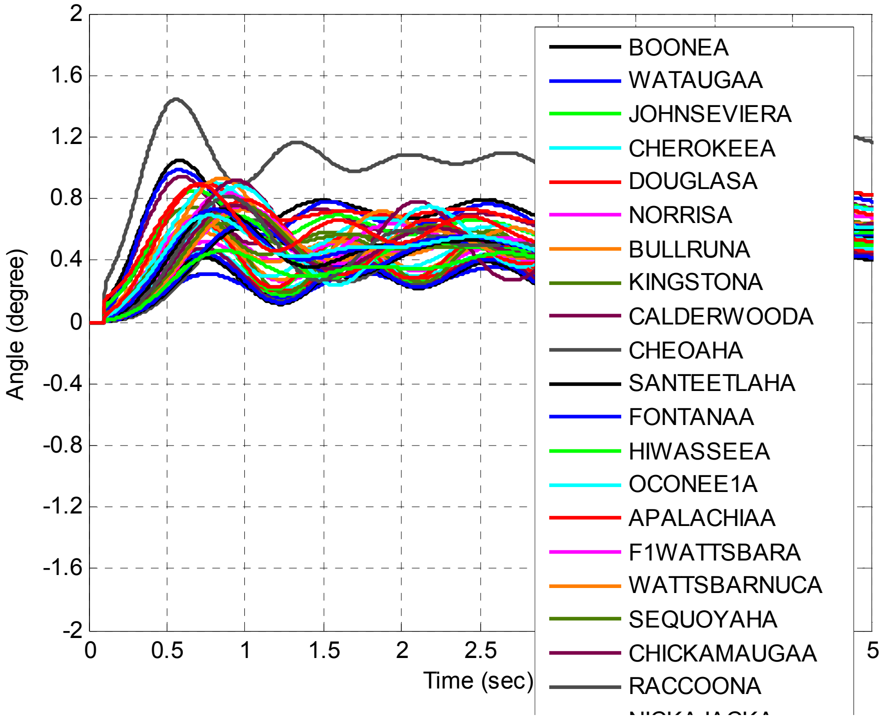

Figure 5.15 Angle of the 230 kV Widows Creek – Crawfish line trip from PSS/E simulation

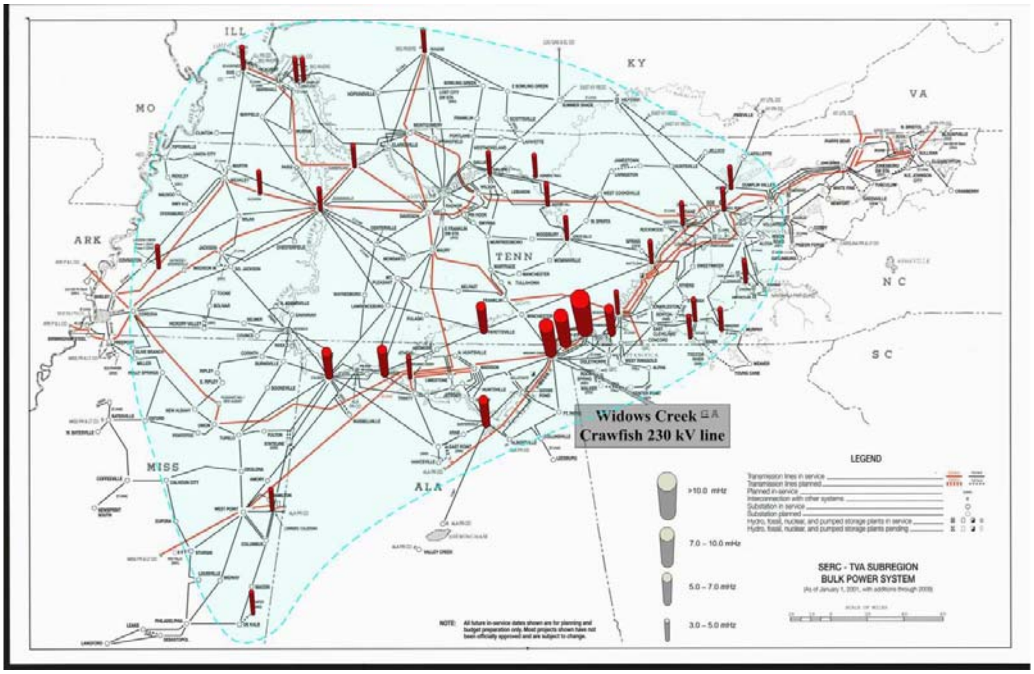

Figure 5.16 Frequency sensitivity map for the 230 kV Widows Creek – Crawfish line trip (map source: TVA)

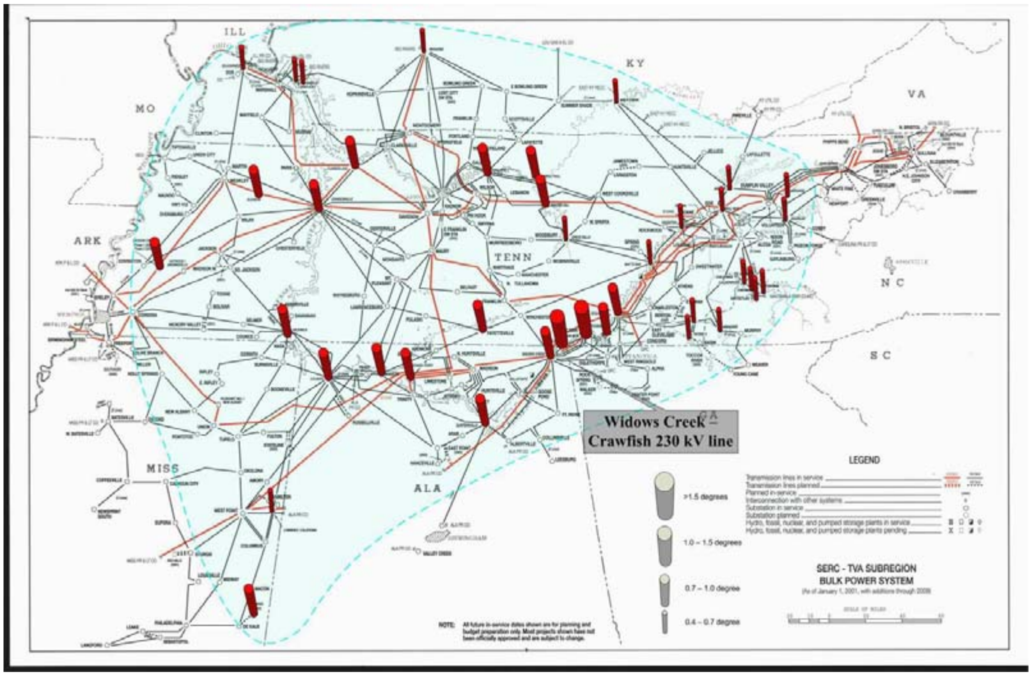

Figure 5.17 Angle sensitivity map for the 230 kV Widows Creek – Crawfish line trip (map source: TVA)

To compare the change of the sensitivity areas due to different line loading conditions, one more 230 kV line is selected to be tripped: the West Ringgold – Alpha line. The pre-outage real power flow on the Widows Creek – Crawfish is 337 MW in the PSS/E model which is larger than that on the West Ringgold – Alpha line (162 MW). The simulation results and sensitivity areas are shown in Figure 5.18 to Figure 5.21. Similar to the previous 230 kV line trip case, all monitoring points are at the sending end of the tripped line. It can be noticed that the sensitivity regions after tripping the West Ringgold – Alpha line (162 MW) are much smaller than in previous case.

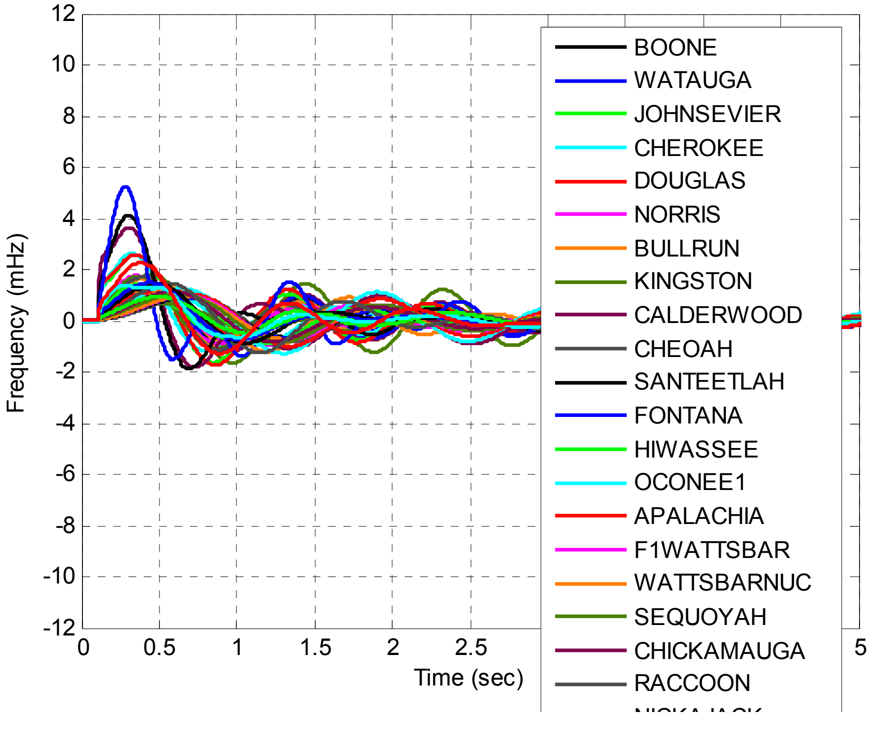

Figure 5.18 Frequency of the 230 kV West Ringgold – Alpha line trip from PSS/E simulation

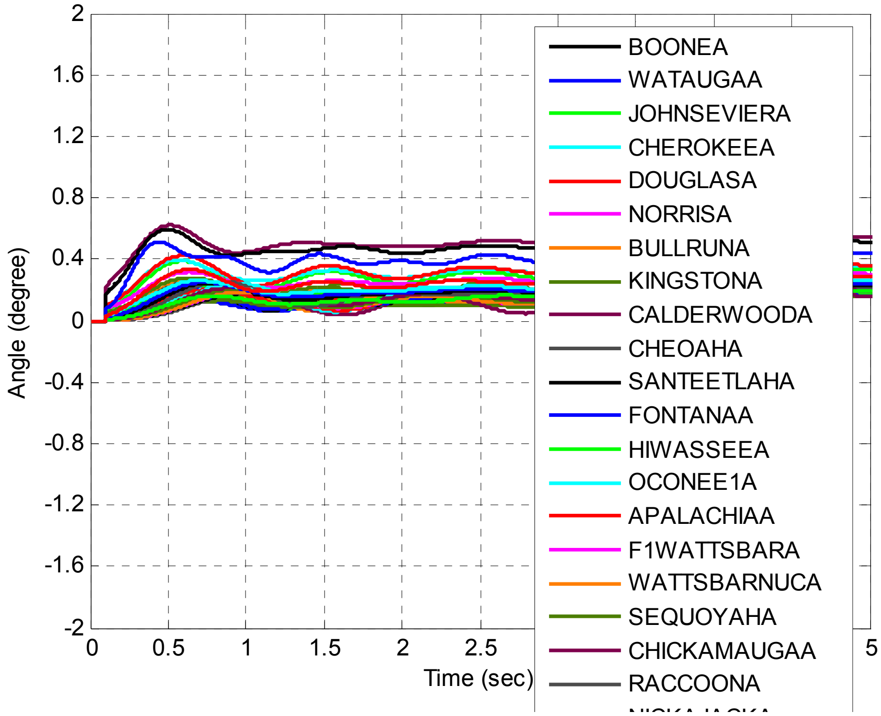

Figure 5.19 Angle of the 230 kV West Ringgold – Alpha line trip from PSS/E simulation

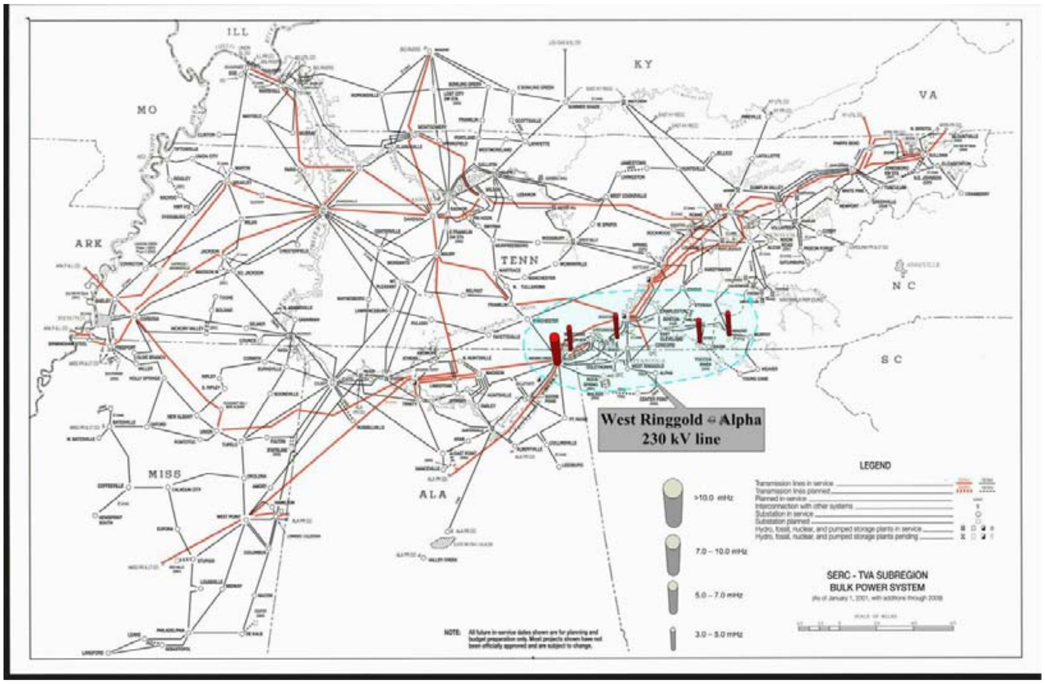

Figure 5.20 Frequency sensitivity map for the 230 kV West Ringgold – Alpha line trip (map source: TVA)

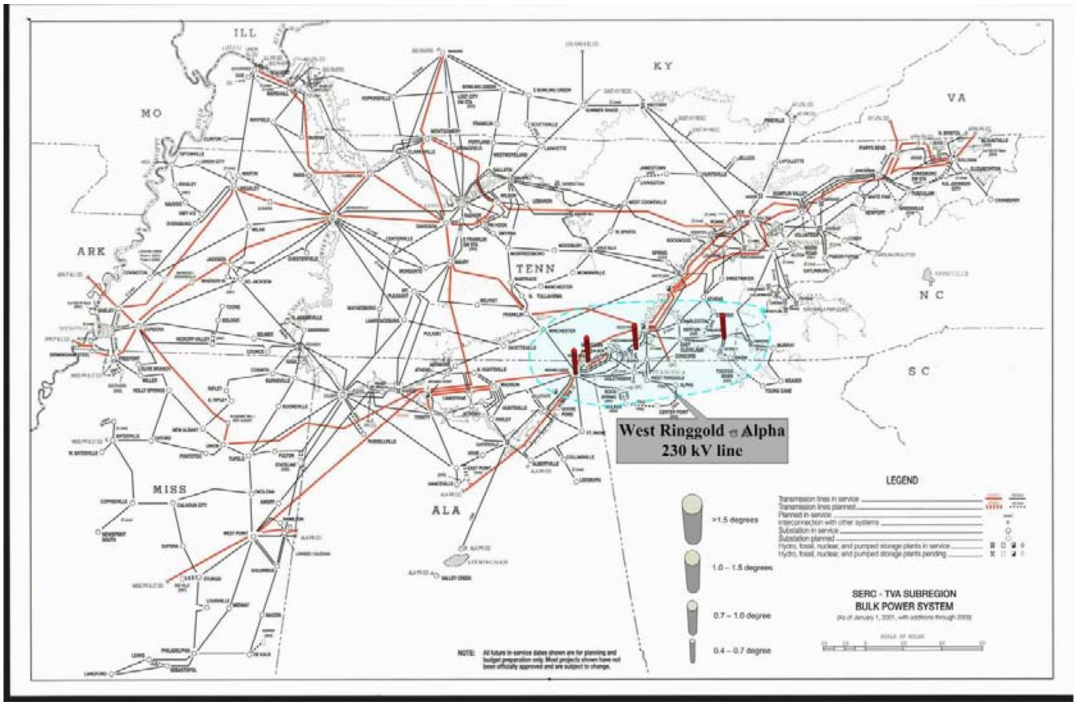

Figure 5.21 Angle sensitivity map for the 230 kV West Ringgold – Alpha line trip (map source: TVA)

From the above discussions, the size of sensitivity region of a line trip disturbance is related to the voltage level of the line and its loading condition before it is tripped.

5.2 FDR Placement Strategy

40 more FDR units will be deployed in the TVA system in the near future to increase the sensor density in that area. For the benefit of better observability of the transmission network, the FDR placement should be able to satisfy the following criteria:

(1) Spread out in the entire TVA area;

(2) Be able to monitor the major transmission corridors;

(3) Be sufficient for the 500 kV transmission line detection and identification; May also cover several important 161 kV substations.

The 500 kV line trip records in the TVA system from January 2007 to June 2008 are studied to identify the vulnerable lines with more outage occurrence than others. Table 5.2 lists 20 transmission lines in the TVA system that experienced more than two outages during this time period. It is suggested that both ends of these lines be monitored.

Table 5.2 500 kV line outage occurrences in TVA from January 2007 to June 2008

Line Name	Outage Occurrence
Cordova - Freeport	11
Browns Ferry - Union	9
Paradise-Montgomery	9
Browns Ferry - West Point	8
Browns Ferry - Trinity	3
Cumberland - Marshall	3
Johnsonville - Gleason SW	3
Bull Run - Roane	2
Davidson - Montgomery	2
French CAMP - Wolf Creek	2
French CAMP - CHOCTAW	2
Johnsonville - Cumberland	2
Lagoon Creek - Weakley	2
Maury - Franklin	2
Phipps Bend - Pocket (KU)	2
Roane - Wilson	2
Valley View - West Vernon	2
West Point - CHOCTAW	2
West Point - Lowndes	2
Widows Creek - Raccoon Mountain	2

45 FDR locations are proposed considering some margin for flexibility, as shown in Figure 5.22. The 20 phase one locations (shown as blue circles) are chosen to be the substations at the ends of the vulnerable 500 kV lines as listed in Table 5.2, and 500 kV substations at important transmission corridors. The phase two locations (shown as purple circles) include nine additional 500 kV substations and four 161 kV substations with high concentrations of 161 kV lines.

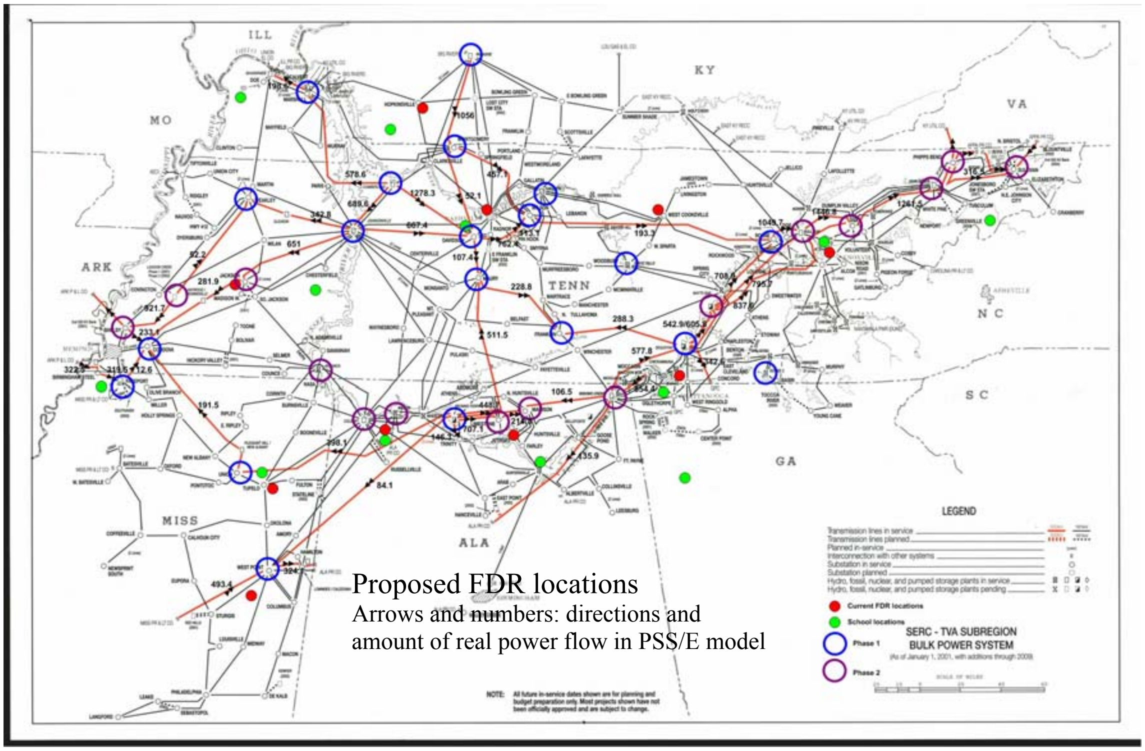

Figure 5.22 Proposed FDR locations (map source: TVA)

5.3 Line Trip Detection with Frequency

The frequency of a line trip event measured by FNET event is shown in Figure 5.23. Unlike the generator trip events discussed in chapter 2, frequency observes some well-damped oscillations after a line outage. Frequency at the sending end of the line will rise due to the machine acceleration; whereas frequency will drop at the receiving end of the line due to machine deceleration caused by the deficit of generation. Moreover, the outage of a transmission line can be a local event with limited impact on the whole system compared with the generation loss event, in which frequency will experience a decline all over the system.

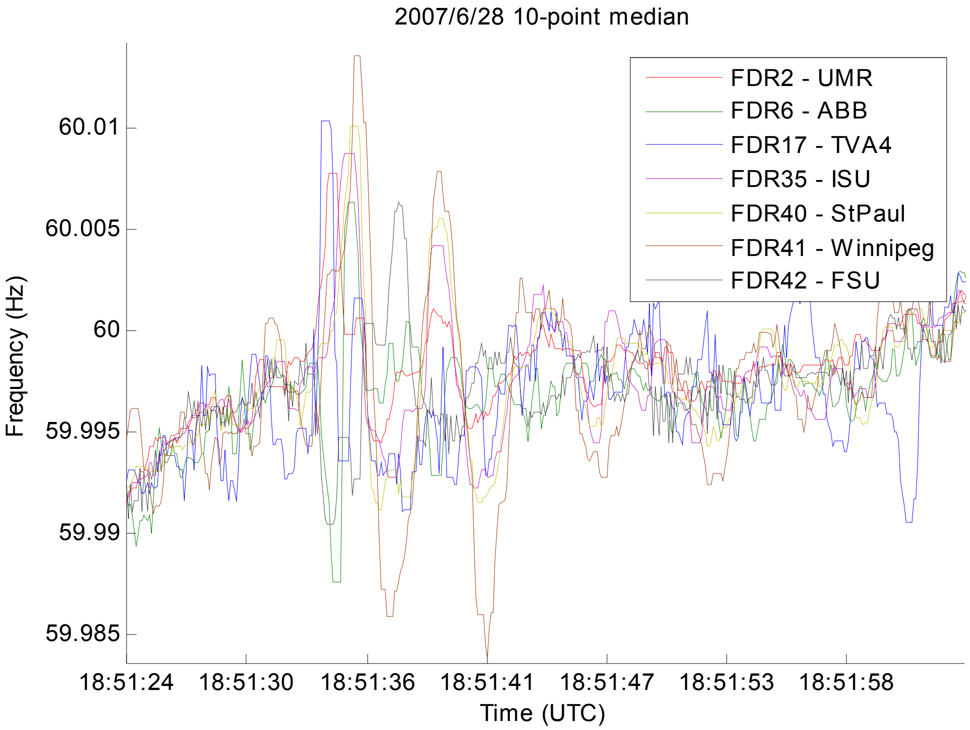

Figure 5.23 Frequency of a line trip event

A line trip trigger is developed to detect such events by examining the frequency variations. The block diagram of this method is shown in Figure 5.24.

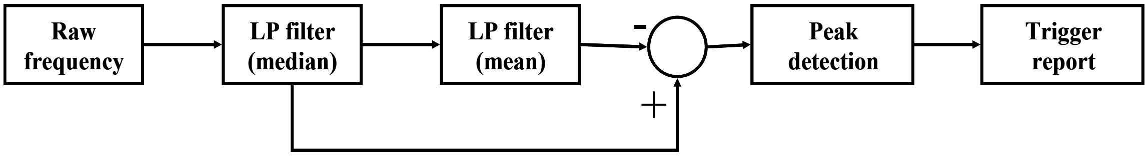

Figure 5.24 Line trip trigger using frequency

To explain the trigger algorithm, the outage of the 500 kV Cumberland – Marshall line on March 28, 2007 is shown from Figure 5.25 to Figure 5.27 as an example. Figure 5.25 shows the raw frequency data where the oscillations caused by the line trip are observable together with other high-frequency noises and possible local dynamics in the distribution network. The first low-pass filter in the block diagram in Figure 5.24 is to remove the high-frequency noises in the raw frequency and a 7-point moving median filter is used. The filtered frequency data for the input data in Figure 5.25 is shown in Figure 5.26.

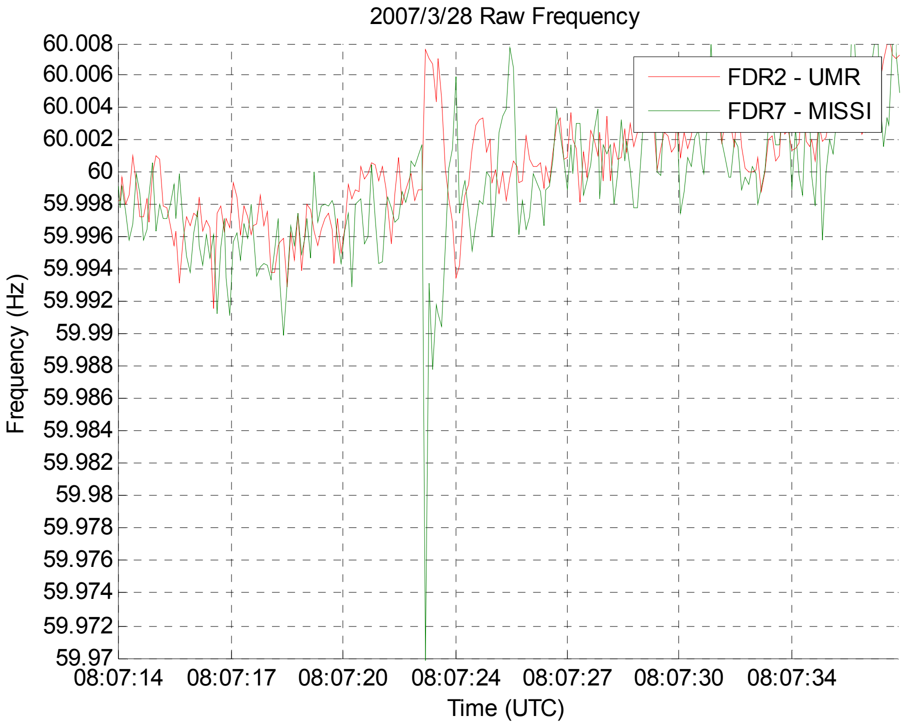

Figure 5.25 Example raw frequency

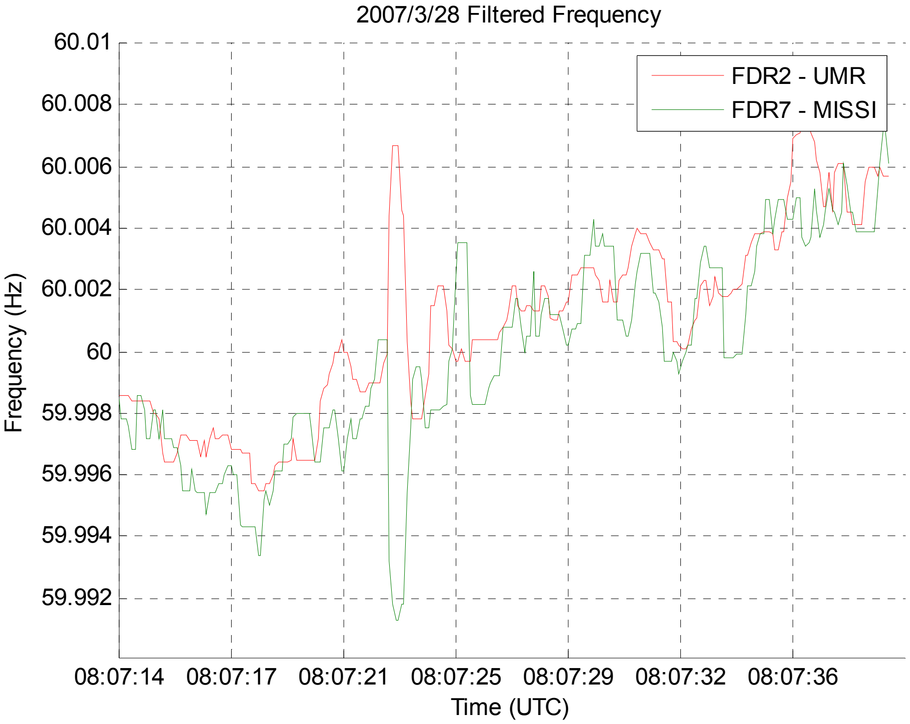

Figure 5.26 Frequency after the median filter

Then the filtered frequency data are fed into the second low-pass filter, a 31-point moving average filter, to get the trend of frequency data which is then subtracted from the filtered data. The signal of interest in line trip detection is the oscillation caused by the line outage, so de-trending is necessary to remove the effects of the data trend and maintain the oscillatory part at the same time. Tests show that the trigger reports more false events if the trend is not removed. Figure 5.27 shows the de-trended data which becomes zero-mean signals and the rapidly varying component of the original frequency is clearly represented.

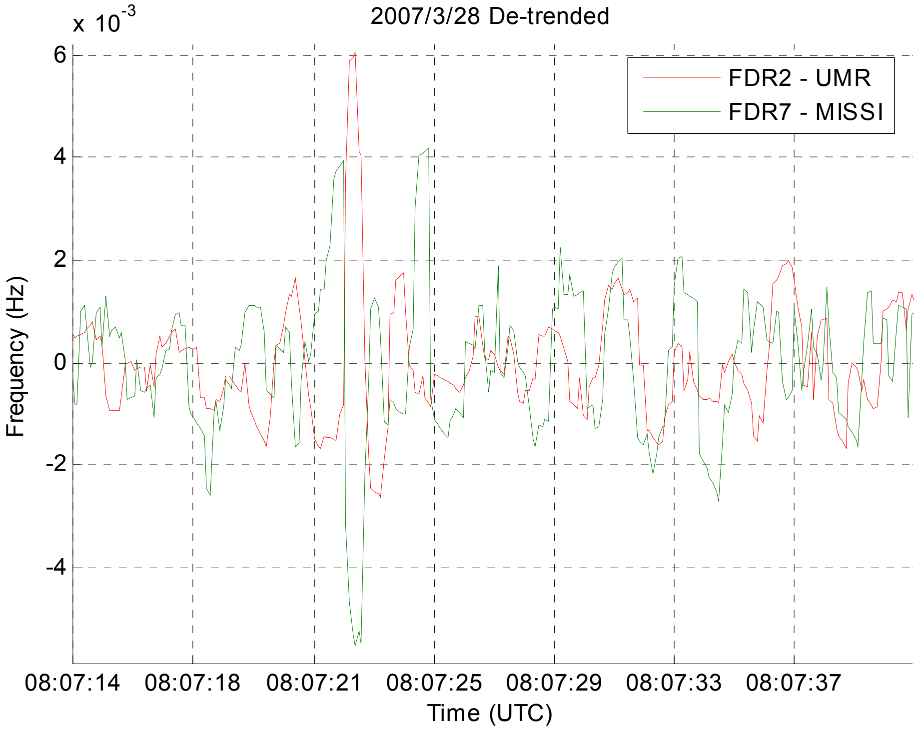

Figure 5.27 De-trended frequency data

Two thresholds are set to detect the initial frequency peaks during the first swing in the de-trended signal. It has been observed that the oscillations caused by line trips are usually well-damped, which means that the peak values of the oscillations are descending. For the detection of line trips in the TVA system, the two thresholds are currently 0.0065 Hz and 0.0045 Hz for the first two peaks, respectively. Within a 2-second time window, if the first peak is larger than the higher threshold and the second peak exceeds the lower threshold, the algorithm will throw a trigger flag and generate reports. The 2-second time window is decided based on the observations from measured line trip events as well as simulation results that the period of the first swing is usually less than 2 seconds.

The line trip trigger using frequency is tested on the data of August 4, 2007. Frequency data from 5 FDR units are scanned. The testing results are listed in Table 5.3. A triggered case is considered a missed one if the frequency does not demonstrate the oscillatory characteristics similar to what is shown in Figure 5.23. The results demonstrate that the method has high accuracy.

Table 5.3 Test results of the line trip trigger using frequency data

FDR ID	FDR name	# of triggered case	# of missed ones
9	UFL	2	0
11	Calvin	6	1
27	RPI	14	4
35	ISU	3	0
38	ISONE	7	0
	Total	32	5

5.4 Line Trip Detection with Angle

As discussed before, in a disturbance (generation trip, load loss or line trip) where generation and load have imbalance, local phase angle and frequency will change simultaneously in response to the disturbance. Line trip disturbances cause obvious oscillations in frequency measured close to the event location. Simulations also show that tripping a line results in a step change in phase angle followed by transient oscillations. The angle measurement for the 500 kV Cumberland – Marshall line trip discussed in the previous section is shown in Figure 5.28. The line trip resulted in noticeable changes in voltage phase angle seen by FDR2. The displayed phase angle is unwrapped and referred to a reference FDR (FDR4 – VT in this example).

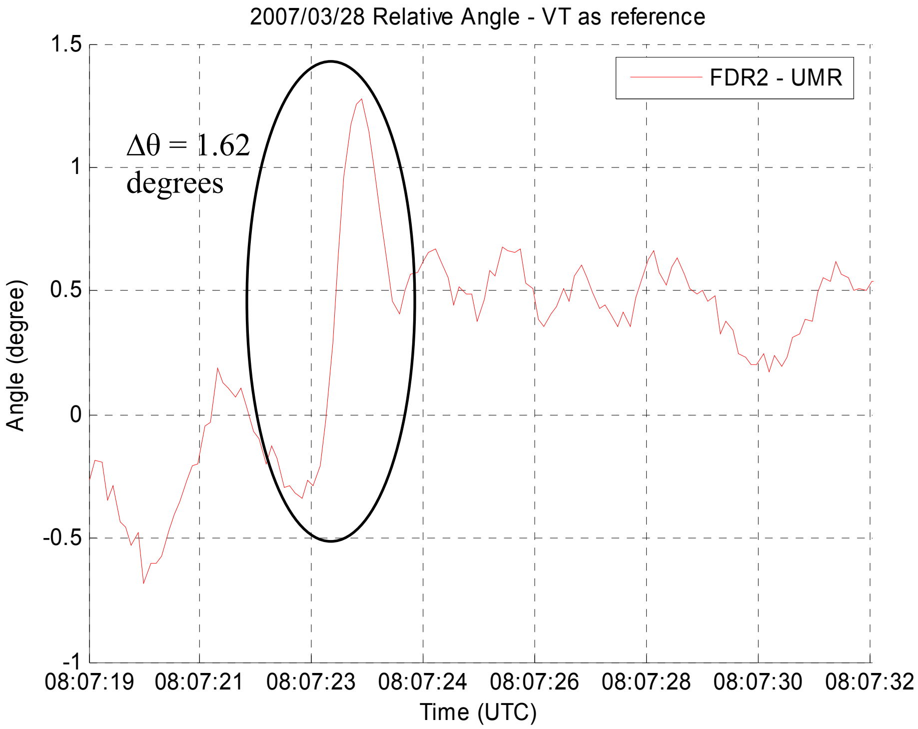

Figure 5.28 Relative Phase angle (VT as reference) of the line trip on March 28, 2007

5.4.1 Comparisons between Triggering Signals

Several signals that can be used in the phase angle trigger are unwrapped angle, de-trended angle, and relative angle. The unwrapped angle is obtained by adding or subtracting 2π from the raw angle measurements whenever a wrap up occurs. The de-trended angle and the relative angle are both obtained based on the unwrapped angle. The de-trending process is similar to the method used to de-trend the frequency signal as described in section 5.3. The relative angle is obtained by subtracting the corresponding measurements of a reference sensor from the angles of interest. Figure 5.29 and Figure 5.30 show the de-trended and unwrapped angle from the UMR unit of the line trip disturbance on March 28, 2007, respectively. And the relative angle signal is shown in Figure 5.28. The delta angle in the figures is the angle change amount during the line trip.

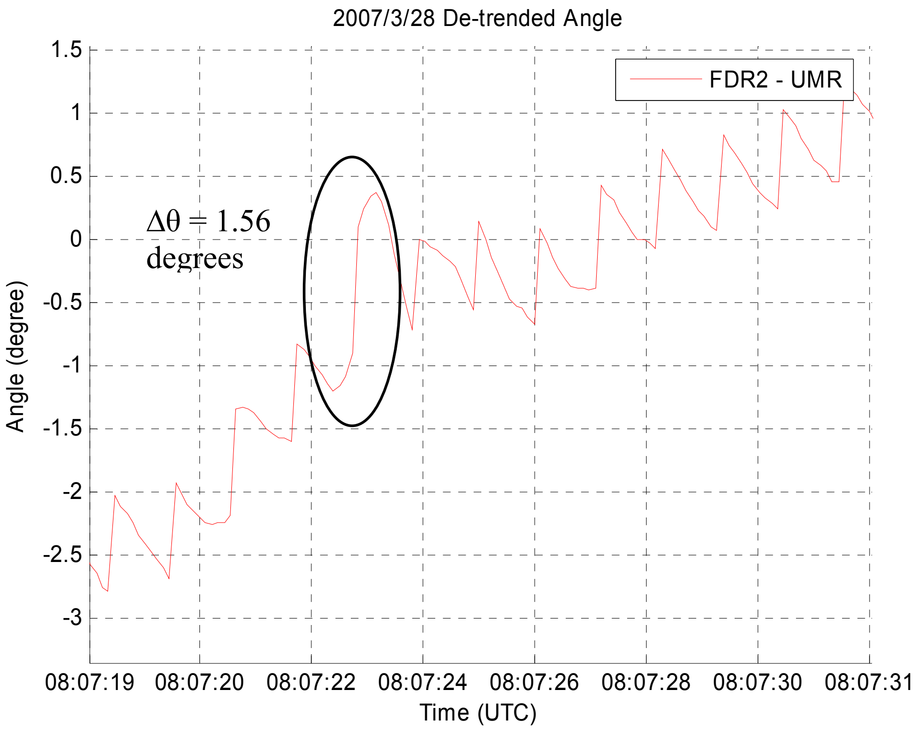

Figure 5.29 De-trended angle of the line trip on March 28, 2007

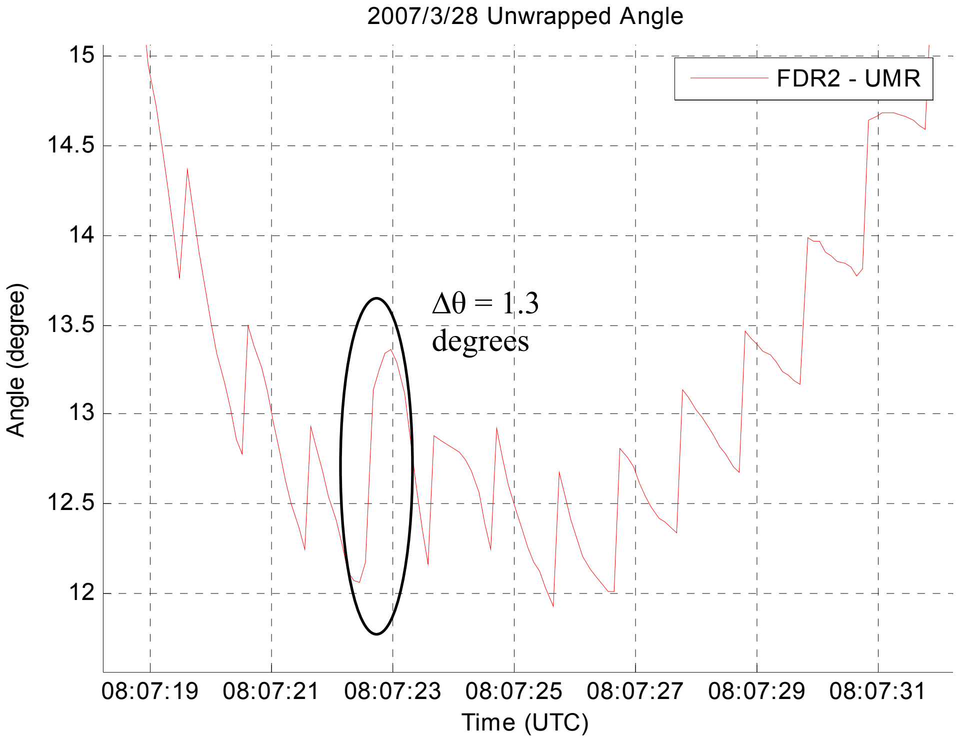

Figure 5.30 Unwrapped angle of the line trip on March 28, 2007

It can be seen that with different signal processing methods the angle change initiated by a line trip is more obvious in the relative angle than in the de-trended or the unwrapped angle. Even after unwrapping, there still exist angle discontinuities larger than 0.5 degree about every second, as shown in Figure 5.29 and Figure 5.30. Those discontinuities may be due to the sampling frequency and algorithm in the FDR firmware [52][55], which contaminates the angle signal used to detect line trips.

Another example of different angle signals is illustrated in Figure 5.31 to Figure 5.33. The angle change in the relative angle is the largest among the three signals. The angle change from the line trip is unnoticeable in the unwrapped angle as the angle trend varies very rapidly. Therefore, the relative angle and de-trended angle are better than the unwrapped angle to detect angle triggers. Two trigger algorithms are shown as follows.

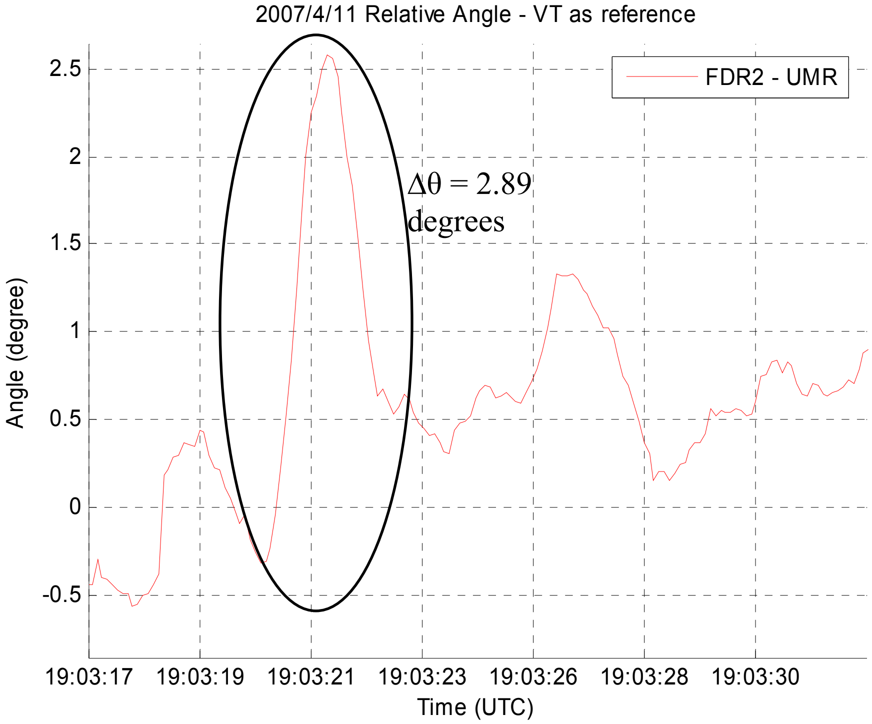

Figure 5.31 Relative angle of the line trip on April 11, 2007 (VT as reference)

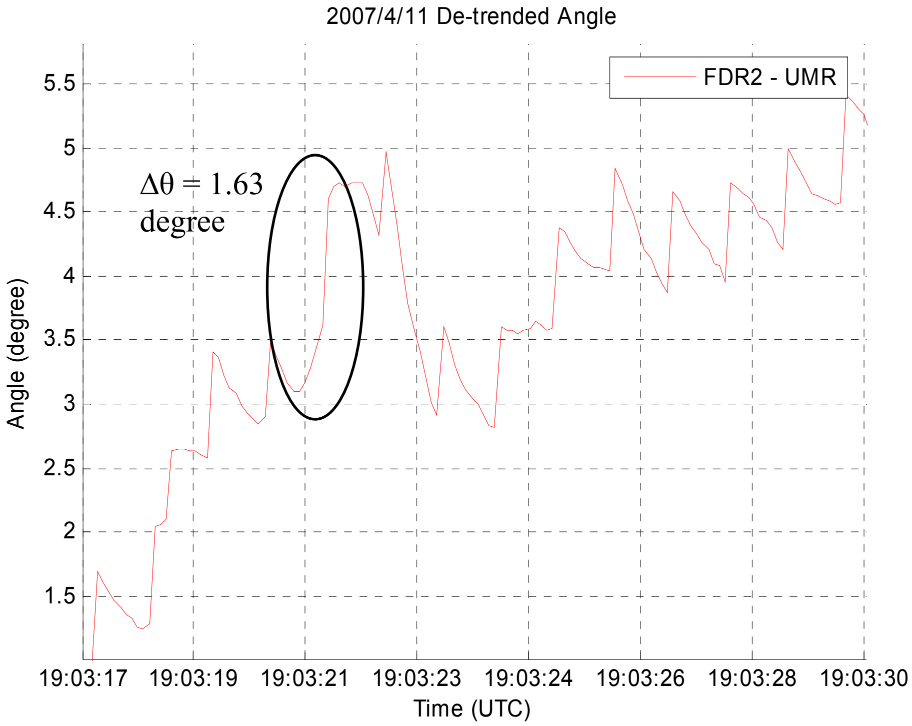

Figure 5.32 De-trended angle of the line trip on April 11, 2007

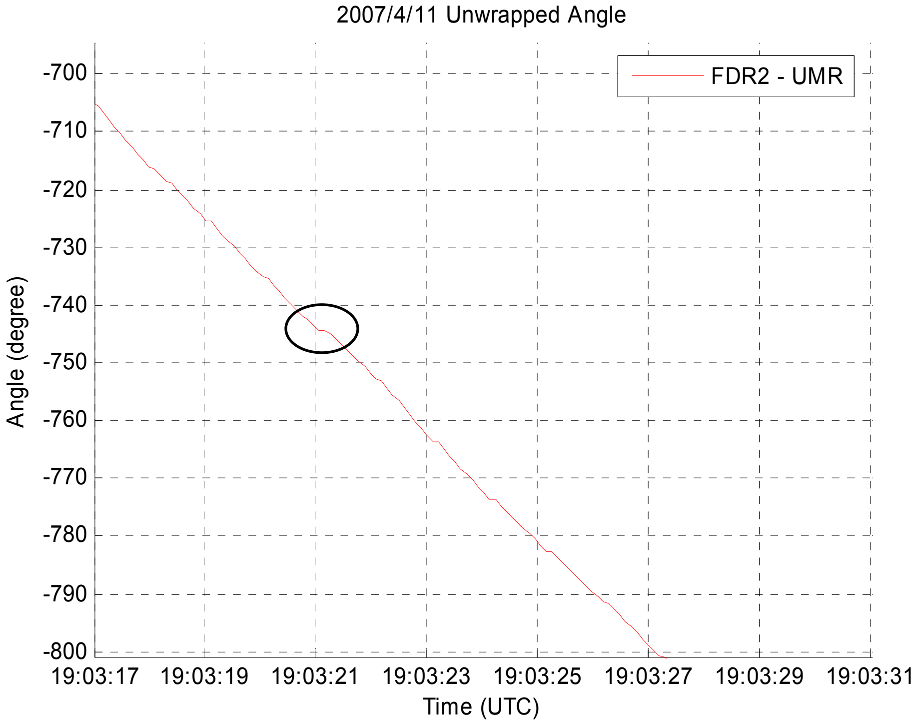

Figure 5.33 Unwrapped angle of the line trip on April 11, 2007

5.4.2 Line Trip Trigger Based on De-trended Angle

Similar to the frequency trigger method, voltage phase angle measured by FNET can also be used to detect line trips. The block diagram of the line trip trigger using de-trended signal is shown in Figure 5.34.

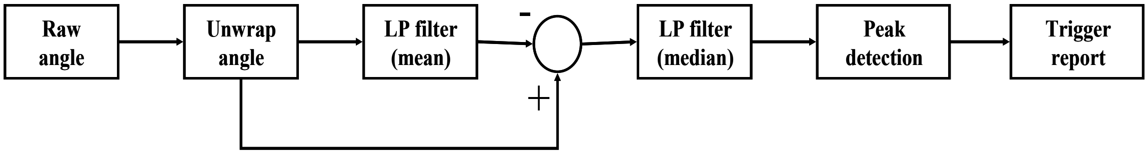

Figure 5.34 Line trip trigger using de-trended phase angle

An example is shown below to explain the idea of the algorithm. Figure 5.35 shows that the angle data measured by FDR units are wrapped around when it exceeds zero or 2π. To view and process the angle data, unwrapping is necessary. A simple way to achieve that is to add or subtract 2π whenever the wraparound appears. The unwrapped angle data for this example are shown in Figure 5.36. The unwrapped angles start from different values within the plotted time frame due to different angle offsets at the measurement locations. Another reason which may attribute to the angle difference is that the FDR units are installed at the distribution voltage level. It is quite possible that the electrical devices such as transformers cause angle shift from the transmission level to the distribution level. For the ease of comparison, all angle curves are normalized with the start at zero value, as is shown in Figure 5.37.

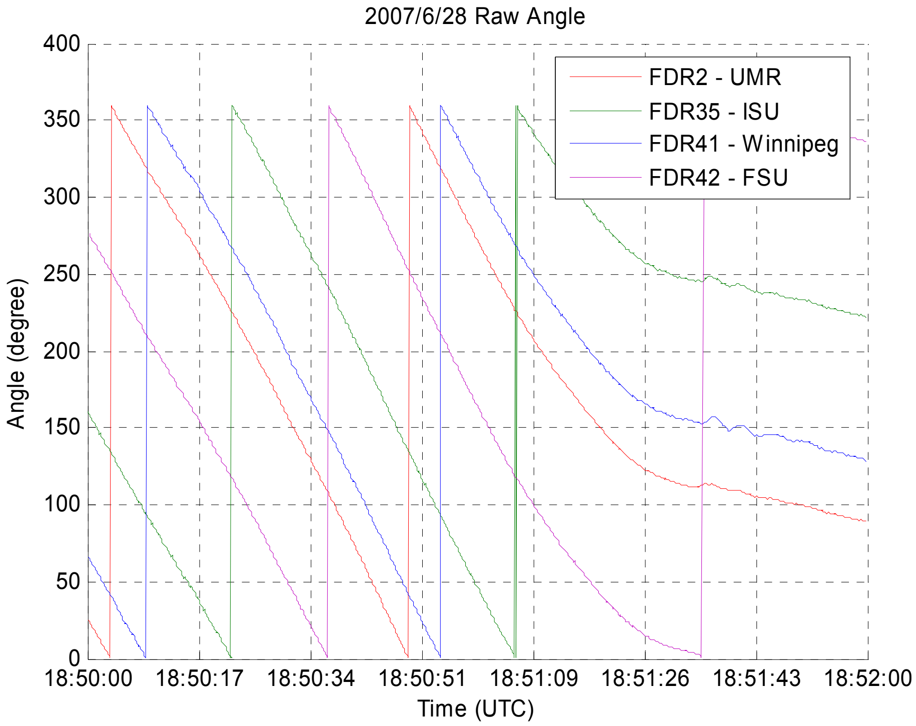

Figure 5.35 Example raw angle data

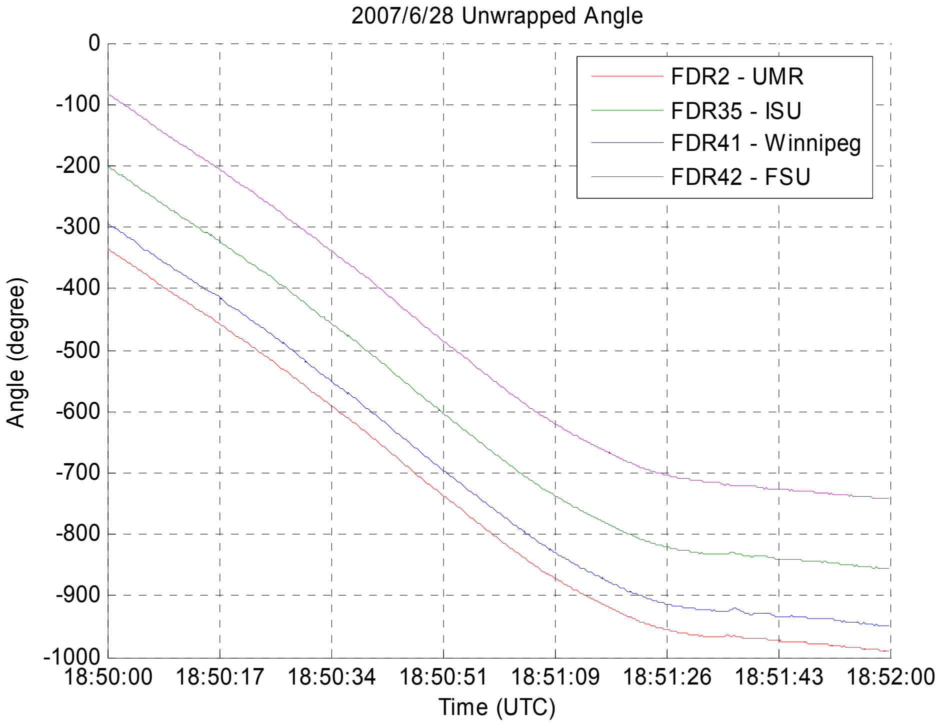

Figure 5.36 Unwrapped angle data

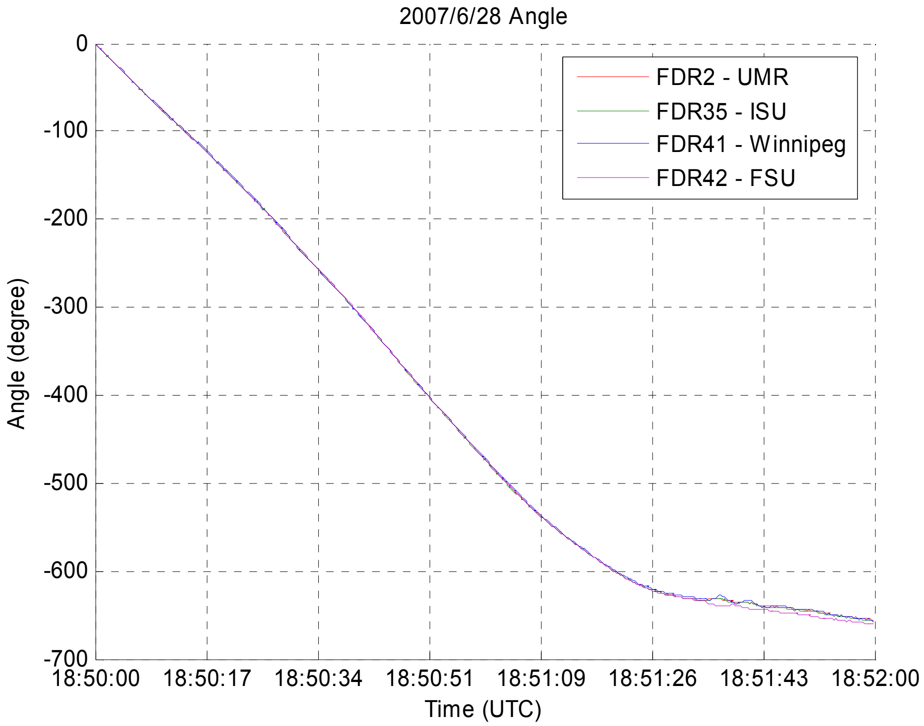

Figure 5.37 All angle data are scaled to start from zero.

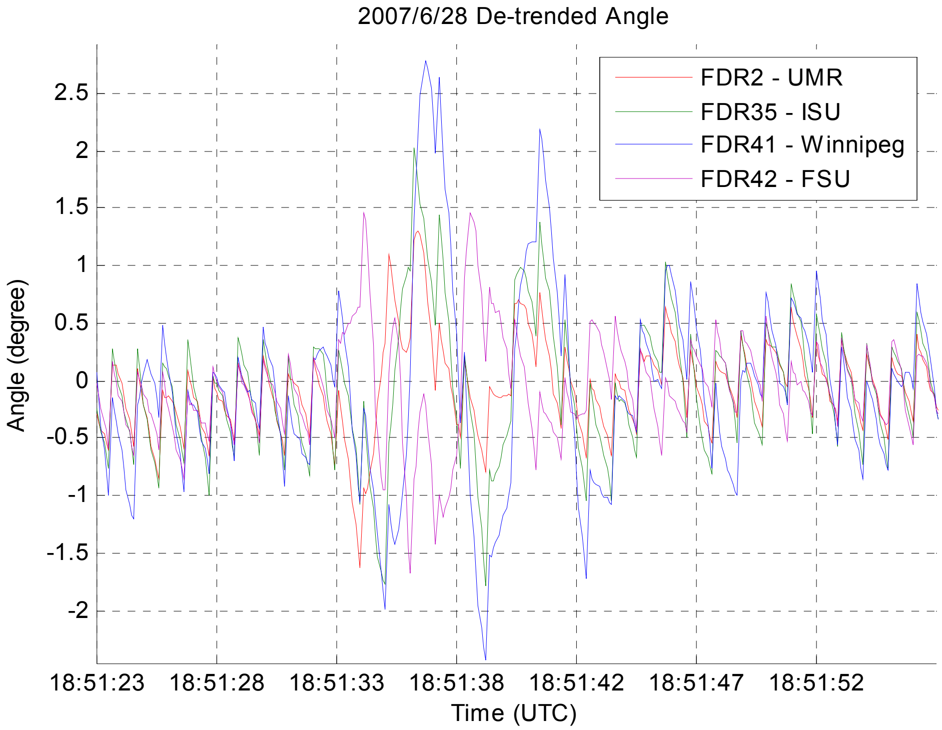

Figure 5.38 De-trended angle data

A low-pass filter (31-point moving mean) is applied to the unwrapped angle data to get the data trend. Then the trend is removed from the unwrapped angle data as shown in Figure 5.38. It can be noticed that the de-trended angle data is still noisy. Another low-pass filter is used to remove the noises in the signals. The resulted data are shown in Figure 5.39. As the high-frequency noises are removed, the oscillation part becomes obvious for detection.

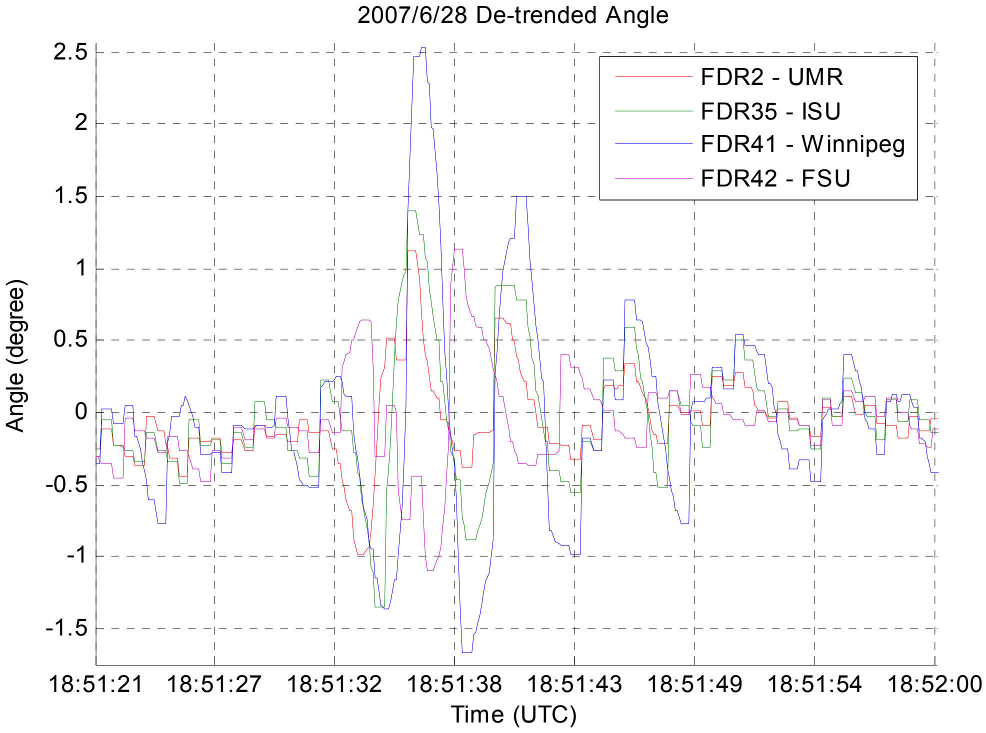

Figure 5.39 De-trended data after removing the noises

5.4.3 Line Trip Trigger Based on Relative Angle

It has been discussed that the angle change due to a line trip disturbance is more obvious in relative angle. A line trip detection algorithm based on relative angle is also developed and the procedures are shown in Figure 5.40. This relative angle-based detection algorithm is simple and computation-efficient because it does not require mean or median filtering which is usually time-consuming.

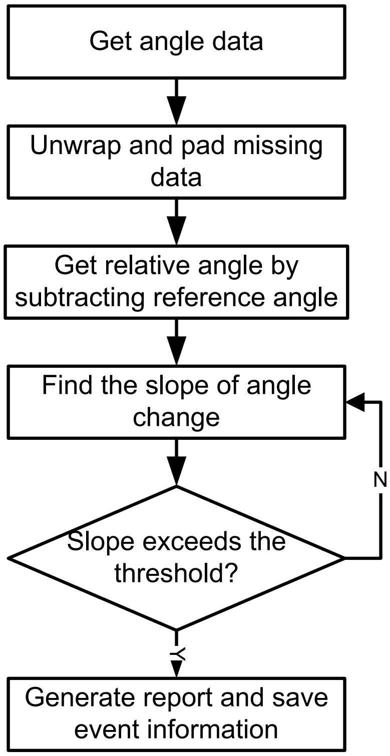

Figure 5.40 Flowchart of the line trip trigger based on relative angle

The data preprocessing includes the unwrapping process as mentioned above and missing data are checked and padded by interpolation if any are found. The FDR device may temporarily stop reporting data due to loss of GPS signals or problems in the Internet connection. The algorithm selects the reference FDR unit from a list of units by checking the data availability. The program performs data preprocessing and event check by scanning the incoming data stream with a 40-second moving window. The size of the moving window is selected based on the observation that unwrapping the angle over a long period of time may cause problem perhaps due to data dropout in the raw measurements. Figure 5.41 shows the relative angles obtained from the data preprocessing for a 500 kV line trip event in the TVA system.

The program detects a line trip event by checking the change in relative angle within a 0.8-second time frame. The time window is selected based on the observation from the confirmed events that the angle change reaches its peak within around 1 second following a line trip. If the angle change exceeds 1.0 degree within 0.8 second and such a slope remains above the threshold within 1.1 seconds, the algorithm will claim a line trip is detected. The current thresholds and time window are selected based on the limited number of confirmed line trip events, which may be adjusted during further test with more confirmed cases.

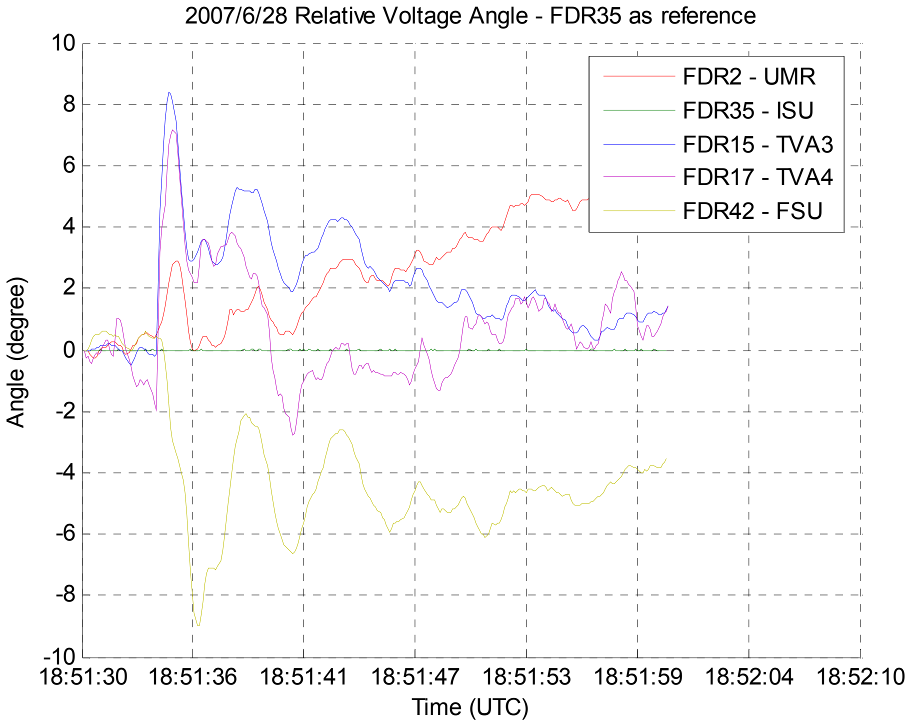

Figure 5.41 Relative angle for a line trip event (FDR35 as reference)

5.5 Summary

This chapter is the first part of the line trip detection and identification study. The line trip sensitivity is studied in this chapter based on simulations with PSS/E. The size of the sensitivity area is related to the voltage level and loading condition of a transmission line. Usually a 500 kV line outage impacts a larger area than an outage at the 161 kV level. 45 future FDR locations in the TVA system are proposed based on the analysis of the confirmed line trip events and the system characteristics in the simulation model. Then line trip detection algorithms are developed which use frequency or angle for detection. Different signals obtained from angle are compared and relative angle is selected. The proposed frequency and angle triggers are simple and can both be implemented fairly easily for real time line trip detection.

Chapter 6 Line Trip Identification

As a continuation of the study in chapter 5, this chapter focuses on single line trip identification. The question of interest is which line is tripped if one occurs. The study in this chapter will employ the simulations with PSS/E extensively based on the Eastern Interconnection model. The model is comprehensive and detailed which contains voltage levels from 765 kV to distribution level. There are 2287 generators and 16016 buses in service in the model. In addition, there are 20093 transmission lines and 7221 branches with transformers. The system's total active power generation is 590476.8 MW and the reactive power generation is 137509.9 MVAR [54]. The simulation will help identifying the characteristics of line trips.

6.1 Line Trip Characteristics – A Close Examination

The objective of line trip study in this work is to utilize wide-area measurements provided by FNET to detect a line outage when it occurs and identify the tripped line. Therefore, it is essential to study the line trip characteristics reflected in the power system parameters such as frequency and phase angle. In this section, the line trip characteristics are examined with PSS/E simulation and real frequency and angle measurements.

When a transmission line is tripped, the angular velocity of the machines at the sending end increases due to the sudden loss of load; while the angular velocity of the machines at the receiving end deceases [62]. The local phase angle and frequency change together. Hence the angle also experiences changes due to the line outage. Some frequency and angle plots of line trip events have been illustrated in Chapter 5. The information in the measurements for line trip identification will be closely examined as follows.

6.1.1 Line Trip Signatures in PSS/E Simulation

In the PSS/E model of the Eastern Interconnection used for this study, 70 transmission lines at 500 kV voltage level have been identified in the TVA system, among which 7 lines carry zero power flow. The PSS/E simulations in this work are carried out on the 63 lines with real power flow greater than zero. 52 monitoring channels are selected including the proposed 45 FDR locations and 7 current FDR locations around the TVA area. Generally a transmission line is tripped by relay actions to clear a fault or it is switched out without any fault involved. Those two different line trip scenarios are considered in the simulations: with and without a fault. Three-phase faults are applied in PSS/E by placing a large shunt susceptance at the faulted bus to drive the voltage at the faulted bus to zero. The typical value recommended is $B = -2.E9$ [63]. Figure 6.1 and 6.2 show an example of tripping the 500 kV Cumberland – Johnsonville line after a three-phase fault. As in chapter 5, the phase angles are all referred to zero at the beginning of the simulation.

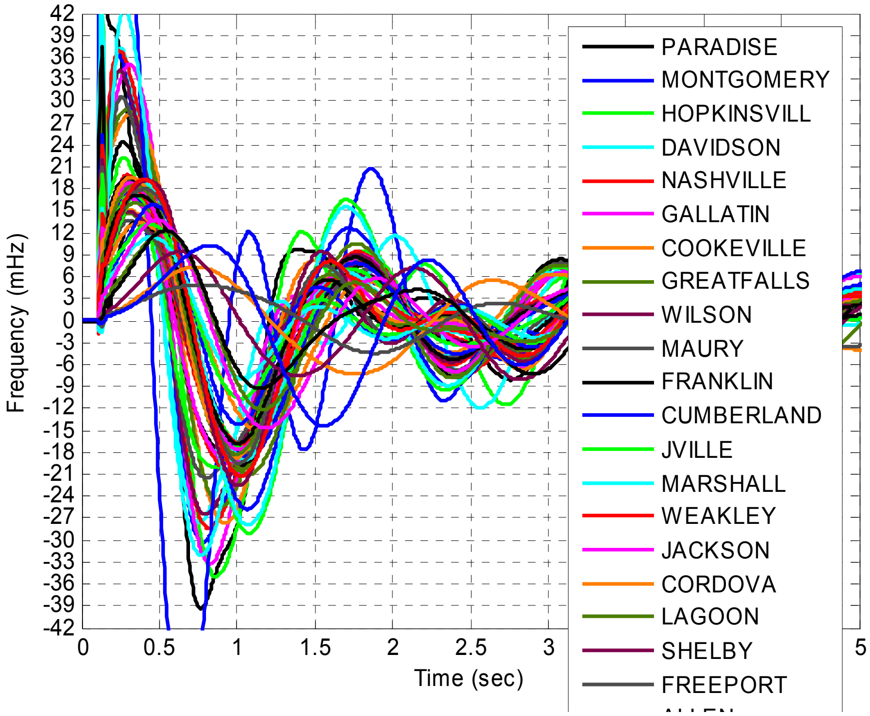

Figure 6.1 Frequency from tripping the 500 kV Cumberland – Johnsonville line after a line fault

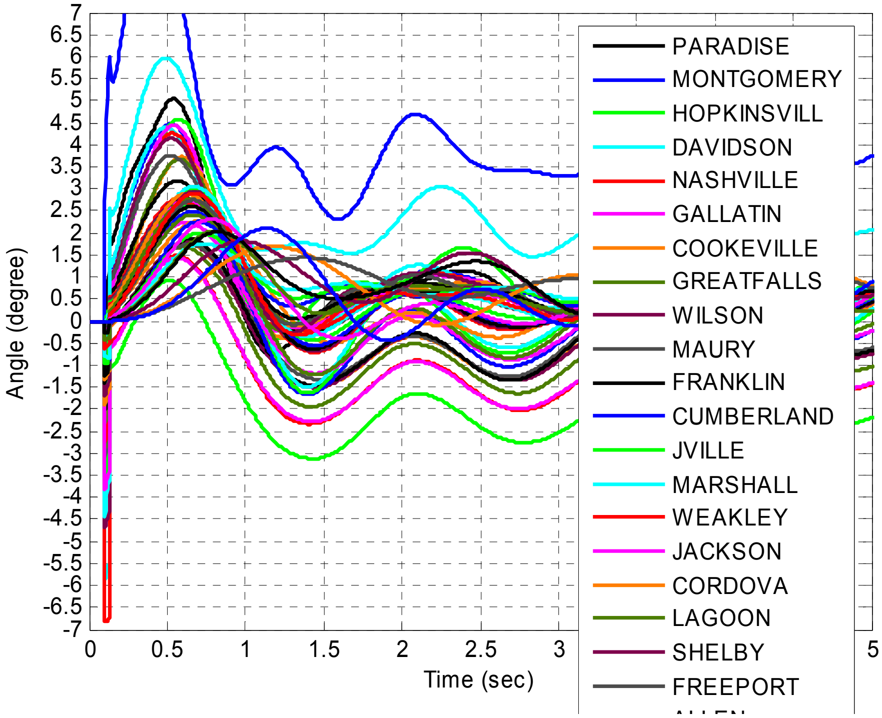

Figure 6.2 Phase angle from tripping the 500 kV Cumberland – Johnsonville line after a line fault

As can be seen in Figure 6.1 and Figure 6.2, the fault is applied at 0.1 second and cleared after 2 cycles (0.0344 second), and at the same time the line is opened. The whole simulation duration is 5 seconds and the simulation time step is 0.005 second. The time step and duration time are used in all the simulations for the line trip identification study. The initial rise in frequency at most places indicates that the voltage dependant load decreases due to the voltage drop in the fault area. Then the frequency at all places experiences oscillations. The fault and line trip also cause oscillations in bus angle as shown in Figure 6.2. In the discussion of this study, all angles are shifted to start from zero for the ease of comparison.

The second scenario considered is tripping a line without applying any fault. Take the line trip at the Cumberland – Johnsonville line as an example again. The simulation results are displayed in Figure 6.3 and 6.4. Both frequency and angle can be divided into two groups by their initial change at the line trip instant. The frequency at the power sending end increases because of the generator acceleration in this area, whereas the frequency at the power receiving end decreases due to the generator deceleration.

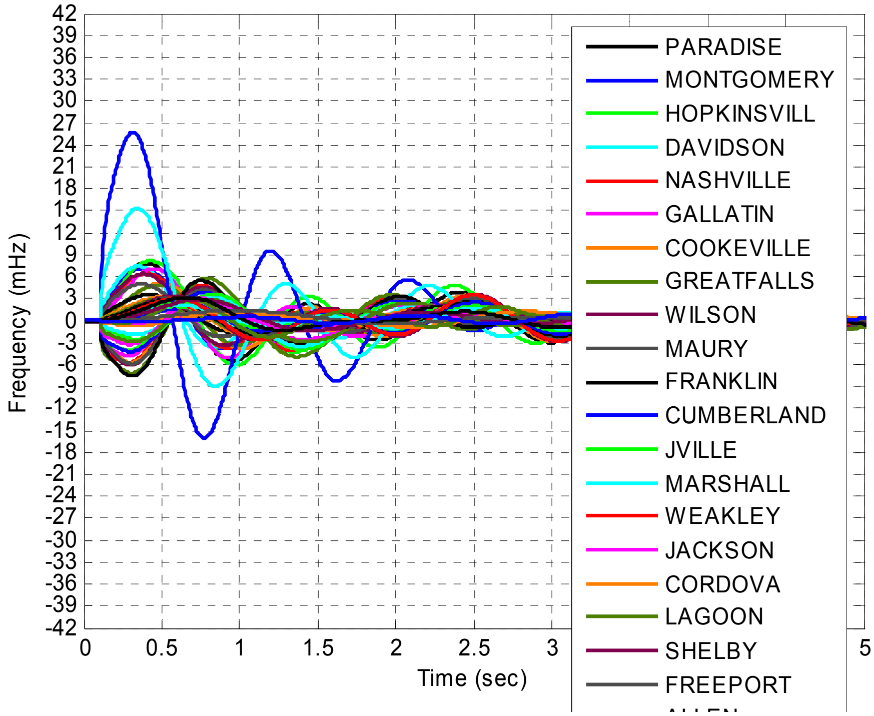

Figure 6.3 Frequency from tripping the 500 kV Cumberland – Johnsonville line without fault

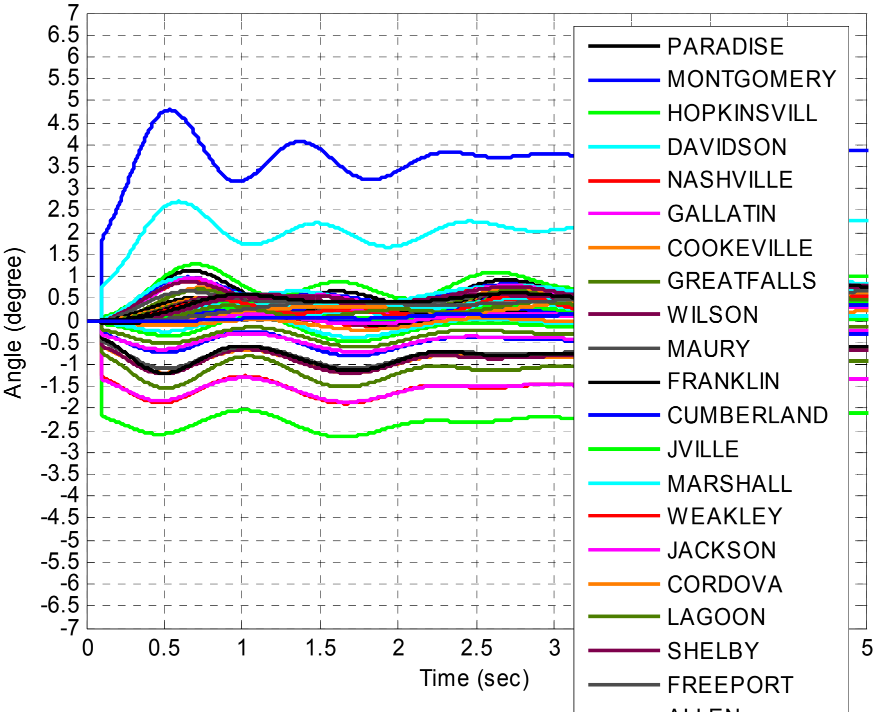

Figure 6.4 Phase angle from tripping the 500 kV Cumberland – Johnsonville line without fault

Apparently the magnitudes of frequency and angle oscillations in Figure 6.3 and Figure 6.4 are much less than in the previous case that involves a line fault. It demonstrates that a line trip following a fault is generally more severe than only tripping the line. Therefore, it is reasonable to focus on the scenario of single line trip without a fault in simulation for line trip detection study because the line trip following a fault usually causes larger variations in frequency and angle thus easier to detect. From this point on, this work will develop the line trip identification algorithm based on the simulation of single line trip without any fault.

Validation tests on the PSS/E simulation results have been conducted to verify whether the derivative of voltage phase angle agrees with the bus frequency since frequency can be obtained by taking the derivative of angle. Figure 6.5 and Figure 6.7 show the comparisons between frequency and angle derivative, phase angle and integrated frequency respectively for tripping the 500 kV Cumberland – Johnsonville line. The derivative of the phase angle in Figure 6.5 is approximated as the angle difference between two adjacent points along the time axis as in (6.1). Δt is the simulation time step which is 0.005 second in this case.

$$\frac{d\theta}{dt} \approx \frac{\Delta\theta}{\Delta t} \tag{6.1}$$

It is clear in Figure 6.5 that the angle derivative (shown as dotted lines) and the bus frequency (shown as solid lines) are very close except that there is a large spike in angle derivative at the instant of the line trip disturbance. It can be noticed in Figure 6.7 that the angle experiences a step change of different size at 0.1 second when the line is tripped. The large spike in the angle derivative is due to such state change demonstrated in the angle, which depends on the way that PSS/E deals with dynamic simulation. The duration of electrical transients may be expected to arise and disappear within a few milliseconds, while electromechanical transients take several seconds. PSS/E is primarily concerned with power system dynamic behavior associated with the energy stored in the rotating inertias of the system, where transients arise and decay away again within a period of a few seconds [64]. Hence, it is possible that the angle state change due to the line trip disturbance is treated as a sudden rise or drop at the trip incident. From this instant till the end of the simulation period (5 seconds in this case), the system dynamic responses reflected in the frequency and phase angle are mainly electromechanical transients.

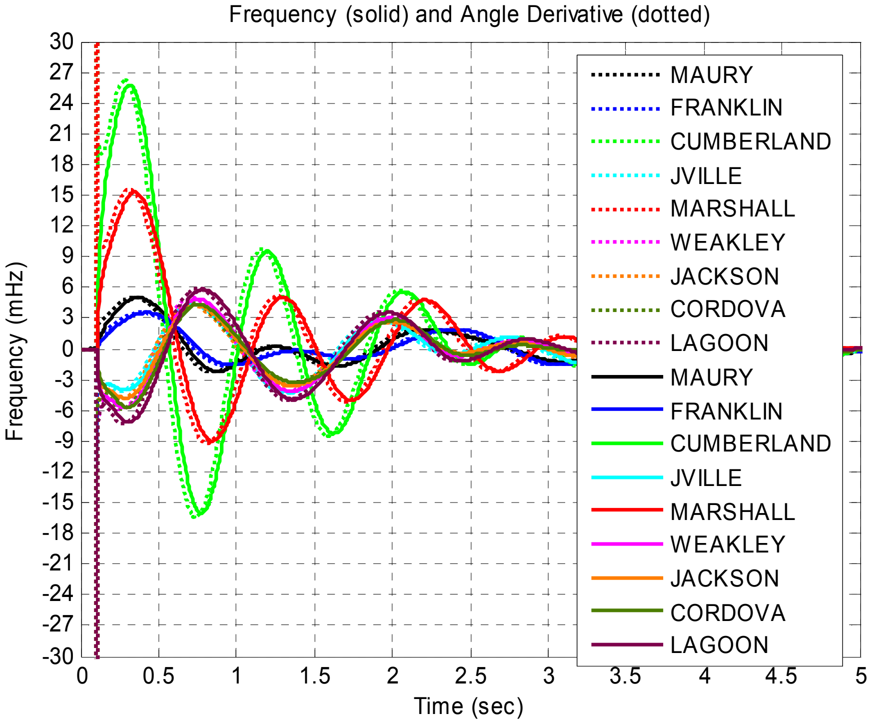

Figure 6.5 Frequency and angle derivative from PSS/E on tripping 500 kV Cumberland – Johnsonville line

The frequency obtained from the simulation is then integrated by the cumulative trapezoidal numerical integration technique as

$$\int_{t}^{t+\Delta t} f dt \approx \frac{f_t + f_{t+\Delta t}}{2} \times \Delta t \qquad (6.2)$$

The integrated frequency in Figure 6.6 does not show any step changes at the moment of line trip as in the phase angle but it includes the oscillatory transients, which indicates the frequency includes the information of the electromechanical responses. After adding the initial angle changes to the integrated frequency at each bus, the integrated frequency is then very close to the phase angle output as shown in Figure 6.7.

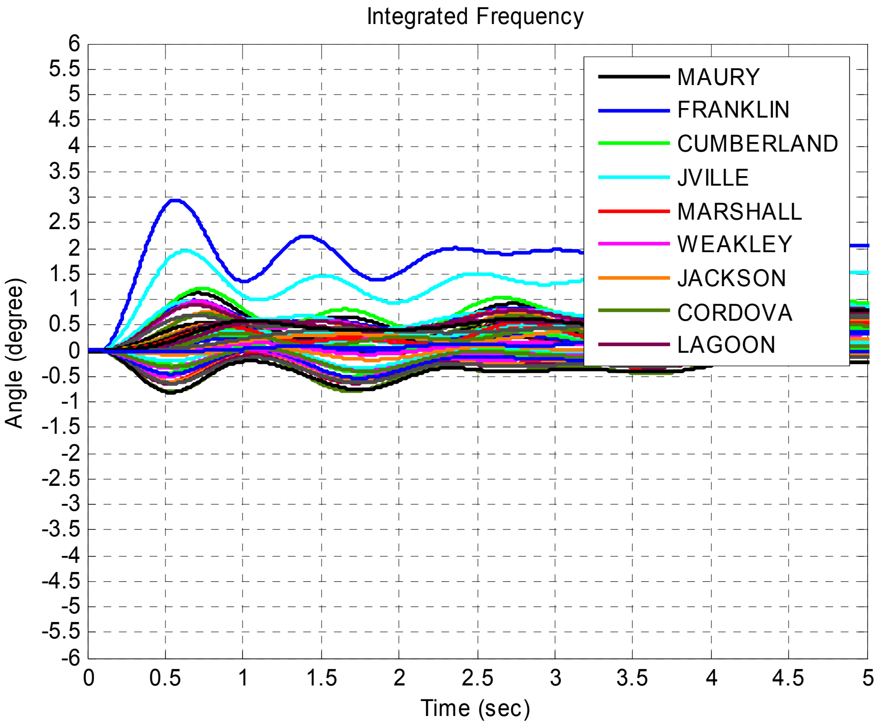

Figure 6.6 Integrated frequency from PSS/E on tripping 500 kV Cumberland – Johnsonville line

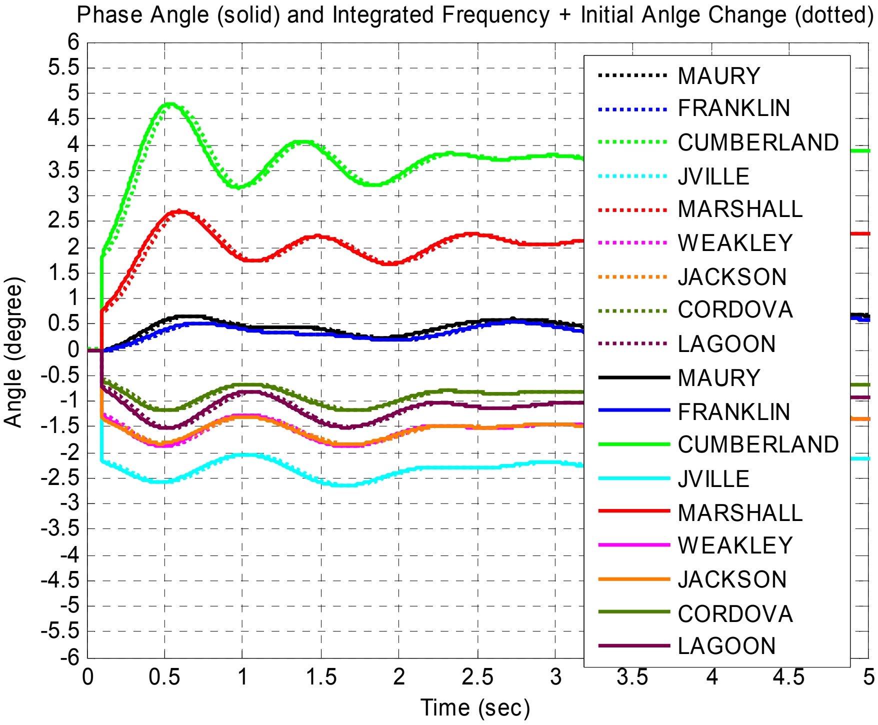

Figure 6.7 Phase angle and integrated frequency plus initial angle state change from PSS/E on tripping 500 kV Cumberland – Johnsonville line

This test also shows that the bus phase angle can be a very useful parameter for line trip identification. If the DC power flow model is considered, then

$$\Delta\mathbf{P} = \mathbf{B'}\,\Delta\boldsymbol{\theta} \tag{6.3}$$

$B'_{ik} = -\frac{1}{x_{ik}}$, assuming a branch from i to k (zero otherwise)

$$B'_{ii} = \sum_{k=1}^{N} \frac{1}{x_{ik}}$$

It can be obtained that

$$\Delta\boldsymbol{\theta} = \mathbf{B'}^{-1}\,\Delta\mathbf{P} \tag{6.4}$$

where $\Delta\mathbf{P}$ is the vector of the changes in bus real power injections, $\mathbf{B'}$ is the bus susceptance matrix, and $\Delta\boldsymbol{\theta}$ is the vector of bus angle changes, x_{ik} is the reactance of the branch from i to k, and N is the number of buses [65]. When a line is tripped, the pre-outage power flow on the line will be redistributed to other lines in the system, which causes a change in angles at all buses. That is, the change in angles directly reflects the effect of a line outage. It is observed that the largest angle changes occur right at the ends of the tripped line, which may not hold for frequency.

6.1.2 Line Trip Signatures in Real Measurements

As an example, Figure 6.8 and Figure 6.9 show the real measurements form FDRs for a line outage at the same 500 kV Cumberland – Johnsonville line in the above simulation case. This 500 kV line trip event occurred at 19:03:19 UTC on April 11, 2007. The real angle measurements are similar with the simulation results in that the line trip caused oscillations in frequency and changes in phase angle. The magnitudes of oscillations resulting from the line trip are different in the simulation and in the real data due to several possible reasons. One is that in the simulations the monitoring points are 500 kV buses, whereas the FNET data are taken from the distribution network. The difference is expected also because the simulation model is an approximation of the real complicated system.

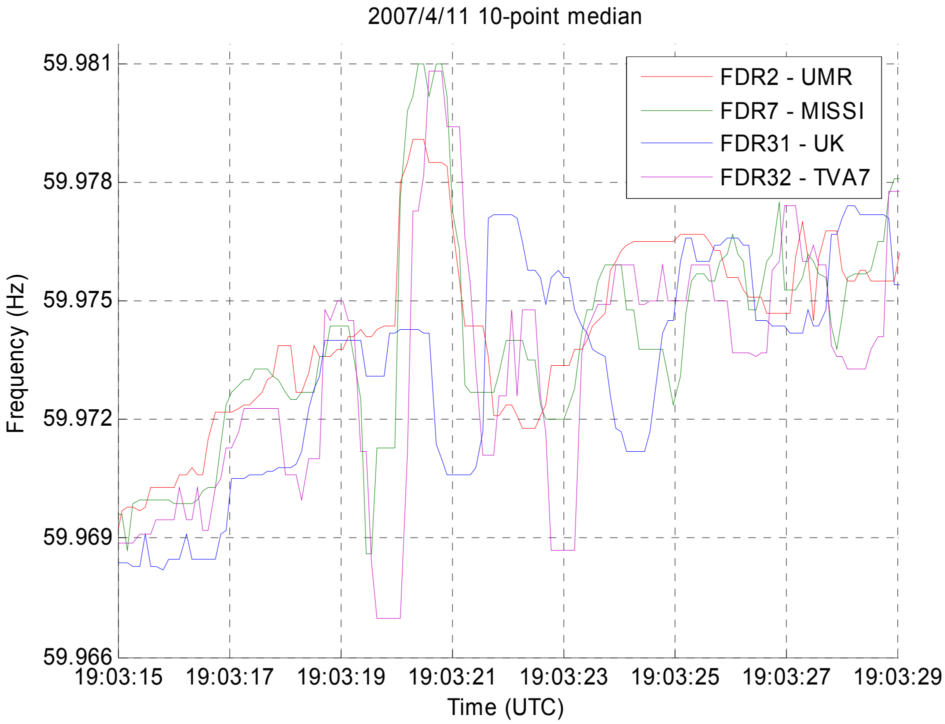

Figure 6.8 Frequency measurements for the line trip at the 500 kV Cumberland – Johnsonville line

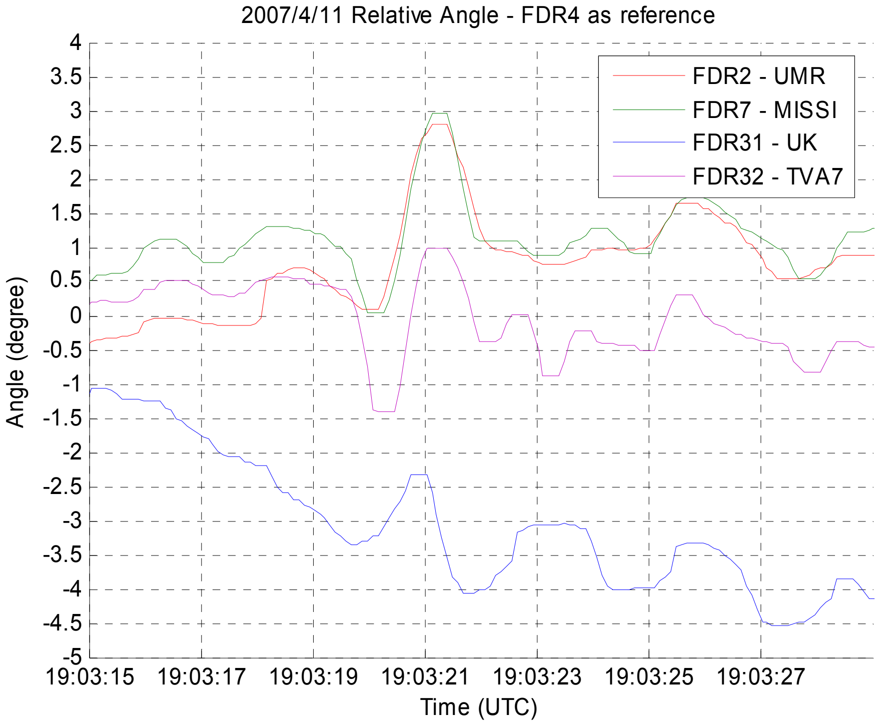

Figure 6.9 Relative angle for the line trip at the 500 kV Cumberland – Johnsonville line (FDR4 as reference)

Another noticeable difference is that the phase angle in the simulation experiences a sharp step change at the line trip instant, while no such change has been observed in the real measurements. The FDRs' output data rate is 10 samples per second hence not targeting the detection of fast electromagnetic transients within several milliseconds. However, the information of the electromechanical transients resulting from the disturbances is well-represented in the measurements.

It has been discussed that the phase angle change directly reflects the power flow transfer in the transmission lines after a line outage. Thus the phase angle measurements can be utilized as detection signals for the purpose of line trip identification.

6.2 500 kV and 161 kV Line Trip Detection

As is shown in Figure 6.5, the transmission network in the TVA area is mostly composed by two voltage levels: 500 kV and 161 kV. The impact of a 500 kV line trip is generally larger than the outage at a 161 kV line since a 500 kV line usually carries more power than a 161 kV line.

6.2.1 500 kV Line Trip Detection Simulation Study

The 63 identified 500 kV transmission lines are tripped one at a time with PSS/E. The frequency and angle at the 52 selected buses are monitored. All the simulation results are similar as in Figure 6.3 and Figure 6.4 although the magnitudes of frequency oscillations and angle changes may be different.

The power flow directions in the 500 kV transmission network are also examined in PSS/E in order to study the power transfer in the system (Figure 5.22). For the transmission corridor in the east of the TVA system, the power flow in PSS/E simulation follows the direction from south to north because there are several nuclear and hydro power plants such as Watts Bar and Sequoyah in the south part of Tennessee, thus power is transferred from the generation source to the load area. If, for example, the sensors located close to this corridor detect angle changes that are out of phase, it can be decided that the tripped line is along this transmission corridor. The locations of the sensors can help to decide at which section of the transmission corridor the line is tripped. However, the 500 kV transmission network is not simple one-direction corridor everywhere in the TVA system as shown in Figure 5.22, which increases the complexity of line trip identification.

As mentioned above, sixty-three 500 kV transmission lines in the TVA region are identified in the PSS/E model and they are tripped one at a time to study the line trip signatures as well as the detection capability of the proposed FDR placement. The frequency and phase angle of the monitored buses are examined and the magnitude of the first swing in frequency and angle are used as criteria to decide if a certain line trip is observable. The visibility threshold is set to be 3 mHz for frequency and 0.5 degree for angle. The thresholds are decided based upon the observation of the measurement sensitivity of the FDR units. Any values below the thresholds are likely to be disguised by noises or dynamics in the distribution network which is beyond the focus of this study. The summary of the simulation result is listed in Table 6.1.

Table 6.1 Summary of simulation on 500 kV line trips in the TVA system

Total	Observable	In frequency and angle	In angle only	Special
63	54	48	6	2

A line outage is considered observable if there exist at least 2 monitoring locations where the first swing peak of frequency and/or angle oscillations exceeds the thresholds. Among the 63 cases processed in PSS/E, 54 are observable and 48 cases can be observed in both frequency and angle, while 6 cases can only be seen in angle according to the thresholds. The simulation summary shows that up to 85.7% of the 500 kV line outages can be observed by the proposed monitoring locations either in frequency or angle or both. It is also observed that the selected monitoring channels can not see a certain line outage if the real power flow on the line is less than 50 MW. Generally at the same voltage level the less power flow on the line, the smaller variation in frequency and phase angle will be induced by the tripping of the line. Although the FDRs are taking measurements at the distribution voltage level thus noises are present in the measurements, most of 500 kV transmission lines are expected to be detected with the 52 FDRs.

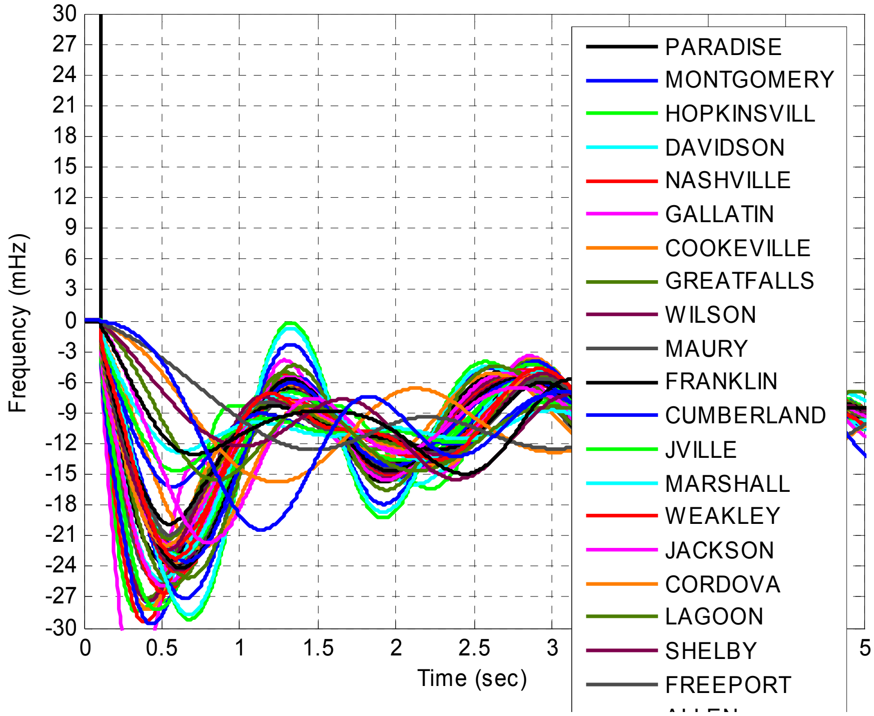

Figure 6.10 Frequency form PSS/E on tripping the 500 kV Paradise – Montgomery line

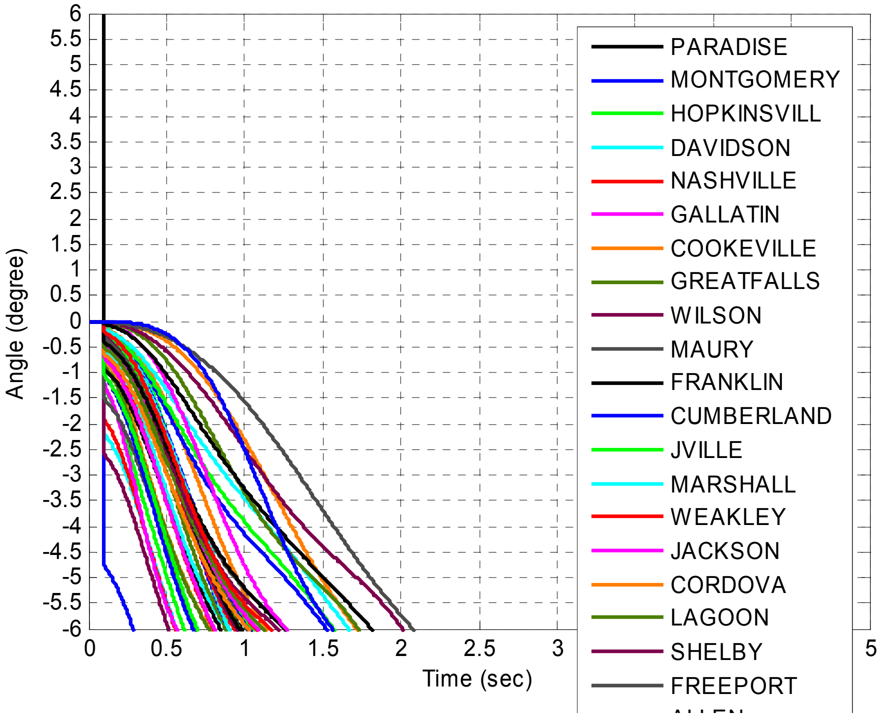

Figure 6.11 Phase angle form PSS/E on tripping the 500 kV Paradise – Montgomery line

Tow special cases are observed during the simulation process in which the frequency and angle are totally different from other cases as in Figure 6.3 and Figure 6.4. One is the tripping of the Paradise – Montgomery line, which results in the separation in both the angle and frequency as shown in Figure 6.10 and 6.11. Paradise is a coal generating plant and the Paradise – Montgomery line is the major route to transfer the generated power out to other areas. Therefore, the tripping of this line looks like a generation loss to the rest of the system. Frequency and angle at all the monitoring locations decrease after the loss of the line, whereas the frequency and angle observed at the Paradise bus goes up rapidly due to machine acceleration.

For the similar reason, the tripping of the Raccoon Mountain – Widows Creek line has the effect of generation loss at Raccoon Mountain, a hydro plant that is connected to Widows Creek through a 500 kV line. The frequency and angle outputs from PSS/E are shown in Figure 6.12 and Figure 6.13. The above two cases show that a line trip event may appear to be generation loss in the measurements, but this study will focus on the typical line trip events with similar signatures as described in section 6.1

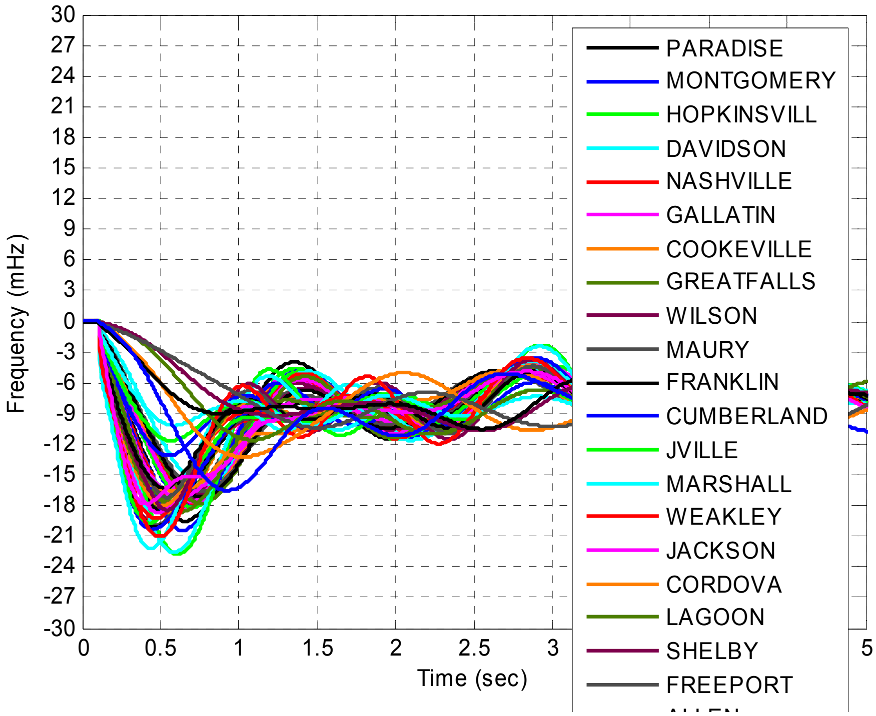

Figure 6.12 Frequency form PSS/E on tripping the 500 kV Raccoon Mountain – Widows Creek line

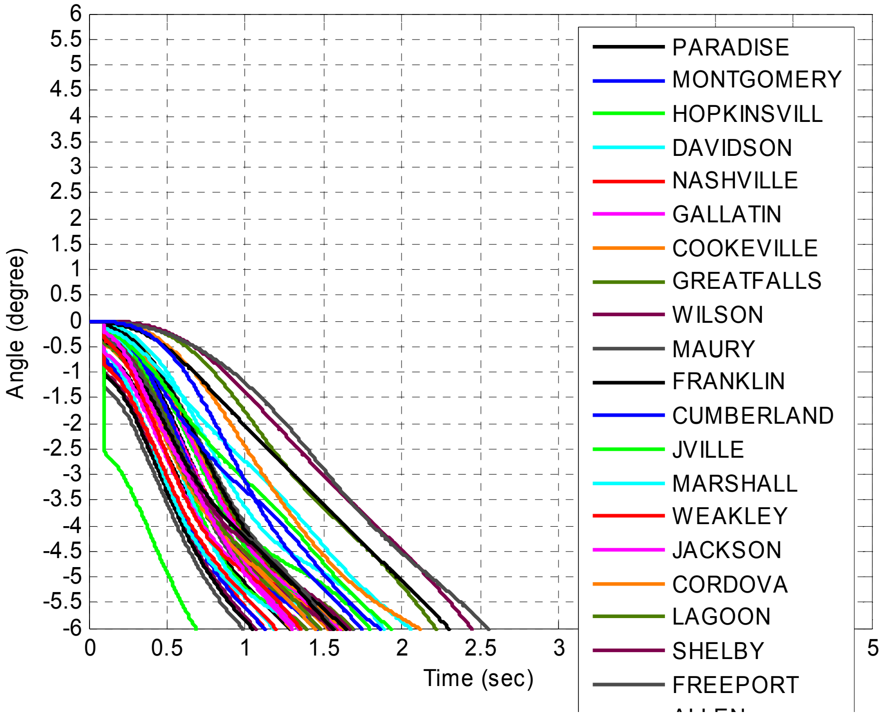

Figure 6.13 Phase angle form PSS/E on tripping the 500 kV Raccoon Mountain – Widows Creek line

6.2.2 161 kV Line Trip Detection Simulation Study

The FDR placement strategy proposed in chapter 5 is mainly aimed at detecting the 500 kV transmission lines. The sensitivity study in chapter 5 shows that a line outage at 161 kV is less severe than that at higher 500 kV level. Hence a lower detection rate of the line outages at 161 kV is expected with the 52 FDRs. It is desirable to answer such questions as what is the visibility of the line outage at 161 kV by the proposed sensor density and what is the minimum number of sensors required to monitor the whole 161 kV network in the TVA area. A summary of the voltage levels of the TVA power system identified in the PSS/E simulation model is listed in Table 6.2. The 500 kV and 161 kV levels are highlighted in red. One can see most of the transmission lines (1253 out of 1552) in the TVA system are at 161 kV.

Table 6.2 Summary of the voltage levels in the TVA transmission system identified in PSS/E

Voltage level (kV)	# of lines	# of buses
500	**70**	**50**
345	2	1
230	12	11
161	**1253**	**964**
138	2	3
115	42	37
69	148	132
46	7	15
23	6	11
13.8	2	72
26	1	2
13.2	4	127
13	3	23
12.47	1	2
2.3	1	4
Total	1552	1454

In the EI model in PSS/E, the range of loading conditions of the 161 kV lines is wide from 0.3 to 619.4 MW with the average at 71 MW and the median at 51 MW. The loading conditions of the 161 kV lines in PSS/E model are summarized in Figure 6.14. It can be seen that the majority of the 161 kV lines carry a real power flow less than 50 MW.

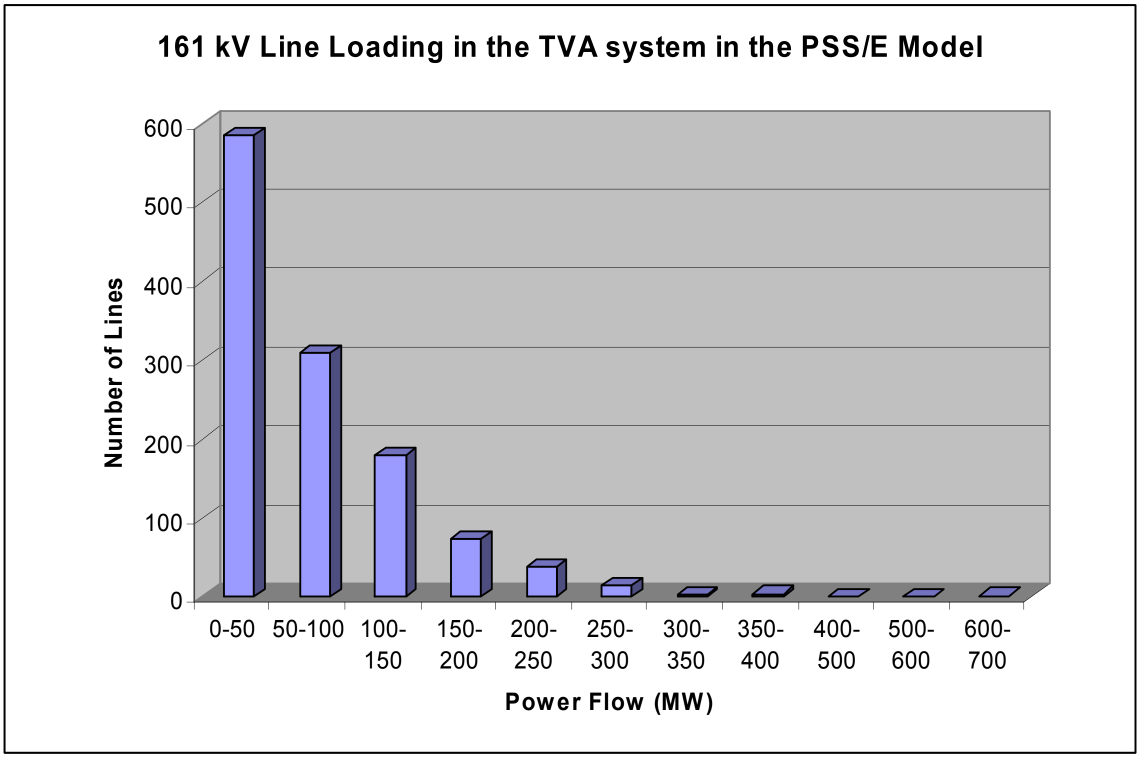

Figure 6.14 161 kV line loading conditions in the TVA system in PSS/E

In order to study the capability of the 52 sensors to detect the line trips at 161 kV, thirty-six 161 kV lines are selected in the manner that the lines are spread out in the TVA system for different loading conditions. The active power flow on the selected lines ranges from 2.7 MW to 328.8 MW with the average at 127.76 MW, larger than the average power flow of all the 161 kV lines. The buses at the same 52 locations but lower voltage levels are also selected (161 kV or lower). The simulation scenario and observability thresholds are the same as in the 500 kV line trip simulations. The simulation results are shown in Table 6.3 and Table 6.4. Out of the 36 simulation cases 16 can be observed either in frequency or angle or both, while 5 of the observable cases can be seen only in angle and 8 of them are directly monitored with the channels on the line ends. Table 6.4 shows that only a small number of 161 kV lines carrying less than 50 MW power flow can be observed by the 52 sensors when they are tripped. As the frequency and angle excursions caused by the 161 kV line trip are smaller compared to those caused by a 500 kV line trip, a smaller percentage of line trips at 161 kV can be detected by the 52 sensors. We are aware that the selected lines may not be comprehensive to represent all the conditions of the 161 kV lines. However, the analysis provides some sense of the detection capability of the proposed measurement density.

Table 6.3 Summary of simulation results of the 161 kV line trips

Total	Observable	In frequency and angle	In angle only	Line ends monitored
36	16	11	5	8

Table 6.4 The power flow range and observable 161 kV line trips in the PSS/E simulation

MW flow	# of selected lines	# of observable cases
0-50	8	1
50-100	10	4
100-150	8	6
150-200	5	2
200-250	4	3
250-300	1	0
Total	36	16

The above analysis demonstrates that 52 FDRs are not adequate to monitor the whole TVA 161 kV transmission network. To answer the question that how many sensors are required to observe the 161 kV line outages more simulations have been performed. The TVA system is divided into 6 areas: northeast, northwest, north central, central, southeast and southwest. The selected lines in each area reflect different loading conditions of the 161 kV lines in the area and 20 lines in total are selected as listed in Table 6.5.

Table 6.5 Selected 161 kV line trip cases for the estimation of required FDR number

Area	From bus #	From bus	To bus #	To bus	MW flow
Northeast	97	Volunteer (500 kV)	98	Volunteer	519.4
	98	Volunteer	458	N Knoxville	328.8
	98	Volunteer	468	Morristown	156.2
	98	Volunteer	1159	Hinds Valley	60.4
	457	N Knoxville	98	Volunteer	26.6
Northwest	16	Marshall	125	Calvert	135.2
	125	Calvert	126	S Calvert	77.4
	125	Calvert	572	E Calvert	5
North Central	71	Wilson (500 kV)	72	Wilson	375.1
	72	Wilson	372	Hermitage	259.4
	72	Wilson	1195	Central Pike	140.3
	72	Wilson	1020	Gladeville	18.9
Central	66	Widows Creek	1046	Bryant	117.2
	418	Morganville	1510	Wallaceville	71.4
	66	Widows Creek	1048	Reese Fry	2.7
Southeast	281	Limestone	273	Jetport	273.3
	281	Limestone	295	N Huntsville	145.7
	281	Limestone	362	Peach	72
Southwest	148	Clarksburg	152	South Jackson	115.5
	152	South Jackson	1092	Dancyville	27.9

All the 1626 identified buses around the TVA system in the PSS/E model are monitored. The simulation and analysis procedures are as follows. First, trip one selected line in PSS/E. Figure 6.15 shows the detailed one-line diagram of the system around the 161 kV Widows Creek – Oglethr line. The red arrow indicates the line flow direction and the real power flow before the line is tripped is 154.7 MW.

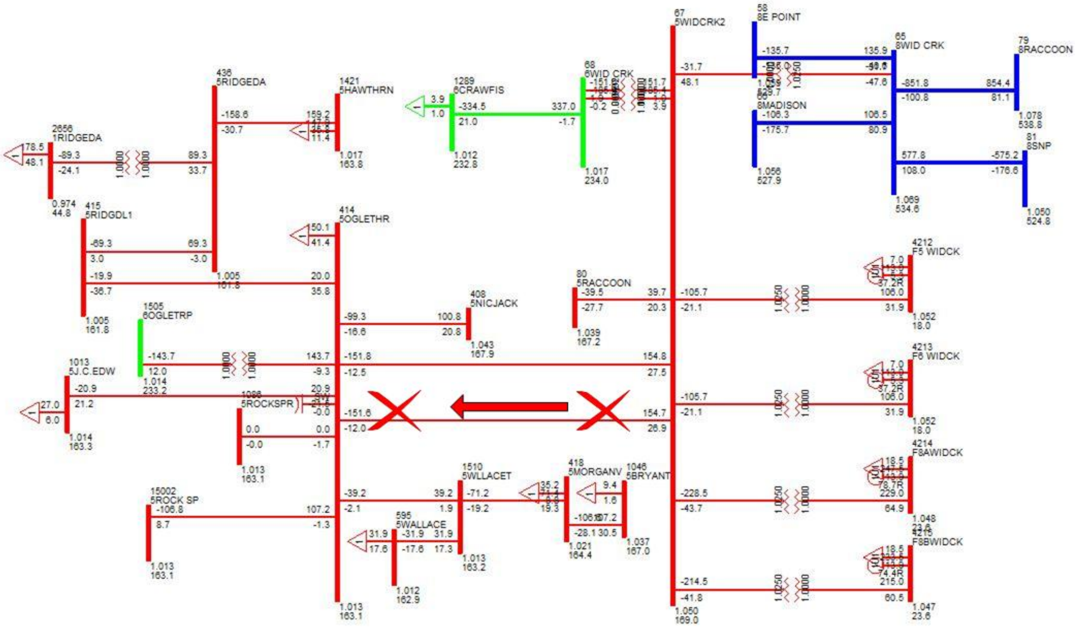

Figure 6.15 Partial one-line diagram of the EI system showing the tripping of the 161 kV Widows Creek – Oglethr line (The red arrow indicates the direction of the power flow on the line.)

Then the peak frequency and angle values during the first swing are found. The magnified frequency and angle outputs are shown in Figure 6.16 and 6.17. The number of buses where the frequency magnitude is greater than 3 mHz is 14 in this example. The percentage of observable locations to all the monitoring locations is

$$14/1626 = 0.86\%$$

which indicates the observing capability of one sensor.

The required number of sensors can be estimated as

$$1/0.86\% = 116$$

so that at least one sensor sees the line trip. For the purpose of line trip detection at least 2 FDRs should observe a disturbance, the required FDR number therefore is

$$\text{The required FDR number} = 116 \times 2 = 232$$

Similarly, the number of required FDRs can be estimated from angle outputs of the simulations. The number of buses where the angle peak during the first swing is larger than 0.5 degree is 16 and the estimated number of FDRs required to detect the line outages is 203.

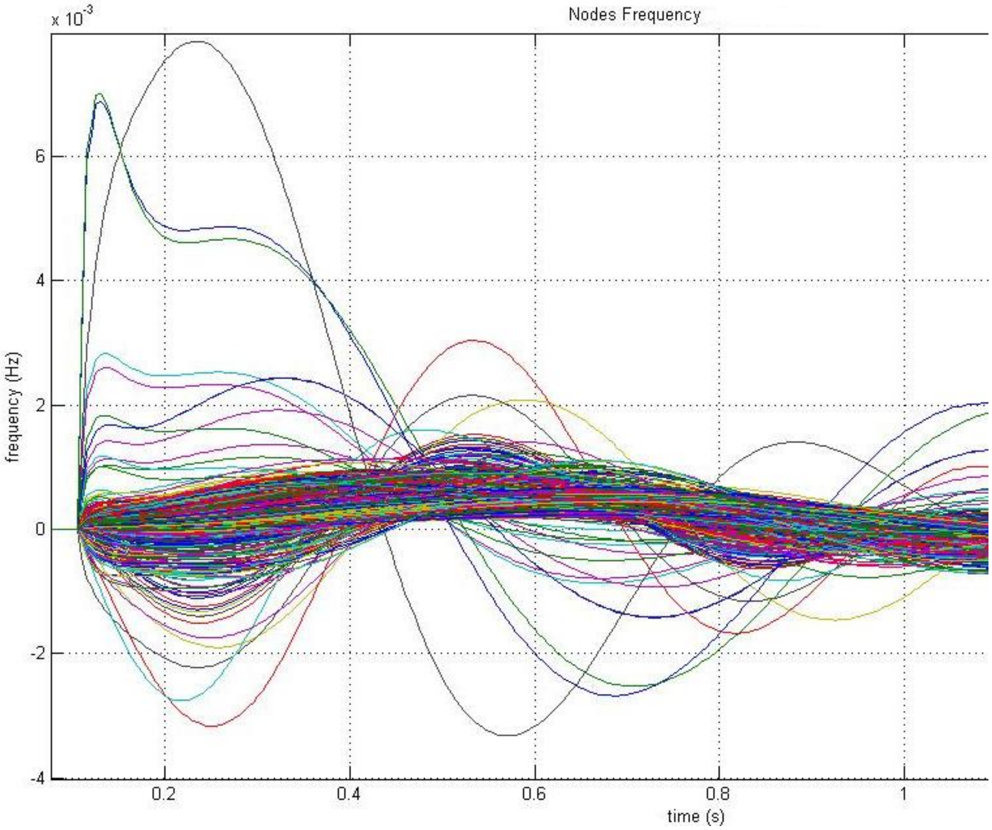

Figure 6.16 Magnified frequency after tripping the 161 kV Widows Creek – Oglethr line

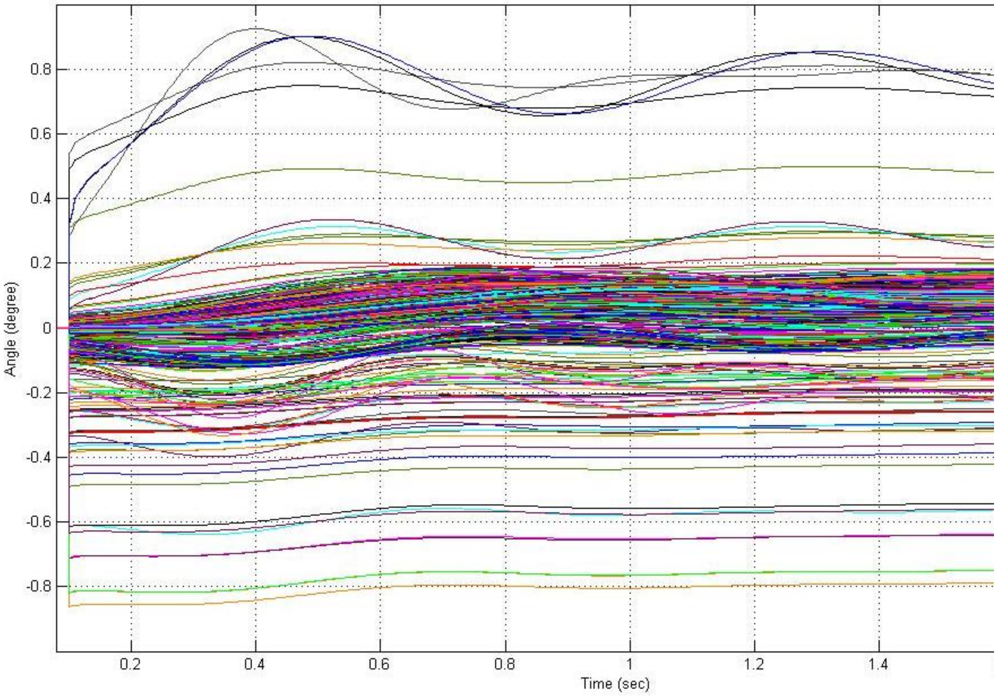

Figure 6.17 Magnified angle after tripping the 161 kV Widows Creek – Oglethr line

All the selected 20 cases are processed by the above method. The estimated numbers of FDRs required detecting the 161 kV line trip in the TVA system are listed in Table 6.6. Six cases are not observable according to the frequency and angle thresholds. 70% of the cases (14/20) are observable in frequency and / or angle. Considering the sensor numbers estimated from frequency and angle together, the average is 119. In other words, at least 119 FDRs are required to observe up to 70% of the 161 kV lines when a single line is tripped in the TVA system.

Table 6.6 Estimation of the FDRs required to detect the 161 kV line trips in the TVA system (N: not observable)

From bus	To bus	MW flow	# est. from freq.	# est. from angle
Volunteer	Volunteer (500 kV)	519.4	19	20
Volunteer	N Knoxville	328.8	88	37
Volunteer	Morristown	156.2	65	50
Volunteer	Hinds Valley	60.4	N	192
N Knoxville	Volunteer	26.6	N	N
Marshall	Calvert	135.2	N	N
Calvert	S Calvert	77.4	N	N
Calvert	E Calvert	5	N	N
Wilson	Wilson (500 kV)	375.1	11	14
Wilson	Hermitage	259.4	62	39
Wilson	Central Pike	140.3	121	130
Wilson	Gladeville	18.9	N	N
Widows Creek	Bryant	117.2	62	71
Morganville	Wallaceville	71.4	96	126
Widows Creek	Reese Fry	2.7	N	N
Limestone	Jetport	273.3	N	192
Limestone	N Huntsville	145.7	N	204
Limestone	Peach	72	N	217
Clarksburg	South Jackson	115.5	71	37
South Jackson	Dancyville	27.9	N	813

6.3 Line Trip Identification

As mentioned at the beginning of this chapter, the objective of the line trip identification algorithm is to locate the tripped line by utilizing the wide-area frequency and phase angle measurements. The current location estimation algorithm in the FNET situation awareness system is using frequency delay of arrival to locate a generator trip. The method can be described with an example shown in Figure 6.18 and Figure 6.19. The event was a generator trip at the Paradise plant on October 26, 2006. As shown in Figure 6.18, there exist measurable delays among the transient frequencies measured at different locations. The delays are an indication of the propagation of the electromechanical wave in the power system. With the delays and the location information of the measurements, the source of the disturbance can be back traced.

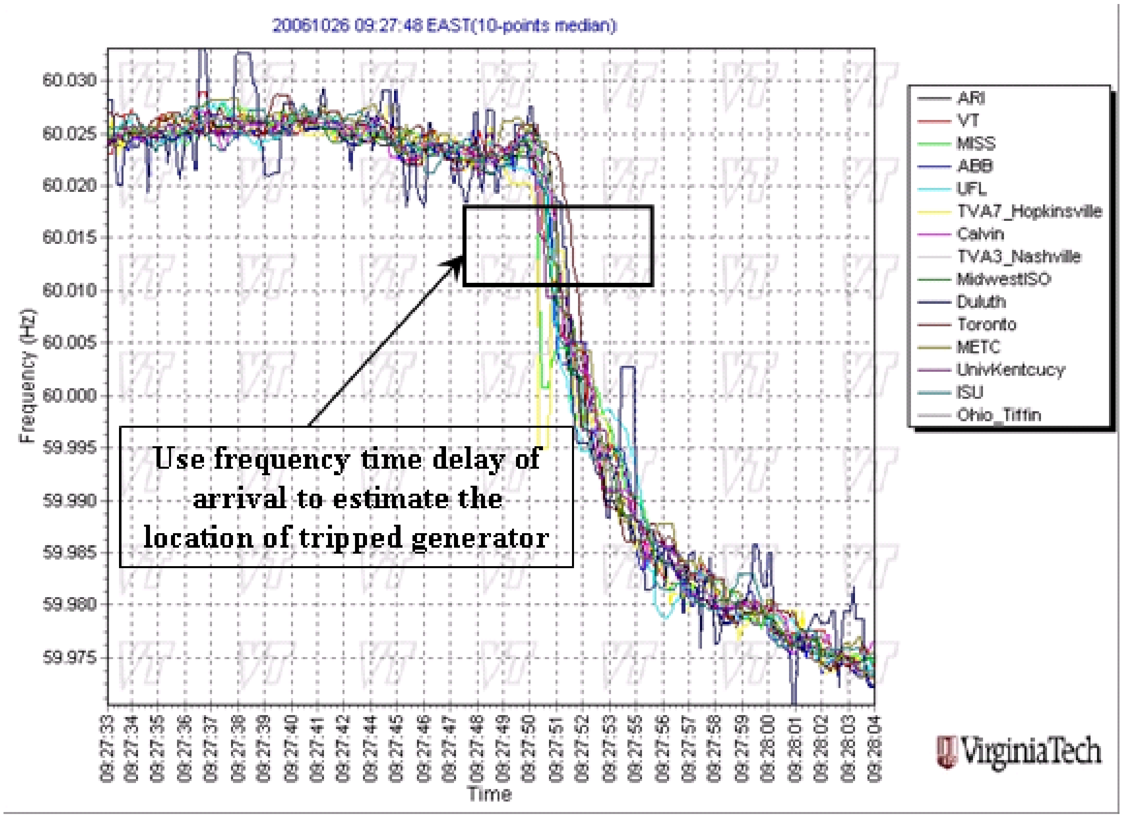

Figure 6.18 An example showing the frequency delay of arrival

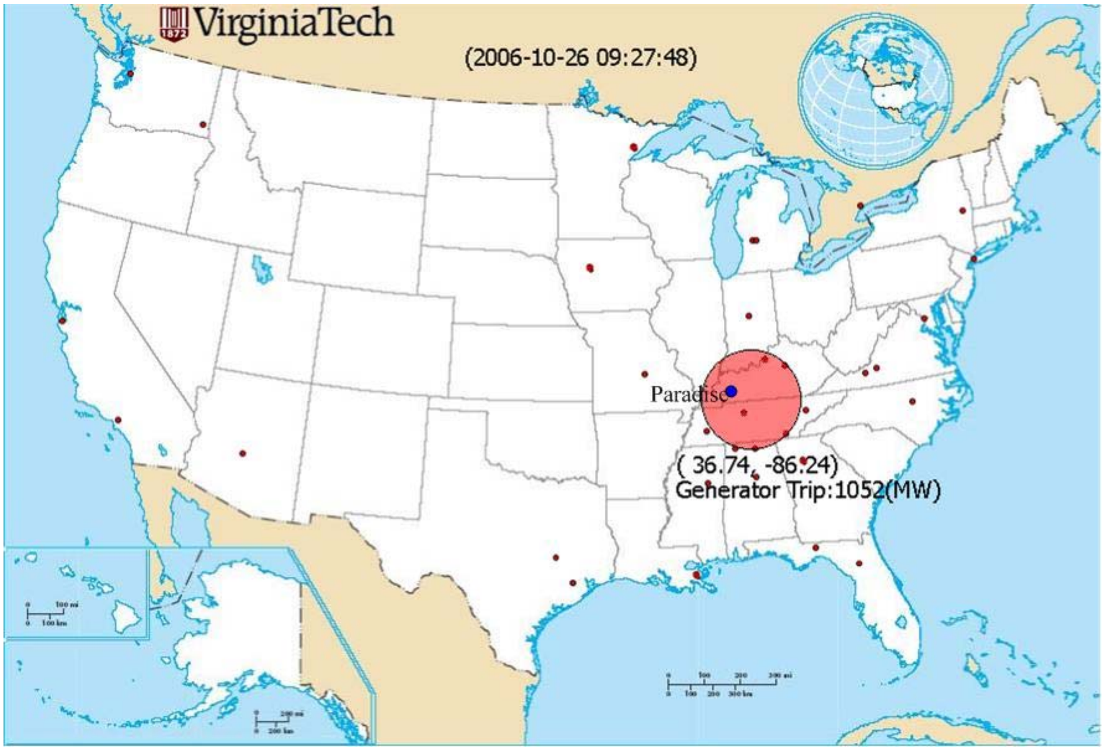

Figure 6.19 The estimated disturbance location of the example. (The estimated location is shown as the red circle. The real location is shown as the blue dot. Map source: USGS)

However, this method can not be easily employed in the identification of line trip events because line trip disturbances have different event signatures as generation loss events. In a generation trip disturbance the frequency all over the system experiences a sharp decline, whereas a line trip disturbance usually causes local frequency oscillations with limited impact to the bulk system. Other difficulties in identification of line outages include limited number of FDRs in the field; and lack of information about the loading conditions in real power systems.

6.3.1 Line Trip Identification Algorithm

As of the time this report was written, the 40 FDRs had not been deployed yet. Taking into account of the limited FDR coverage and confirmed line trip events, an algorithm based on the simulation results and measurements is considered to be a practical approach.

The first important step is feature extraction as to define the features that uniquely describe a line trip case. It has been discussed that the phase angle change indicates the active power redistribution due to the loss of a line. For a certain line outage, the resulted angle changes at different locations are usually different. Moreover, the outage of different lines may cause different angle change amount at a certain location. Therefore, a combination of the angle change magnitudes at all the monitoring locations can be taken to form a feature vector for a certain line trip.

This work proposes a simple line trip identification algorithm that locates a line outage by matching the feature vectors obtained from real measurements with those in the line outage case library constructed based on the PSS/E simulation. With the increase of the FDR coverage and confirmed events, it is possible to build the signature library based on the line trip cases observed in measurements.

To construct the signature database, all the sixty-three 500 kV lines identified in the TVA system are tripped one at a time, then the peak frequency and angle values from each monitoring channel are extracted and stored in a vector as the signature of the line trip. The flow chart to form the line trip case library is shown in Figure 6.20.

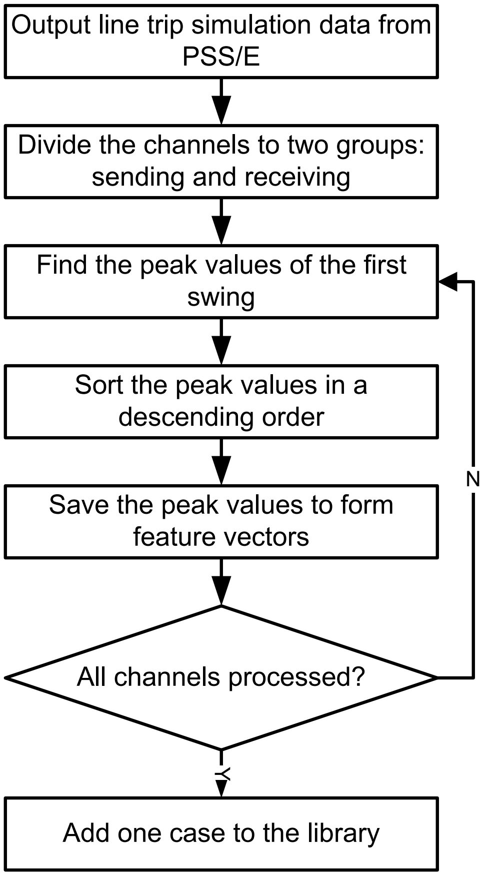

Figure 6.20 Flowchart of building the line trip case library from simulation data

After the frequency and angle outputs are obtained from the PSS/E simulation, the monitoring channels are divided into two groups based on the sign of the initial change. The group with initial rise is identified as the power sending group and that with initial drop falls into the power receiving group. The division of the groups is to find correctly the peak values of the first swing. Then the peak values are saved in a feature vector together with the location where the measurement is taken. All the observable 500 kV line trip cases are processed this way and a signature library is hence formed.

The method to employ this signature library in line trip detection is illustrated in Figure 6.21. Once the line trip trigger detects a line trip, the identification program is activated. The first 3 steps in Figure 6.21 are data pre-processing that may have been processed during line trip detection. If so, the program can start with finding the angle change magnitudes based on the relative angle directly.

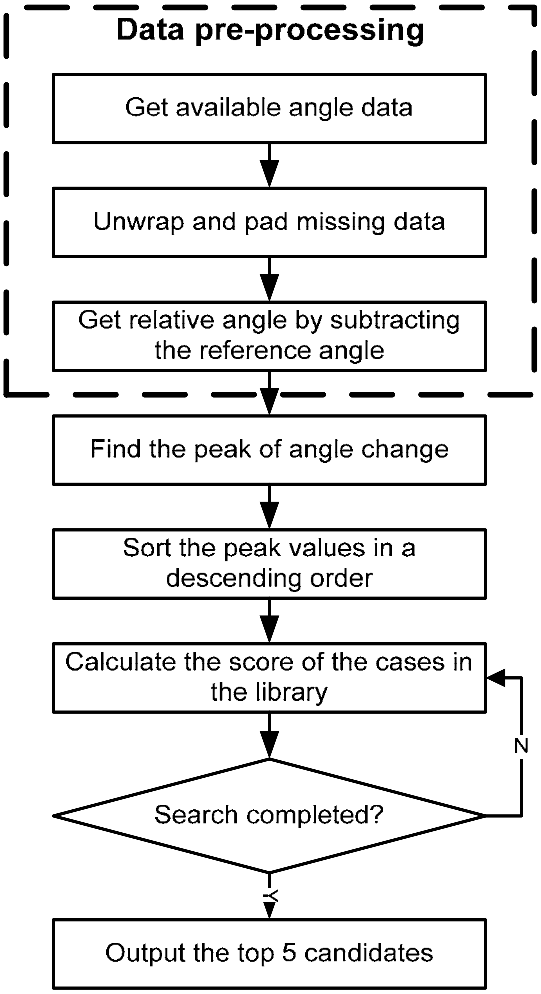

Figure 6.21 Line trip identification procedures

The procedure to find the angle change peak is visualized in Figure 6.22. t_1 is the time when the line trip is detected and t_2 is the time when the relative angle reaches its peak. The time window displayed in the figure is 30 seconds since the output data rate of an FDR is 10 samples per second. The pseudo code for the angle peak detection is as follows, where $\Delta\theta$ is the angle change value and θ_{pre} is the pre-disturbance angle value which is approximated as the average value over 10 samples before the detection time.

```
$t_2 = t_1 + 2$
$\theta_{pre} = mean(\theta(t_1 - 10 : t_1))$
$\Delta\theta' = \infty$
While ( $\Delta\theta' > 0$ )
        $\Delta\theta' = sign(\theta(t_2) - \theta_{pre}) \times (\theta(t_2 + 1) - \theta(t_2))$
        $t_2 = t_2 + 1$
$\Delta\theta = abs(\theta(t_2) - \theta(t_1))$
```

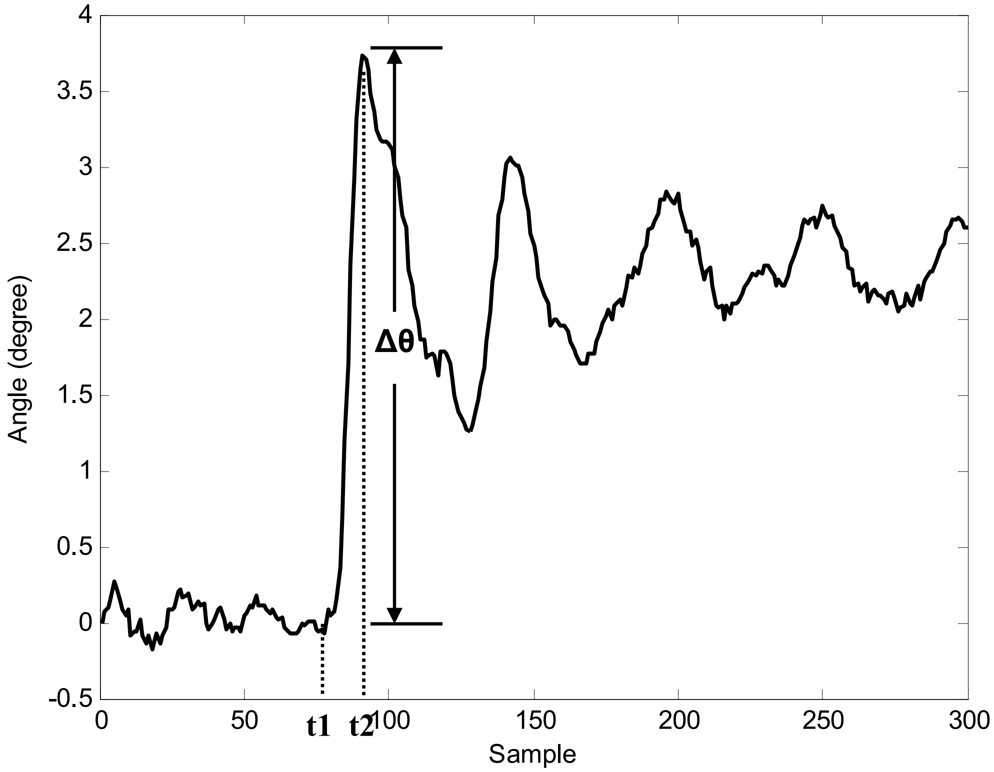

Figure 6.22 Angle peak detection from the relative angle

Once the angle change peak value $\Delta\theta$ is found for each available FDR, an observed feature vector is formed in which the angle peak values are sorted in a high to low order in the same format as the signature library. In some instances not all FDRs are reporting valid data during a certain event. Therefore the program selects only the corresponding channels in the signature library for comparison.

At lease one criterion is required to describe how close an observed line trip disturbance matches those in the signature library. In this work, the normalized Euclidean distance (ED) is used for this purpose [66]. The ED is selected because its computation is simple and the computation time is currently not an issue as the size of observation feature vectors is small due to the limited number of available FDRs for a single line trip incident. For an observed feature vector $\Delta\theta_{observed}$ of a line trip disturbance

$$\Delta\theta_{observed} = \left[\Delta\theta_{1,observed} \quad \cdots \quad \Delta\theta_{n,observed}\right]^T \tag{6.5}$$

where n is the number of available FDRs during the event, the corresponding signature vector $\Delta\theta_{library}$ from the case library is

$$\Delta\theta_{library} = \left[\Delta\theta_{1,library} \quad \cdots \quad \Delta\theta_{n,library}\right]^T \tag{6.6}$$

Normalize the vectors by dividing by their norms

$$\Delta\theta_{observed-N} = \left[\Delta\theta_{1,observed} \quad \cdots \quad \Delta\theta_{n,observed}\right]^T \Big/ \left\|\Delta\theta_{observed}\right\|$$

$$\Delta\theta_{library-N} = \left[\Delta\theta_{1,library} \quad \cdots \quad \Delta\theta_{n,library}\right]^T \Big/ \left\|\Delta\theta_{library}\right\|$$

The two vectors represent two points in the $n-D$ space, $\Delta\theta_{observed-N}, \Delta\theta_{library-N} \in \Re^n$. The ED between the two points to the signature vector of the case l in the database is then calculated by

$$d_l = \sqrt{\left(\Delta\theta_{1,observed-N} - \Delta\theta_{1,library-N}\right)^2 + \ldots + \left(\Delta\theta_{n,observed-N} - \Delta\theta_{n,library-N}\right)^2} \tag{6.7}$$

The EDs are ranking criteria that quantify the closeness of an observed tripped line to the line outage cases in the database. Hence the best match is the case with the smallest ED value. The program then report 5 cases with the least EDs as the top five candidates of the possible lines.

6.3.2 Testing Examples

The method is tested with both simulation data and real measurements.

1. Test with PSS/E simulation data

Take the 500 kV Cumberland – Johnsonville line as an example. The map of the area around Cumberland is shown in Figure 6.23 and the test result is listed in Table 6.7. Sixteen channels are included in the test case to be identified since it is likely that not all FDRs report data in every event. The program finds exactly the tripped line as the top candidate with a zero ED as expected. Other candidate lines are close to the tripped line electrically, which confirms the relationship between the angle changes and the location of the tripped line.

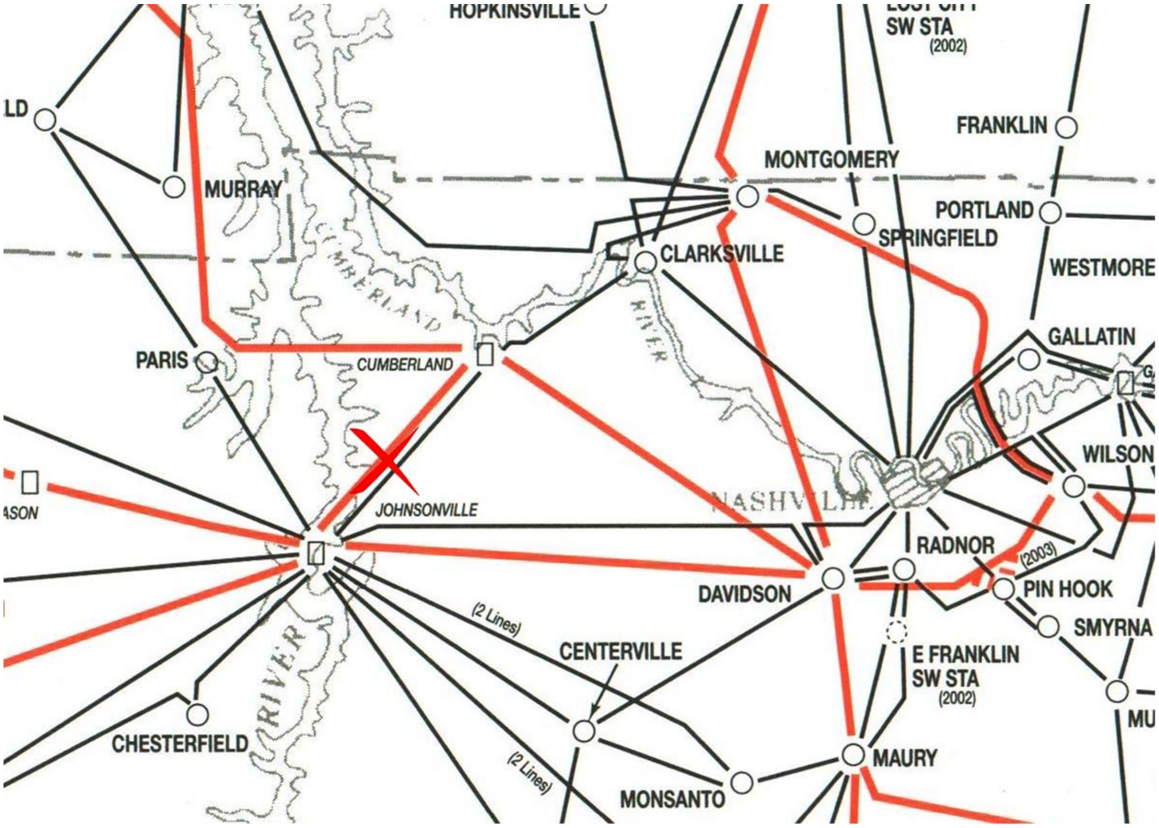

Figure 6.23 The area around the Cumberland – Johnsonville line (marked with the red cross. map source: TVA)

Table 6.7 Test results on the simulation data for the Cumberland – Johnsonville line trip

Rank	From bus	To bus	ED	Case ID
1	**Cumberland**	**Johnsonville**	**0**	**11**
2	Cumberland	Davidson	0.03612	9
3	Cumberland	Marshall	0.06532	10
4	Davidson	Pin Hook	0.10951	12
5	Johnsonville	Davidson	0.13892	18

Then the angle output from the PSS/E is added white Gaussian noises with different Signal-to-Noise ratios (SNR) to see the effects of noise on the algorithm. Figure 6.24 shows the angle data with 20 dB SNR Gaussian noises added.

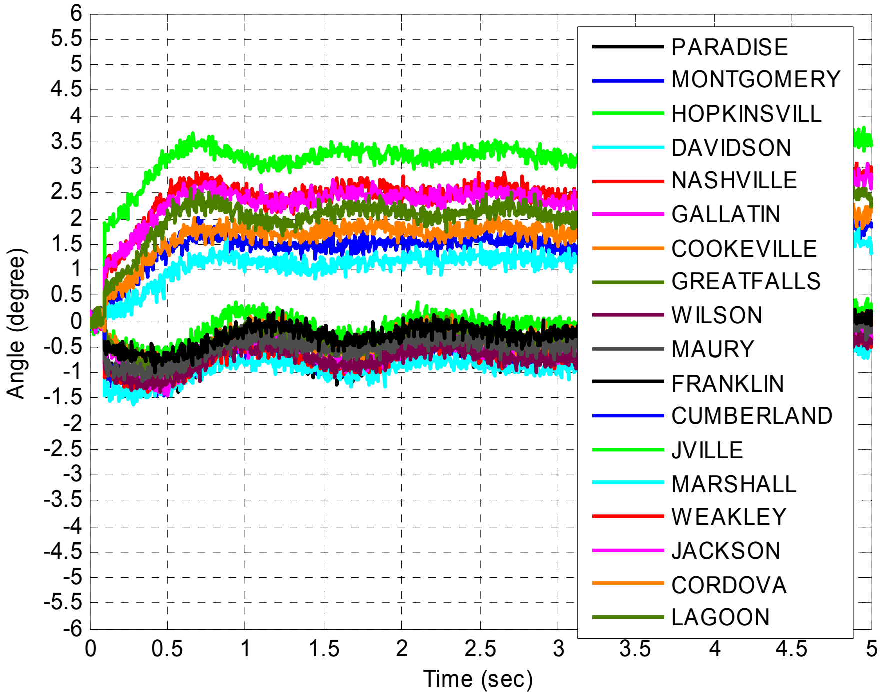

Figure 6.24 Angle from PSS/E on tripping the 500 kV Cumberland – Johnsonville line with noises added (SNR: 20 dB)

The angle outputs with noises added are pre-processed with an 11-point moving median filter to suppress the noises before fed into the line trip detection algorithm. The same filtering process is also applied to the real angle measurements. The results are shown in Table 6.8 through Table 6.10, where the correct lines are highlighted in red.

Table 6.8 Test results on the simulation data for the Cumberland – Johnsonville line trip with noises added (SNR: 20 dB)

Rank	From bus	To bus	ED	Case ID
1	**Cumberland**	**Johnsonville**	**0.25491**	**11**
2	Johnsonville	Davidson	0.34559	18
3	Cumberland	Marshall	0.43843	10
4	Cumberland	Davidson	0.50785	9
5	Browns Ferry	West Point	0.51234	7

.

Table 6.9 Test results on the simulation data for the Cumberland – Johnsonville line trip with noises added (SNR: 15 dB)

Rank	From bus	To bus	ED	Case ID
1	Cumberland	Marshall	0.22178	10
2	**Cumberland**	**Johnsonville**	**0.25611**	**11**
3	Johnsonville	Gleason	0.26443	19
4	Birmingham Steel	Freeport	0.26887	2
5	Browns Ferry	Union	0.31031	4

Table 6.10 Test results on the simulation data for the Cumberland – Johnsonville line trip with noises added (SNR: 10 dB)

Rank	From bus	To bus	ED	Case ID
1	Jackson	Haywood	0.23632	16
2	Cumberland	Marshall	0.29916	10
3	Johnsonville	Gleason	0.30847	19
4	Johnsonville	Jackson	0.31211	17
5	**Cumberland**	**Johnsonville**	**0.32132**	**11**

One can notice that the EDs are larger from the noise-contaminated data compared to those in the noise-free case because the angle change peak values calculated are affected by the noises. Moreover, the rank of the correct line is lowered as the SNR decreases. Despite the presence of the noise, the program is able to find the tripped line as one of the top 5 candidates when the SNR is as low as 10 dB.

2. Test on real measurements

Two testing examples on real measurements are illustrated here. One is the 500 kV Sequoyah – Bradley line outage due to lightning at 18:51 UTC on June 28, 2007; the other is the 500 kV Cumberland – Davidson trip at 13:22 UTC on December 16, 2006. Figure 6.25 shows the locations of the lines and the current FDR locations around the TVA area.

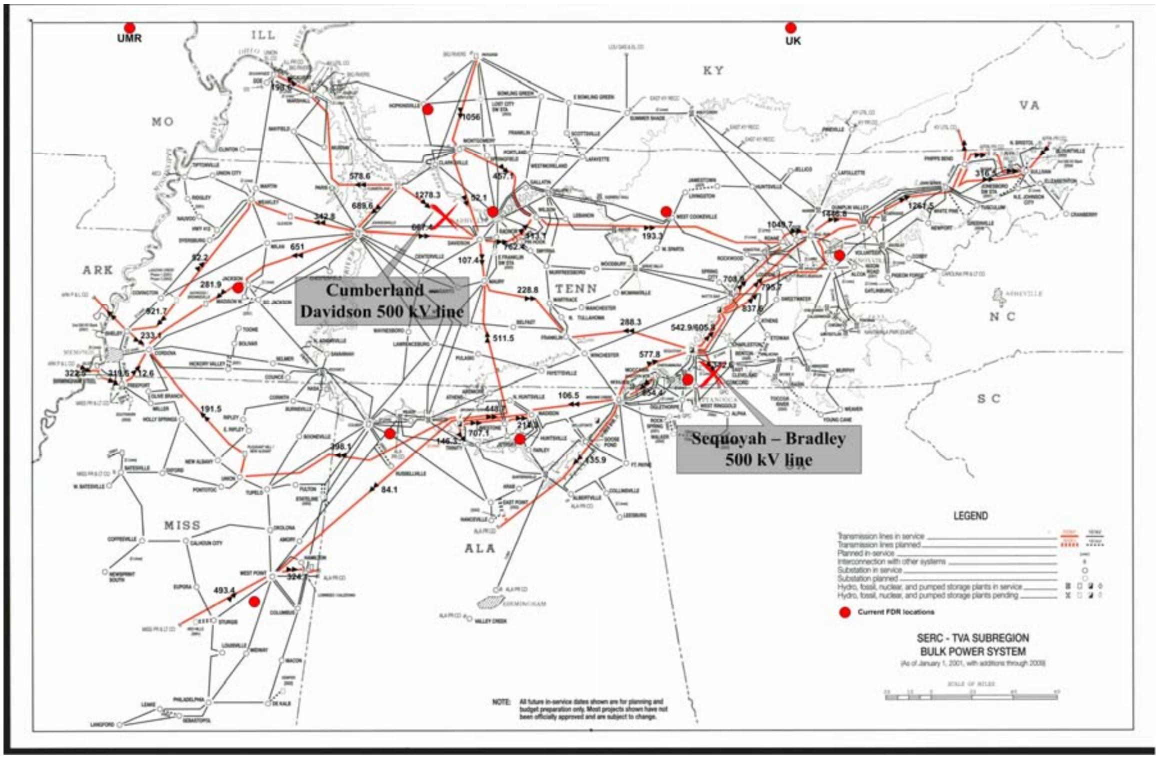

Figure 6.25 Line trip locations (marked as red crosses) and current FDR locations around the TVA area (marked as red dots. map source: TVA)

Although there are 9 units installed in the TVA system, they do not all report data all the time. Typically only 2 or 3 are available at the same time, thus making the testing difficult. Current FDRs did not see some known line outage, thus reducing the training cases. Furthermore, the angle data from some older FDRs in the TVA area have angle discontinuity problem as shown in Figure 6.26 caused by the old firmware [55]. The discontinuity can be as large as about 15 degrees, which makes the data unusable for line trip identification.

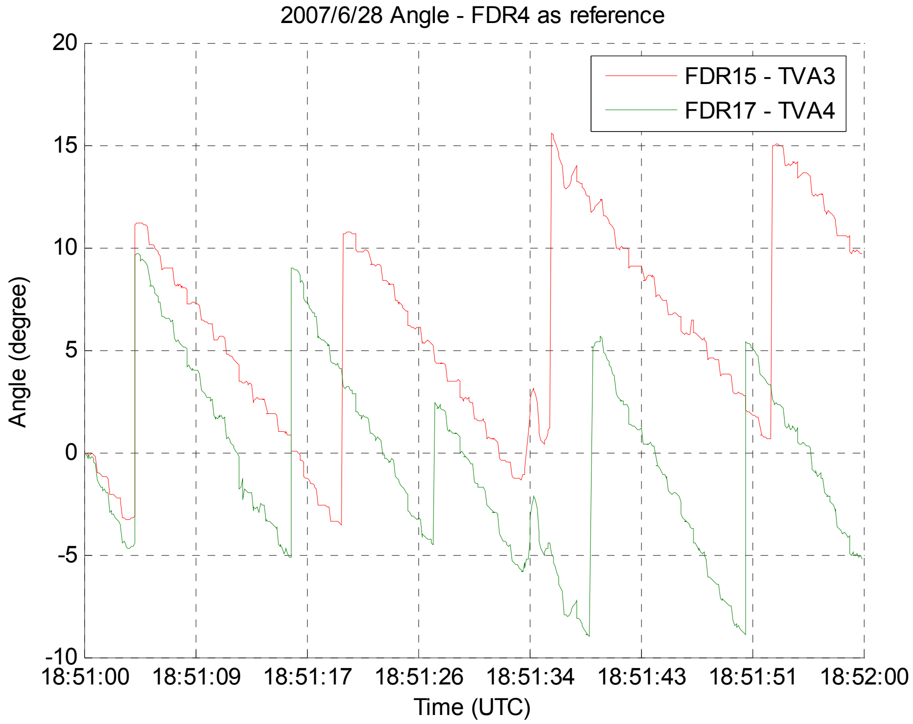

Figure 6.26 Angle discontinuity problem due to old firmware

The angle data from 2 available FDRs for the Sequoyah – Bradley line trip on June 28, 2007 are shown in Figure 6.27. The angles from FDR2-UMR and FDR42-FSU experienced sudden change at the time of the line trip and the changes are out of phase. The angle change vector is identified as

$$\Delta\theta_{observed} = \begin{bmatrix} 3.8105 & 3.108 \end{bmatrix}$$

The corresponding channel name vector is

$$FDR = \begin{bmatrix} '2UMR' & '42FSU' \end{bmatrix}$$

The line trip identification program then starts searching the cases in the database, forms the corresponding feature vector composed of the information of two channels and calculates the ED for each match. After the search is completed, the program compares all the EDs and reports 5 likely lines, as listed in Table 6. 11.

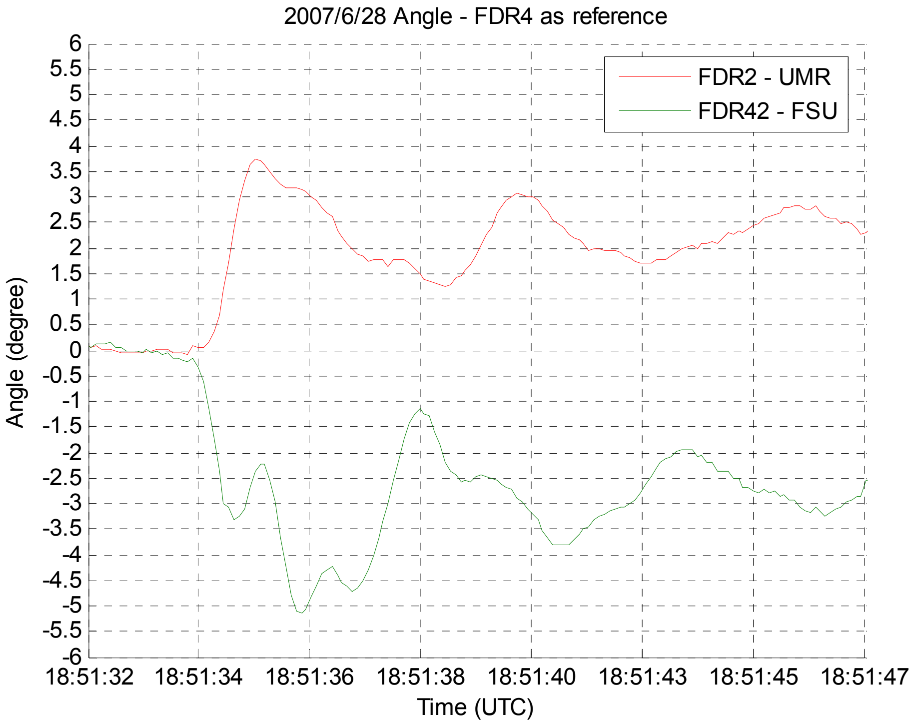

Figure 6.27 Relative angle of the Sequoyah – Bradley line trip on June 28, 2007 (FDR4 as reference)

Table 6.11 Test results on the real measurements for the Sequoyah – Bradley line trip

Rank	From bus	To bus	ED	Case ID
1	**Sequoyah**	**Bradley**	**0.015547**	**31**
2	Widows Creek	Sequoyah	0.1919	42
3	West Point	Lowndes	0.19959	39
4	Union	Pleasant Hill	0.26583	34
5	Bull Run	Volunteer	0.27415	8

Although there are only 2 FDRs available in this case, the program is able to find the correct line as the top 1 candidate with the ED much smaller than other cases. Neither of the two FDRs is in the TVA area, one in Missouri and one in Florida (not shown in Figure 6.28). This case indicates that the algorithm may be able to locate a line outage correctly even when the measurements are relatively far away if the measurements demonstrate the similar features as that in the database.

The second example is the Cumberland – Davidson line trip at 13:22 UTC on

December 16, 2006. Three available FDRs are FDR2-UMR, FDR31-UK and FDR32-TVA7 with only TVA7 in the TVA area. The angle measurements from the three units are referred to FDR4 and the angle change at UMR and UK is out of phase with that at TVA7 as can be seen in Figure 6.28.

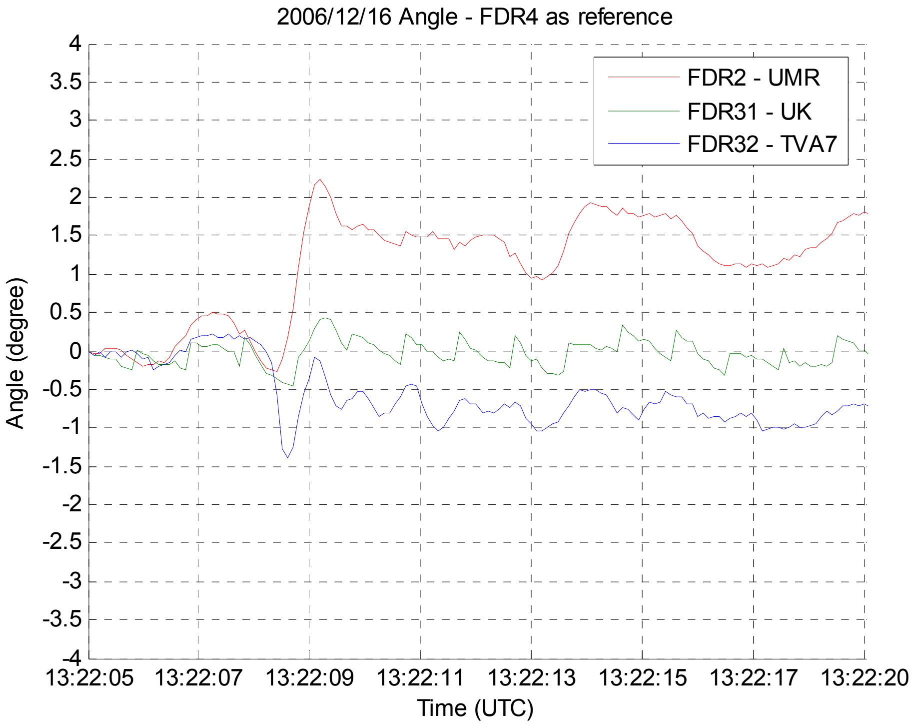

Figure 6.28 Relative angle of the Cumberland – Davidson line trip on December 16, 2006 (FDR4 as reference)

The angle change vector is hence

$$\Delta\theta_{observed} = [2.6188 \quad 0.8766 \quad 1.387]$$

and the corresponding FDRs are

$$FDR = ['2UMR' \quad '31UK' \quad '32TVA7']$$

The calculated EDs and ranks are listed in Table 6.12 and the correct result is ranked as the third. Four out of five of the possible lines found by the program are connected to either end of the correct line. One possible reason is that the outages of the nearby lines result in similar angle change combinations at the three FDR locations. With more FDRs deployed in the area, the line trip signatures are expected to be more distinct, thus the program can achieve better results.

Table 6.12 Test results on the real measurements for the Cumberland – Davidson line trip

Rank	From bus	To bus	ED	Case ID
1	Davidson	Pin Hook	0.02793	12
2	Johnsonville	Davidson	0.12375	18
3	**Cumberland**	**Davidson**	**0.18292**	**9**
4	West Point	Lowndes	0.28917	39
5	Cumberland	Marshall	0.32946	10

6.3.3 Discussion

The line trip identification algorithm described in this chapter is mainly based on PSS/E simulation and several real line trip events. There are very limited real measurements that can be used to test the algorithm due to the current low FDR density in the TVA area. TVA has provided a list of 100 line trip event records from 2007 to 2008. However, only 10 can be observed with data from FNET. On average only 4 to 5 units in or close to the TVA area are available in each case and units with high-quality angle data are even less. Of note is that not all the FDRs around the TVA area report data during a disturbance, so higher sensor coverage is required for better visibility. Moreover, the responses observed in the measurements may change as the operating conditions vary over hours and seasons.

For instance, the 500 kV Browns Ferry – Union line was tripped both on November 13, 2007 and April 10, 2008, for which the frequency and angle are shown in Figure 6.29 to Figure 6.32. The difference is clear that both frequency and angle magnitudes are larger in the line trip on November 13 while smaller in the one on April 10. FDR7-MISSI observed the frequency and angle transients during both events but the observations are quite different. Possible causes to the differences include the change in the system condition and various line trip causes: pollution in the earlier case and relay misoperation in the later one.

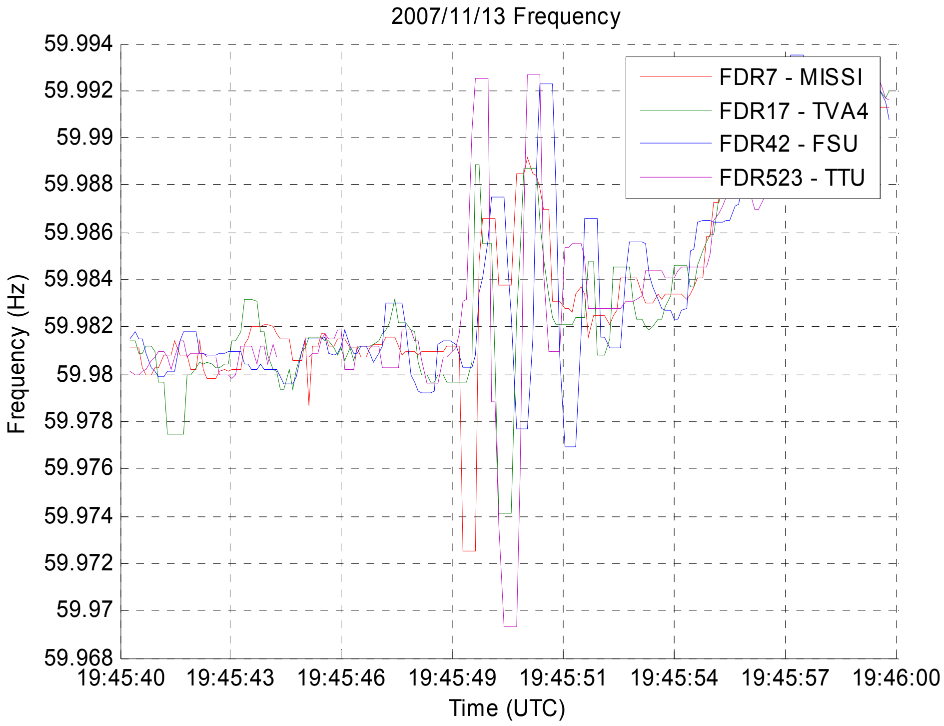

Figure 6.29 Frequency of the line trip at Browns Ferry – Union on November 13, 2007

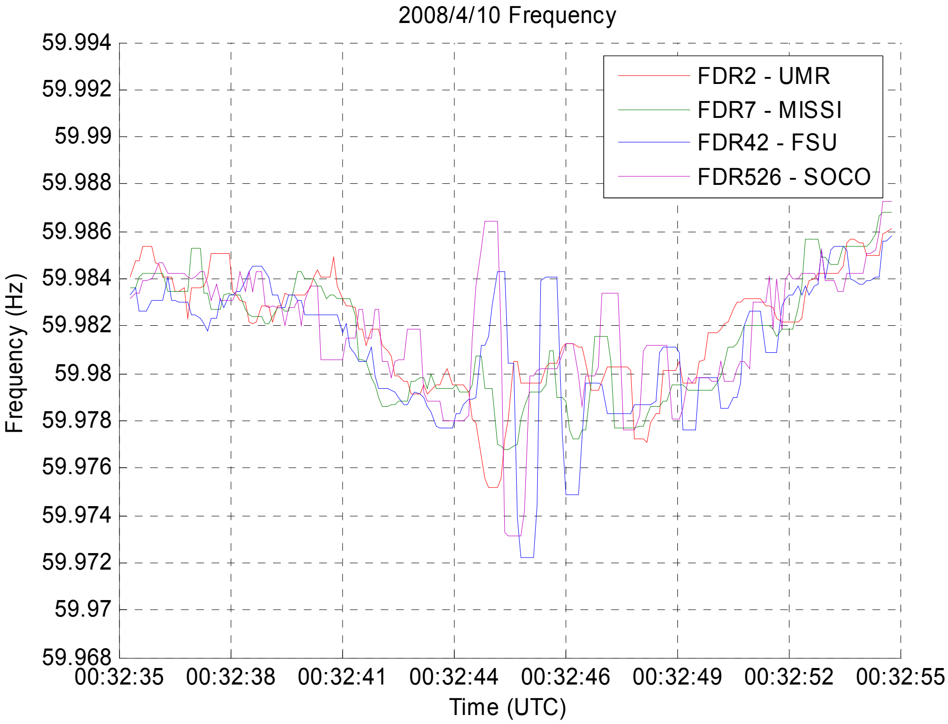

Figure 6.30 Frequency of the line trip at Browns Ferry – Union on April 10, 2008

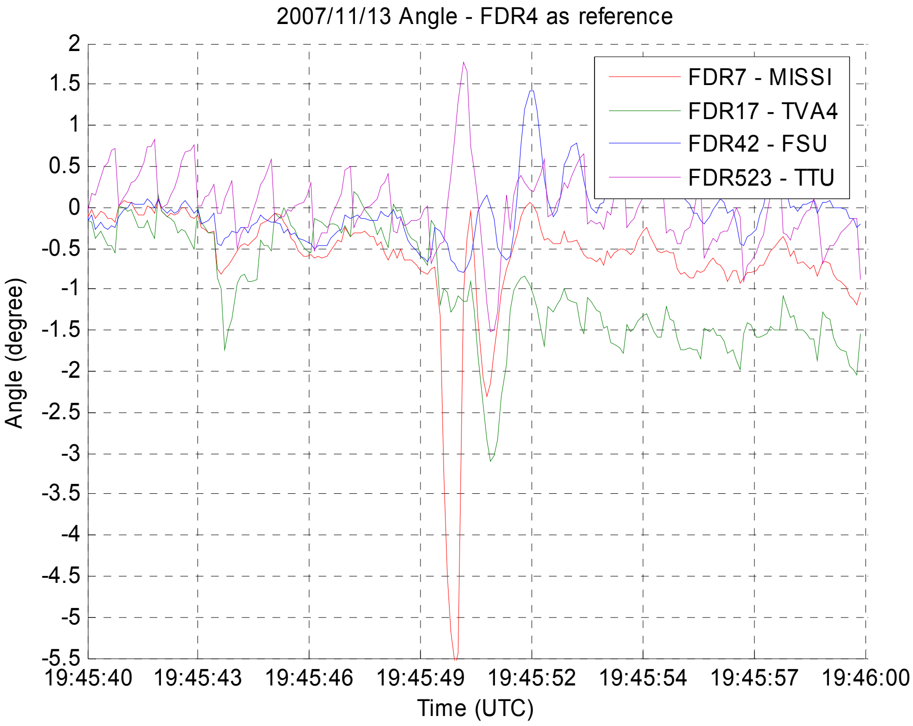

Figure 6.31 Relative angle of the line trip at Browns Ferry – Union on November 13, 2007 (FDR4 as reference)

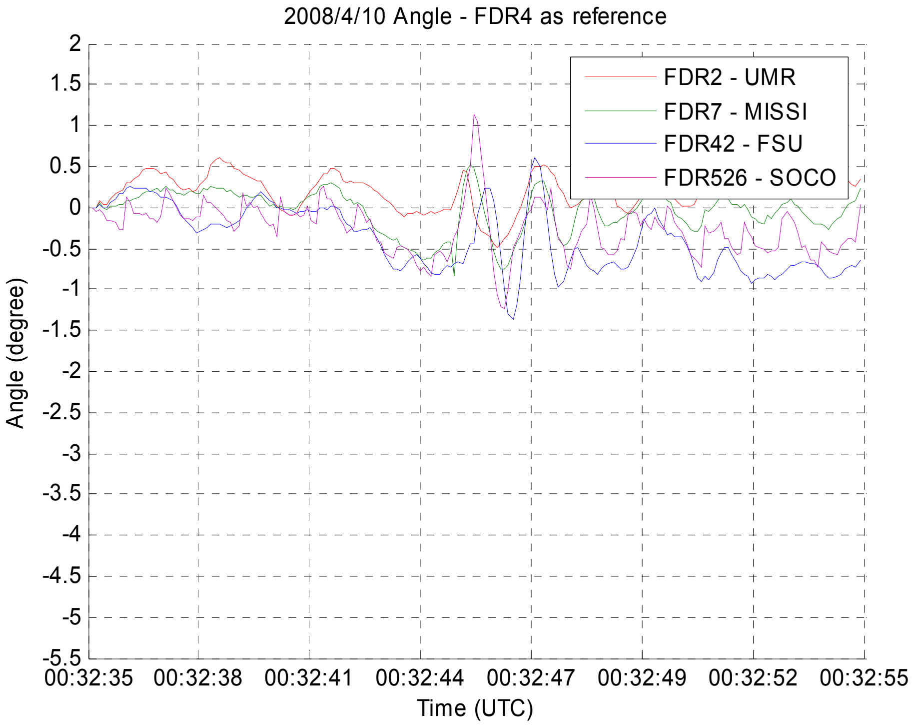

Figure 6.32 Relative angle of the line trip at Browns Ferry – Union on April 10, 2008 (FDR4 as reference)

In future testing and implementation of the identification algorithm, the system conditions of different seasons should be taken into account. With the growing number of installed FDRs and confirmed line trip events, it is very possible and practical to improve the case library with line trips observed in real measurements for different operating conditions. The correlation between the causes of the line outages and the observed measurements should be further analyzed in order to improve the case library. An expert system may be formed for higher accuracy and efficiency.

In addition to the identification algorithm proposed in this chapter, there exist other methods such as Neural Network for identification of power quality events [67][68] and pattern recognition for power system security analysis [69][70].

Chapter 7 Conclusions and Future Work

7.1 Conclusions

This dissertation has addressed the topic of monitoring the wide-area power systems at distribution level. Statistical analysis of noticeable disturbances in the three major North American Interconnections shows that that significant generation-loss like events are more common than large load-drop like events. Generation-trip like events in both the EI and the WECC Interconnections are more likely to be encountered in heavy load season. The event occurrence by hour demonstrates distinct characteristics during different seasons in the EI and the WECC, which indicates differences in the generation and load profile and control schemes. On average, the EI experiences a major disturbance about every 3 days with an estimated generation-load mismatch greater than 500 MW. The WECC experiences a disturbance almost every 1.5 days with the estimated power mismatch amount exceeding 200 MW.

Typical frequency disturbance excursions and their possible causes are illustrated. Loss of generation causes sudden frequency decline. And loss of load induces sharp frequency rise. Typical frequency excursions differ from each other in the three Interconnections. Possible reasons include different frequency responses, generation types, contingency reserve distribution, reserve development, and AGC actions.

A proportional relationship between the largest frequency change rate and total amount of frequency drop is obtained from theoretical analysis and also verified by the wide-area measurements. Comparison shows that the ratio by which the two are related is close in the three major Interconnections: the EI, the WECC and the ERCOT. The linear relationship between frequency deviation and generation/load mismatch during disturbances is examined based on exact power mismatch amount in the 129 confirmed events in the EI, which shows that the frequency response of the system varies in different seasons as the generation and load profiles change. The inertia and frequency response characteristics of an Interconnection can be estimated and monitored provided the information of the actual generation/load mismatch and accurate frequency measurements. As an application, the estimated frequency response and inertia can be employed to improve the generation/load mismatch calculation in the event detection program.

Several major disturbances in the EI system are examined including a three-phase fault in the transmission network, an event involving line events and generator trips, an islanding incident, the Florida outage, and faults in HVDC systems. Plenty of information about systems' response to disturbances, as well as to control actions and protection schemes is reflected in measurements from distribution networks. The comparison between measurements from FDR and PMU shows that measurements taken from the low voltage level demonstrate high quality for monitoring disturbances in the transmission networks.

The dynamic performances of AC/DC systems are examined. By monitoring the two ends of the HVDC links, the effects of frequency sensitive damping controls are observed as the frequency transients at one side are reflected at the other. On the other hand, it is confirmed in the wide-area measurements that the HVDC links between asynchronous Interconnections prevents the disturbances in on system form propagating to another.

With the assist of the visualization techniques, the propagation of disturbances as electromechanical waves can be better understood. An automated visualization tool has been developed that can generate frequency and angle replay for disturbances in the EI system. An attempt has been made to display the steady-state angle distribution in the EI. Simulation results show that the angle distribution does not follow any obvious geographically related trend.

Unlike generation or load loss events, line outages generally cause well-damped oscillations in local frequency and rapid changes in angle. Due to the fact that a single line trip generally has limited impact on the entire interconnected system, higher sensor density is required for detecting such disturbances. For the instance of monitoring the TVA system, 52 sensors (including current and future deployment) are sufficient for monitoring the major 500 kV transmission lines and part of the 161 kV networks if they are placed at the proposed locations. Both frequency and angle can be employed as the line trip detection signals. The detection algorithms developed in the work can be easily implemented for real-time line trip detection.

A signature library for all the single line trip cases at 500 kV in the TVA system is established with PSS/E simulations. The feature vector for each line trip case is formed as the angle magnitudes during the first swing at all the observing points. In spite of the limited sensor coverage and lack of confirmed cases for training the algorithm, the identification program is tested with simulation and real measurements with reasonable accuracy. We are aware that the EI model used for simulations is not sufficient to represent all the operating conditions therefore may be not comprehensive to include all the possible characteristics of a line outage. However, with the deployment of more sensors, the signature library can be expanded to represent the line trip disturbances during different seasons and operating conditions.

7.2 Contributions

This work has made unique contributions in the areas of the wide-area monitoring of power systems at distribution level and disturbances detection. First, this work examines the disturbances in the bulk transmission power systems from a wide-area point of view by providing comparisons of the characteristics of noticeable generation/load loss events in the three major North American Interconnections both from statistical perspective and dynamic response perspective. No analysis of this nature has been presented due to limited access to such wide-area measurements across North America and data sharing among utilities. The frequency response estimation presented in chapter 2 will help to calibrate the values used in current FNET event detection algorithm thus improving the power mismatch estimation. The analysis of the various major disturbances offers valuable insights to the system dynamic responses. A database of the event signatures shall greatly assist the study of event detection and location estimation, and further, the design of wide-area controls to prevent severe system failures.

Second, the automated visualization tool using computer graphics designed in this work improves the power system visualization capabilities by correlates the measurements with their geographic locations. This dissertation makes the first attempt to view the phase angle over the Eastern Interconnection both in simulation and measurements obtained at distribution level. The work in chapter 4 extends the potential applications of angle measurements at lower voltage level, which has been confined mainly by the uncertainty of the phase shift at each sensor location.

Another major contribution of this work is approaching the line trip detection and identification based extensively on distribution-level wide-area measurements, which has not been addressed in previous works. Being aware of the system topology change is critical because inadvertent line outages can be very dangerous. This work proposes a methodology with which the topology change in the transmission networks can be detected and identified based on frequency and angle measurements and simulation results. The measurement-based algorithms do not require detailed system topology information which is not readily available in most of the cases. The uniqueness of the algorithms also lies in the inclusion of the information from both frequency and angle. Previously, frequency has been examined extensively in various FNET related applications such as detection of generation/load mismatch disturbances. However, the detection of line trips can be very difficult if it relies solely on frequency because no direct relationship is observed between the frequency transients and the closeness of the monitoring point to the tripped line at least from simulation results. Moreover, the line loading characteristics may complicate the line outage frequency signature such that tripping a line connecting to a generator is similar to a generation loss event in frequency. Phase angles, however, reflect the loading information of transmission lines therefore can serve as a good detection parameter.

7.3 Potential Future Work

More applications of the wide-area measurements are worth of further investigation as future research in the areas addressed by this dissertation. The statistical analysis of the generation/load mismatch events in the North American Interconnections can be continued to include the ERCOT and the Quebec systems as more FDRs are being employed in these Interconnections and the number of detected events grows. At the same time, the frequency response characteristics in the Interconnections should be continuously monitored which assists not only the improvement of the event detection program but also the study of system inertia and the electromechanical wave propagation speeds in different Interconnections, which may help to improve the accuracy of event location estimation.

This work has described the observations in the low-voltage measurements for several types of major disturbances. This signature library can be expanded by including more typical disturbances, which can be utilized as a knowledge database for event classification. The valuable knowledge of the power system dynamics during disturbances invites future research into areas like mode shapes and controllability. Moreover, with several HVDC systems in North America being monitored by FNET, the effects of the HVDC systems on the overall AC/DC system dynamic performance can be further examined with first-hand measurements to study the controllability of HVDC system in damping dangerous inter-area oscillations.

In order to better utilize the distribution-level measurements from FNET, more attention should be paid to calibration of the angle measurements. This work has made the first attempt to observe directly the angles but more important work is ahead to figure out the angle shift at each FDR location and adjust it accordingly to make the angle more meaningful. Thus the advantage of wide sensor coverage of FNET can be fully taken to observe the hourly or seasonal change in the voltage profile of the large Interconnections. Besides the phase shifts, there exist discontinuities in angle as shown in chapter 6 which may be corrected by hardware improvement. Although out of the scope of this dissertation, the improvement of the angle data quality shall greatly help the disturbance detection and identification study including the line outage detection. Another continuation of the topic of angle visualization is to display the angles from the wide-area view point and provide early warning of stability problems.

This work has developed the algorithms for line trip detection and identification based on simulation results and real measurements. More training cases are required to tune the algorithms, which is presently limited by the current sensor coverage in the target system. The significance of the work in this report is that it has explored and confirmed the viability of relying on wide-area measurements at distribution level for line outage detection and identification. Algorithms other than what have been can also be investigated such as expert system and pattern recognition, etc.

Further future research in the area of disturbance detection may include oscillation detection and mitigation. With the low-cost and easily-deployable power system monitoring made available by FNET, high sensor density in a regional power network is within reach. With such wealth of information, it is very realistic to say that the oscillation patterns or modes are fully exposed and can be exploited for the design of control and damping systems. As one example, with sufficient number of power system stabilizers (PSS) in any of the three major Interconnections, wide-area control should already be close to reality. That is, the coordination of a group of wide spread power system stabilizer using wide area measurement information is well within our reach and could be one very attractive study.

References

[1] J. F. Hauer, N. B. Bhatt, K. Shah, and S. Kolluri, "Performance of "WAMS East" in providing dynamic information for the North East Blackout of August 14, 2003," *IEEE Power Engineering Society General Meeting*, vol. 2, pp. 1685-1690, 2004.

[2] D. Divan, G. A. Luckjiff, W. E. Brumsickle, J. Freeborg, and A. Bhadkamkar, "A grid information resource for nationwide real-time power monitoring," *IEEE Trans. Industry Applications*, vol. 40, pp. 699-705, 2004.

[3] A. G. Phadke, "Synchronized phasor measurements in power systems," *IEEE Computer Applications in Power*, vol. 6, pp. 10-15, 1993.

[4] M. Zhou, V. A. Centeno, J. S. Thorp, and A. G. Phadke, "An alternative for including phasor measurements in state estimators," *IEEE Trans. Power Systems*, vol. 21, no. 4, pp. 1930-1937, Nov. 2006.

[5] W. Jiang, V. Vittal, and G. T. Heydt, "A distributed state estimator utilizing synchronized phasor measurements," *IEEE Trans. Power Systems.*, vol. 22, no. 2, pp.563-571, May 2007.

[6] J. S. Thorp, A. G. Phadke, and K. J. Karimi, "Real time voltage-phasor measurements for static state estimation," *IEEE Trans. Power App. Syst.*, vol. PAS-104, no. 11, pp. 3098-3106, Nov. 1985.

[7] G. Zhang, P. Hirsch, and S. Lee, Wide area frequency visualization using smart client technology," *Proc. IEEE Power Eng. Soc. General Meeting, 2007*, pp. 1-8, Jun. 2007.

[8] Z. Zhong, C. Xu, B. J. Billian, L. Zhang, S.-J. S. Tsai, R. W. Conners, V. A. Centeno, A. G. Phadke, and Y. Liu, "Power System Frequency Monitoring Network (FNET) implementation," *IEEE Trans. Power Systems*, vol. 20, pp. 1914-1921, 2005.

[9] Xia, Tao, Zhang, Hengxu, Gardner, Robert, Bank, Jason, Dong, Jingyuan, Zuo, Jian, Liu, Yilu, Beard, Lisa, Hirsch, Peter, Zhang, Guorui, and Dong, Rick, "Wide-area Frequency Based Event Location Estimation," *IEEE Power Engineering Society General Meeting*, pp. 1-7, 2007.

[10] Benmouyal, G., Schweitzer, E.O., and Guzman, A., "Synchronized phasor measurement in protective relays for protection, control, and analysis of electric

power systems," *2004 57th Annual Conference for Protective Relay Engineers*, pp. 419-450.

[11] S. S. Tsai, L. Zhang, A. G. Phadke, Y. Liu, M. R. Ingram, S, C, Bell, I. S. Grant, D. T. Bradshaw, D. Lubkeman, and L. Tang, "Study of global frequency dynamic behavior of large power systems," *IEEE PES Power System Conference and Exposition*, New York, pp. 328-335, Oct. 2004.

[12] North America Electric Reliability Council, "Understand and calculate frequency response," 2003, NERC Training Resources Working Group.

[13] A. Bykhovsky and J. H. Chow, "Power system disturbance identification from recorded dynamic data at the Northfield substation," *International Journal Electrical Power & Energy Systems*, vol. 25, pp. 787-795, 2003.

[14] N. Jaleeli, L. S. VanSlysk, "NERC's new control performance standards," *IEEE Trans. Power Systems*, vol. 14, pp. 1092-1099, 1999.

[15] L.-R. Chang-Chien, Y.-J. Lin, and C.-C Wu, "A real-time contingency reserve scheduling for an isolated power system," *IEEE Trans. Reliability*, to be published.

[16] North America Electric Reliability Council, "2006 Summer assessment reliability of bulk power systems in North America". Available at: http://www.nerc.com/files/summer2006.pdf.

[17] North America Electric Reliability Council, "2006/2007 Winter assessment reliability of bulk power systems in North America". Available at: http://www.nerc.com/files/winter2006-07.pdf.

[18] P. Kundur, *Power System Stability and Control*, New York: McGraw-Hill, 1994.

[19] T. Inoue, H. Taniguchi, Y. Ikeguchi, and K. Yoshida, "Estimation of power system inertia constant and capacity of spinning-reserve support generators using measured frequency transients," *IEEE Trans. Power Systems*, vol. 12, pp. 136-143, 1997.

[20] D. P. Chassin, Z. Huang, M. K. Donnelly, C. Hassler, E. Ramirez, and C. Ray, "Estimation of WECC system inertia using observed frequency transients," *IEEE Trans. Power Systems*, vol. 20, pp. 1190-1192, 2005.

[21] North America Electric Reliability Council, "Disturbance control performance". Available at: http://www.nerc.com/files/BAL-002-0.pdf.

[22] B.M. Pasternack, and N.B. Bhatt, “The Rockport plant – analysis of temporary fast turbine valving tests,” *IEEE Trans. Power Systems*, vol. 3, pp. 529-540, 1988.

[23] Bhatt, N.B., “Field experience with momentary fast turbine valving and other special stability controls employed at AEP's Rockport plant,” *IEEE Trans. Power Systems*, vol. 11, pp. 155-161, 1996

[24] Dalke, G., Baum, A., Bailey, B., Daley, J.M., Duncan, B., Fischer, J., Hesla, E., Hoerauf, R., Hornbarger, B., Lee, W.-J.; Love, D.J., McCullough, D., Mozina, C., Nichols, N., Padden, L., Patel, S., Al Pierce, Pillai, P., Poletto, G., Rifaat, R., Sanders, M.K., Shelton, J.M., Stringer, T.N., Weber, J., Wu, A., and Young, R., “Application of islanding protection for industrial and commercial generators-an IEEE industrial application society working group report,” *2006 59th Annual Conference for Protective Relay Engineers*, pp. 12.

[25] Hou, D. and Tziouvaras, D.A, “Out-of-step protection enhancements,” *2004 Eighth IEE International Conference on Developments in Power System Protection*, pp. 5-10.

[26] Taylor, C.W., and Lefebvre, S., “HVDC controls for system dynamic performance,” *IEEE Trans. Power Systems*, vol. 6, pp. 743-752, 1991.

[27] Report, IC, “Dynamic Performance Characteristics of North American HVDC Systems for Transient and Dynamic Stability Evaluations,” *IEEE Trans. Power Systems*, vol. PAS-100, pp. 3356-3364, 1981.

[28] Samuelsson, O., Hemmingsson, M., Nielsen, A.H., Pedersen, K.O.H., and Rasmussen, J., "Monitoring of power system events at transmission and distribution level," *IEEE Trans. Power Systems*, vol. 21, pp. 1007-1008, 2006.

[29] FRCC, “FRCC Event Analysis Team Interim Recommendations Report”. Available at https://www.frcc.com/Reliability/Shared%20Documents/FEAT%20Interim%20Report.pdf.

[30] NERC news release, “NERC Issues Reliability Advisories on February Florida Outage”. Available at http://www.nerc.com/news_pr.php?npr=102.

[31] NERC, “NERC’s Bulk Power System Event Classification Scale”. Available at http://www.nerc.com/page.php?cid=5|63|252.

[32] The ABB group, "The HVDC Transmission Québec - New England". Available at http://www.abb.com/.

[33] Donahue, J.A., Fisher, D.A., Raling, B.D., and Tatro, P.J., "Performance testing of the Sandy Pond HVDC converter," *IEEE Trans. Power Delivery*, vol. 8, pp. 422-428, 1993.

[34] Manitoba Hydro, "Nelson River DC Transmission System". Available at http://www.hydro.mb.ca/corporate/facilities/ts_nelson.shtml.

[35] Dhaliwal, N.S., Recksiedler, L.D., and Tang, D.T.Y., "Operating experiences of the Nelson River HVDC system," *IEEE Transmission and Distribution Conference*, pp. 174-180, 1996.

[36] Hou, D., and Fischer, N., "Deterministic High-Impedance Fault Detection and Phase Selection on Ungrounded Distribution Systems," *Power Systems Conference: Advanced Metering, Protection, Control, Communication, and Distributed Resources*, pp. 112-122, 2006.

[37] Chapman, D.G., and Jost, F.A., "Operation of an isolated hydro plant supplying an hvdc transmission load," *IEEE Trans. Power Apparatus and Systems*, vol. 95, pp. 1099-1104, 1976.

[38] Chand, J., "Auxiliary Power Controls on the Nelson River HVDC scheme," *IEEE Trans. Power Systems*, vol. 7, pp. 398-402, 1992.

[39] Mao, X.M., Zhang, Y., Guan, L., Wu, X.C., and Zhang, N., "Improving power system dynamic performance using wide-area high-voltage direct current damping control," *Generation, Transmission & Distribution, IET*, vol. 2, pp. 245-251, 1992.

[40] J.S. Thorp, C.E. Seyler, and A.G. Phadke, "Electromechanical wave propagation in large electric power system", *IEEE Tran. Circuits and Systems I: Fundamental Theory and Applications*, vol. 45, pp. 614-622, 1998.

[41] Overbye, T.J. and Weber, J.D., "Visualizing the electric grid," *IEEE Spectrum*, vol. 38, pp. 52-58, 2001.

[42] Pires de Azevedo, G., Sieckenius de Souza, C. and Feijo, B.; "Enhancing the human-computer interface of power system applications," *IEEE Trans. Power Systems*, vol. 11, pp. 646-653, 1996.

[43] Weber, J.D. and Overbye, T.J., “Voltage contours for power system visualization,” *IEEE Trans. Power Systems*, vol. 15, pp. 404-409, 2000.

[44] Naoki Kobayashi, Takeshi Yamada, Hiroshi Okamoto, Yasuyuki Tada, Atsushi Kurita and Yasuji Sekine, “Visualization of results of load flow calculation and dynamic simulation,” *Electrical Engineering in Japan*, vol. 116, pp. 35-48, 1996.

[45] Mota, Ad.A., Mota, L.T.M. and Morelato, A., “Teaching power engineering basics using advanced web technologies and problem-based learning environment,” *IEEE Trans. Power Systems*, vol. 19, pp. 96-103, 2003.

[46] Ohashi, T. and Ono, T., “Visualization and interactive simulation for power system operation and education,” *Fourth International Conference on Advances in Power System Control, Operation and Management*, vol. 2, pp. 802-807, 1997.

[47] Overbye, T.J., “Visualizing the interaction between the transmission system and power markets,” *IEEE Power Engineering Society Summer Meeting*, vol. 2, pp. 1019-1024, 2001.

[48] Lisa S. Avila, Sebastien Barre, Rusty Blue, Berk Geveci, Amy Henderson, William A. Hoffman, Brad King, C. Charles Law, Kenneth M. Martin, and William J. Schroeder, *The VTK user's guide: updated for VTK version 4.4*, Clifton Park, NY: Kitware Inc., 2004.

[49] Will Schroeder, William Schroeder, Ken Martin, Kenneth William Martin, and Bill Lorensen, *The Visualization Toolkit: An Object-oriented Approach to 3D Graphics*, Clifton Park, NY: Kitware Inc., 2004.

[50] MathTools Ltd. “MIDEVA, MATCOM & Visual MATCOM user’s guide,” 1999.

[51] William Ford and William Topp, *Data Structures with C++ and STL, Second Edition*, Prentice Hall, 2001.

[52] J. Zuo, "The Frequency Monitor Network (FNET) Design and Situation Awareness Algorithm Develop," Ph.D. dissertation, Department of Electrical and Computer Engineering, Virginia Tech, Blacksburg, 2008.

[53] “Map Projection”. Available at http://en.wikipedia.org/wiki/Map_projection.

[54] S.J.S Tsai, "Study of Global Power System Frequency Behavior Based on Simulations and FNET Measurements," Ph.D. dissertation, Department of Electrical and Computer Engineering, Virginia Tech, Blacksburg, 2005.

[55] K.J.H. Khan, "Wide Area Power System Monitoring Device Design and Data Analysis," Master thesis, Department of Electrical and Computer Engineering, Virginia Tech, Blacksburg, 2006.

[56] http://earth.google.com/.

[57] "KML documentation introduction". Available at http://code.google.com/apis/kml/documentation/.

[58] Shankar, M., Stovall, J., Sorokine, A., Bhaduri, B. and King, T., "Visualizing energy resources dynamically on earth," *IEEE Power Engineering Society General Meeting*, pp. 1-4, 2008.

[59] Wolk, R.M., "Utilizing Google Earth and Google Sketchup to visualize wind farms," *IEEE International Symposium on Technology and Society*, pp. 1-8, 2008.

[60] Weili Ding, Feng Zhu and Yingming Hao, "Interactive 3D City Modeling using Google Earth and Ground Images," *Fourth International Conference on Image and Graphics*, pp. 849-854, 2007.

[61] Chadil, N., Russameesawang, A. and Keeratiwintakorn, P., "Real-time tracking management system using GPS GPRS and Google earth," *5th International Conference on Electrical Engineering/Electronics, Computer, Telecommunications and Information Technology*, vol. 1, pp. 393-396, 2008.

[62] Bi, T.S., Song, X.N., Wu, J.T. and Yang, Q.X., "Novel method for disturbance identification in power systems," *IEEE Power Engineering Society General Meeting*, pp. 1-5, 2006.

[63] Power Technologies, INC, *PSS/E-29 Program Operation Manual: Volume I*, Schenectady, NY, 2002, pp. 7-27.

[64] Power Technologies, INC, *PSS/E-29 Application Guide: Volume I*, Schenectady, NY, 2002, pp. 1-2.

[65] Wood, A.J. and Wollenberg, B.F., *Power Generation, Operation and Control: Second Edition*, New York, NY: John Wiley & Sons, Inc, 1996, pp. 107.

[66] Hazra, J. and Sinha, A.K., "Identification of catastrophic failure in power systems using pattern recognition," *IEEE Power India Conference*, pp. 1-7, 2006.

[67] Santoso, S., Powers, E.J., Grady, W.M. and Parsons, A.C., “Power quality disturbance waveform recognition using wavelet-based neural classifier. I. Theoretical foundation,” *IEEE Trans. Power Delivery*, vol. 15, pp. 222-228, 2000.

[68] Santoso, S., Powers, E.J., Grady, W.M. and Parsons, A.C., “Power quality disturbance waveform recognition using wavelet-based neural classifier. II. Application,” *IEEE Trans. Power Delivery*, vol. 15, pp. 229-235, 2000.

[69] Pang, Chok K., Koivo, Antti J. and El-Abiad, Ahmed H.; “Application of Pattern Recognition to Steady-State Security Evaluation in a Power System,” *IEEE Trans. Systems, Man and Cybernetics*, vol. 3, pp. 622-631, 1973.

[70] Chang, C.S., Chung, T.S. and Lo, K.L., “Application of pattern recognition technique to power system security analysis and optimization,” *IEEE Trans. Power Systems*, vol. 5, pp. 835-841, 1990.

Appendix I. Confirmed Disturbances in the EI from 2007 to 2008

Plant	Date	Time (UTC)	MW Estimate	Actual MW
North Anna	1/3/2007	23:03:27	905	500
Browns Ferry	1/11/2007	14:18:45	1019	1139
L/O Mystic U7	1/17/2007	18:45:04	462	540
Paradise	1/24/2007	14:56:01	921	921
Oconee U1&U2	2/15/2007	21:54:10	1385	1692
Indian Point	2/28/2007	11:33:50	955	1018
Amos U2	3/2/2007	4:25:30	851	765
Belews Creek U2	3/2/2007	21:37:34	1109	1137
Sequoyah U2	3/13/2007	19:27:12	1181	1161
Gentleman	3/18/2007	4:06:43	771	626
Conemaugh U1	3/21/2007	20:41:41	797	841
W H Zimmer	3/24/2007	3:13:17	1547	1296
Gavin 1	3/31/2007	2:39:56	1487	1309
Indian Point U3	4/6/2007	15:09:07	753	936
Salem U1	4/30/2007	19:02:50	706	830
Lacygne	5/3/2007	14:58:59	729	394
Palisades U1	5/8/2007	17:23:42	902	806
Sherburne	5/14/2007	14:21:02	738	657
Grand Gulf	5/19/2007	16:27:12	808	1268
Campbell U3	5/19/2007	18:30:07	820	678
Salem U2	5/24/2007	6:32:29	765	1153
Montour U1	5/27/2007	19:15:04	558	697
Amos 3	6/1/2007	13:15:47	1140	1197
Cardinal U1	6/7/2007	2:50:41	605	632
Keystone	6/9/2007	5:59:25	908	846
Browns Ferry U1	6/9/2007	16:00:34	742	840

Plant	Date	Time (UTC)	MW Estimate	Actual MW
Belews Creek U1	6/12/2007	15:40:52	870	1137
Iatan U1	6/16/2007	4:50:52	697	658
Belews Creek U2	6/19/2007	5:09:01	693	1050
Cumberland	6/23/2007	14:23:10	1052	1200
Keystone	6/27/2007	8:50:07	774	807
Braidwood	6/27/2007	14:21:13	875	1236
Darlington U1	6/29/2007	17:35:12	713	1000
North Anna2	6/29/2007	21:53:56	864	954
Conemaugh	7/1/2007	23:34:16	756	849
Amos U3	7/2/2007	16:49:42	1076	1262
Bulls Run U1	7/3/2007	13:55:35	663	900
Gavin U1	7/4/2007	13:27:43	1038	1286
Iatan U1	7/7/2007	20:37:54	570	663
Cumberland U1	7/17/2007	0:40:22	934	1269
Cumberland U1	7/21/2007	2:44:25	686	501
Baldwin U1	7/25/2007	19:01:41	872	587
Rockport,Petersburg,Newton	8/4/2007	21:44:14	2387	4000
Salem U2	8/6/2007	17:11:22	952	1150
Amos U3	8/6/2007	19:39:22	1037	1298
Belews Creek U2	8/10/2007	4:57:41	1003	1135
Seminole U1,2,3(SPP)	8/16/2007	3:26:58	690	1195
Braidwood Nuclear	8/18/2007	19:10:21	685	919
Braidwood U2	8/23/2007	20:30:52	870	1112
Cumberland U2	8/24/2007	7:50:13	691	893
Donald C. Cook U1	8/28/2007	17:53:13	921	1060
Mountaineer U1	9/1/2007	13:48:00	1089	1297
Rockport U2	9/4/2007	16:57:07	745	1331
Jeffrey Energy Center U2 U3	10/3/2007	15:26:37	1112	1376
New Madrid U2	10/20/2007	9:50:29	714	559

Plant	Date	Time (UTC)	MW Estimate	Actual MW
Byron	10/23/2007	4:35:29	766	648
Mitchell U2	11/4/2007	9:26:35	634	590
Amos U3	11/9/2007	2:49:25	1095	1304
Monroe U1	11/20/2007	15:14:35	877	754
FTWARTIN U2 (PJM)	12/15/2007	19:32:34	511	477
Monroe U1	12/18/2007	21:43:00	664	723
Cardinal/TIDD U3	1/10/2008	12:36:29	588	645
Laramine River U1	1/12/2008	15:12:11	640	546
Palisades U1	1/13/2008	10:21:06	867	839
Coal Creek U1	1/15/2008	12:42:54	489	519
Lacygne U1	1/15/2008	16:26:07	621	377
Zimmer	1/15/2008	17:20:27	493	312
Sequoyah U1	1/17/2008	0:25:57	918	1225
Conemaugh U1	1/18/2008	14:00:54	837	847
Seabrook U1	1/20/2008	4:02:58	694	1250
Paradise U1	1/20/2008	20:21:40	561	669
Gibson U4	1/20/2008	20:37:30	653	618
King U1	1/21/2008	12:58:20	420	475
Wyman	1/22/2008	20:21:58	499	649
Conemaugh U1	1/30/2008	19:47:11	728	842
Willco U4	1/31/2008	6:41:16	442	411
Amos U2	1/31/2008	6:49:34	774	800
Amos U3	1/31/2008	15:18:25	905	1145
Cardinal/TIDD U1	1/31/2008	22:26:11	628	534
Limerick U2	2/1/2008	9:44:41	911	1172
Donald C Cook U1	2/2/2008	10:29:46	923	1003
Coyote U1	2/3/2008	23:56:29	460	389
Homer City U2	2/6/2008	16:34:31	510	506
Nebraska City U1	2/7/2008	17:44:09	570	503

Plant	Date	Time (UTC)	MW Estimate	Actual MW
Gibson U5	2/8/2008	14:55:06	592	612
Louisa U1	2/9/2008	9:22:29	599	537
Amos U3	2/15/2008	0:56:34	964	960
Coffeen U2	2/19/2008	14:27:55	624	551
Rush Island U2	2/25/2008	20:50:16	482	573
Bull Run U1	3/7/2008	7:11:49	719	459
Amos U2	3/7/2008	9:42:57	653	674
Mill Creek U4	3/7/2008	21:54:44	545	474
Conemaugh U2	4/5/2008	5:00:13	713	409
Lacygne U1	4/5/2008	16:07:23	686	378
Petersburg U3	4/7/2008	19:12:37	501	511
Newton U2	4/8/2008	10:54:47	561	549
Zimmer U1	4/22/2008	8:58:51	909	287
Cumberland U2	4/23/2008	20:27:30	689	801
Ghent U1	4/28/2008	5:12:31	525	410
Gavin U2	4/29/2008	19:20:49	1212	1320
Cumberland U2	5/1/2008	9:43:09	986	797
Cayuga U1	5/9/2008	16:09:33	557	462
Rockport U1	5/9/2008	21:03:29	795	934
Cardinal/TIDD U1	5/10/2008	3:48:28	770	616
Monroe U4	5/13/2008	14:03:30	720	757
Bull Run U1	5/14/2008	16:22:59	887	839
Brandon U1	5/16/2008	14:07:51	622	639
Monroe U3	5/22/2008	9:23:52	617	611
Millstone U2	5/22/2008	17:59:47	651	871
Conemaug U1 U2	5/25/2008	7:43:15	895	723
Kammer/Mitchell U2	5/25/2008	11:17:03	421	538
Conemaugh U2	5/26/2008	6:18:54	498	678
Cardinal/TIDD U1	5/27/2008	13:12:12	573	618

Plant	**Date**	**Time (UTC)**	**MW Estimate**	**Actual MW**
Rockport U2	5/29/2008	17:00:21	1080	1305
Millstone U2	6/28/2008	15:46:33	754	900
Monroe	7/25/2008	3:59:41	698	771
Kintigh	8/5/2008	14:11:56	577	675
Bruce U8	8/14/2008	7:24:25	840	818
Newton U1&2	8/19/2008	10:12:18	1000	1168
Cumberland U2	9/4/2008	2:39:38	885	1228
Trenton Channel U9	9/8/2008	16:17:00	590	440
Monticello U1	9/12/2008	3:48:12	520	602
Watts Bar U1	9/20/2008	13:05:44	1035	1204
Cook U1	9/21/2008	0:05:20	733	1029
Homer City	9/21/2008	21:47:15	616	580
Conesville U4	9/29/2008	7:43:30	639	515
Amos U1	10/3/2008	18:47:37	689	771
Browns Ferry U2	10/5/2008	3:09:29	999	1142
Bruce U6	10/7/2008	4:44:11	738	872

Appendix II. Development Manual for the Visualization Tool

1. Install the Visualization Toolkit (VTK)

The information for installing the Visualization Toolkit (VTK) can be found in chapter 1 and chapter 2 of 'The VTK User's Guide Updated for Version 5'. VTK compiles and runs on many different computer platforms. In this program, VTK applications are developed in Windows platform using Microsoft Visual C ++ (MSVC++). To install VTK, the source code will have to be compiled to produce libraries and executables. To develop C++ applications and extend VTK, a source code installation is needed. The machine must be running Windows95, Windows98, Windows ME, Windows NT 4.0, Windows 2000 or Windows XP. A C++ compiler should be installed on the computer.

(1) Get the source code

The current program is using VTK 5.0. The latest release of VTK source code can be downloaded from http://www.vtk.org/get-software.php.

(2) Install CMake

CMake is an open-source, cross-platform Make tool for configuring and managing the build process. Simple, platform independent files (CMakeLists.txt) are used to describe the build process and capture dependencies. When CMake is run, it produces native build files for the particular compiler/operating system. For example, on Windows MS Visual C ++ workspaces are created.

(Learn more about CMake at http://www.cmake.org; download CMake from http://www.cmake.org/HTML/Download.html.)

(3) Run CMake

After installation, there should be a CMake entry in the Start menu under Programs->CMake->CMakeSetup. Running CMake requires three basic pieces of information: where the source code directory is, which directory to place the binaries (these are generated as a result of compiling the source code), and which compiler to use. The CMake interface is shown in Figure II.1. CMake is used to generate projects, makefiles, or workspace. It runs with a GUI that allows users to easily set compile flags. These flags can be set by left-mouse clicking in the building flag value. The directories can be specified with the ‘Browse’ button. After that, click once the ‘Configure’ button. CMake will display a dialog from which you can select the compiler. At this point, one can customize the variables. After that, click the ‘Configure’ button again, until all the variables are satisfactory and colored grey. Then click the ‘OK’ button.

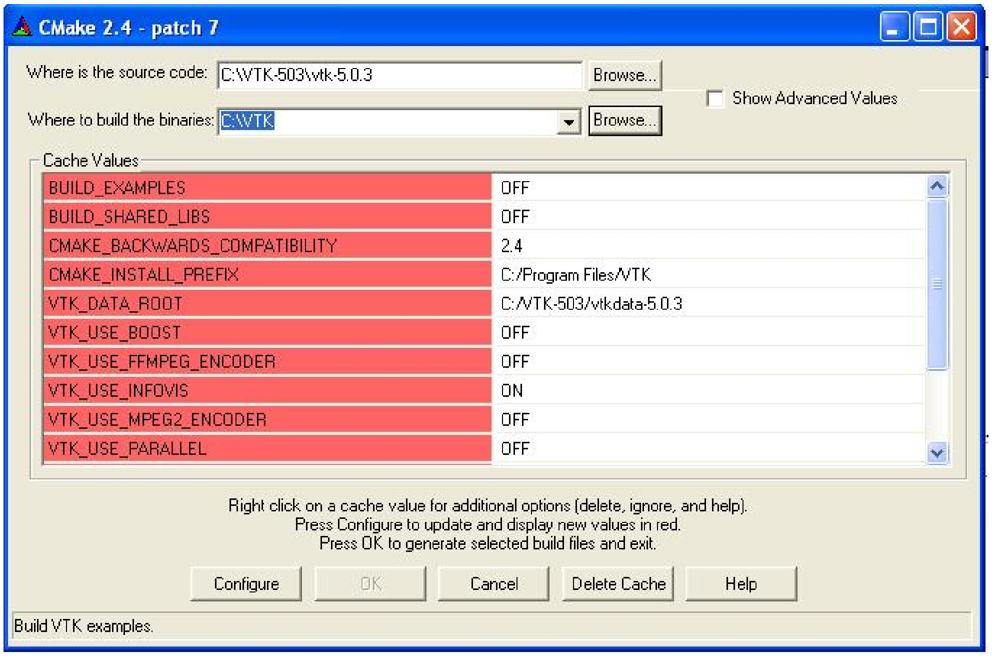

Where is the source code: C:\VTK-503\vtk-5.0.3

Where to build the binaries: C:\VTK

BUILD_EXAMPLES	OFF
BUILD_SHARED_LIBS	OFF
CMAKE_BACKWARDS_COMPATIBILITY	2.4
CMAKE_INSTALL_PREFIX	C:/Program Files/VTK
VTK_DATA_ROOT	C:/VTK-503/vtkdata-5.0.3
VTK_USE_BOOST	OFF
VTK_USE_FFMPEG_ENCODER	OFF
VTK_USE_INFOVIS	ON
VTK_USE_MPEG2_ENCODER	OFF
VTK_USE_PARALLEL	OFF

Right click on a cache value for additional options (delete, ignore, and help).
Press Configure to update and display new values in red.
Press OK to generate selected build files and exit.

Build VTK examples.

Figure II. 1 Run Cmake to build the VTK libraries

(4) Build the library

For Microsoft, a project file will be located in the specified binary path. Simply load this project file (VTK.sln for .NET), select the ALL_BUILD project, and compile it. The MSVC++ interface is shown in Figure II.2. (**Note**: Do not use the MSVC++ ‘Rebuild All’ menu to rebuild the source code. This deletes all CMakeLists.txt files which are then automatically regenerated as part of the build progress. MSVC++ will then try reloading them and an error will result. Instead, to rebuild everything, remove the VTK binary directory, rerun CMake, and then do a normal build.)

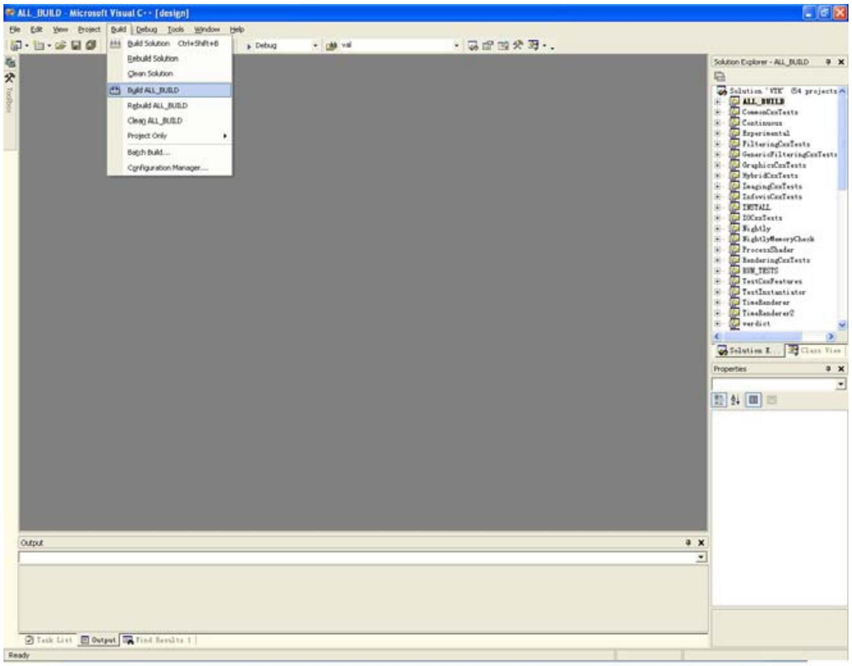

Figure II. 2 Build the VTK libraries in MSVC++

2. Install and Configure MATCOM Math Library

(1) Install MATCOM

Run mat4501vc.exe, a widow will appear as shown in Figure II.3. The default installation directory is C:\matcom45. During installation, the software will ask if Matlab has been installed on the machine, answer NO to this question. It also requires a file cl.exe, which can be found at C:\Program Files\Microsoft Visual Studio .NET 2003\Vc7\bin; if Microsoft Visual Studio. NET has been installed with default directory.

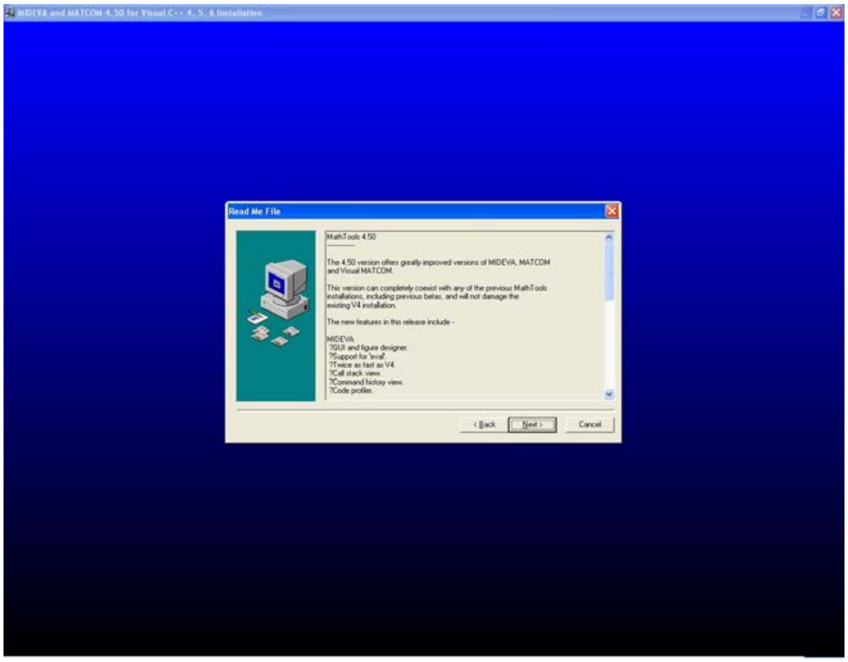

MathTools 4.50

The 4.50 version offers greatly improved versions of MIDEVA, MATCOM
and Visual MATCOM.

This version can completely coexist with any of the previous MathTools
installations, including previous betas, and will not damage the
existing V4 installation.

The new features in this release include -

MIDEVA
?GUI and figure designer.
?Support for 'eval'.
?Twice as fast as V4.
?Call stack view.
?Command history view.
?Code profiler.

Figure II. 3 Install MATCOM math library

(2) Configure MATCOM for Microsoft Visual Studio. NET

Add an environment variable to PATH as 'C:\Program Files\Microsoft Visual Studio .NET 2003\Commom7\IDE'. Go to the directory 'C:\Program Files\Microsoft Visual Studio .NET 2003\Vc7\PlatformSDK\Lib' and copy the required files. (msvcrt.lib, kernel32.lib, user32.lib, netapi32.lib, advapi32.lib, gdi32.lib, comdlg32.lib, comctl32.lib, oldnames.lib, wsock32.lib). Paste the files in C:\Program Files\Microsoft Visual Studio 8\VC\lib. Replace the matlib.h in C:\matcom45\lib with the current one in the application folder.

To test if the installation is successful, run the software and type magic(5) in the command window of the MATCOM. It should display a 5 × 5 matrix, as shown in Figure II.4.

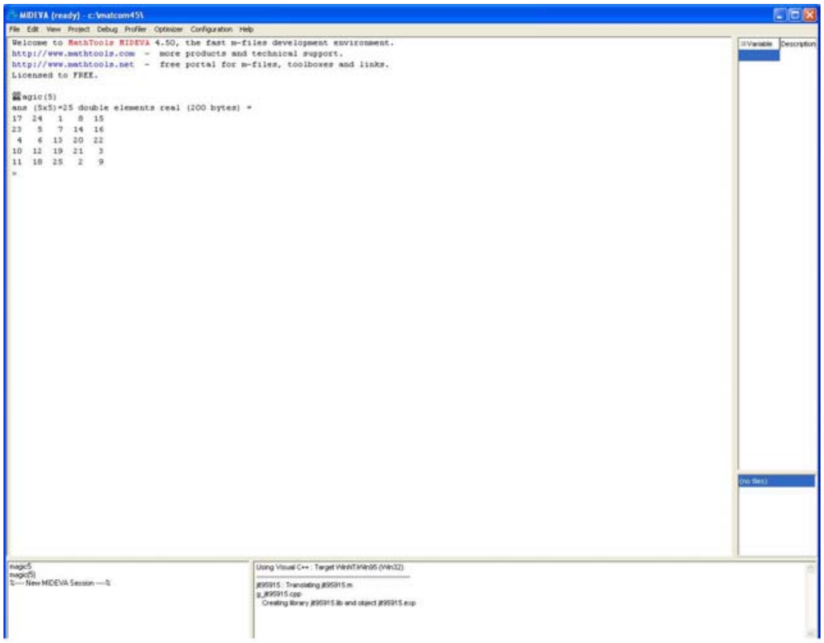

```
Welcome to MathTools MIDEVA 4.50, the fast m-files development environment.
http://www.mathtools.com  -  more products and technical support.
http://www.mathtools.net  -  free portal for m-files, toolboxes and links.
Licensed to FREE.

magic(5)
ans (5x5)=25 double elements real (200 bytes) =
17  24   1   8  15
23   5   7  14  16
 4   6  13  20  22
10  12  19  21   3
11  18  25   2   9
»
```

```
magic5
magic(5)
%---- New MIDEVA Session ----%
```

```
Using Visual C++ : Target WinNT/Win95 (Win32)
----------------------------------------------------------------
#95915 : Translating #95915.m
g_#95915.cpp
   Creating library #95915.lib and object #95915.exp
```

Figure II. 4 Test the installation of MATCOM

3. Create a C++ Project

To modify or debug an application using VTK, the easiest way is to create a C++ project with CMake. It will help to properly set the parameters. To use the MATCOM library, the files v4501v.lib, ago4501.dll, v4501v.dll, and matlib.h should be put into the same folder as the application. A simple text file ‘CmakeLists.txt’ is required. The CmakeLists file for the visualization tool is as follows.

```
# The project name is MovieGen.
PROJECT (MovieGen)

FIND_PACKAGE(VTK)
IF(NOT VTK_DIR)
  MESSAGE(FATAL_ERROR ″Please set VTK_DIR.″)
ENDIF(NOT VTK_DIR)
INCLUDE(${VTK_USE_FILE})

# Find the MATCOM library.
```

```
FIND_LIBRARY(matcom NAMES v4501v PATHS C:/matcom45/lib)

# Link the libraries
LINK_LIBRARIES(
  vtkRendering
  vtkGraphics
  vtkImaging
  vtkIO
  vtkFiltering
  vtkCommon
  v4501v
)

# Include the header and source files
SET(SRCS
movie.h
ReadData.h
Movie.cpp
ReadData.cpp
)

ADD_EXECUTABLE(AutoMovie ${SRCS})
```

Put the CmakeList.txt file and other header and sources files in a same directory. In this case, the files are movie.h, ReadData.h, Movie.cpp, and ReadData.cpp. Each file will be discussed in detail.

Then run CMake. Select the source and binary directories as the same one. A MSVC++ project will be established in the specified directory. By opening the MovieGen.sln, one can modify the header and source files, or debug and compile the project.

4. The Structure of the Program

As mentioned in section 3, this program includes two header files and two source files. Functions to read measurement data and location information are declared in ReadData.h. The functions are as follows.

```
void ReadUnitConfig() – read unit information fro UnitConfig.txtp;
void ReadEventLocation() – read event time and location information from EventLocation.txt;
void FormatTime() – format time;
void ReadEventData() - read and treat event data from generated text files;
void ReadOneUnitData() - read data from one file;
void MovingMedian() - moving median process;
void combsort() - sort data (used in moving median);
void DataCondition() - remove noises;
void TreatDelay() - find and treat units with 1-second delay.
```

The file ReadData.h also declared some structures and vectors to hold and pass data. The definition of each function is in the file ReadData.cpp. The file movie.h also declares functions to process frequency data and visualize them. Following are the functions. The specific definition of the functions can be found in Movie.cpp.

```
static vtkWindowToImageFilter *ImgRender() – form each movie frame;
Mm GenMesh() – MATCOM function to interpolate frequency data and form measurement matrix.
```

To use classes and functions in VTK, corresponding header files should be included in the established C++ project. All required VTK header files are included in movie.h. They have similar names as 'vtkClassName.h'.

The file 'matlib.h' is included to use the MATCOM library. The Matrix<LIB> matrix type is called Mm. For example, XI, YI, minFreq and maxFreq are declared as

```
Mm XI, YI;
Mm minFreq, maxFreq;
```

Besides them, MATCOM has over 300 mathematical functions. Refer to the MATCOM manual for more information.

Read Data

The procedure of reading data is illustrated in Figure II.5.

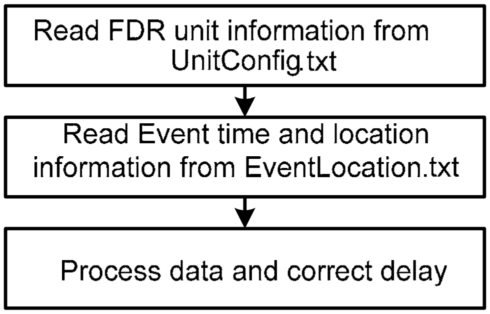

Figure II. 5 Procedures to read data

1) ReadUnitConfig( ) - Read Unit Configuration

The FDR information is obtained from the "UnitConfig.txt" file by ReadUnitConfig( ). Then, the FDR information is stored in the global vectors defined in ReadData.cpp as below. The format of UnitConfig.txt can be found in Figure II.6. So far only the Eastern Interconnecton is considered in this visualization program.

```
vector<FDRInfo> EastFDR;        // for East Units
vector<FDRInfo> WeccFDR;        // for WECC Units
vector<FDRInfo> TxFDR;          // for Texas Units
```

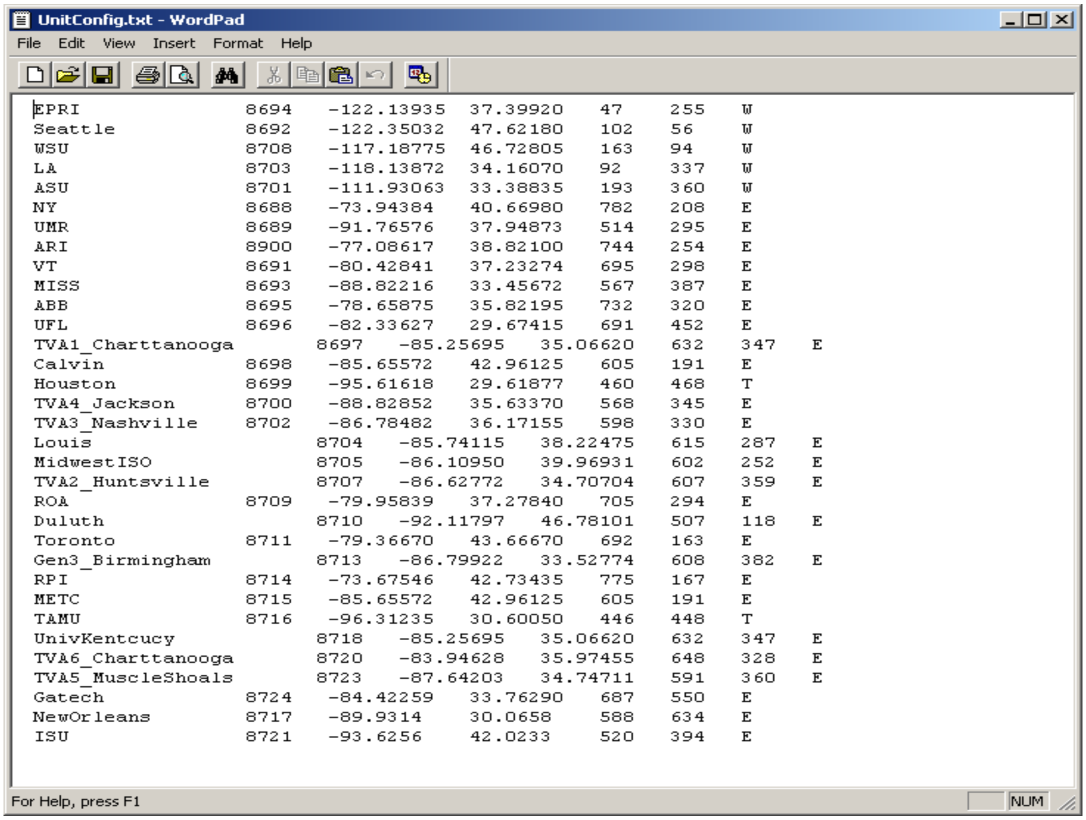

```
EPRI              8694   -122.13935  37.39920   47    255   W
Seattle           8692   -122.35032  47.62180   102   56    W
WSU               8708   -117.18775  46.72805   163   94    W
LA                8703   -118.13872  34.16070   92    337   W
ASU               8701   -111.93063  33.38835   193   360   W
NY                8688   -73.94384   40.66980   782   208   E
UMR               8689   -91.76576   37.94873   514   295   E
ARI               8900   -77.08617   38.82100   744   254   E
VT                8691   -80.42841   37.23274   695   298   E
MISS              8693   -88.82216   33.45672   567   387   E
ABB               8695   -78.65875   35.82195   732   320   E
UFL               8696   -82.33627   29.67415   691   452   E
TVA1_Charttanooga       8697   -85.25695   35.06620   632   347   E
Calvin            8698   -85.65572   42.96125   605   191   E
Houston           8699   -95.61618   29.61877   460   468   T
TVA4_Jackson      8700   -88.82852   35.63370   568   345   E
TVA3_Nashville    8702   -86.78482   36.17155   598   330   E
Louis                   8704   -85.74115   38.22475   615   287   E
MidwestISO              8705   -86.10950   39.96931   602   252   E
TVA2_Huntsville         8707   -86.62772   34.70704   607   359   E
ROA               8709   -79.95839   37.27840   705   294   E
Duluth                  8710   -92.11797   46.78101   507   118   E
Toronto           8711   -79.36670   43.66670   692   163   E
Gen3_Birmingham         8713   -86.79922   33.52774   608   382   E
RPI               8714   -73.67546   42.73435   775   167   E
METC              8715   -85.65572   42.96125   605   191   E
TAMU              8716   -96.31235   30.60050   446   448   T
UnivKentcucy            8718   -85.25695   35.06620   632   347   E
TVA6_Charttanooga       8720   -83.94628   35.97455   648   328   E
TVA5_MuscleShoals       8723   -87.64203   34.74711   591   360   E
Gatech            8724   -84.42259   33.76290   687   550   E
NewOrleans        8717   -89.9314    30.0658    588   634   E
ISU               8721   -93.6256    42.0233    520   394   E
```

Figure II. 6 Example of UnitConfig.txt

Figure II.7 shows the illustration of the vector of the FDR information. N is the total number of FDR units in the EI. To access the member variables of each vector element, users can use the syntax as follows.

EastFDR[i].Name (i: the number of elements from 0 to N)

WeccFDR[i].fLongitude

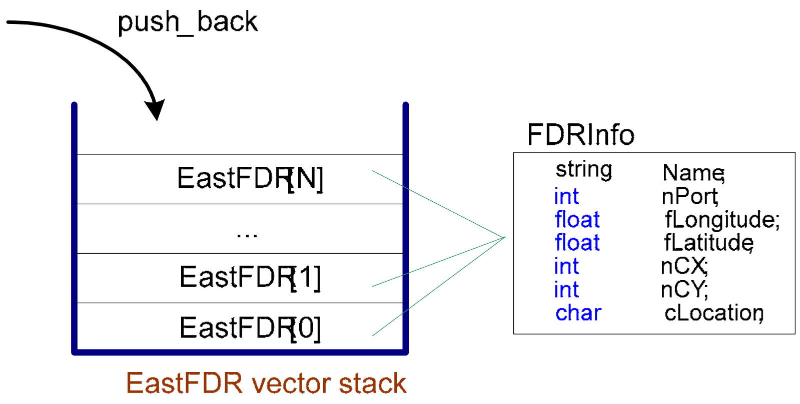

Figure II. 7 Illustration of the vector of the FDR information

2) Read Event Information - ReadEventLocation( ) and FormatTime( )

ReadEventLocation( ) reads the event information such as the event time and the location zone from "EventLocation.txt" as shown in Figure II.8. The file is generated automatically after a disturbance is detected and the Triangulation module estimates the event location. Then, the data are stored in the global variables as follows.

```
int m_Year, m_Mon, m_Day;        // Year, Month, Day
int m_Hour, m_Min, m_Sec;        // Hour, Min, Sec
```

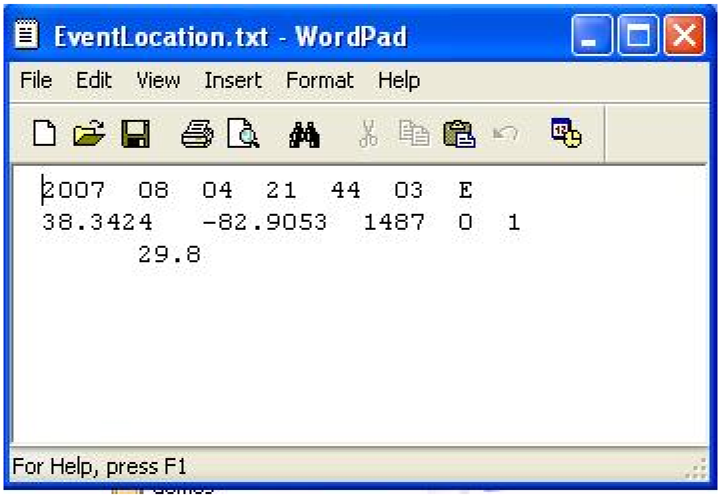

```
2007  08  04  21  44  03  E
38.3424   -82.9053  1487  0  1
      29.8
```

Figure II. 8 Example of EventLocation.txt

If there are errors to read "EventLocation.txt" file, the error message is written in "ErrorMessage.txt".

FormatTime( ) makes Month, Day, Hour, Min, Sec to two-character variable, and stores them to the global variables as follows.

```
char m_cMon[3], m_cDay[3], m_cHour[3], m_cMin[3], m_cSec[3];
```

Data Conditioning in C++

ReadEventData( ) is the function that reads and filters frequency data. The procedures are shown in Figure II.9.

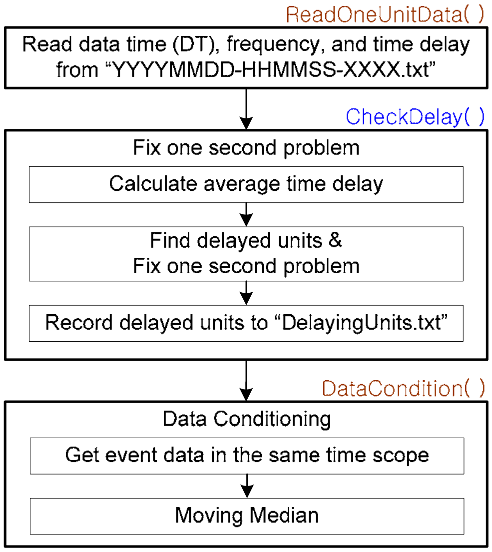

Figure II. 9 Procedure of data conditioning

First, this function calls ReadOneUnitData() to read data from "YYYYMMDD-HHMMSS-XXXX.txt"files, i.e. "20060730_025016_ASU.txt". These files contain data time, frequency data measured by FDR units, and time delay as shown in Figure II.10. The number of records of these data is maximally 350. If there exist missing data, the number of records is smaller than that.

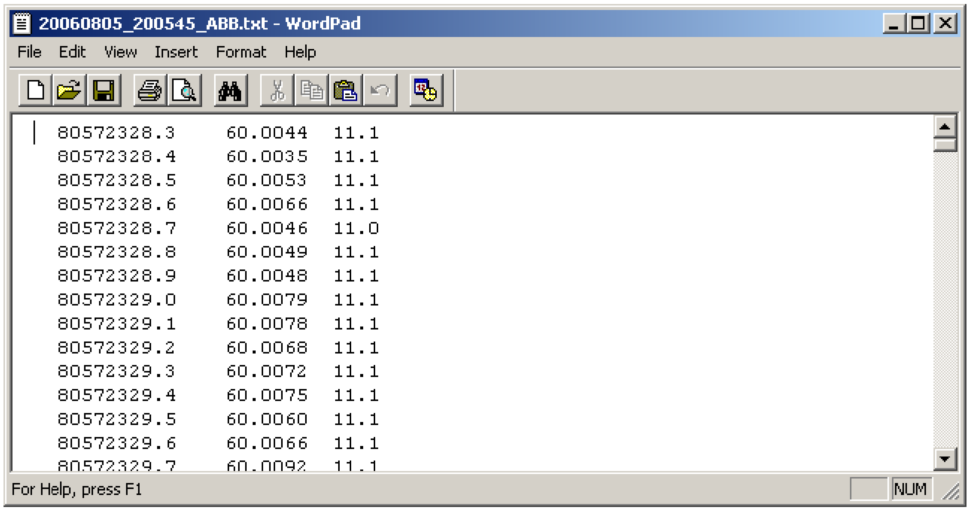

```
80572328.3   60.0044   11.1
80572328.4   60.0035   11.1
80572328.5   60.0053   11.1
80572328.6   60.0066   11.1
80572328.7   60.0046   11.0
80572328.8   60.0049   11.1
80572328.9   60.0048   11.1
80572329.0   60.0079   11.1
80572329.1   60.0078   11.1
80572329.2   60.0068   11.1
80572329.3   60.0072   11.1
80572329.4   60.0075   11.1
80572329.5   60.0060   11.1
80572329.6   60.0066   11.1
80572329.7   60.0092   11.1
```

Figure II. 10 Example of YYYYMMDD-HHMMSS-XXXX.txt file

After reading data, it stores the data into UnitData, a vector of the FDRData type. The format of UnitData is as shown in Figure II.11.

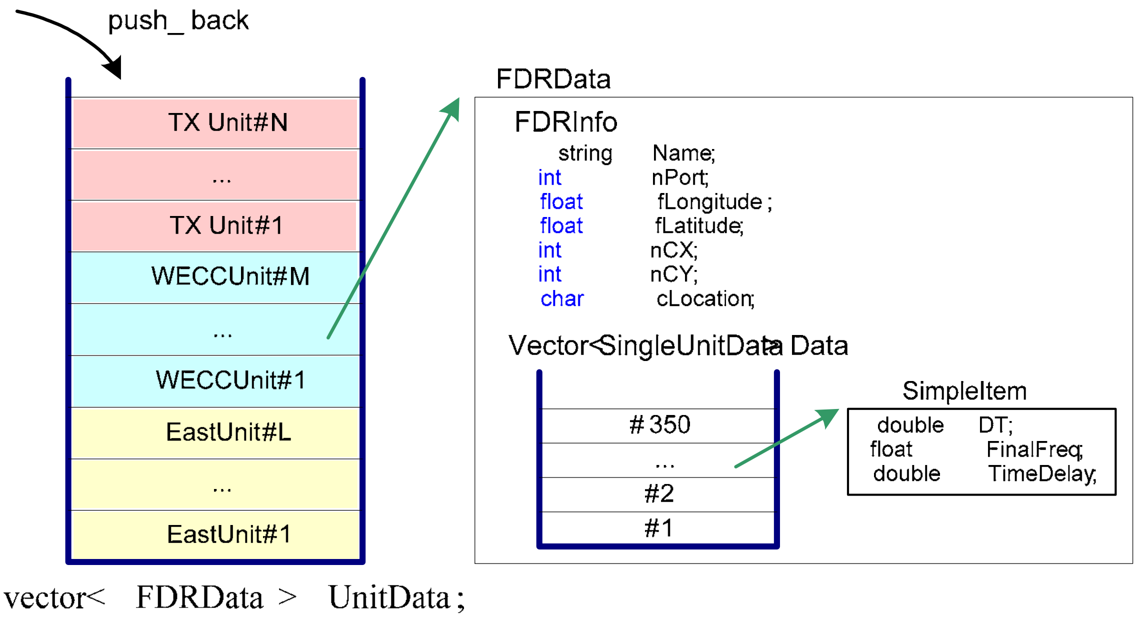

Figure II. 11 Format of the UnitData vector

Then, the function TreatDelay( ) is called. This function checks the delayed units to fix the one-second problem. The one-second problem is that the time stamps of a few abnormal FDR units are one second ahead of the normal units due to the timing buffer design in the units. Normally, the time delay is about 11.1 ~ 11.2 seconds. However, the time delay of abnormal units is about 10.1 ~ 10.2 seconds. Therefore, this TreatDelay( ) fixes the one-second delay issue by searching the units whose average time delays are between 9.5 to 10.5 seconds and then subtracting one second from their time stamps to make them aligned with the normal units.

The function ReadEventData( ) also calls DataCondition( ) that makes sure the available data are in the vector UnitData. If a FDR has too many missing data such that the number of data of from that FDR is smaller than 100, this FDR is discarded from further analysis. After that, all data are filtered by 9-point moving median by MovingMedian( ) to remove the noises. The data over a 9-point moving window are sorted by the function combsort( ), then the value at the center of the window is selected as the median of this time window.

Generate Measurement Matrix for Display

Frequency measurements from limited number of FDR units are interpolated over the whole EI area. The area defined by -105 and -66 degrees longitude, and 24 to 52 degrees latitude, is divided into N×M small mesh grids. The longitudes and latitudes are used directly here because the program assumes Simple Cylindrical projection method to display FDRs on a map image.

The function Mm GenMesh( ) processes frequency and location data to form a N×M measurement matrix. This function employs the functions in MATCOM, such as mean( ), meshgrid( ), and griddata( ). The MATCOM library enables useers to conveniently use math functions in the similar fashion as in Matlab, which saves coding time. However, the griddata() function in MATCOM provides only simple interpolation methods such as nearest neighbor or linear. Before accessing any MATCOM library functionality, call initM on application initialization. Call exitM before the application terminates in order to finalize the library. initM may be called multiple times as it is protected by a static variable. MATCOM_VERSION is a constant defined in matlib.h, which assures that the versions of the library DLL and matlib.h match. The following is the initialization of the MATCOM library in the program.

```
initM(MATCOM_VERSION);          //initialize the MATCOM library
……
exitM();                        //exit the MATCOM library
```

The main procedures to generate the measurement matrix are shown in Figure II.12. And the corresponding codes are as follows.

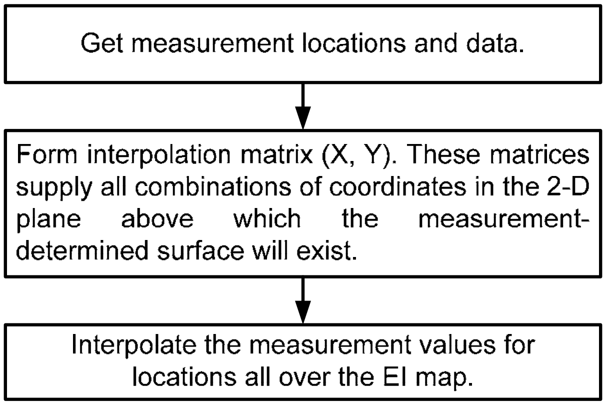

Figure II. 12 Procedures to generate measurement matrix

```
//indx is the index of the movie frame.
Mm GenMesh(Mm indx)
{
        //Define vectors and matrices.
        Mm freq;
        Mm UnitXcor, UnitYcor, UnitX, UnitY;
        Mm xmin, xmax,ymin,ymax, interval, X, Y, Xout, Yout;
        Mm periZ, Z, ZI;
        Mm datalength;  //length of data
        UINT m, n;

        //Get the latitudes and longitudes of FDRs. Use latitudes and longitudes to form the
meshes.
        for (m = 0; m < UnitData.size(); m++)
        {
                UnitXcor(m+1) = UnitData[m].FdrInfor.fLongitude;
                UnitYcor(m+1) = UnitData[m].FdrInfor.fLatitude;
        }

        xmin = -105;            //the minumum of longitude
        xmax = -66;             //the maximum of longitude
        ymin = 24;              //the minimum of latitude
        ymax = 52;              //the maximum of latitude

        interval = 1;           //the resolution step for meshgrid()
```

```
        //Prepare the boundary vectors X, Y.
        X =
(BR(colon(xmin,interval,xmax)),colon(xmin,interval,xmax),xmin*ones(1.0,length(colon(ymin,interva
l,ymax))),xmax*ones(1.0,length(colon(ymin,interval,ymax))));

        Y =
(BR(ymin*ones(1.0,length(colon(xmin,interval,xmax)))),ymax*ones(1.0,length(colon(xmin,interval,x
max))),colon(ymin,interval,ymax),colon(ymin,interval,ymax));

        //Prepare the location vectors for meshgrid: Connect X and UnitXcor; Connect Y and
UnitYcor.
        Xout = (BR(X),UnitXcor);
        Yout = (BR(Y),UnitYcor);

        //Form matrices (X,Y) for interpolation
        meshgrid(colon(xmin,interval,xmax),colon(ymin,interval,ymax),i_o,XI,YI);

        //Form frequency matrix for visualization
        datalength = 1200;      //number of data points
        for (m = 0; m < UnitData.size(); m++)
        {
                for (n=0; n < datalength.r(); n++)
                        {
                                freq(n+1,m+1) = UnitData[m].Data[n].FinalFreq;
                        }
        }

        //Find minimum and maxmum frequency values for color mapping
        minFreq = mmin(mmin(freq));
        maxFreq = mmax(mmax(freq));

        //Form frequency vector for boundary:average frequency of FDR measurements
        periZ = mean(freq(indx,c_p))*ones(1.0,length(Y));

        //Form frequency vector for griddata: connect boundary frequency and frequency
measurements
        Z = (BR(periZ),freq(indx,c_p));
```

```
        //Form interpolation matrix with griddata(), interpolation method: linear
        ZI = griddata(Xout,Yout,Z,XI,YI,TM("linear"));

        //Return the interpolated matrix
        return ZI;
}
```

Form Movie Frames

The function GenMesh( ) prepares the interpolated measurement matrix that can be used by the function vtkWindowToImageFilter *ImgRender( ). This function utilizes the classes in the VTK library to generate movie frames and save them to an AVI file.

The visualization tool uses an instance of vtkPolyData to represent measurements. The coordinates of each measurement are represented by points, and the corresponding frequency values are represented by the scalars. Then vtkLookupTable maps the frequency scalars to colors. Finally vtkActor represents all the geometries (lines, points, etc.) in a render window.

Some graphic models and their functionalities are

- RenderWindow - contains final image
- Renderer - draws into render window
- Actor - combines properties / geometry
- Mappers - represent geometry
- Transformations - position actors

It is simple to use the pre-defined classes in VTK, which involves creating an instance of a certain class, calling the member functions by defined pointers, and deleting the pointer to release memory. Following is an example.

```
vtkPolyData *Surf = vtkPolyData::New();             //Create an instance of vtkPolyData
Surf->SetPoints(points);                            //Set points to the polydata.
Surf->Delete();                                     //Delete the pointer after using it.
```

The procedures to generate one movie frame are shown in Figure II.13. The function vtkWindowToImageFilter *ImgRender( ) obtains data and time stamps for each frame from the main function, and returns each generated image to the main function. The frames are then written into an AVI file with vtkAVIWriter. Some vtk-format files are read by the function to mask out irrelevant areas and display the state borders and coast lines. They are

EI-border.vtk – defines the borders of states in EI, to be displayed in black.

EI-landmask.vtk – defines the land area outside EI, to be masked in dark grey.

EI-ocean-lake-new.vtk – defines the ocean and lake areas, to be masked in blue.

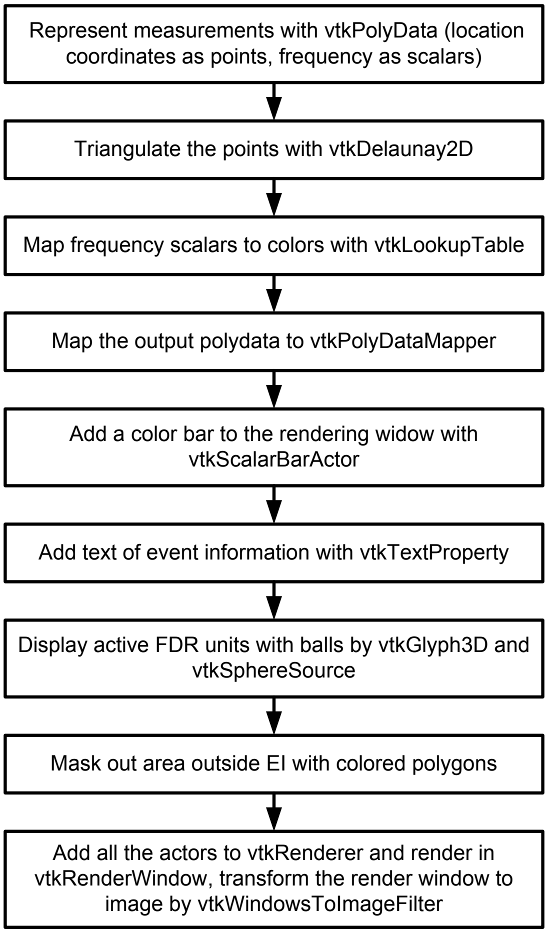

Figure II. 13 Procedures to generate a movie frame

Appendix III. KML File for Overlaying an Image on Google Earth

```
<?xml version="1.0" encoding="UTF-8"?><kml
xmlns="http://earth.google.com/kml/2.1">
  <Folder>
    <name>Ground Overlay</name>
    <description>Examples of ground overlays</description>
    <GroundOverlay>
      <name>Map Overlay 1</name>
      <description>Let's see if a simple lat-lon graph will map nicely to the
globe.</description>
      <Icon>
        <href>FL3.png</href>
      </Icon>
      <LatLonBox>
        <north>55</north>
        <south>22</south>
        <east>-60.5</east>
        <west>-107.8</west>
        <rotation>0</rotation>
      </LatLonBox>
    </GroundOverlay>
  </Folder>
</kml>
```